Understanding and modeling of void closure mechanisms in hot metal forming processes

Michel Saby

To cite this version:

Michel Saby. Understanding and modeling of void closure mechanisms in hot metal forming processes. Other. Ecole Nationale Supérieure des Mines de Paris, 2013. English. NNT : 2013ENMP0075 . pastel-00979301

HAL Id: pastel-00979301
https://pastel.hal.science/pastel-00979301
Submitted on 15 Apr 2014

ParisTech
INSTITUT DES SCIENCES ET TECHNOLOGIES
PARIS INSTITUTE OF TECHNOLOGY

MINES
ParisTech

École doctorale n° 364: Sciences Fondamentales et Appliquées

Doctorat ParisTech

THÈSE

pour obtenir le grade de docteur délivré par

l’École nationale supérieure des mines de Paris

Spécialité “Mécanique Numérique”

présentée et soutenue publiquement par

Michel SABY

le 11 décembre 2013

Compréhension et modélisation des mécanismes de refermeture de porosité dans les procédés de mise en forme des métaux à chaud

–

Understanding and modeling of void closure mechanisms in hot metal forming processes

Directeurs de thèse : **Pierre-Olivier BOUCHARD, Marc BERNACKI**

Jury

M. Michel BELLET,	Professeur, CEMEF, Mines ParisTech	Président
M. Laurent DELANNAY,	Professeur, iMMC, Université catholique de Louvain	Rapporteur
M. Franck MOREL,	Professeur, LAMPA, Arts et Métiers ParisTech	Rapporteur
M. Pedro PONTE CASTAÑEDA,	Professeur, MEAM, University of Pennsylvania	Examinateur
M. Pierre-Olivier BOUCHARD,	Professeur, CEMEF, Mines ParisTech	Directeur de thèse
M. Marc BERNACKI,	Chargé de Recherche, HDR, CEMEF, Mines ParisTech	Directeur de thèse
Mme Joëlle DEMURGER,	Ingénieur de Recherche, Ascometal CREAS	Invitée
M. Yvon MILLET,	Ingénieur de Recherche, TIMET Savoie	Invité

THÈSE

MINES ParisTech
Centre de Mise en Forme de Matériaux – CEMEF
1 rue Claude Daunesse - CS 10207
06904 Sophia Antipolis cedex, France

Contents

Remerciements

En tout premier lieu, je tiens à remercier très sincèrement mes deux directeurs de thèse, Marc et Pierre-Olivier. Directeurs, ils ne l'étaient d'ailleurs pas encore au début de ma thèse, puisque les deux ont soutenu leur HDR entre 2010 et 2013, et que P.O. est désormais Professeur : Bravo à vous deux ! Merci Marc pour ton incroyable réactivité et tes mails à 3h30 du matin. Merci P.O. pour ta disponibilité, malgré les heures de décalage horaire lors de ton séjour outre-atlantique.

Je tiens ensuite à remercier tous les membres de mon jury : MM. Laurent Delannay et Franck Morel qui ont accepté de rapporter ce manuscrit (après avoir déjà accepté de rapporter une autre thèse qui s'est soutenue la veille de la mienne), ainsi que M. Pedro Ponte Castañeda pour avoir bravé les (très) mauvaises conditions météo à Philadelphie pour venir ce jour, et M. Michel Bellet pour m'avoir fait l'honneur de présider ma soutenance dont la date sera difficile à oublier : le 11-12-13 ! Merci également aux deux représentants du consortium industriel, Mme Joëlle Demurger et M. Yvon Millet, d'avoir pu vous rendre présents ce jour au titre du projet Cicaporo, et d'avoir férocement défendu les bénéfices industriels de mon modèle face aux questions incisives des théoriciens.

A ce titre, je souhaite également remercier l'ensemble des partenaires industriels pour m'avoir fait confiance lors du déroulement de cette thèse : Isabelle Poitreault et Mihaela Teaca (Industeel), Evelyne Guyot et Benjamin Martin (Creusot Forge, Areva NP), Myriam Delhomme (CRV, Constellium), Eric Georges et Ludovic Bourgeon (Aubert&Duval Les Ancizes, Issoire), Yvon Millet et Julien Jourdan (Timet Savoie), ainsi que Joëlle Demurger, Didier Lawrjaniec et Gianni Boi (Ascometal CREAS, et désormais collègues). Merci pour votre réactivité, notamment concernant la lecture de mes publications avant soumission, ainsi que vos précieux commentaires lors des réunions d'avancement de thèse à Paris, où nous avons partagé ensemble de succulents repas froids et en plastique.

Je ne saurais oublier toutes les personnes qui ont joué un rôle non-négligeable dans l'avancée de mes travaux de thèse. Je pense notamment à Emile Roux qui m'a sorti d'un certain nombre de pétrins numériques alors que, de mon profil de métallurgiste, je m'initiais à la méthode des éléments finis. Je pense également à Sébastien Brzuchacz du Cetim (Pôle EPI, Senlis) pour m'avoir gracieusement accueilli (et à plusieurs reprises) aux installations de tomographie Tomopic et m'avoir accompagné dans ma quête d'informations concernant ces mystérieux échantillons poreux bougrement opaques !

Je ne pourrais clore cette page de remerciements sans remercier la météo particulièrement généreuse dont bénéficie le Cemef, grâce à qui, par la richesse des activités qu'elle permet, j'ai pu rencontrer une foule de gens incroyables. Je pense notamment aux interminables heures de grimpe à lézarder à la Turbie en plein soleil pendant les fraîches journées d'hiver, ou encore les séances moites au fond des gorges du Loup lors des longues soirées de Juin, grâce auxquelles j'ai pu *croiter* mon premier (et dernier ?) 7c. Merci à toute la bande de grimpeurs du 06 : Alex, Nico Lesage, Titi, Anne, Mathilde, Roman, Ced&Cel, Vince&Sandra, et tous les autres du Cov, de l'US Cagnes escalade, ou avec qui j'ai pu grimper en falaise. Je remercie tout particulièrement Petit Nico pour les découvertes musicales lors des séances de pan et tes imitations des cultissimes répliques de nos films préférés.

Sans oublier, bien évidemment : la Climbing Coloc (Be careful in this time !!), Oliv (et bé ouais), Guigui (triple mystique), puis Jerem (la machine). Merci les gars !

De la grimpe, mais pas que ! Un énorme merci à Nico Dondon pour ton énergie inépuisable, que ce soit pour raconter des histoires à répétition [*rouhouuu*], pour ne jamais attraper froid dans l'eau limpide des magnifiques canyons des Alpes-Maritimes [malgré quelques frissons parfois, mais pour des raisons toutes différentes], pour tes riches enseignements de passing et de LaTeX (Kile!), ou encore les ascensions express des plus beaux sommets du Mercantour tel que le Pétoumier en raquettes ou le Gélas en chaussures sans semelle.

Un grand merci également à toute la bande de percussions africaines qui m'en ont fait prendre plein les tympans pendant les séances de midi, à Jean-Mi pour la masse de rythmes que tu m'as appris, et à Ben pour les sessions de percus improvisées, à l'occasion de la naissance de Mila, ou simplement de la préparation d'un succulent barbeuc chez Margaux et toi.

Un énorme merci à Andrea et à Steffen, qui m'ont fait le plaisir de partager avec moi le bureau pendant ces trois ans, et qui ont subi mes sauts d'humeur et mes innombrables grognes contre certains outils informatiques dont je tairai le nom. Bravo à vous d'avoir aussi réussi à soutenir en 2013, We did it!

Un grand merci aussi à tous les thésards du Cemef avec qui j'ai partagé des repas, des conférences, des réunions, ou encore des exams : Ana-Laura, Ziad, Son, Ugo, Koffi, Fadi, Rebecca, Dorian, et tous les autres.

Il est temps à présent d'exprimer toute ma gratitude à ma famille: à mon frère Pascal qui a toujours été à mes côtés lors des décisions importantes, et à mes parents, Angelika et Alain, qui ont toujours su trouver les mots pour me soutenir, en toutes circonstances, même quand le moral était au plus bas. Ce fût un soutien constant qui s'est vu redoutablement efficace, et je vous dois incontestablement une part de réussite dans cette grande aventure.

Cette grande aventure, je l'ai surtout traversée grâce à l'inflexible soutien de María, sans qui je n'aurais clairement jamais réussi à finir ma thèse dans de telles conditions. Tu as toujours été à mes côtés, même lorsque nous n'étions pas physiquement réunis. Tu as toujours cru en moi, et tu as gravi des montagnes pour moi (au sens propre ET au figuré) ! Je n'oublierai jamais tous les efforts et toutes les concessions que tu as faites pour que nous puissions rester une équipe durant ces dures mais belles années.

C'est pourquoi je te dédie ce manuscrit, fruit de notre réussite à tous les deux.

Merci à tous !
Michel

à María

Introduction

Industrial needs for large metal components for aerospace, transport, or energy applications constantly increase. After casting, the presence of internal voids may be observed in large ingots or preforms. According to client specifications, such internal defects must obviously be eliminated before delivery, as they may significantly affect the mechanical properties of final products. Void elimination is classically performed during the first steps of elaboration, involving hot metal processes (e.g. hot forging or hot rolling).

Prior to delivery, the final soundness of the workpieces is systematically verified. The detected presence of voids in the final workpieces may involve rejection of the workpiece and is, consequently, extremely costly. Designing the forming process in order to enhance void closure is thus of utmost importance. Finite element simulations of processes is generally used, involving the use of a prediction model for void closure. The accuracy of process design is thus mainly driven by the accuracy of the prediction model.

There is at present a lack of understanding of void closure mechanisms. As a consequence, the existing models for void closure are currently unable to provide satisfactory predictions in an industrial context.

Void closure generally involves two stages: the *mechanical closure* of the void (reducing the void volume to zero), and the final bonding of internal surfaces providing complete healing and thus a sound material [Park and Yang, 1996]. The present work focuses on the first stage only: the mechanical closure.

The objective of this work is thus to better understand the involved mechanisms and to define a new reliable prediction model for void closure. This work was supported by an industrial consortium *Cicaporo* involving six partners:

- TIMET Savoie,
- ArcelorMittal (Industeel),
- Areva (Creusot Forge),
- Ascometal (CREAS),
- Aubert&Duval (Les Ancizes and Issoire) and
- Constellium (CRV Services).

Among all industrial data, common statements and common issues regarding void closure are pointed out: large workpieces are concerned, and hot metal forming processes are used to obtain void closure. Nevertheless, such a consortium involves a large diversity in terms of initial void states, processes (hot forging, hot rolling) and materials (various grades of steel, Ti-alloys, Al-alloys). A very important feature of the new developed model is its versatility regarding the wide framework that is considered.

Mean-field models merge as powerful tools to predict voids evolution during process simulation. A *mean-field* model is a function of the current thermo-mechanical state and a set of initial parameters, which is able to predict the evolution of a variable (e.g. the void volume) at any point of a workpiece, during process simulation. The required computation cost of *mean-field* models is generally negligible, as it simply requires the evaluation of a mathematical function.

According to literature, two main approaches were used to study void closure:

- the macroscopic approach, in which entire workpieces containing explicit voids are studied using plasticine [Ståhlberg et al., 1980] or *full-field* finite element simulations [Tanaka et al., 1986, Dudra and Im, 1990, Banaszek and Stefanik, 2006, Kakimoto et al., 2010, Chen et al., 2012] and
- the micro-analytical approach, in which the evolution of an initial geometry in an infinite matrix is analytically predicted [Rice and Tracey, 1969, Budiansky et al., 1982, Duva and Hutchinson, 1984, Zhang and Cui, 2009].

In the present work, a new meso-scale approach is proposed in order to take advantage of both main approaches. The meso-scale approach enables the mechanisms of void closure to be accurately studied at the micro-scale, using *full-field* explicit simulations in a representative volume element (RVE), and using boundary conditions that are representative of the thermomechanical conditions during macroscopic processes.

A wide campaign of simulation at the micro-scale is performed in order to build and calibrate a new *mean-field* prediction model for void closure. The new prediction model for void closure is finally implemented in the finite element software for metal forming FORGE [2011] and compared to existing *mean-field* models from literature using real industrial process cases.

This document is composed of five chapters.

Chapter 1 presents the state-of-the-art of the present work. First, a review of industrial issues within the consortium *Cicaporo* is presented. The framework of the present study and the ranges of values are defined in terms of materials, thermomechanical conditions and initial void states.

It is followed by an extensive literature review of qualitative and quantitative results dealing with void closure. The two main approaches are described and numerous criteria and models for void closure are presented. Their hypotheses are discussed within the ranges of interest regarding the industrial issues and their limitations are pointed out. The great potential of the meso-scale approach is underlined.

Chapter 2 describes the meso-scale and all relative numerical tools that were developed to accurately study void closure mechanisms. The general assumptions are exposed. The RVE methodology is described in details, including the application of boundary conditions and the generation of tridimensional mesh containing a void. Finally, the use of the meso-scale approach is validated regarding the numerical parameters to ensure the results validity.

Chapter 3 presents an experimental validation of the *full-field* simulations performed using the finite element software FORGE [2011]. Simulations of hot compression testing are carried out on samples containing initial voids. The position and the morphology of these voids are obtained using X-ray microtomography on initial samples and after compression. Thee tridimensional experimental observations are compared to the finite element results in order to validate the *full-field* simulations. Then the validated *full-field* formalisms is used at two levels in the following chapters: at the RVE-scale in Chapter 4 to define and calibrate the *mean-field* model for void closure, and at the workpiece-scale in Chapter 5 to compare a few explicit *full-field* simulations of entire processes containing voids, to the new *mean-field* model.

Chapter 4 is dedicated to the study of void closure mechanisms at the micro-scale. The wide campaign of RVE-simulations is described. A parametric sensitivity study to material behaviour, to void morphology (geometry and orientation), and to thermomechanical loading is presented. This study enables identifying the major parameters to be considered for the new prediction model for void closure. The equations for the new prediction model are presented and the calibration step is illustrated with a few examples.

Chapter 5 describes the implementation of the new *mean-field* model in the finite element software FORGE [2011]. The new model is compared to two recent existing *mean-field* models from the literature using a real case of open die forging and a real case of hot rolling. *Full-field* simulations of the processes containing explicit voids are also performed and are considered as reference case for the comparison. The benefits of the new *mean-field* model are underlined and the assumptions are discussed.

The conclusions are finally given and numerous perspectives are proposed according previous discussions.

During this PhD thesis, a paper was published in an international journal:

- M. Saby, M. Bernacki, E. Roux, and P.-O. Bouchard. Three-dimensional analysis of real void closure at the meso-scale during hot metal forming processes. *Computational Materials Science*, 77:194–201, 2013b,

two papers were published in proceedings:

- M. Saby, E. Roux, M. Bernacki, and P.-O. Bouchard. Multiscale analysis of void closure during hot forming process. In *Proceedings of the 29th Forging Industry Technical Conference*, 2012c

- M. Saby, M. Bernacki, and P.-O. Bouchard. Analyse multi-échelle de la refermeture de porosités, appliquée à la mise en forme des métaux à chaud. In *Actes du 11e Colloque National en Calcul des Structures CSMA*, 2013a

and two presentations were held in international conferences:

- M. Saby, M. Bernacki, P.-O. Bouchard, and E. Roux. Sensitivity study for void closure relative to macroscopic mechanical loadings, using finite element simulations at a meso-scale. In *8th European Solid Mechanics Conference*, 2012a

- M. Saby, M. Bernacki, E. Roux, S. Brzuchacz, and P.-O. Bouchard. Sensitivity study for closure of real void relative to macroscopic mechanical loadings, using finite element simulations at meso-scale. In *European Congress on Computational Methods in Applied Science and Engineering*, 2012b.

NB: In this document, references to *papers* are made using the form: [Saby et al., 2013b], and references to *authors* are made with the form: Saby et al. [2013b].

Chapter 1

State-of-the-art

Contents

Résumé français

Ce chapitre présente un état de l'art de l'ensemble des études recensées relatives à la refermeture de porosité. Il est divisé en deux parties.

La première partie présente une synthèse de la problématique industrielle, réalisée à partir de l'ensemble des données recueillies auprès des différents partenaires industriels. Les différents matériaux, procédés, et états de porosités initiaux sont listés afin de clairement définir le domaine d'étude. Les états initiaux de pores présentent généralement des formes complexes (allongées, polygonales ou interdendritiques). Leur position est très majoritairement située sur l'axe central des lingots. Les orientations sont variables (selon l'axe principal du lingot, en V-ségrégés ou distribuées aléatoirement). Les tailles de pores rencontrées varient d'environ 0,01 mm à 45 mm. Plusieurs nuances d'aciers, d'alliages de titane et d'aluminium sont concernées par la problématique industrielle. Les comportements à chaud sont en revanche relativement similaires. L'écrouissage est faible et est souvent suivi d'un adoucissement. Les coefficients de sensibilité à la vitesse de déformation m sont compris entre 0,1 et 0,3. Au cours des procédés, les trajets de chargement thermo-mécaniques présentent des profils d'évolutions très différents. Cependant, la plage de valeurs de la triaxialité des contraintes $[-1, 0]$ est représentative de l'ensemble des procédés recensés. Les vitesses de défomation varient de 0,01 à 10 s^{-1}. Les contraintes d'écoulement varient de 10 à 100 MPa.

La seconde partie dresse un bilan des études existantes traitant de la refermeture de porosité dans la litérature. Il est montré que les approches explicites macroscopiques permettent d'obtenir de nombreux résultats qualitatifs quant aux paramètres pocédés influents sur la refermeture de porosité. Des étude quantitatives empiriques ont également proposé plusieurs modèles et critères relatifs à la refermeture de porosité. Ils sont en grande majorité basés sur le produit de la triaxialité des contraintes et de la déformation équivalente. Ensuite, les études micro-analytiques traitant de la refermeture de porosité sont présentées, et les modèles analytiques qui en découlent sont décrits. Leurs hypothèses sont discutées vis-à-vis de la problématique industrielle. Une comparaison finale de l'ensemble des modèles recensés (empiriques, analytique, et semi-analytique) est proposée sur le domaine d'intérêt défini dans la première partie. Il est montré que les hypothèses sont fortement restrictives, notamment en terme de géométrie initiale de pore (géométrie sphérique exclusivement considérée), et prise en compte du changement de forme de la porosité en cours de déformation. Le modèle semi-analytique de Zhang et al. [2009] semble être le modèle le plus avancé.

1.1 Introduction

This chapter presents an extensive state-of-the-art regarding studies dealing with void closure in hot metal forming. It is divided in two sections.

The first section deals with industrial issues. The issues are described in order to evaluate the variety in terms of materials, processes and initial states of voids. The main objective of this section is to draw a clear framework of the parameters to be considered, and to determine their ranges of interest.

The second section describes the main results from literature regarding studies about void closure. Qualitative results, and quantitative models are described and discussed. An extensive comparison of existing models in the literature is presented. Their hypotheses and ability to predict void closure in an industrial context are discussed.

1.2 Industrial issues

A review of industrial issues is presented in this section. All data regarding initial observations of porosity, materials and process conditions were collected and analyzed in order to accurately draw the frame of the current work.

1.2.1 Initial void observations

Historical and recent studies regarding void observations were collected from each industrial partner, and are summarized in Table 1.1. The voids are observed using ultrasonic (US) testing techniques and visual inspection (metallography).

Source	Ingot type	Pos.	Shape	Direction	Size (mm)	Obs.
Timet	∅830×2000 as–cast	Center	–	–	0.01–0.1	Visual
Aubert&Duval	600×600×2000 as–cast	Center	Interdendritic	–	< 45	US
Improsound[1]	185×185 as–cast	Center	Elongated	Billet axis	5×20	Visual
	365×265 as–cast	–	Equiaxed	–	0.03	US
Ascometal	∅500×2700 as–cast	Center	Elongated	V–segregate	5×25	Visual
CRMC[2]	178T as–cast	–	–	–	<40	–
	161T as–forged	Center	Polygonal	–	–	–
	2.6T as–cast	–	–	Billet axis	3–7 × 20	Visual
	550×550 forged	–	Interdendritic	–	1–20	Visual
	550×550 rolled	–	Polygonal	Billet axis	0.25×0.1	Visual
	550×550 rolled	–	Polygonal	Equiaxed	∅0.8	Visual
Constellium	–	Center	Elongated	Diffuse	0.1–0.7	US, μtomo

Table 1.1: Available industrial void observations.

Ultrasonic scanning allows a localization of defects in the workpiece, and provides an order of magnitude of void size. For the detections of voids, the *flat-bottom hole equivalence* is used. This technique consists in comparing the signal amplitude to the response of a flat-bottom hole. The correlation of signals provides an evaluation of the void's diameter. This technique shows accurate results for the case of voids that present a relatively flat shape in

---

[1] Improsound was a common industrial project from the European Commission that was supported by the Research Fund for Coal and Steel, see Llanos et al. [2008].

[2] CRMC stands for *Centre de Recherche des Matériaux du Creusot*, and includes observations from Industeel and Creusot Forge.

the direction perpendicular to the ultrasonic wave. However, the technique becomes rather limited in the case of more complex geometries, such as tortuous morphologies or cluster of voids.

A precise morphology examination can be obtained using metallography. Excellent resolutions can be obtained by using adequate observation equipment (i.e. microscope). The main limitation of this technique is that it is destructive, and that only 2D information is obtained, according to the cutting plane.

From all observations given in Table 1.1, it can be stated that voids are mostly located at the core of ingots (central axis). According to several cases, higher void densities are also observed in the upper half of the ingot, at the head (i.e. feeder), or at the foot of the ingot.

From a general point of view, void shapes are rather complex. They are generally angular (assumed polygonal), and may sometimes even present an interdendritic structure, typical from shrinkage effect during cooling of the ingots. Many observed voids were elongated in the direction of the billet axis, or in the direction of the V-segregates.

The size of voids is rather disperse. Tiny voids with an average diameter $[10, 30]\mu m$ were observed at Timet on Ti-alloys, as well as in the Improsound[1] report Llanos et al. [2008] on steels. Larger voids, up to 40 mm, were observed in the largest ingots (at CRMC[2] and Aubert&Duval). In the case of Aubert&Duval, the values obtained using US measurements may actually represent the size of an area containing a cluster of small voids, which individual sizes within the range $[0.2, 1]$ mm.

1.2.2 Materials

The alloys that are mainly considered regarding industrial issues are given in Table 1.2. Various grades of steels were identified, as well as two grades of titanium alloys and three grades of aluminium alloys.

Among all materials, one behaviour law was selected for each partner, according to common agreements, in order to get a representative sampling of the materials considered within industrial issues. The behaviour laws are visco-plastic with strain hardening (power-law), or with strain hardening–softening (Hansel-Spittel, GNHB-type). For the Ti-alloy, the behaviour is given using tabulated curves (obtained from experimental data).

Source	Materials
Timet	Ti-alloy1, Ti-alloy2
Aubert&Duval	Steel10, Steel11, Steel12, Steel13, Steel14
Ascometal	Steel20, Steel21, Steel22, Steel23, Steel24
Industeel	Steel30
Creusot Forge	Steel40
Constellium	Al-alloy1, Al-alloy2, Al-alloy3

Table 1.2: Affected materials and their corresponding type of casting (exact grades are not given here for confidential reasons).

From a general point of view, flow stress values present comparable orders of magnitude for all materials, as presented in the example given in Fig. 1.1.

Strain hardening behaviour

Material laws in Fig. 1.1 present rather heterogeneous strain hardening properties. Steel10, 20, 30 and Al-alloy1 exhibit monotonous hardening features, with different coefficients. The case of Steel40 presents a comparable strain hardening, but it is followed by a softening behaviour after a certain value of cumulated strain. The softening behaviour is also a typical characteristic of Ti-alloys. In the case of Ti-alloy1, a maximum value of flow stress is reached at a very early stage of deformation, followed by a slightly decreasing softening behaviour.

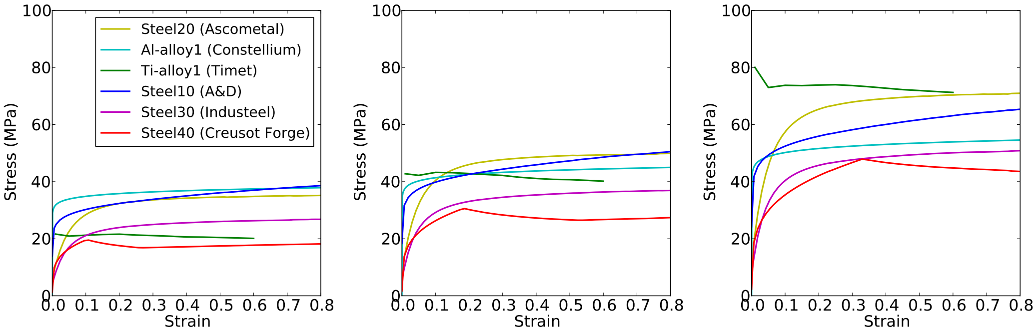

(a) $\dot{\bar{\varepsilon}} = 0.01\ \mathrm{s}^{-1}$ (b) $\dot{\bar{\varepsilon}} = 0.1\ \mathrm{s}^{-1}$ (c) $\dot{\bar{\varepsilon}} = 1\ \mathrm{s}^{-1}$

Figure 1.1: Stress-strain curves of selected materials at working temperature, for various strain-rate values.

Materials' dependence to strain-rate

The dependence to strain-rate varies between materials. From Fig. 1.1, the strongest dependence can be seen for the Ti-alloy1. Its average value of flow stress increases by a factor 3.5 between cases (a) and (c). The smallest influence is observed in the case of Al-alloy1 and Steel10.

1.2.3 Processes

From each industrial partner, one typical process was chosen. The objective here is to precisely understand what material undergoes in each considered process, and to draw a framework regarding thermo-mechanical conditions. The choice was made in order to obtain the largest diversity in terms of ingot geometry, and considered process.

In total, six industrial cases (ingot + process) were simulated with the finite element software FORGE [2011], according to existing industrial data. The software is briefly described in Appendix A. The simulations were performed at the macroscopic scale, using void-free ingots:

- Forging of cylindrical ingot between hammer and flat dies at Timet.
- Forging of rectangular ingot between hammer and flat dies at Industeel.
- Forging of cylindrical ingot between V-shaped dies at Creusot Forge.
- Incremental cogging of cylindrical ingot at Aubert&Duval.
- Rolling of rectangular bloom at Ascometal.
- Rolling of plate at Constellium.

The simulations of forging (Industeel, Creusot Forge), rolling (Ascometal) and incremental cogging (Aubert&Duval) were computed at Cemef using FORGE®. Input data were provided by each partner. The forging simulations for Timet and the plate rolling simulations for Constellium were performed in-house using DEFORM and LAM3, respectively. Fig. 1.2 illustrates the diversity of geometries and processes that are involved in the current framework.

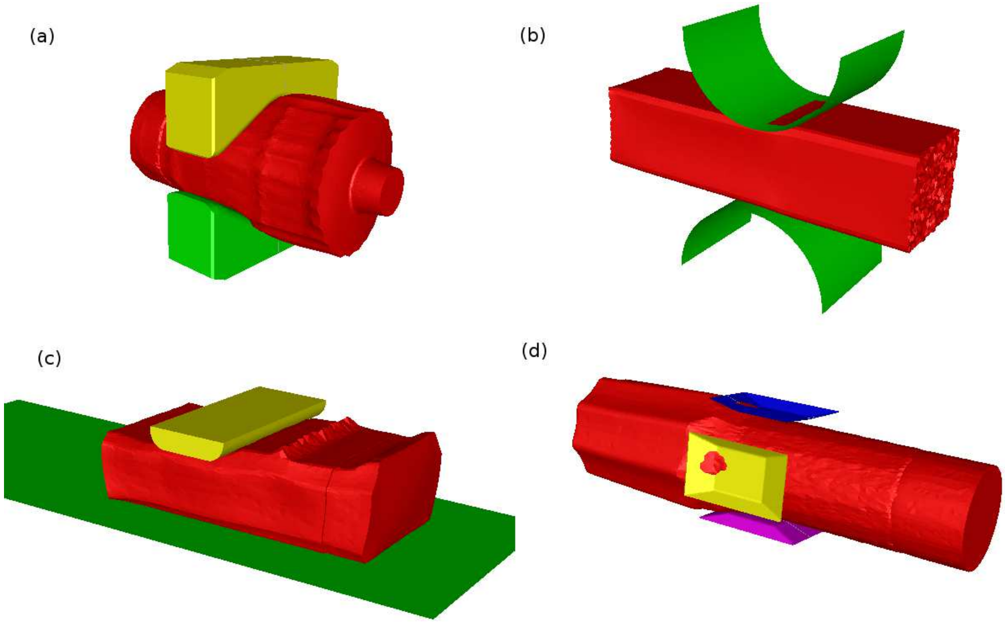

Figure 1.2: Ingot geometries and process overview for (a) forging at Creusot Forge, (b) rolling at Ascometal, (c) forging at Industeel, (d) incremental cogging at Aubert&Duval.

All processes are multi-pass processes, and lead to long computation times. They will not be described in further details for two main reasons. First, most industrial data (workpiece geometries, pass depths, working temperatures) are strictly confidential data. Second, these data would, in fact, not bring significant information to further discussion, since the crucial information is the local thermo-mechanical state during the process. The description will thus be focused on local loading paths.

To obtain such information, the point tracking technique was used. This technique enables thermo-mechanical fields to be recorded during the whole process, for a given point at every increment step. The field values are interpolated using the values computed at integration points. The position is actualized according to the displacement field at each increment step.

1.2.4 Thermo-mechanical local loadings

For each industrial case, several points of interest were defined in the workpieces. Centerline positions were chosen according to initial void observations (Table 1.1). The points were then tracked for each multi-pass process in order to obtain the local thermo-mechanical loading paths. The evolutions of strain-rate, temperature, von Mises equivalent stress and stress triaxiality ratio are presented in this section.

Evolution of strain-rate

For the four processes given in Fig 1.2, the values of strain-rate are presented for a cross-section in Fig. 1.3. The measured strain-rate values (given in log-scale) strongly vary between the four presented processes. In Fig. 1.4, the values recorded using point tracking are plotted for all processes. These values are within the range $[0.001, 0.1]$ s^{-1} for forging processes, in the interval $[0.1, 1]$ s^{-1} for incremental cogging, and in the interval $[1, 10]$ s^{-1} for rolling.

Let us now focus on the evolution profile of each curve. For the cases of free forging (Industeel, Timet), each stroke induces a rapid increase of the local strain-rate, followed by a rather constant value, then a brutal stop. The material mainly undergoes a quasi steady deformation over the whole stroke duration, with a strain-rate around 0.01 s^{-1}.

In the cases of rolling (Ascometal, Constellium), the material undergoes more continuous strain-rate profiles. The local deformation accelerates then decelerates, by passing through the rolling cylinders. The maximum value of strain-rate is higher, around 5 s^{-1}.

The strain-rate profile for incremental cogging presents common aspects with rolling and forging, i.e. a slight increase and a brutal stop. The average value of strain-rate is about 0.5 s^{-1}.

In the case of forging at Creusot Forge the values present rather complex evolutions. The values of strain-rate (about 5.10^{-3} s^{-1}) present the lowest values over all considered cases.

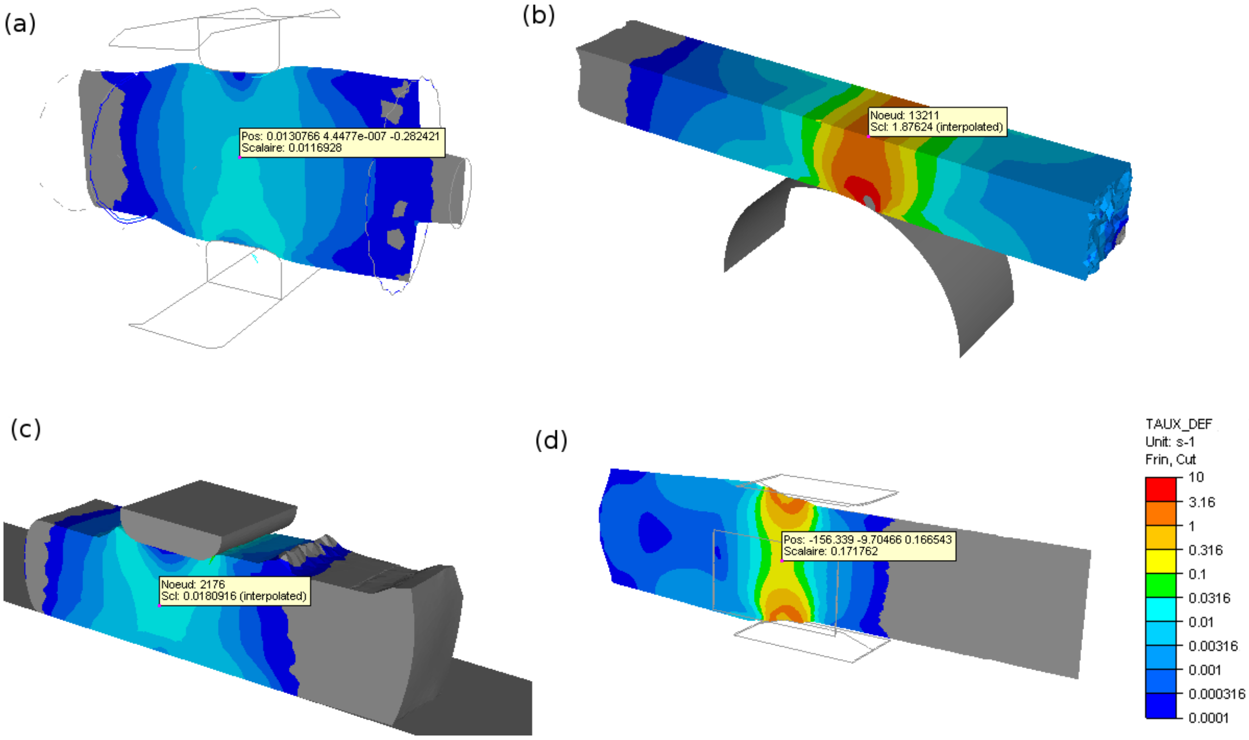

Figure 1.3: Maps of strain-rate for the four processes with cutting planes at the core of each workpiece, in log-scale: (a) forging at Creusot Forge, (b) rolling at Ascometal, (c) forging at Industeel and (d) incremental cogging at Aubert&Duval.

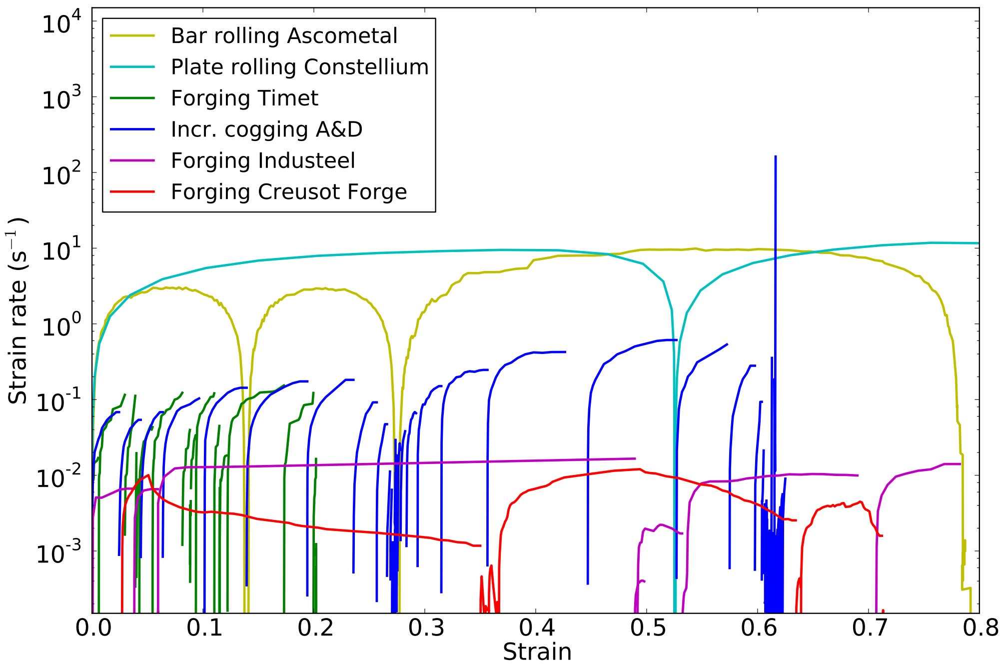

Figure 1.4: Evolution of equivalent strain-rate of a centerline point tracked during multi-pass processes.

Evolution of temperature

Let us now focus on the evolution of temperature during processes. The values were obtained using the point tracking technique described previously, and are plotted in Fig. 1.5. The figure shows that the temperature slightly increases due to self heating during each deformation stroke/pass. The highest temperature increase is about 10°C. A few temperature drops can also be observed, such as in the case of incremental cogging (Aubert&Duval) at 0.27 and 0.6 strain. This is due to natural loss of temperature of the workpiece (heat transfer with dies and with surrounding air). This effect can be neglected since the resulting drop does not exceed 2°C.

Nominal working temperatures are typical for hot forming processes, i.e. around 1100°C for Ti-alloys, around 1200°C for steels and around 450°C for Al-alloys. The previous increases and drops may thus be insignificant with respect to workpiece temperatures. Isothermal conditions can therefore be assumed.

Evolution of von Mises equivalent stress

The values of von Mises equivalent stress are driven by the material's behaviour law (previously presented in Fig. 1.1) taking into account the real process conditions presented in Figs. 1.4 and 1.5. The resulting values are plotted in Fig. 1.6. They were obtained using the identical point tracking technique described previously for strain-rate and temperature. The values of von Mises equivalent stress vary with a factor about 3 between forging processes (lowest values) and rolling processes (highest values). The equivalent stress for incremental cogging is between the two previous cases. Similar evolution profiles can be observed as the ones for strain-rate. The forging processes induce rather steady values with brutal decrease, while rolling processes induce smoother curves.

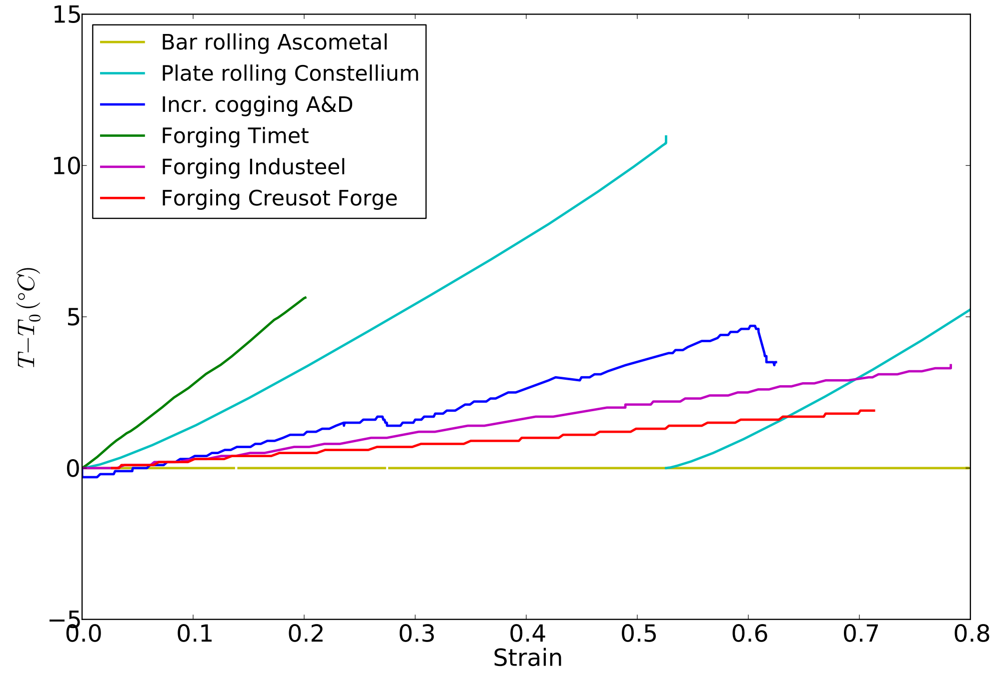

Figure 1.5: Temperature increase of a centerline point tracked during simulation processes.

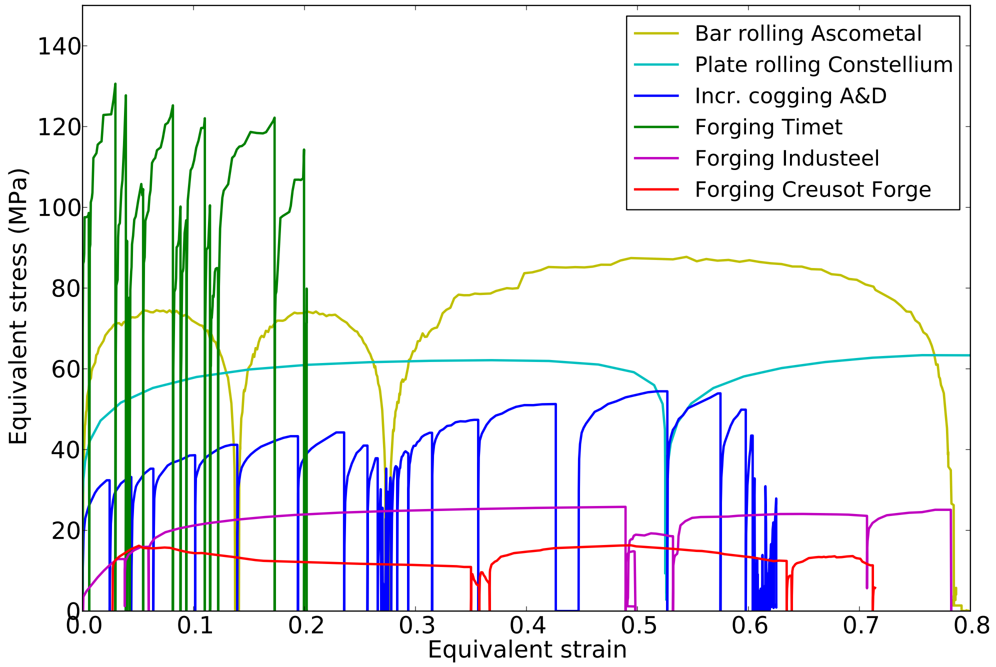

Figure 1.6: Evolution of von Mises equivalent stress of a centerline point tracked during simulation processes.

Evolution of stress triaxiality ratio

The stress triaxiality ratio is defined as the ratio between the mean stress σ_m (or the isostatic pressure p) and the von Mises equivalent stress $\bar{\sigma}$, such that:

$$T_X = \frac{\sigma_m}{\bar{\sigma}} = \frac{-p}{\bar{\sigma}}. \tag{1.1}$$

The ratio is positive for tensile state, and negative for compressive state. The particular value $T_X = \frac{1}{3}$ describes uniaxial tension and $T_X = -\frac{1}{3}$ uniaxial compression. When $T_X \approx 0$, shearing stresses are predominant.

In Fig. 1.7, the evolutions of stress triaxiality ratio are plotted versus cumulated equivalent strain. This choice was made as it presents the advantage that the integral of stress triaxiality ratio with cumulated strain is easy to visualize (using the area under the curve). This integral is often used in the literature as an indicator for void closure Tanaka et al. [1986], Nakasaki et al. [2006], Llanos et al. [2008]. It might provide a first approximation of void closure and will be discussed later in section 1.3 and compared to further criteria.

The curves in Fig. 1.7 exhibit a few isolated extreme values. When isolated, these extreme values of stress triaxiality ratio have no significant impact on void closure, as the void does not undergo any deformation at this instant. The sharp peaks can thus be simply ignored.

On the contrary, according to the criterion mentioned above, the area under curve provides an indication whether the conditions are favorable for void closure, or not. Negative areas are favorable for void closure.

In the present chapter, the objective of Fig. 1.7 is only to illustrate the variety of mechanical loading paths that may be encountered within the industrial consortium. An extensive discussion regarding the efficiency of each process would not be relevant here, as the criteria was not yet clearly defined, and may in fact be insufficient to accurately predict void closure (discussed in Chapter 4).

Nevertheless, Fig. 1.7 shows great interest to set the ranges of interest within this study. For forging processes (Industeel, Creusot Forge) the evolution presents a rather smooth decrease and mostly remains within the range $[-0.7, -0.5]$. The evolution of stress triaxiality ratio in the case of plate rolling (Constellium) reaches similar values in the interval $[-0.7, -0.5]$. These three cases can be seen as the processes providing the most compressive states.

The evolution of T_X for bar rolling (Ascometal) is comparable to the one of plate rolling (Constellium), starting and ending with very compressive states, and presenting a rather constant value over the main deformation range. Nevertheless, the case of bar rolling (Ascometal) presents less compressive states. It is worth noticing that the third pass presents more compressive values, while the two previous ones are rather tensile. The values remain in the interval $-\frac{1}{3} < T_X < \frac{1}{3}$.

The case of incremental cogging (Aubert&Duval) presents the highest amplitude variations, even though most of the values are within the range $-\frac{1}{3} < T_X < \frac{1}{3}$ as well. Higher values are briefly reached, leading to very tensile states for several strokes ($T_X > \frac{1}{3}$).

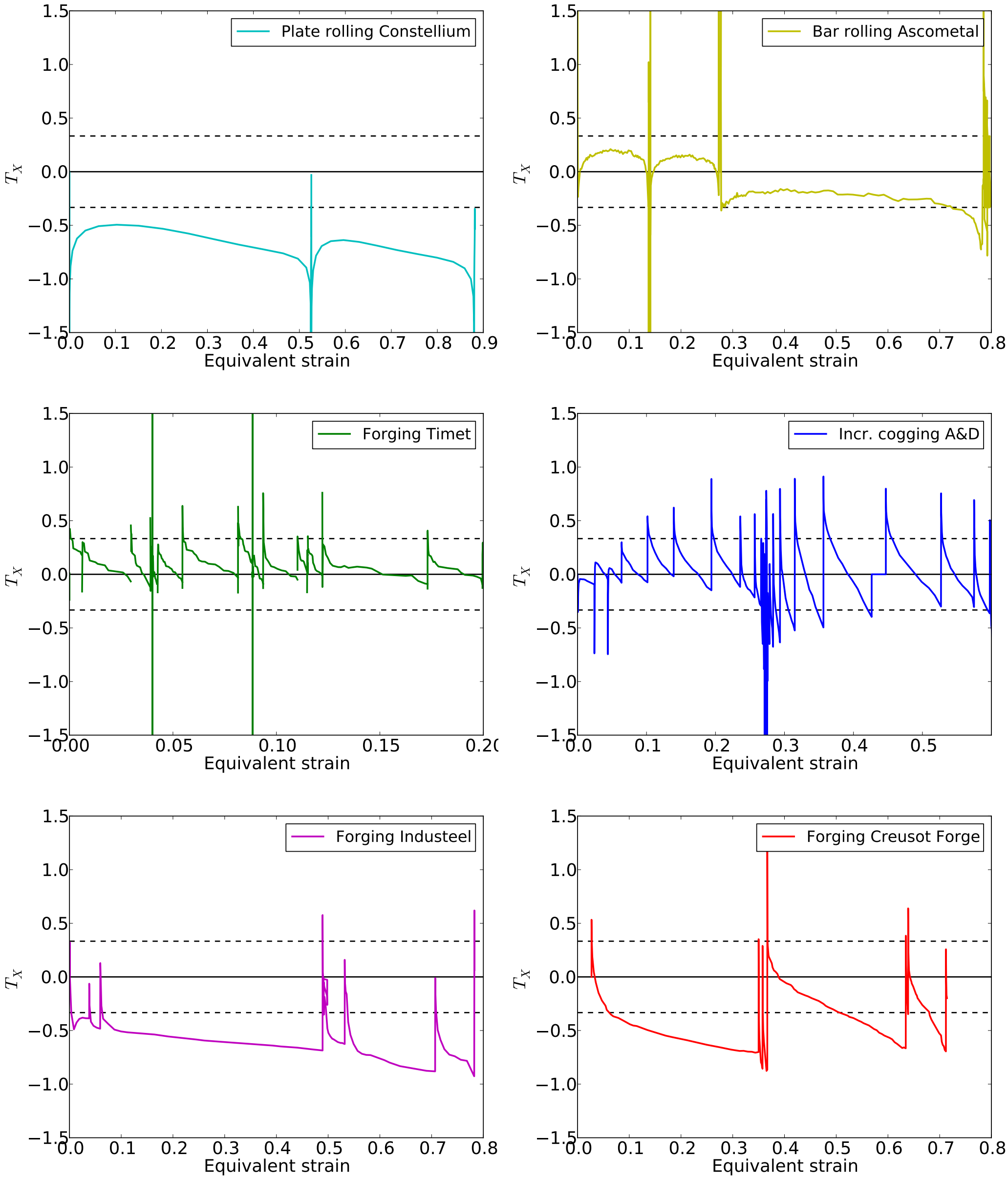

Figure 1.7: Evolution of stress triaxiality ratio of a centerline point tracked during simulation processes.

1.2.5 Conclusions

Industrial issues were analyzed according to initial void states, materials and process conditions. It was found out that:

- Initial void geometries present complex shapes, such as interdendritic, polygonal, or elongated shapes. Their position in the ingots is mainly centerline, and their orientation is not unique. They may be oriented along the ingot's axis, along the V-segregates, or even present random orientations. Void sizes are between $[0.01, 45]$ mm. The void-to-billet ratios are generally about 10^{-4} to 10^{-3}, and do not exceed 0.075 within the industrial framework.

- Various material behaviours were identified. Materials with monotonous strain hardening may be distinguished from the ones presenting a subsequent softening behaviour. Nevertheless, comparable orders of magnitude regarding flow stress values were observed in the considered working conditions. The strain-rate sensitivities of materials are within the range $m = [0.1, 0.3]$.

- Six different types of processes are considered. From the resulting local thermo-mechanical loadings, the following conclusions are made:
  - Temperature evolution of a material point is insignificant and can be neglected.
  - strain-rate values vary on a range $[0.01, 10]$ s^{-1}.
  - The flow stress values vary on a range $[10, 100]$ MPa.
  - Stress triaxiality ratios present very different evolution profiles. The values vary on a range $[-1.0, +0.6]$. Here, positive values may lead to an opening phenomenon of voids. Void growth is a part of ductile damage micro-mechanisms that leads to coalescence and final fracture Schlüter et al. [1996]. Many studies were conducted according to theories developed by Rice and Tracey [1969] or Gurson [1977]. Yet, the present work is restricted to void closure only, i.e. on the range $T_X = [-1, 0]$.

1.3 Literature review: models and criteria for void closure

According to literature, void closure generally involves two stages: the *mechanical closure* of void, bringing internal surfaces into contact and reducing void volume to zero; and the *final bonding* of the internal surfaces providing complete healing and thus a sound material [Park and Yang, 1996]. The present work focuses on the first stage: the mechanical closure. A review of the most important results from literature regarding mechanical closure is given in this section.

Two different approaches are presented in literature regarding the mechanical closure phenomenon: (i) an explicit macroscopic approach, and (ii) a micro-analytical approach.

- The explicit macroscopic approach consists in studying a whole process with a workpiece in which voids are explicitly defined. The influence of various parameters on void closure is studied using experimental data [Ståhlberg et al., 1980, Wallerö, 1985] or finite element simulations [Hwang and Chen, 2002, Tanaka et al., 1986, Dudra and Im, 1990, Banaszek and Stefanik, 2006, Kakimoto et al., 2010, Chen et al., 2012]. Criteria and prediction models are presented in a first section, as well as a discussion regarding their benefits and limitations.

- The micro-analytical approach considers a single void in an infinite matrix [Rice and Tracey, 1969, Budiansky et al., 1982, Duva and Hutchinson, 1984, Zhang and Cui, 2009]. The void volume evolution is analytically predicted, according to a certain number of assumptions. A review of these analytical prediction models is presented in a second section, and the assumptions are discussed.

A third section mentions Gurson-based models [Gurson, 1977]. Such models were initially developed for predicting the global behaviour of porous materials and were dedicated to ductile fracture (void growth under positive stress triaxiality ratios). However, interesting features were found out regarding void evolution and are compared to the approaches regarding void closure.

1.3.1 Macroscopic approach

Due to the great industrial interest in understanding void closure, numerous studies on void closure were conducted using the macroscopic explicit approach. This approach enables a process to be partially or fully described and the closure mechanisms to be studied in accurate process conditions. The influence of process parameters is studied in order to establish qualitative or quantitative relationships between the parameters and the void closure efficiency.

This review focuses on forging and rolling processes. Main qualitative results are summarized first, with a brief description of the studies conditions (considered processes, types of voids). In a second part, existing prediction models are presented and discussed.

Qualitative results

The macroscopic explicit approach generally involves experimental testing or numerical simulation. From a general point of view, the following statements are found out:

(i) large deformations, especially in the first stages of forming processes, are preferred for better void closure [Tomlison et al., 1958, Ståhlberg et al., 1980, Keife and Ståhlberg, 1980, Zutang and Meng, 1994, Wallerö, 1985, Hwang and Chen, 2002, Chen, 2006, Chun et al., 2006, Banaszek and Stefanik, 2006, Chen et al., 2011, Llanos et al., 2008];

(ii) a relevant choice of process configuration may considerably improve the void closure efficiency: shaped-dies for forging [Dudra and Im, 1990, Tomlison et al., 1958, Park and Yang, 1997a, Shah et al., 1986, Chun et al., 2006, Kim et al., 2002, Banaszek and Stefanik, 2006] and large roll radius for rolling [Wallerö, 1985, Chen, 2006, Chen et al., 2011, Llanos et al., 2008, Ståhlberg, 1986];

(iii) temperature gradient in the workpiece also plays an important role and it is shown that a colder skin improves the closure of centerline voids [Ståhlberg and Keife, 1992, Pietrzyk et al., 1995, Överstam and Jarl, 2004, Banaszek and Stefanik, 2006, Llanos et al., 2008, Park and Yang, 1997b].

(iv) friction with dies may also improve the voids closure efficiency [Hwang and Chen, 2002, Chen, 2006].

Hot forging Further details are given here for *open die forging* and *cogging* processes. The conditions are briefly summarized in Table 1.3. Most studies consider steel in its typical working temperature (900-1250°C). Aluminium, plasticine and lead (Pb) are also used. Height reduction ratios vary between 10 and 40% per pass. In general, it is shown that larger values are preferred for a better closure. In the case of multi-pass forging, it is shown that the reduction of the first pass is predominant [Chun et al., 2006].

Source	Material	Process, billet dim. (mm)	T (°C)	Reduc. (%) or eq. strain	strain-rate (s^{-1})	Void shapes	Void/billet ratios
Dudra and Im [1990]	Steel, plasticine	Open die Ø2800	1230	30%	0.01	2D cylinder	0.07
Park and Yang [1996, 1997a]	Steel	Open die Ø100 x L80	1000–1200	0.35	0.01	Cylinder	0.1
Kim et al. [2002]	Steel	Multipass 300x350	1043→848	40%	0.1–0.2	Sphere, cylinder	0.03
Överstam and Jarl [2004]	Steel	Open die	1100	–	–	–	–
Banaszek and Stefanik [2006]	Steel	Open die Ø80 x L80	1100–1250	0.15–0.25	0.1–0.2	2D cylinder	0.05–0.12
Chun et al. [2006]	Steel	Multipass	1000	30%	–	–	–
Nakasaki et al. [2006]	Steel, plasticine	Open die 95 x 75 x L200	1000	10-25%	–	–	–
Lee et al. [2007]	Steel	Cogging Ø90 x L220	800, 1000, 1200	0.8	–	Natural	0.5
Kakimoto et al. [2010]	Aluminium	Compression	450	80%	–	Sphere, cylinder	0.01, 0.05, 0.1, 0.2
Kakimoto et al. [2010]	Steel, Pb-valid.	Open die Ø40 and 35x35 x L36	900–1200	30%	0.02–2	Open cylinder	0.05
Chen et al. [2010]	Steel	Open die Ø25 x 40	1150–1200	42%	–	Sphere, cylinder, tetrahedron	0.025-0.125
[Agouti, 2012, chap IV]	Aluminum	Multi-pass forging	420	1.3 – 8.9	0.02 – 0.2	Natural	0.001

Table 1.3: Review of tested conditions regarding main studies on forging processes.

Överstam and Jarl [2004] investigated the effects of natural cooling and the one due to the contact with the tools. Surface cooling generally has a positive effect on void closure. The study shows that the effect of temperature gradient is significant for small billets (size $< 200 \times 200$ mm), but becomes negligible for large billets.

The influence of strain-rate has not been studied regarding void closure evolution.

Different tool shapes were investigated: bowl-shape [Tomlison et al., 1958, Banaszek and Stefanik, 2006], V-shape [Tanaka et al., 1986, Chen et al., 2012], FML (Free of Mannesmann effect at Lower press load) [Dudra and Im, 1990], and BFTV (Bottom Flat Top V) [Park and Yang, 1997a]. Concave tools are shown to provide better void closure. The positive effect of concave dies, compared to flat dies, results from a more compressive stress triaxiality states at the billets center. This is coherent with the effect of temperature gradient (colder skin) mentioned previously, as both involve more compressive states at the core of workpieces.

Banaszek and Stefanik [2006] studied the evolution of a 2D–section of a billet containing circular voids during hot forging. They proposed a relation between the total surface area of defects and forging parameters (i.e. upper die speed, relative reduction and starting temperature). A statistical analysis on case studies was performed using finite element simulations and several experimental validation cases. The authors concluded that void closure is enhanced when using asymmetrical concave dies in the early stages, and flat dies in the final stages of forging.

Hot rolling For the studies regarding rolling processes, steel was mostly studied as well (see Table 1.4). The technical report *Improsound* [Llanos et al., 2008] relates a large quantity of results regarding the optimization of multi-pass hot rolling. Several pass-schedules are studied. It is shown that a one-pass schedule brings better void closure than a two-pass schedule with identical cumulated reduction ratios. Further studies regarding multipass schedules confirmed that the effect of the first pass is predominant regarding void closure. Lower numbers of passes with large reductions, and without turning the billet between the passes, are recommended for better void closure. Wallerö [1985] studied the effect of rolling conditions and concluded that passes involving large spread are favourable as well.

Source	Material	Process, billet dim. (mm)	T (°C)	Reduc. per pass	Roll diam (mm)	Void shapes	Void/sheet ratios
Wallerö [1985]	Steel, plasticine	Multipass	1100	2–20%	–	Artificial	0.05
Pietrzyk et al. [1995]	Steel	Multipass, 200x200	1200	4–16%	450	2D Cyl.	0.25
Wang et al. [1996]	Steel	3–pass, H20x150x80	900–1200	30, 50, 70%	300	Half-open	0.06
Nakasaki et al. [2006]	Steel, plasticine	1–pass, 80x60x200	1000	8–33%	220	Open cylinder	–
Llanos et al. [2008]	Steel	Multipass, 137x137 or 365x265	1100–1200	2–15%	510–670	Natural + Artificial	0.015–0.06
Toda et al. [2009]	Aluminium	2–pass 3x0.6x0.6 (samples)	pass 400°C(50%), pass 320°C(50%)		–	Natural (X-ray tomo)	1.7–8.3 $\times 10^{-3}$
		Compression	540	6–60%	–		

Table 1.4: Review of tested conditions regarding main studies on rolling processes.

The tested temperatures are comparable to the ones tested for forging (900-1200°C). As for forging, the temperature gradient between the skin and the core of the workpieces is shown to improve void closure.

Rolling of aluminium was studied as well by Toda et al. [2009]. The study deals with a succession of rolling passes at various temperatures. A diffuse state of voids is tracked using X-ray microtomography according to various compression ratios and annealing periods. A geometry dependence is observed regarding void closure. An increase of void fraction is also pointed out during high temperature exposure, such as void growth or reopening of closed voids.

Initial void state Model holes are generally used to investigate the influence of parameters on void closure. The geometries typically involve spheroidal or cylindrical shapes.

Hot compression tests on aluminum samples containing cylindrical voids were conducted by Kakimoto et al. [2010] (see Fig 1.8). The study shows that the critical reduction required for complete void closure is mainly influenced by the height h_0 of the void (in the compression direction). The perpendicular dimension did not show any significant effect on void closure.

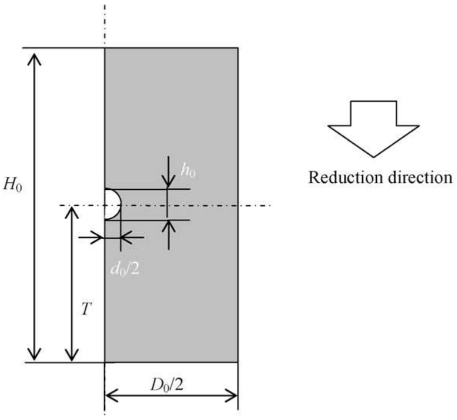

Figure 1.8: Dimensions used for the hot compression tests performed by Kakimoto et al. [2010], acording to various conditions $h_0/d_0 = 1, 2, 5$; $H_0/T = 2, 4$; $d_0/D_0 = 0.01, 0.05, 0.1, 0.2$.

Closure mechanisms are discussed by Chen et al. [2010] with respect to various void shapes (spherical, tetrahedral, and cylindrical), at different positions in a billet under compression (see Fig. 1.9). Long cylindrical voids present a two-stage mechanism: firstly, the upper and lower surfaces rapidly enter into contact, and secondly, the small subsequent holes are more hardly closed up. It is also shown that tetrahedral voids are longer to completely close than spherical voids.

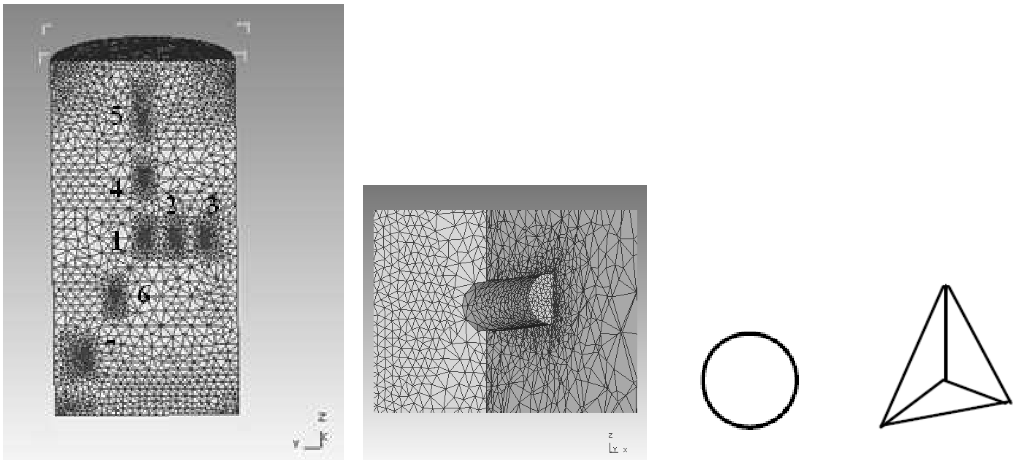

(a) (b) (c) (d)

Figure 1.9: Tested positions (a) and void shapes (b,c,d) in Chen et al. [2010].

The change of position in the billet induces a change in closure rate. Closure is faster in the center of the billet. However, it is shown that the behaviour remains unchanged at any tested position within the billet. In the technical report *Improsound* [Llanos et al., 2008], rolling trials were performed in order to compare different initial states. A billet was designed to contain several pre-defined void states that were inserted in its center (see Fig. 1.10). The pre-defined states were a 3×3 matrix of holes, a central single hole, and a natural porosity state. From metallographic examinations, it is shown that the hole in the center of the billet is completely closed, whereas those off-center are only partially closed.

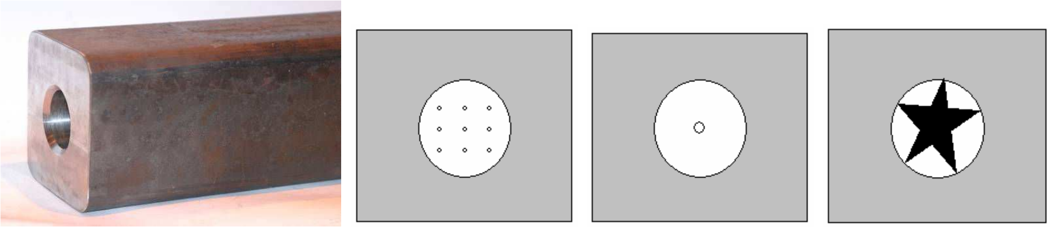

(a) (b) (c) (d)

Figure 1.10: Rolling pilot plant trial billet (a) with pre-defined porosity states (b) 3×3 matrix, (c) central hole, and (d) natural state (schematically represented), Improsound [Llanos et al., 2008].

The effect of the hole's position in the billet is also presented by Wang et al. [1996]. In these experiments, the holes were drilled in the direction perpendicular to the rolling direction (see Fig. 1.11) and were drilled from the surface of the billet, providing half-opened holes. This contrasts with the holes defined in [Llanos et al., 2008], which are oriented along the deformation direction and fully embedded in the billet. In the rolling trials performed by Wang et al. [1996], the holes were better closed when positioned near the billet's surface. This result is mainly attributed to the value of hydrostatic pressure at the positions of the voids. It is also shown that shear is helpful for void closure.

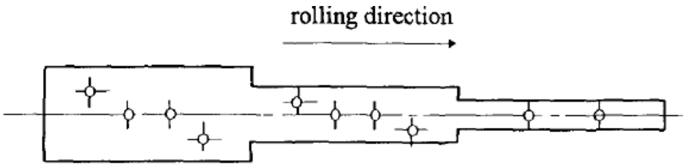

Figure 1.11: Rolling trials performed in Wang et al. [1996].

From the rolling trials in the Improsound report Llanos et al. [2008], it was also shown that natural holes are harder to close than artificial drilled holes. This result is in good agreement with the results from Chen et al. [2010], mentioning that in the case of complex initial void shapes, subsequent small voids are created during compression and are more hardly eliminated. Simple void geometries might therefore not fairly represent the closure behavior of natural voids.

The influence of initial state is also demonstrated in Toda et al. [2009]. Different closure behaviors were observed using 3D X-ray microtomography on Al-Mg alloy containing hydrogen micropores with various initial geometries. Some micropores remain visible after 60% compression, while others are completely closed. A combination of effects related to initial shape and position is the most plausible explanation.

Criteria for void closure

Keife and Ståhlberg [1980] studied the deformation of round and square voids in a rigid-perfectly plastic material. They proposed a simple upper bound model based on the plane-strain condition, considering two different simple deformation modes around the voids. They concluded that the reduction R_c necessary for complete void closure is a function of initial void volume fraction V_0, such that $R_c \sim V_0^{1/2}$.

Tanaka et al. [1986] proposed the use of the hydrostatic integration Q as an indicator for void closure. The parameter Q is the integral of stress triaxiality ratio $T_X = \frac{\sigma_m}{\bar{\sigma}}$ over the cumulated strain:

$$Q = \int_0^{\bar{\varepsilon}} -T_X d\bar{\varepsilon}. \tag{1.2}$$

Nakasaki et al. [2006] discussed the use of Q as a parameter for void closure in hot forging and rolling conditions. Based on experimental and numerical results, an expression for the total void area reduction is obtained by linear regression. In the case of rolling, the hydrostatic integration parameter is revised to Q^+, for reasons that are not explicitly given.

Hydrostatic integration was later used by Kakimoto et al. [2010] to compare the closure of a void in different configurations of forging. In this paper, numerical simulations are performed after validations using experiments on lead billets. A cylindrical hole is drilled through the billet with a void-to-billet diameter ratio of 0.05, and multi-pass forging is performed. It is found out that the critical value of hydrostatic integration for complete void closure is $Q \geq 0.21$. The authors used this criterion to investigate four forging parameters and proposed industrial improvements regarding process design. Although the qualitative results regarding process optimization shows great interest, the quantitative analysis to obtain the Q-criterion remains questionable. In this paper, experimental validations were performed using workpieces containing a drilled open-hole, which may have a rather different behaviour than an internal void.

Nevertheless, recently Chen and Lin [2013] used the Q criterion to study the evolution of shape parameters in the three directions x, y, z. They introduced a tridimensional version of the Q criterion, using three values $Q_i \quad (i \in x, y, z)$. The authors proposed a phenomenological expression to fit the aspect ratios of an ellipsoidal void according to Q_i.

$$S_i = (C_1 + S_{i0}) \exp(-Q_i/C_2) + C_3, \quad \text{with} \quad Q_i = \int_0^{\bar{\varepsilon}} \frac{s_i}{\bar{\sigma}} d\bar{\varepsilon}, \tag{1.3}$$

where s_i is the the component of the stress deviator tensor $\mathbf{s}$ in the i direction. S_i and S_{i0} are the aspect ratios and their initial values, respectively. C_1, C_2 and C_3 are fitting coefficient that are obtained using FE-simulations. Fitting values are obtained for several positions in a billet under a given forging process.

Tanaka et al. [1986] also proposed an empirical void closure parameter VCP based on Q value, with a series of six coefficients C_{ij} obtained by linear regression based on numerical simulations of compression:

$$VCP = \sum_{i=0}^{2} \sum_{j=0}^{2-i} C_{ij} \left[\ln(1+\bar{\varepsilon})\right]^i \left[\ln(1-Q)\right]^j, \tag{1.4}$$

The parameter returns a degree of closure (0-100%) of a virtually existing void, at any position in the billet. In the technical report *Improsound* [Llanos et al., 2008], a wide campaign of numerical simulations and experimental observations about hot rolling was performed, and C_{ij} coefficients were obtained as well. Process design was performed using maps of void closure parameter obtained using the previous model.

A simple stress-triaxiality-based (STB) model for void closure was introduced in the commercial code FORGE [2011], Lasne [2008] and was implemented as:

$$\frac{\Delta V}{V_0} = K_c T_X \Delta\bar{\varepsilon}. \tag{1.5}$$

The variation of void volume fraction at each increment step is assumed proportional to the product of stress triaxiality ratio with incremental strain. Under constant stress triaxiality ratio, Eq. 1.5 becomes:

$$\frac{V}{V_0} = 1 + K_c T_X \bar{\varepsilon}. \tag{1.6}$$

The proportionality coefficient $K_c = 5$ (default value) was identified using simulation of compression tests on a single spherical void. Note that by summing ΔV in Eq. 1.5 over the increments of deformation, the sum $\sum_0^t T_X \Delta\bar{\varepsilon}$ can be seen as the discretized form of Q in Eq. 1.2,

$$\sum_0^{\bar{\varepsilon}} \frac{\Delta V}{V_0} = K_c \sum_0^{\bar{\varepsilon}} T_X \Delta\bar{\varepsilon} \quad \approx K_c \int_0^{\bar{\varepsilon}} T_X d\bar{\varepsilon} = K_c(-Q). \tag{1.7}$$

Using the criterion of closure $Q = 0.21$, the predicted volume reduction can be computed as:

$$\left.\frac{V}{V_0}\right|_{(Q=0.21)} = 1 + \sum_0^{\bar{\varepsilon}} \frac{\Delta V}{V_0} = 1 + 5(-0.21) \approx 0. \tag{1.8}$$

Final void volume equals to 0, i.e. void is closed.

In all the studies presented above, the void-to-billet dimension ratio remains relatively large, i.e. around an average value of 0.1. Though, a large number of tiny voids usually exist in workpieces Llanos et al. [2008]. Tiny voids can hardly be considered by such a macroscopic approach, since their volume is very small and becomes negligible with respect to the volume of the workpiece. As pointed out in 2009 by Zhang and Cui [2009], Zhang et al. [2009], there is at present *a lack of applicable and accurate criterion in evaluating void closure*. Based on micromechanical results from the literature, the authors proposed two numerical models for void closure. After a brief review of the main steps used within the micromechanical approach, the most recent criteria are presented and discussed in the following section.

1.3.2 Micro-analytical approach

In the micromechanical analysis, a single void in an infinite incompressible matrix is considered. The constitutive relations for the matrix are of the power-law type, with m the power exponent:

$$\mathbf{s} = \frac{2}{3}\frac{\sigma_0}{\dot{\varepsilon}_0}\left(\frac{\dot{\bar{\varepsilon}}}{\dot{\varepsilon}_0}\right)^{m-1}\dot{\boldsymbol{\epsilon}}, \qquad \text{with } \operatorname{tr}(\dot{\boldsymbol{\epsilon}}) = 0, \tag{1.9}$$

where $\dot{\boldsymbol{\epsilon}}$ is the strain-rate tensor, $\mathbf{s}$ is the deviatoric part of the stress tensor $\boldsymbol{\sigma}$, $\dot{\bar{\varepsilon}}$ and $\dot{\varepsilon}_0$ are, respectively, the effective and the reference strain-rate, σ_0 is the reference stress. The evolution of the initial void is studied with respect to various mechanical parameters, for different types of materials which properties are controlled by the power exponent: linearly viscous materials ($m = 1$), rigid-perfectly plastic materials ($m = 0$), and the general case of non-linear viscous materials ($0 < m < 1$).

A large number of studies regarding void evolution in an infinite matrix were reviewed by Huang and Wang [2006]. In these studies, voids are typically assumed to have a spherical (or ellipsoidal), or cylindrical shape. Most studies do not consider any change of shape during deformation, and the resulting equations often become inappropriate for large deformations (which is generally the case to obtain void closure).

Rigid-perfectly plastic material

Gurson-based models Gurson [1977] established a relation providing a yield criterion for porous materials, as a function of void volume fraction f. The void evolution $\dot{f}$ is governed by the condition of incompressibility of the matrix, leading to a simple void growth law given by:

$$\dot{f} = (1 - f)\operatorname{tr}(\dot{\boldsymbol{\epsilon}}^{pl}), \tag{1.10}$$

where $\dot{\boldsymbol{\epsilon}}^{pl}$ is the plastic strain-rate tensor. To obtain a yield criterion for porous materials, the material model used in Gurson's analysis is rigid-perfectly plastic ($m = 0$). A spherical cell, composed of matrix material containing a concentric spherical void, is considered. Based on cell calculations, an upper bound solution for yield criterion is proposed for the macroscopic behavior of porous metals.

Tvergaard [1982] proposed corrective coefficients $q_1 = 1.5$, $q_2 = 1.0$ to Gurson's model. Gurson-Tvergaard's model is widely used in the framework of ductile fracture due to void nucleation, growth and coalescence. Additionally, Tvergaard and Needleman [1984] introduced a modified void volume fraction $f^* = f^*(f)$ for $f > f_c$, where f_c is a critical value over which the coalescence phenomenon takes place. Nevertheless, void coalescence is out of the scope of this work, since it is not supposed to occur in the case of void closure. Various modified Gurson-based models are available in the literature, taking into account some additional mechanisms, such as isotropic and kinematic hardening, and the effect of strain-rate sensitivity. Recently, Scheyvaerts et al. [2011] extended Gurson's model to ellipsoidal voids in shear and tension conditions, using a constitutive law considering both elastic regime and plastic hardening. However, very few studies focused on pure void closure.

From the Gurson-Tvergaard model, Ragab [2004] found an expression to evaluate the volumetric strain-rate of a spherical void,

$$\frac{\dot{V}}{3\dot{E}_e V} = \frac{q_1 q_2}{2}\sinh\left(\frac{3}{2}q_2|T_X|\right), \tag{1.11}$$

where $\dot{E}_e$ is the remote equivalent strain, and q_1 and q_2 are the coefficients obtained by Tvergaard [1982]. In this equation, the void is assumed to remain spherical.

Analytical solutions Rice and Tracey [1969] proposed a model for the evolution of a spherical void in a rigid-perfectly plastic matrix ($m = 0$). In the analysis, the void undergoes an uniaxial loading with axisymmetric stress conditions. As no analytical expression can be obtained, approximate Rayleigh-Ritz solutions were obtained using the variational principle. The velocity field is defined as:

$$\mathbf{v} = \mathbf{v}_0 + \tilde{\mathbf{v}}, \tag{1.12}$$

with $\mathbf{v}_0 = \dot{\mathbf{E}} \cdot \mathbf{x}$ the remote velocity field, where $\dot{\mathbf{E}}$ is the remote strain-rate tensor at infinity, $\mathbf{x}$ is the spatial coordinates vector, and $\tilde{\mathbf{v}} = D\mathbf{v}_D + \mathbf{v}_E$ is the local velocity change due to the presence of a void. The first term $\mathbf{v}_D$ thus describes the spherically symmetric deformation due to the volume change of the void, where D is the normalized dilatation rate, and $\mathbf{v}_E$ describes the shape change of the void. Under high stress triaxiality, it is shown that the influence of $\mathbf{v}_D$ is much larger that the one of $\mathbf{v}_E$, and the void's shape change can be neglected. The approximation of *high stress triaxiality* thus leads to:

$$\mathbf{v} = \dot{\mathbf{E}} \cdot \mathbf{x} + D\mathbf{v}_D. \tag{1.13}$$

The minimum principle, which consists in minimizing a functional $F(\mathbf{v})$ is used to obtain a velocity field. The normalized dilatation rate D is obtained as:

$$D = \frac{\dot{V}}{\dot{E}_e V} = \begin{cases} 0.850 \exp\left(\frac{2}{3} T_X\right) & \forall \quad T_X > 0, \\ -0.826 \exp\left(-\frac{2}{3} T_X\right) & \forall \quad T_X < 0. \end{cases} \tag{1.14}$$

where $\dot{E}_e = \sqrt{\frac{2}{3}\dot{\mathbf{E}} : \dot{\mathbf{E}}}$ is the remote equivalent strain. The coefficients are analytical values that result from the Rayleigh-Ritz procedure.

Linear viscous material

In the case of linear viscous (or Newtonian) materials $m = 1$, analytical solutions were calculated by Budiansky et al. [1982] for an extended number of constant stress triaxiality ratios $T_X = \frac{\sigma_m}{\bar{\sigma}}$. The volume rate of a sphere may be expressed as:

$$\frac{\dot{V}}{\dot{\bar{\varepsilon}} V} = \frac{9}{4} T_X. \tag{1.15}$$

Nonlinear viscous material

Analytical solutions Budiansky et al. [1982] studied the deformation of a spherical void in a nonlinear viscous matrix. As for the case presented above, the authors showed that no analytical solution may be obtained, and the Rayleigh-Ritz procedure is used. The *high stress triaxiality* (HST) approximation is also used to only consider the radially symmetric contribution of the velocity field. Using this approximation, the volumetric strain-rate of the spherical void is obtained:

$$D_{sp}^{HST} = \frac{\dot{V}}{\dot{E}_e V} = \frac{3}{2}\left(\frac{3m}{2}|T_X| + G(m)\right)^{\frac{1}{m}} \qquad \forall \quad |T_X| \gg 1. \tag{1.16}$$

In the case of *low stress triaxiality* (LST), an expression for volumetric strain-rate is proposed by Tvergaard [1984]:

$$D_{sp}^{LST} = \frac{\dot{V}}{\dot{E}_e V} = \frac{3}{2}\left(\frac{3m}{2} + G(m)\right)^{\frac{1}{m}} |T_X| \qquad \forall \quad |T_X| \ll 1. \tag{1.17}$$

In these equations,

$$\begin{cases} G(m) = (1-m)(1+(\ln(3)-2/3)\,m) & \approx (1-m)(1+0.432m) \qquad \forall \quad T_X > 0, \\ G(m) = (1-m)(1+\dfrac{2\pi}{9\sqrt{3}}m) & \approx (1-m)(1+0.403m) \qquad \forall \quad T_X < 0. \end{cases} \tag{1.18}$$

Note that for $m = 1$, $G(m) = 0$ and both Eqs. (1.16, 1.17) reduce to Eq. 1.15.

Duva and Hutchinson [1984] proposed an extension of Eqs. 1.16 and 1.17 for any stress triaxiality ratios, using an interpolation approximation. The expression of volumetric strain-rate for a sphere D_{sp} gives:

$$D_{sp} = \left(\frac{\dot{V}}{\dot{E}_e V}\right)_{sp} = \frac{3}{2}\left(\frac{3m}{2}|T_X| + G(m)\right)^{\frac{1}{m}} + c_1|T_X| + c_2 \qquad \forall \quad T_X, \tag{1.19}$$

which, in the case of void closure ($T_X < 0$), leads to:

$$D_{sp} = \left(\frac{\dot{V}}{\dot{E}_e V}\right)_{sp} = \frac{3}{2}\left(-\frac{3m}{2}T_X + (1-m)(1+0.403m)\right)^{\frac{1}{m}} - c_1 T_X + c_2, \tag{1.20}$$

where parameters c_1 and c_2 are tabulated functions of m Zhang and Cui [2009]. The volumetric strain-rate is plotted in Fig. 1.12a for $m = 0.2$. Note that there is a slight difference between values proposed by the generalized formula and the solution given by Budiansky et al. [1982] using the high stress triaxiality approximation. The authors argued that the solution in Eq. 1.16 *underestimates the deformation rate*, due to the approximation made by Budiansky et al. [1982] on the velocity field. Indeed, the relative error obtained between the generalized formula Eq. 1.20 and both Eqs. 1.16 and 1.17 on their respective domain of validity is plotted in Fig. 1.12b. A greater difference (about 20-25%) can be seen around $|T_X| = 1$, i.e. at the boundary between both approximations. The generalized formula for D_{sp} was proposed in order to approach Eqs. 1.16 and 1.17 on their respective domain of validity, and thus considers the same approximations. Note that the relative error is slightly negative at very low stress triaxiality values, without great influence of m-value.

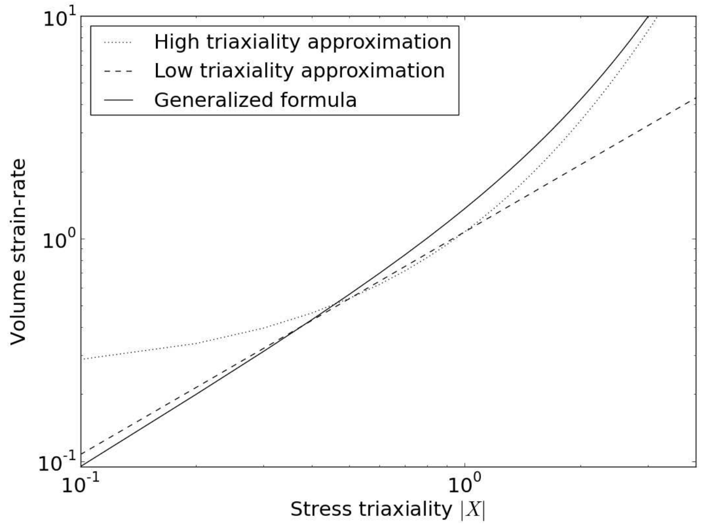

(a) $m = 0.2$

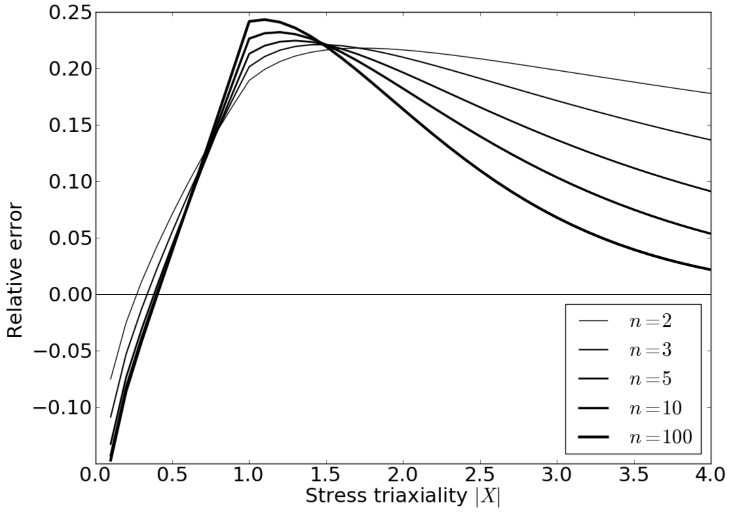

(b)

Figure 1.12: (a) Normalized volumetric strain-rate for a sphere D_{sp} given by Eq. 1.20 (Generalized formula), compared to *high* and *low stress triaxiality* approximations given by Eq. 1.16 and Eq. 1.17, respectively; and (b) the relative deviation between Eq. 1.20 and Eq. 1.16 of Eq. 1.17 on their domain of validity, for various values of m (given as $n = 1/m$).

A similar analysis was performed by He and Hutchinson [1981], considering the deformation of a penny-shaped crack. The Rayleigh-Ritz solution for the volumetric strain-rate of a *crack* gives:

$$\left(\frac{\dot{V}}{\dot{E}_e V}\right)_{cr} = \frac{D_{cr}}{\lambda} = \frac{1}{\lambda}\frac{6}{\pi\sqrt{1+3m}}\left(|T_X| + \frac{2}{3}\right) \quad \text{for } \lambda \ll 1, \tag{1.21}$$

where $\lambda = a/b$ is a shape factor, as shown in Fig. 1.13 ($\lambda \ll 1$ for a penny-shaped crack).

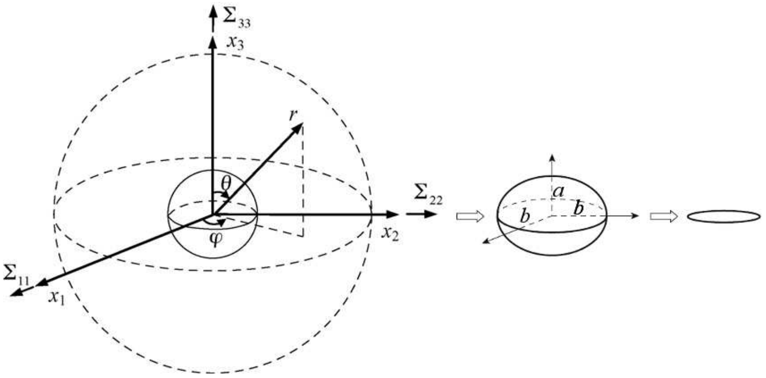

Figure 1.13: Void evolution from spherical shape to a crack Zhang and Cui [2009], Zhang et al. [2009].

Using an interpolation scheme, Zhang and Cui [2009] proposed an expression for the transition state from spherical to finally crack-like mode. The evolution of void volume can be expressed as:

$$\frac{V}{V_0} = \left|\frac{D_{\dot{\lambda}}\exp(-D_{cr}E_e) - D_{cr}\exp(-D_{\dot{\lambda}}E_e)}{D_{\dot{\lambda}} - D_{cr}}\right| \exp(D_{sp}E_e), \tag{1.22}$$

where $D_{\dot{\lambda}}$ corresponds to the change-rate of the aspect ratio of a spherical shape, which is obtained using a Rayleigh-Ritz procedure on spherical voids:

$$D_{\dot{\lambda}} = \left(\frac{\dot{\lambda}}{\dot{E}_e}\right) = 2.5 - (1-m)\left[(29-45m)\left(1 + \frac{3}{3T_X - 2}\right)^3 - \frac{2}{9}\right]. \tag{1.23}$$

Semi-empirical solution From the analytical model in Eq. 1.20 for a spherical void (assumed to remain spherical) the same authors alternatively proposed a semi-empirical extension for considering the change of shape during deformation [Zhang et al., 2009]. The authors introduced an empirical dependence to void shape λ, assuming that it depends on the cumulated strain, only. The coefficient c_2 in Eq 1.20 is replaced by a polynomial function of cumulated strain and leads to Eq. 1.24. The values for parameters c_1, c_2, c_3, c_4 are numerically obtained using finite element calculations based on a cubic cell model containing a spherical void (Fig. 1.14). The volume of void is obtained using different values of stress triaxiality ratio $|T_X|$, and are given in tables in [Zhang et al., 2009] for various values of m.

Note that the dependence in triaxiality ratio is consistent with the results presented in Section 1.3.1 dealing with the product of stress triaxiality ratio with effective strain. Eq. 1.24 is also in good agreement with qualitative results from process studies presented

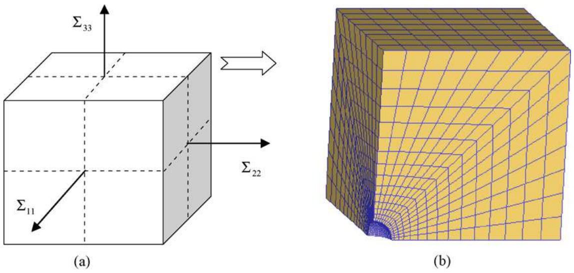

Figure 1.14: The cubic cell model used for obtaining c_i values Zhang et al. [2009].

above in Section 1.3.1, which relates that pore closure is faster for high reduction ratios and large negative stress triaxiality levels. Here, the effect of power exponent, i.e. of a material property, is also considered.

$$\frac{\dot{V}}{\dot{E}_e V} = \frac{3}{2}\left(\frac{3m}{2}|T_X| + G(m)\right)^{\frac{1}{m}} + c_1|T_X| + 3c_2E_e^2 + 5c_3E_e^4 + c_4. \tag{1.24}$$

Integration of Eq. 1.24 over the strain path (assuming constant triaxiality ratio during deformation) leads to:

$$\frac{V}{V_0} = \exp\left(-E_e\left[\frac{3}{2}\left(\frac{3m}{2}|T_X| + G(m)\right)^{\frac{1}{m}} + c_1|T_X| + c_2E_e^2 + c_3E_e^4 + c_4\right]\right). \tag{1.25}$$

The authors studied the evolution of void volume as a function of macroscopic strain E_e for several values of power exponents and stress triaxiality levels. It is shown that stress triaxiality might considerably increase void closure, as shown in Fig. 1.15a, and that decreasing m has a positive influence on void closure, as shown in Fig. 1.15b. It is noteworthy that large stress triaxiality have an effect since the earliest stages of void closure, by increasing the initial rate of closure. The macroscopic strain required for void closure is thus reduced by increasing stress triaxiality.

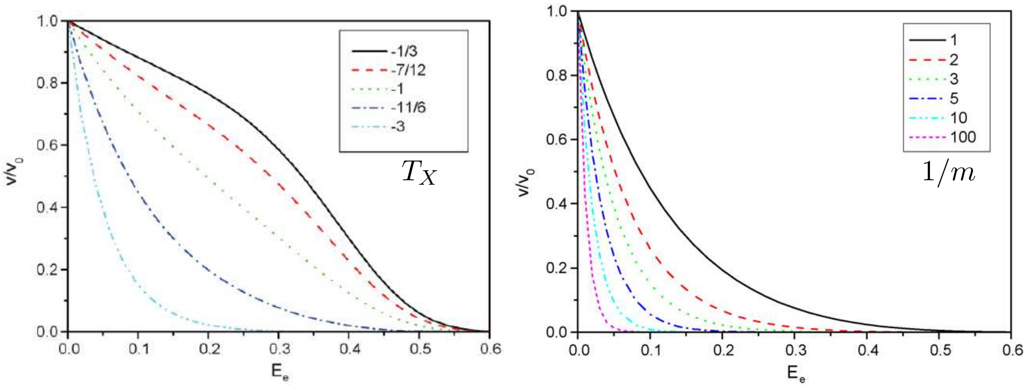

(a) Influence of T_X, for $m = 1/3$ (b) Influence of power exponent m, for $T_X = -3$

Figure 1.15: Effect of stress triaxiality ratio and of power exponent on void closure, from Zhang et al. [2009].

Lee and Mear [1992, 1994] discussed the validity of Gurson's models regarding a material containing aligned spheroidal voids in axisymmetric loading conditions. Various shapes were considered, such as penny-shaped, oblate, prolate, or cylindrical voids. The authors provided qualitative results regarding the evolutions of ellipsoidal voids under various triaxiality ratios. It is pointed out that initial void shape may have a significant influence on void closure. Randomly orientated ellipsoids are also discussed. It is concluded that it is extremely difficult to obtain accurate results, although bounds and estimates were proposed by Ponte Castañeda [1991]. The qualitative data in Lee and Mear [1994] were used by Zhang and coworkers [Zhang and Cui, 2009, Zhang et al., 2009] to compare with the results obtained from Eqs. 1.22 and 1.25.

1.3.3 Comparison of models

Comparison by Zhang and Cui [2009]

The analytical model in Eq. 1.22 was discussed by Zhang and Cui [2009]. The results were compared with data from Lee and Mear [1994] in Fig. 1.16. As it can be seen for $m = 0.33$, the interpolation scheme and the numerical data are in very good agreement for all tested stress triaxiality ratios. The authors implemented Eq. 1.22 in a FE code to compute their prediction model at the macroscopic scale in a void-free process. They used the case of a billet under uniaxial compression, as shown in Fig. 1.17. The model was able to predict the volume of voids with very good accuracy, providing considerable reduction CPU time (the authors showed a reduction by a factor of 10).

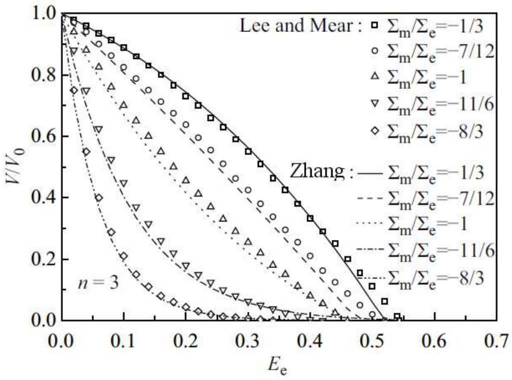

Figure 1.16: Comparison of void evolutions, with $m = 0.33$, given by Eq. 1.22 and by Lee and Mear, from [Zhang and Cui, 2009].

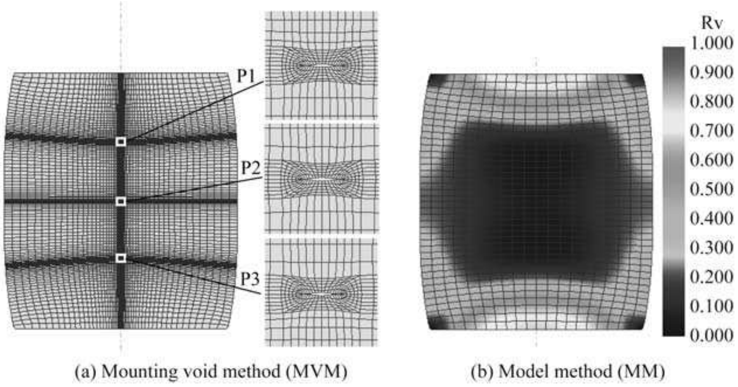

(a) Mounting void method (MVM)

(b) Model method (MM)

Figure 1.17: Comparison of the results at 32% billet reduction, from [Zhang and Cui, 2009].

Comparison by Zhang et al. [2009]

Zhang et al. [2009] compared their semi-analytical model (Eq. 1.25) with the models of Gurson (G), Gurson-Tvergaard (GT), Budiansky-Hutchinson-Slutsky (BHS), the results of Lee and Mear [1992, 1994], as well as the finite element (FE) results that were used for calibration. The comparison is made for two values of stress triaxiality ratios and is presented in Fig. 1.18. The plot for G and GT-models were obtained using Eq. 1.11, using the values $q_1 = q_2 = 1$, and $q_1 = 1.5$ and $q_2 = 1$, respectively. The plot for BHS-model was obtained Eq. 1.16. For very compressive stress triaxiality ratios $T_X = -2$, Fig. 1.18a shows that all models predict a roughly similar evolution of void volume, although G and G-T models seem to slightly overestimate void closure. For the less compressive triaxiality ratio $T_X = -0.6$, Fig. 1.18b shows that two different behaviors are predicted by the models. This difference is attributed to the assumption made in the G, G-T, and BHS models, that the spherical/spheroidal void remains spherical/spheroidal during deformation. This difference rises with strain E_e, since the actual shape of the void deforms towards a crack-shape. This difference is less marked with larger negative stress triaxiality ratios (Fig. 1.18a), as the change in shape is slighter. This observation was also made by Lee and Mear [1994]. This is coherent with the *high triaxiality* assumption of BHS model.

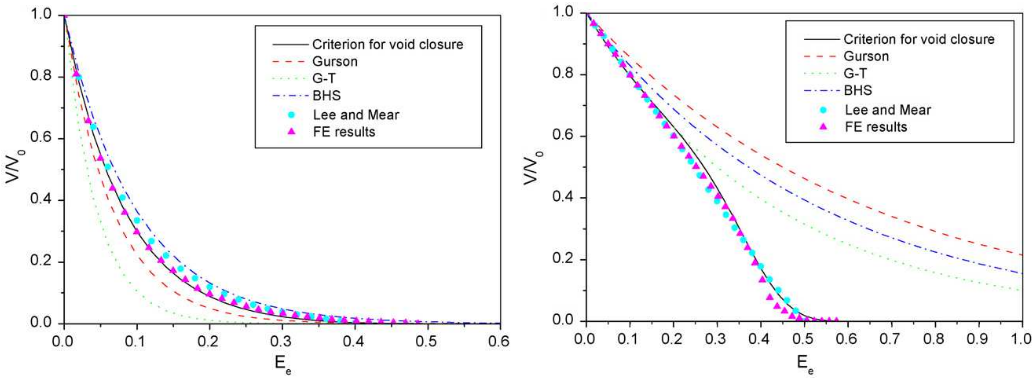

(a) $T_X = -2$ (b) $T_X = -0.6$

Figure 1.18: Comparison of the criterion of Zhang et al. [2009] (Eq. 1.25) plotted in black line, with data from literature and FE simulations on cell model, with $m = 0.2$, from [Zhang et al., 2009].

The model of Zhang et al. [2009] was recently implemented in the commercial finite element code DEFORM–3D™ by Zhang et al. [2012]. The influence of various process parameters on void closure was studied using upsetting, blocking and multi-pass forging. The influence of die-shapes is discussed in order to enhance void closure and thus material soundness. Although the model showed good agreement with the result from the literature regarding the evolution of a sphere under constant boundary conditions (Fig. 1.18), no validation of the model under complex loadings was presented. The accuracy of the presented results remains thus questionable in the case of industrial processes. This point will be discussed in Chapter 5.

Comparison of all models

A comparison of all models is now proposed in order to discuss the reliability of the models within the range of values of interest of the present work. According to the literature, the stress triaxiality ratio T_X and the material parameter m are the two parameters that were taken into account. According to the review on industrial issues (section 1.2), the range of interest for the stress triaxiality values is $T_X = [-1, 0]$. This range is extended to $T_X = [-1.2, 0]$ in the present comparison.

The simple behaviour law in Eq. 1.9 that is used in the analytical and semi-analytical models Budiansky et al. [1982], Duva and Hutchinson [1984], Zhang and Cui [2009], Zhang et al. [2009] is insufficient to model the behaviour of hot metals presented in section 1.2. However, several values of m are considered in order to illustrate the dependence of the models to material behaviour.

In total, six values of stress triaxiality ratios T_X and three values of m were defined and void volume evolutions are plotted in Fig. 1.19. The six models are synthetically recalled in Table 1.5 with the values of coefficients that were used to plot the 18 configurations.

Model	Type	Equation	Constants values
STB [Lasne, 2008]	Empirical	Eq. 1.5	$K_C = 5$
Tanaka et al. [1986]	Empirical	Eq. 1.4	C_{ij} (Table. 1.6)
Gurson-Tvergaard [1982]	Analytical	Eq. 1.11	$q_1 = 1.5$, $q_2 = 1$
Budiansky et al. [1982]	Analytical	Eq. 1.16	–
Duva and Hutchinson [1984]	Analytical	Eq. 1.20	c_1 and c_2 (Table. 1.7)
Zhang and Cui [2009]	Analytical	Eq. 1.22	–
Zhang et al. [2009]	Semi-analytical	Eq. 1.25	c_1, c_2, c_3, c_4 (Table. 1.8)

Table 1.5: Equations of the models used to plot Fig. 1.19.

C_{00}	C_{01}	C_{02}	C_{11}	C_{12}	C_{22}
0.0114	0.84	-2.48	2.17	12.6	-1.98

Table 1.6: Values of coefficients C_{ij} in Eq. 1.4, from Tanaka et al. [1986].

m	1.0	0.5	0.2	0.3	0.1	0.01
c_1	0.	0.5951	0.7061	0.8049	0.9002	1.0066
c_2	0.	-0.5479	-0.6571	-0.7340	-0.7874	-0.8329

Table 1.7: Values of coefficients c_1 and c_2 in Eq. 1.20 resulting from analytic solutions from Duva and Hutchinson [1984], tabulated in Zhang and Cui [2009].

m	1.0	0.5	0.2	0.3	0.1	0.01
c_1	0.5048	0.4911	0.6016	1.1481	2.9132	6.5456
c_2	6.4675	0.8002	-0.6981	-4.2026	-11.6464	-15.3775
c_3	14.2610	53.8018	72.6397	108.2114	185.5622	324.4417
c_4	-0.3379	-0.2314	-0.1243	-0.2480	-0.6511	-1.9575

Table 1.8: Values of coefficients c_1, c_2, c_3 and c_4 in Eq. 1.25 resulting from calibration using finite element simulations obtained by Zhang et al. [2009].

From Fig. 1.19, it can be seen that Gurson-Tvergaard curves coincides with the ones of Duva and Hutchinson [1984] for $m = 0.01$, even though their expressions are rather different. Gurson-Tvergaard was developed for perfectly-rigid plastic materials (which corresponds to the case $m = 0$). The good agreement comes from the fact that both models are based on the same assumptions and consider the evolution of a spherical void. This is no longer the case for larger m values, as the model of Gurson-Tvergaard is valid for perfectly-rigid plastic materials, exclusively.

The influence of material parameter m was neither considered in both empirical models (STB Lasne [2008], Tanaka et al. [1986]).

The curves from Budiansky et al. [1982] model tends to get closer to the ones of Duva and Hutchinson [1984] for $T_X \leq 1$. This is coherent with the fact that Duva and Hutchinson

[1984] is an extension of Budiansky et al. [1982] (based on *high triaxiality* assumption) to all values of T_X. Both models are superimposed in the case of linear viscous materials ($m = 1$), since both equations reduce to Eq. 1.15 for linearly viscous materials.

The comparisons made in Zhang and Cui [2009] and Zhang et al. [2009] covered the range $-2.7 < T_X < -0.33$ (in Figs. 1.16 and 1.18). Both comparisons were made for a single value of m (for $m = 0.33$ and for $m = 0.2$, respectively). In Fig. 1.19, both models are plotted over the range of interest for T_X, and for the three values of m. Rather good agreement between both models is observed over the range $-1.2 < T_X < -0.4$ as well, notably for the value $m = 0.3$. Void closure is obtained around similar strain values. Void evolution is roughly similar, although a few differences may be pointed out. The analytical model provides monotonous curves, whereas the semi-analytical model induces several changes of slope. The latter also exhibits an asymptotic final closure, unlike the analytical model that presents a rather steep decrease until complete closure.

Larger deviations can be observed for the less compressive triaxiality values ($-0.2 < T_X < 0.0$), especially for extreme values of m ($m \to 0$ and $m = 1$). Such values of triaxiality were unfortunately not discussed in the papers, but may require full attention, as they belong to the range of interest within the present work. Very different initial behaviours are predicted between the analytical model and the semi-empirical model. Let us finally note that, for the analytical model, the value of strain that is required for complete closure using $T_X = 0.0$ is lower than for $T_X = -0.2$, which is physically counter-intuitive. The best agreement between the analytical and semi-empirical models is obtained for $T_X = -0.4$, i.e. close to the particular case of uniaxial compression ($T_X = -\frac{1}{3}$). The curves also show good agreement with the STB model, except for the value $m = 1$ (although such a value remains excessively elevated regarding the ranges of interest within this work).

The empirical model of Tanaka et al. [1986] systematically underestimates void closure, although the general tendency regarding the dependence on stress triaxiality is respected. However, the evolution of void volume with strain remains rather different from analytical models.

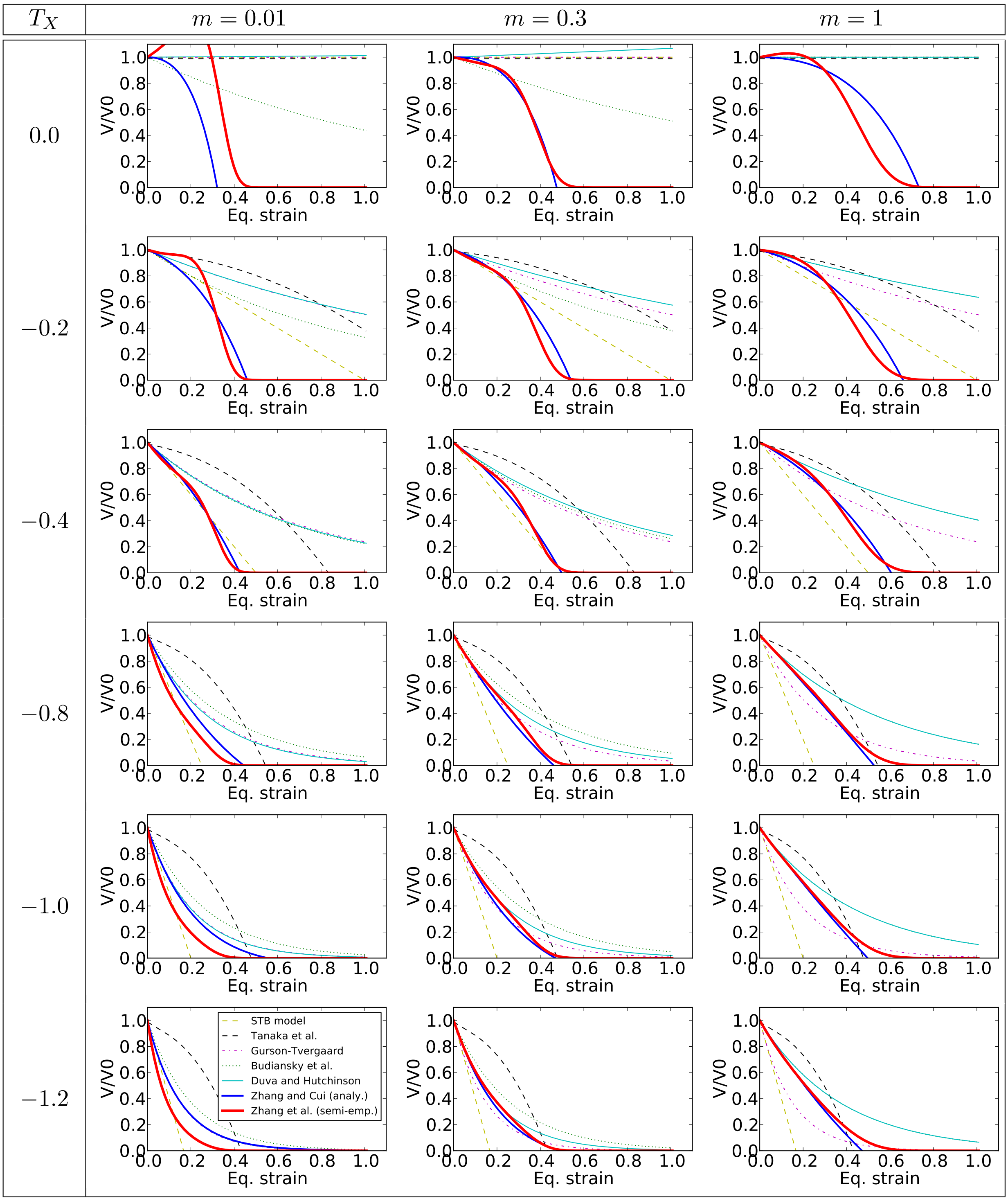

Figure 1.19: Comparison models given in Table 1.5 (STB model [Lasne, 2008], Tanaka et al. [1986], Gurson-Tvergaard [1982], Budiansky et al. [1982], Duva and Hutchinson [1984], Zhang and Cui [2009] and Zhang et al. [2009]) over the range $-1.2 < T_X < 0.0$ and for $m = \{0.01, 0.3, 1\}$.

1.3.4 Conclusions

Two main approaches are used in the literature to study void closure: the macroscopic approach and the micro-analytical approach.

- Using the macroscopic approach, it is possible to study void closure according to accurate industrial conditions (voids, process). Important improvements are pointed out in the literature regarding process design. Nevertheless, this approach is very limited by the fact that the obtained results entirely depend on process-conditions and initial porosity state (geometry and position). A full explicit description is systematically required and no generalization is possible. In addition, due to the large disparity between voids and workpieces dimensions, numerical simulation using *full-field* explicit descriptions at the workpiece scale usually involves very heavy computations.

- The micro-analytical approach is able to predict the analytical evolution of an isolated void in an infinite matrix under constant mechanical loadings. The mechanical analysis requires a rather large number of assumptions, especially regarding the material's behaviour and initial analytical void shape. Therefore, this approach remains questionable with respect to industrial issues. In addition, there is at present a lack of validation cases regarding such approaches.

From the most advanced studies, empirical, analytical and semi-empirical models were discussed. The STB model and the model of Tanaka et al. [1986] are based on empirical results that were obtained from experiments and numerical simulations. They were initially calibrated for the case of spherical voids using a given material law. Both models respect the general tendency relative to stress triaxiality ratio. They do not consider any dependence to material behaviour. Further calibration of these models is possible to consider additional parameters. However, new coefficients might at best predict void closure for a given geometry and a given material, and must be repeated for any configurations. Generalization is at present not permitted using such models.

Among all analytical models, the one from Zhang and Cui [2009] seems to be the most advanced as it covers the largest range of stress triaxiality ratios, material behaviour, and considers the change in void shape during deformation. However, this model suffers from limitations as well. Firstly, the evolution of a sphere is exclusively predicted, although it was shown [Lee and Mear, 1994] that initial void shape might significantly influence the void closure behaviour. Secondly, the reliability of the model remains questionable as there is a lack of validation cases in the literature. In addition, some counter-intuitive observations were made at low compressive stress triaxiality ratios (Fig. 1.19).

The semi-empirical model from Zhang et al. [2009] suffers from comparable limitations as the previous from the same author. Spherical initial voids are exclusively considered and a lack of validation cases was stated.

The initial state of voids (morphology) will therefore be intensively studied within this work, as complex geometries were pointed out in the industrial review, and according to the significant influence that was qualitatively exhibited in literature. The dependence to mechanical state will also be further studied in order to better predict the phenomenon over the entire range of stress-triaxiality and deformation. The influence of material parameters will also be further studied, notably regarding actual behaviours of hot metals (e.g. strain hardening or softening effects).

To consider all these new influences, void closure will be studied at the meso-scale, involving the use of a representative volume element. This approach is described in Chapter 2.

Chapter 2

Description of the meso-scale approach

Contents

Résumé français

Etant données les fortes limitations des deux approches macroscopiques en champ complet, et micro-analytique, présentées au chapitre précédent, une approche de type méso-scopique est présentée dans ce chapitre.

L'utilisation d'un volume élémentaire représentatif (VER) est présentée. L'application de conditions aux limites représentatives des trajets de chargement thermo-mécaniques industriels est décrite. Il est montré que la méthode utilisée permet de respecter un profil de triaxialité des contraintes sur un trajet de déformation de façon très précise. La méthode permet également d'appliquer des grandeurs mécaniques constantes (triaxialité des contraintes, vitesse de déformation), en dépit de la non-linéarité de la loi de comportement utilisée.

La génération de maillages 3D de VER contenant un pore réel dont la morphologie a été obtenue par microtomographie est ensuite décrite. L'utilisation d'éllipsoïdes de morphologie équivalente, basée sur la matrice d'inertie de pores réels, est également détaillée. Une validation numérique de l'approche est finalement présentée.

L'influence des paramètres numériques (taille de maille et dimensions du VER) sur les résultats des simulations est discutée et un jeu de valeurs assurant la fiabilité des résultats est donné.

Finalement, un cas de refermeture d'un pore réel dans un VER avec conditions aux limites représentatives d'un chargement industriel réel est comparée à un cas de simulation explicite du procédé industriel concerné. L'accord est très bon en terme de prédiction du volume et le gain en terme de temps de calcul est significatif.

2.1 Introduction

The final objective of this PhD work is to obtain a reliable numerical tool that can be industrially used for process design in terms of void closure efficiency. From an industrial point of view, such numerical tool shall therefore fulfill the two following requirements:
i) to provide a representative prediction of void closure and
ii) to minimize the required computation time.

As pointed out in the previous chapter, the *full-field* explicit description is often used in the literature, using an entire workpiece containing explicit voids. Using adequate numerical features (e.g. mesh size, time step), this description may become extremely accurate for studying void closure in real process conditions, *according to a given case study*. Yet, the obtained results naturally are *case-dependent*. This remark makes this approach particularly unsuitable for a sustainable industrial use, as a detailed knowledge of the actual void state is required. Moreover, there is at present a lack of applicable techniques to easily and precisely observe the actual state of voids in the workpieces during production. Metallography may provide high resolution imaging of voids, but it is a destructive technique. Ultrasonic testing is non-destructive and may provide a good localization but the actual void shape is captured with a rather low resolution. X-ray microtomography might show great interest as it is also non-destructive and provides an accurate description of the void shape; however it is a rather costly technique and is unfortunately limited to relatively small samples, while the presence of voids is known to be a typical feature of large workpieces. To summarize, the *full-field* explicit description at the workpiece scale can provide an excellent but costly simulation of the actual phenomena in accurate conditions (partially fulfilling requirement (i)), which makes it unsuitable to understand the phenomenon from a general point of view. Requirement ii) is anyway far from being fulfilled, according to the heavy computations that are involved.

Mean-field models appear to be excellent candidates to fulfill requirement (ii). A *mean-field* model is a function that is able to predict the evolution of a given variable (e.g. void volume) at any point of a workpiece during process, according to a certain number of parameters. They can easily be implemented in a finite element code, as they depend on mechanical fields (typically stress and strain) and a set of initial parameters. This prediction function is therefore automatically computed at any integration point, providing maps of void closure. Process design can be performed using these maps. Existing prediction functions from literature were discussed in Chapter 1. They were either obtained analytically [Budiansky et al., 1982, Duva and Hutchinson, 1984, Zhang and Cui, 2009], semi-analytically [Zhang et al., 2009], or empirically [Tanaka et al., 1986, Lasne, 2008]. A certain number of limitations were shown in terms of void volume prediction, making such functions unsuitable to fulfill requirement (i). Within this work, a new *mean-field* model is sought in order to better predict void volume evolution.

Void closure is in fact a micro-scale problem. It is influenced by *local* thermo-mechanical fields, no matter the macroscopic thermo-mechanical fields in the entire workpiece. The use of a Representative Volume Element (RVE) was chosen to separate macro- and micro-scales. Void closure can therefore be studied at the micro-scale using a *full-field* description (enabling the best level of details) and using boundary conditions that are representative of what a material point undergoes during industrial processes.

The use of an RVE can be seen as an accurate tool to understand void closure, according to various input parameters. This chapter presents a detailed description of this tool. First, the application of boundary conditions is presented. It is followed by a detailed description of the generation of tridimensional meshes for the RVE.

2.2 General assumptions

The separation of micro- and macro-scales requires the condition that the void dimensions are *small* with respect to the workpiece dimensions. From this condition, two main assumptions can be made:

1. The presence of voids in a workpiece has no influence on the macroscopic deformation of the workpiece. This assumption distinguishes the present approach from the one of Gurson, in which the presence of a void volume fraction modifies the yield stress of the global material. In the present work, it is neglected as initial void fraction is generally very low. In addition, it is expected to decrease and tend to zero.
2. The thermo-mechanical fields that are obtained from the macroscopic scale are considered as *locally* homogeneous and can be used as *remote* boundary conditions at the RVE-scale.

These assumptions will be discussed in Chapter 5.

2.3 Boundary conditions

The RVE is a cuboid of dimensions D_x, D_y and D_z. Three symmetry planes (Oxy), (Oyz), and (Oxz) are defined. The boundary conditions are applied on the three remaining planes of the RVE, i.e. in each spatial direction, as presented in Fig 2.1. It is chosen to apply a normal velocity along z-axis, and normal stresses along x and y-axes. This choice presents the advantage of providing an accurate control of both the deformation state and the stress state.

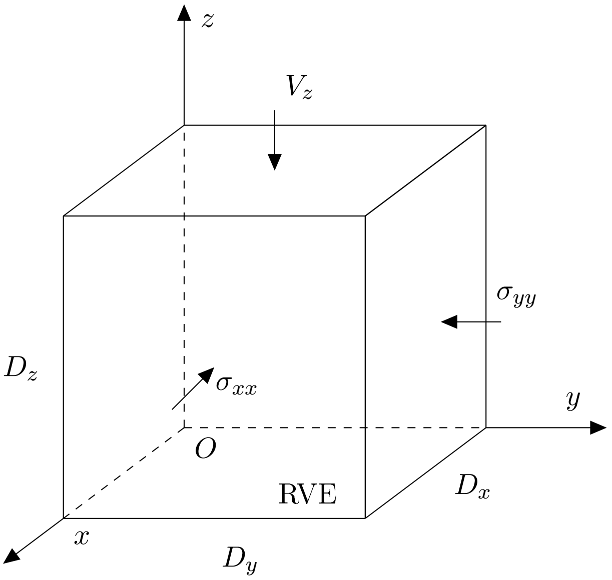

Figure 2.1: RVE with imposed boundary conditions.

Equivalent strain, as well as stress triaxiality ratio were shown to have first order influences on void closure. As discussed in Chapter 1, this was demonstrated using the micro-analytical approach [Budiansky et al., 1982, Duva and Hutchinson, 1984, Lee and Mear, 1994], the macroscopic explicit approach [Tanaka et al., 1986, Ståhlberg, 1986] and more recently using the meso-scale approach [Zhang et al., 2009].

The objective is thus to impose a given evolution of stress triaxiality ratio *vs.* equivalent strain. Stress triaxiality ratio is defined as $T_X = \frac{\sigma_m}{\bar{\sigma}}$, where $\sigma_m = \frac{1}{3}\mathrm{tr}(\boldsymbol{\sigma})$ is the mean stress and $\bar{\sigma} = \sqrt{\frac{3}{2}\boldsymbol{\sigma} : \boldsymbol{\sigma}}$ is the von Mises equivalent stress. Equivalent strain is defined as $\bar{\varepsilon} = \sqrt{\frac{2}{3}\boldsymbol{\varepsilon} : \boldsymbol{\varepsilon}}$.

2.3.1 Real industrial conditions

Mechanical fields were previously recorded using the point tracking method, described in the previous chapter in section 1.2.4. The obtained ranges were defined in terms of strain-rates $\dot{\bar{\varepsilon}} = [0.01,\ 10]\ \mathrm{s}^{-1}$, and stress triaxiality ratio $T_X = [-1, 0]$. The case of steel hot rolling from Ascometal is used as an illustrative example. Time-dependent boundary conditions are imposed on the RVE. Values for zz-strain and xx- and yy-stresses that were obtained from the void-free simulation for a material point are applied as such on the three directions of the RVE.

The values were measured at several points in the RVE and homogeneity was verified throughout the RVE (see Fig. 2.2). Local variations can be observed at the edges of the cuboid, resulting from the local application of boundary conditions. However, using a sufficiently large RVE, these local fluctuations will not impact the values of stress triaxiality ratio in the zone of interest, i.e. the center of the RVE. The choice of RVE dimensions is discussed in section 2.5.2.

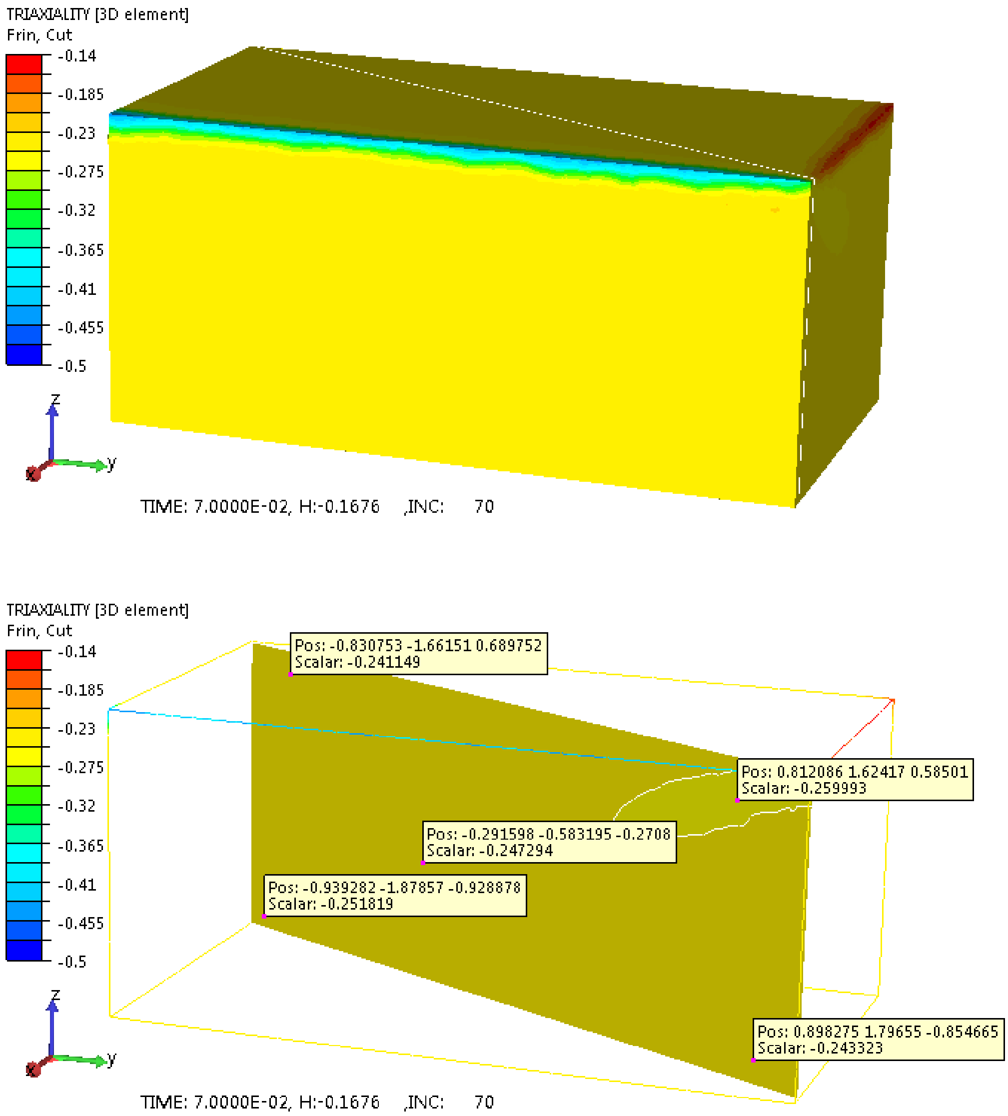

Figure 2.2: Value of stress triaxiality ratio in the RVE under hot rolling BC.

The values measured using point tracking for a central point in the RVE are then compared to the ones from the process simulation. The accuracy of xx- and yy-stresses and zz-strain was verified in Figs. 2.3a,b,c. Boundary conditions are thus applied with good accuracy in each spatial direction.

It was shown that the evolution of stress triaxiality ratio *vs.* equivalent strain was a key parameter for void closure. It is therefore also plotted in Fig. 2.3d. Apart from the slight difference observed for the final strain values, the figure shows that the evolution of stress triaxiality ratio *vs.* equivalent strain, is represented in the RVE with very good accuracy.

2.3.2 Imposed mechanical state

In order to quantitatively (and independently) study the influence of mechanical parameters on void closure, a constant mechanical state must be imposed. In this section, a method to impose a constant stress triaxiality ratio and constant strain-rate is presented.

From the definition of stress triaxiality ratio, there is no unicity of the relationship between the stress tensor and the stress triaxiality ratio. In fact, an infinite number of stress states can lead to the same stress triaxiality ratio. Here, an additional condition is introduced by assuming axisymmetric conditions such that the prescribed boundary conditions $\sigma_{xx} = \sigma_{yy}$. This choice was made in a first approach and may be considered as another general hypothesis within this work. It will be discussed in Chapter 5 as well. The prescribed stress triaxiality ratio can be expressed as:

$$T_X^* = \frac{\sigma_m}{\bar{\sigma}} = \frac{\sigma_{xx} + \sigma_{yy} + \sigma_{zz}}{3\bar{\sigma}} = \frac{2\sigma_{xx} + \sigma_{zz}}{3\bar{\sigma}}, \tag{2.1}$$

and equivalent von Mises stress reduces to:

$$\bar{\sigma} = |\sigma_{xx} - \sigma_{zz}|. \tag{2.2}$$

It comes:

$$\begin{aligned} \sigma_{xx} &= \left(T_X + \frac{1}{3}\right)\bar{\sigma} \quad \forall \sigma_{zz} \leq \sigma_{xx}, \\ \sigma_{xx} &= \left(T_X - \frac{1}{3}\right)\bar{\sigma} \quad \forall \sigma_{zz} \geq \sigma_{xx}. \end{aligned} \tag{2.3}$$

In Eq. 2.3, the values of remote stress σ_{xx} (and σ_{yy}) can be obtained knowing the remote equivalent von Mises stress in the RVE. The remote equivalent von Mises is given by the material behaviour according to the remote strain conditions that are imposed using the velocity boundary condition (Eq. 2.4). According to the axisymmetric loading conditions, it comes $\varepsilon_{xx} \approx \varepsilon_{yy}$. The equivalent strain is thus reduced to the expression:

$$\bar{\varepsilon} \approx |\varepsilon_{zz}| = \left| \ln\left(\frac{D_z^0 - D_z}{D_z^0}\right) \right|, \tag{2.4}$$

where D_z and D_z^0 are the current height and the initial height of the RVE, respectively.

The constant prescribed strain-rate $\dot{\bar{\varepsilon}}^*$ is imposed using a normal velocity V_z on the upper surface of the RVE, i.e. along the z-axis (see Fig. 2.1),

$$V_z(t) = -\dot{\bar{\varepsilon}}^* D_z(t). \tag{2.5}$$

The tridimensional boundary conditions are thus applied as shown in Fig. 2.1, using the values given by Eq. 2.5 and Eq. 2.3.

The obtained stress triaxiality field is presented in Fig. 2.4. For all cases, the measured stress triaxiality field T_X is rather homogeneous throughout the RVE, except at the edges, due the local application of boundary conditions. Apart from this, the value of stress triaxiality ratio T_X varies on a range $T_X^* \pm 0.02$ (green color) around the prescribed value, over the whole RVE. In the case of $T_X^* = -1.0$, the values of T_X tend to be slightly higher (less compressive) than the prescribed value, but remain on the range $T_X^* - 0.02 < T_X < T_X^* + 0.06$ (yellow and green colors).

The imposed values are verified by plotting, for several prescribed values T_X^*, the values of xx–stress and yy–stress *vs.* time in Fig. 2.5a,b, and $\dot{\bar{\varepsilon}}$ *vs.* time in Fig. 2.5c. The values are measured using point tracking at a central position of the RVE. The evolutions of xx–stress and yy–stress are directly imposed by Eq. 2.3 and their evolution is proportional to the one of the behaviour law (i.e. stress–strain curve). The evolution of measured strain-rate shows that the value is imposed with very good accuracy with respect to the prescribed value $\dot{\bar{\varepsilon}}^{*} = 1\ \mathrm{s}^{-1}$. This remark shows that the approximation that is made in Eq. 2.4 is acceptable.

The evolution of the stress triaxiality ratio is plotted in Fig. 2.5d. The figure verifies that the values of stress triaxiality remains constant over the whole deformation range. The values of σ_{xx} and σ_{yy} (see Fig. 2.5b) are driven by the boundary conditions given in Eq. 2.3. The figure shows that their value faithfully follows the evolution of $\bar{\sigma}$, the latter being driven by the behaviour law of the material under $\dot{\bar{\varepsilon}}^{*} = 1\ \mathrm{s}^{-1}$ (black line).

Regarding the measured values of T_X, the highest discrepancy is about 4% superior to the prescribed condition $T_X^{*} = -1$ (obtained around $\bar{\varepsilon} = 0.2$). For the less compressive state $T_X^{*} = 0$, the measured value of T_X is slightly inferior to the prescribed value (about 2%). The obtained discrepancies are acceptable. The presented method is thus suitable to impose a constant stress triaxiality ratio in the RVE.

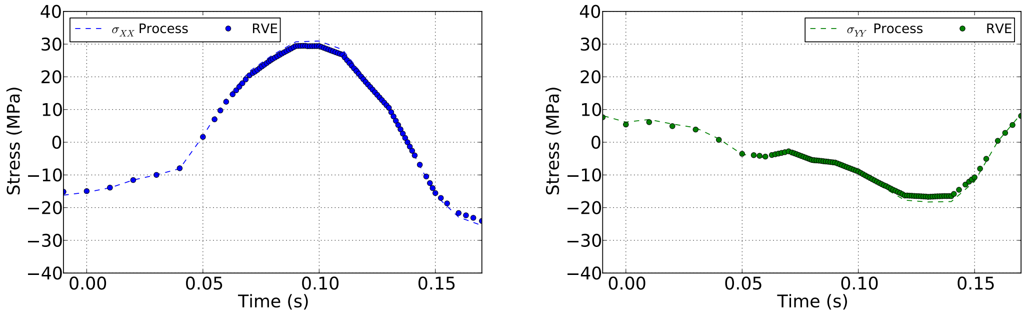

(a) *xx*-stress *vs.* time

(b) *yy*-stress *vs.* time

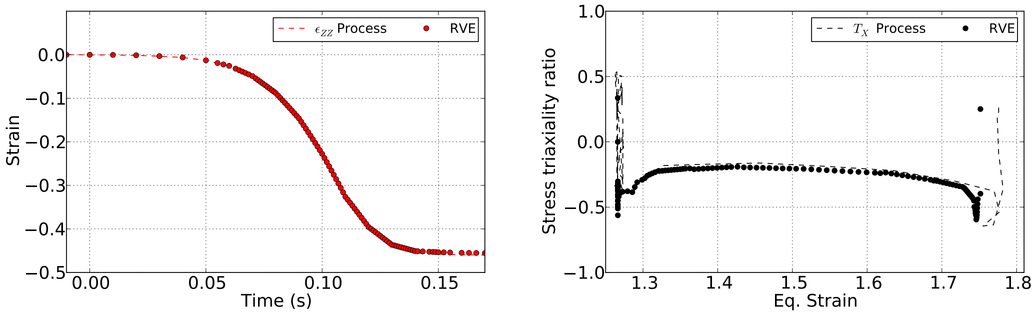

(c) *zz*-strain *vs.* time

(d) stress triaxiality ratio *vs.* equivalent strain

Figure 2.3: Comparison of mechanical variables obtained from void-free process simulation (dashed lines) and RVE with boundary conditions (dots).

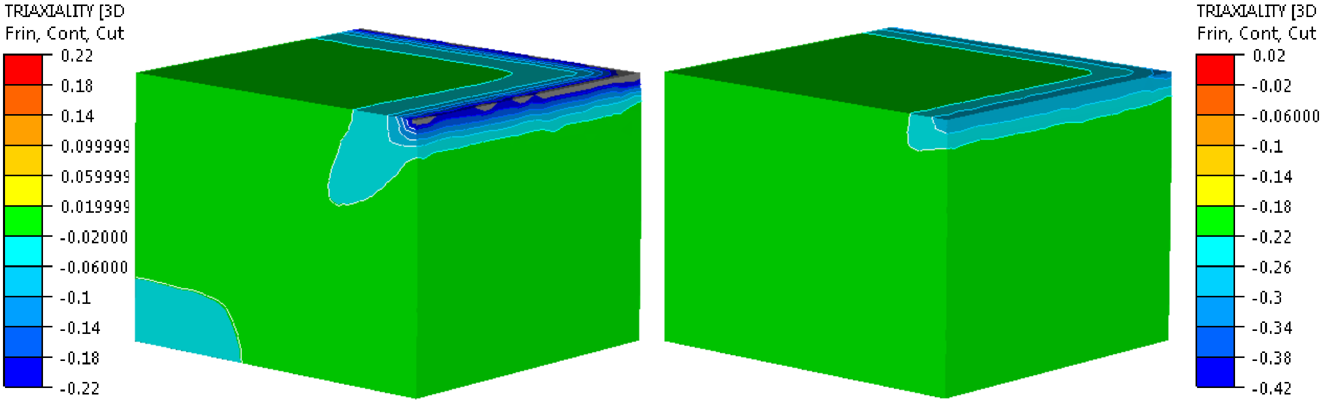

(a) $T_X^* = 0$ (b) $T_X^* = -0.2$

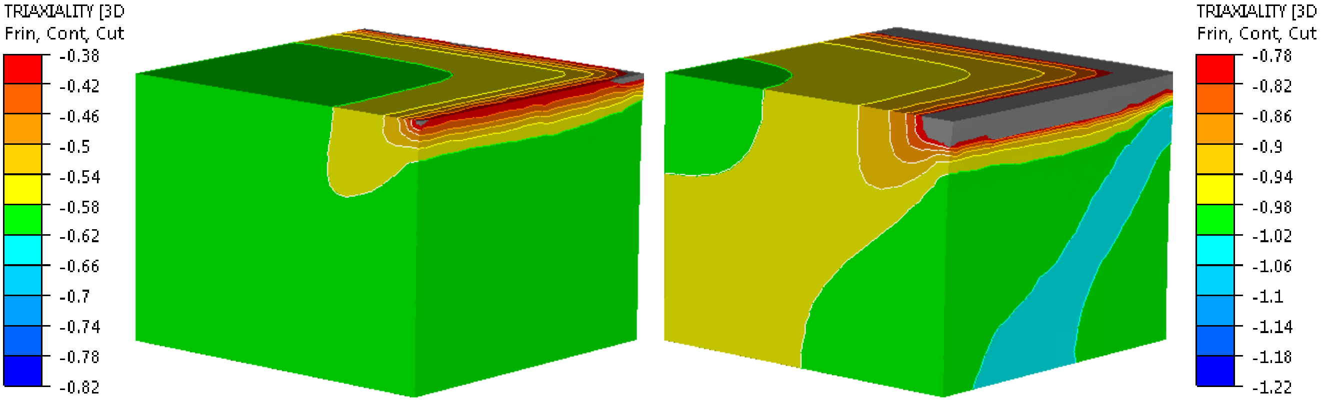

(c) $T_X^* = -0.6$ (d) $T_X^* = -1.0$

Figure 2.4: Stress triaxiality field for various prescribed boundary conditions T_X^*, for $\bar{\varepsilon} = 0.2$. For each case, the legend represents the range $T_X^* \pm 0.22$.

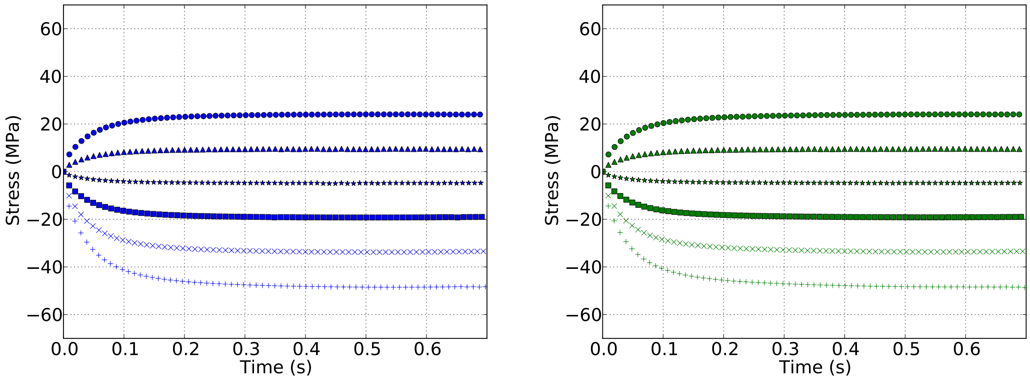

(a) xx-stress *vs.* time

(b) yy-stress *vs.* time

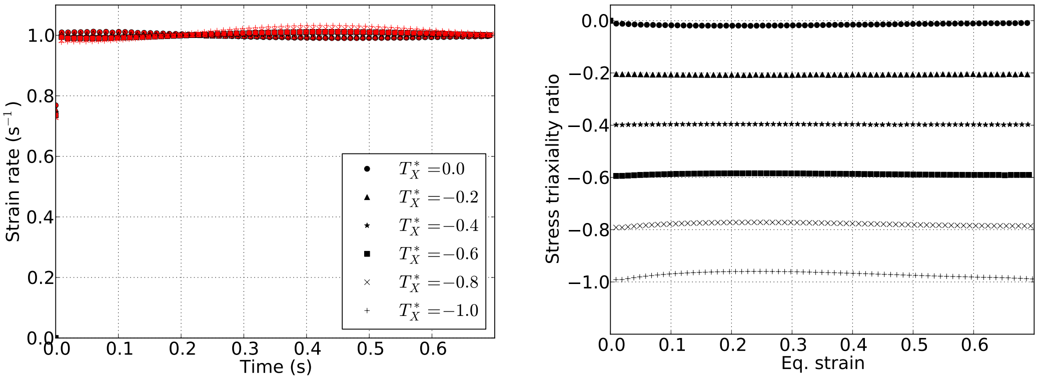

(c) zz-strain *vs.* time

(d) stress triaxiality ratio *vs.* equivalent strain

Figure 2.5: Measured evolutions of mechanical fields at the center of the RVE, under various prescribed boundary conditions $T_X^* = \{-1.0, -0.8, -0.6, -0.4, -0.2, 0.0\}$ and $\dot{\bar{\varepsilon}}^* = 1\ \mathrm{s}^{-1}$.

2.4 Generation of a 3D Representative Volume Element

This section describes the generation of a tridimensional RVE containing internal void. It is firstly presented for the case of real-void morphology obtained from experimental observation. Then, the generation of an RVE containing a *morphology-equivalent* geometry is detailed.

2.4.1 Real-void morphology obtained from 3D microtomography

X-ray microtomography

X-ray microtomography is a relatively recent technique that enables tridimensional non-destructive examination of materials [Maire et al., 2001, Salvo et al., 2003]. It is divided in two successive steps: an acquisition step and a reconstruction step. For the acquisition step, the sample is placed between the X-ray source and the detector on a rotating stage, as schematically presented in Fig. 2.6. Rotation is discretized in several hundreds of rotation angles. For each angle of rotation a projection radiograph is acquired from the detector. All projection radiographs are then numerically treated during the reconstruction step to generate a tridimensional grayscale image.

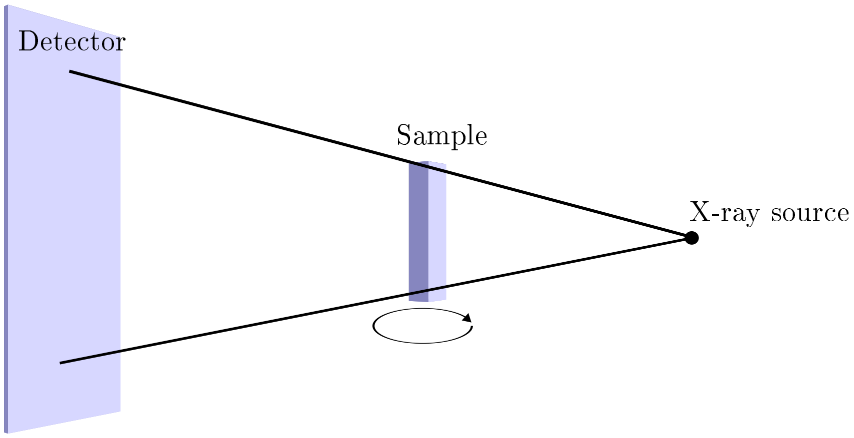

Figure 2.6: Schematic drawing of the acquisition step of a tomograph.

Over the last decade, synchrotron lighting source was often used in the literature to observe void evolution in steel samples Everett et al. [2001], Bouchard et al. [2008], Maire et al. [2008] and in aluminum samples Buffière et al. [1999], Morgeneyer et al. [2008], Horstemeyer et al. [2003]. As these studies focus on void evolution under tensile conditions, dealing with ductile damage, the results remain out of the scope of the present work. Nevertheless the methodology shows great potential of using X-ray microtomography for studying void closure.

Toda et al. [2009] used synchrotron microtomography to study the closure of hydrogen micropores in Mg-Al alloy under hot and cold deformation and annealing. The study shows attractive results in terms of accuracy of the tridimensional images obtained with samples containing voids under compression.

Using synchrotron's monochromatic light presents the main advantage of providing a high resolution (about 1 μm voxel size) for the 3D image, due to the high energy and quality of the incoming X-ray photons. It is also possible to perform microtomography using an X-ray tube. In this case, the photons are accelerated using an acceleration tension that varies between 220 kV and 450 kV for classical tomographs. The obtained resolution is generally limited to about 10 μm voxel size. Another difference with synchrotron light is that an X-ray tube generates a conic beam, while synchrotron provides a parallel beam. Magnification is therefore possible using an X-ray tube by shifting the sample in the conic beam. Lee et al. [2007, 2011] used a 450 kV–tomograph to obtain a tridimensional image of a porous $\varnothing 90$ mm$\times$200 mm steel sample. A tridimensional mesh was generated and FE simulations using the commercial finite element code DEFORM–3D™ were performed under hot compression. The final mesh was compared with a second tridimensional image of the deformed sample, and a good agreement was obtained. Due to the very low availability of synchrotron facilities and the promising results found in literature using X-ray tube, the latter solution was chosen within this work.

3D images of industrial samples

Several porous specimen were collected by various partners and are listed in Table 2.1.

Partner	Alloy	Sample	Dimensions (mm)	Tomograph	Voxel size (μm)
Timet	Ti-alloy1	T1	$27 \times 27 \times 90$	CETIM	21
		T2	$20 \times 20 \times 50$	CETIM	31
				Fraunhofer	15
		TB	$7 \times 7 \times 90$	CETIM	13
Aubert&D.	Steel14	AD	$40 \times 40 \times 330$	CETIM	100
Ascometal	Steel24	JD20	$\varnothing 20 \times 85$	CETIM	128
		JD47	$10 \times 10 \times 85$	Fraunhofer	102
Constellium	Al-alloy1	C701av	$10 \times 8.2 \times 6.1$	Internal	12
		C701ap	$6.1 \times 6.1 \times 6.1$	Internal	12
		CA	$7.9 \times 7.7 \times 8.2$	Internal	18
		CG	$7.8 \times 7.9 \times 8.4$	Internal	18
		C3	$9.2 \times 9.2 \times 9.2$	Internal	18

Table 2.1: List of samples that were observed using X-ray microtomography at CETIM, Fraunhofer, or directly provided from internal data.

The samples were extracted from critically porous workpieces according to a previous localization of voids using ultrasonic testing. In a first phase, two Ti-alloy samples (T1 and T2) and two steel samples (AD and JD20) were collected in order to constitute a various sampling of various materials and void state. They were observed by X-ray microtomography at CETIM[1] and Fraunhofer[2]. At CETIM, a direct access to the microtomograph facility was provided. The scanning parameters could be carefully adjusted in order to enhance the quality of the tridimensional images. Regarding the Fraunhofer facilities, no access was provided. The scans were performed by the Fraunhofer Institut and the results were shipped.

According to the results obtained during the first phase, two further samples (TB and JD47) were then analyzed in a second phase. The 3D images of the samples of Al-alloy

---

[1] CETIM Senlis, Pôle EPI, BP 80067 52 avenue Felix Louat, 60304 Senlis cedex, France

[2] Fraunhofer Institut Zerstörungsfreie Prüfverfahren IZFP, Campus E3.1, 66123 Saarbrücken, Germany

had been previously obtained from internal work at Constellium and were received as such between the first and the second phase.

The maximum dimensions of a sample to be scanned are defined according to several parameters:

- The energy of the X-ray beam, which depends on the acceleration tension.
- The attenuation coefficient of the material. The beam intensity obey to the Beer–Lambert law
$$I = I_0 e^{(-\alpha D)}, \tag{2.6}$$
where I_0 is the incident intensity, α the attenuation coefficient and D the path length. The attenuation coefficient is a material property which increases with the atomic number. Within the materials in Table 2.1, the steels present the largest attenuation coefficients, then the Ti-alloy and finally the Al-alloy.
- The detector sensitivity.
- The spatial capabilities to contain the sample inside the chamber, considering its 360°–rotation.

Using X-ray tubes, the highest energy source (i.e. 450 kV acceleration tension) enables larger samples to be scanned, but the X-ray source focal is generally larger. This reduces the radiographs' sharpness. Sharper images may be obtained using the lowest energy source (i.e. 220 kV acceleration tension) as their focal is smaller, but the maximum acceptable thickness is reduced. A compromise had therefore to be found for each sample to obtain the best quality of images.

Examples of tridimensional reconstructed images are given in Figs. 2.7, 2.8, 2.9, 2.10 and 2.11. For each sample, a global 3D overview and 2D–slices (in the three spatial directions) are presented. For the samples T1, T2 and AD, the number and size of voids was lower than it was expected according to previous ultrasonic estimation. It is notably the case for the two Ti-alloy samples, in which only a few submillimetric voids (0.1 – 0.5 mm) were detected.

The steel sample AD presented millimetric voids (1 – 10 mm), and the obtained image had a relative low contrast due to the excessive sample-to-void thickness ratio. Nevertheless, two particularly porous zones could be identified, showing good agreement with the previous ultrasonic indications.

The Al-alloy sample C3 contains rather dispersed submillimetric voids (0.1 – 0.5 mm). The obtained contrast is better than the one for Ti-alloys, due to the difference of absorption coefficient.

The sample JD20 provided the best contrast. It was due to the relative small dimensions of the sample combined with a low sample-to-void thickness ratio. Centerline millimetric voids were observed throughout the sample. A continuous porous zone was identified at the lowest half of the sample as it is presented in Fig. 2.11. The upper half is mainly composed of three isolated voids with dimensions about 3 – 10 mm. They present a rather tortuous aspect.

Image filtering

X-ray microtomography generally involves a certain number of artifacts. Using thick samples, the transmitted light intensity might be relatively low and the sensitivity range of the detector may induce noise on the grayscale radiographs. They also appear on the

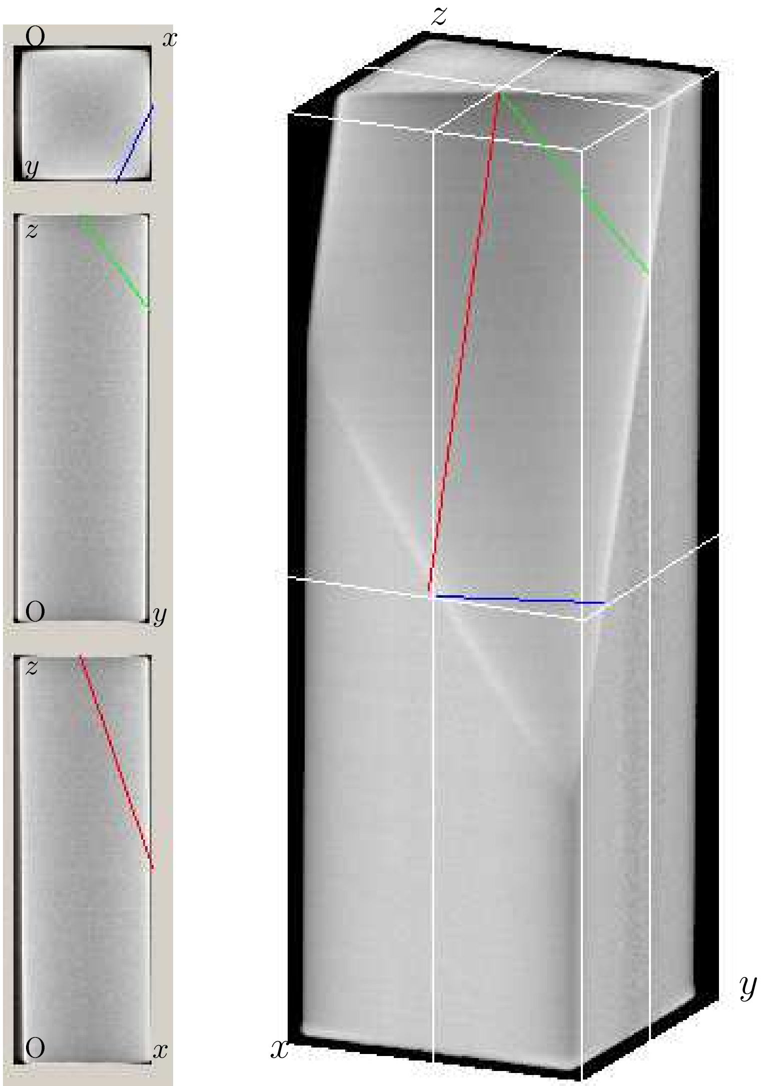

Figure 2.7: Tridimensional raw image of sample T1 (Ti-alloy) obtained using X-ray microtomography, and 2D slices along each spatial direction.

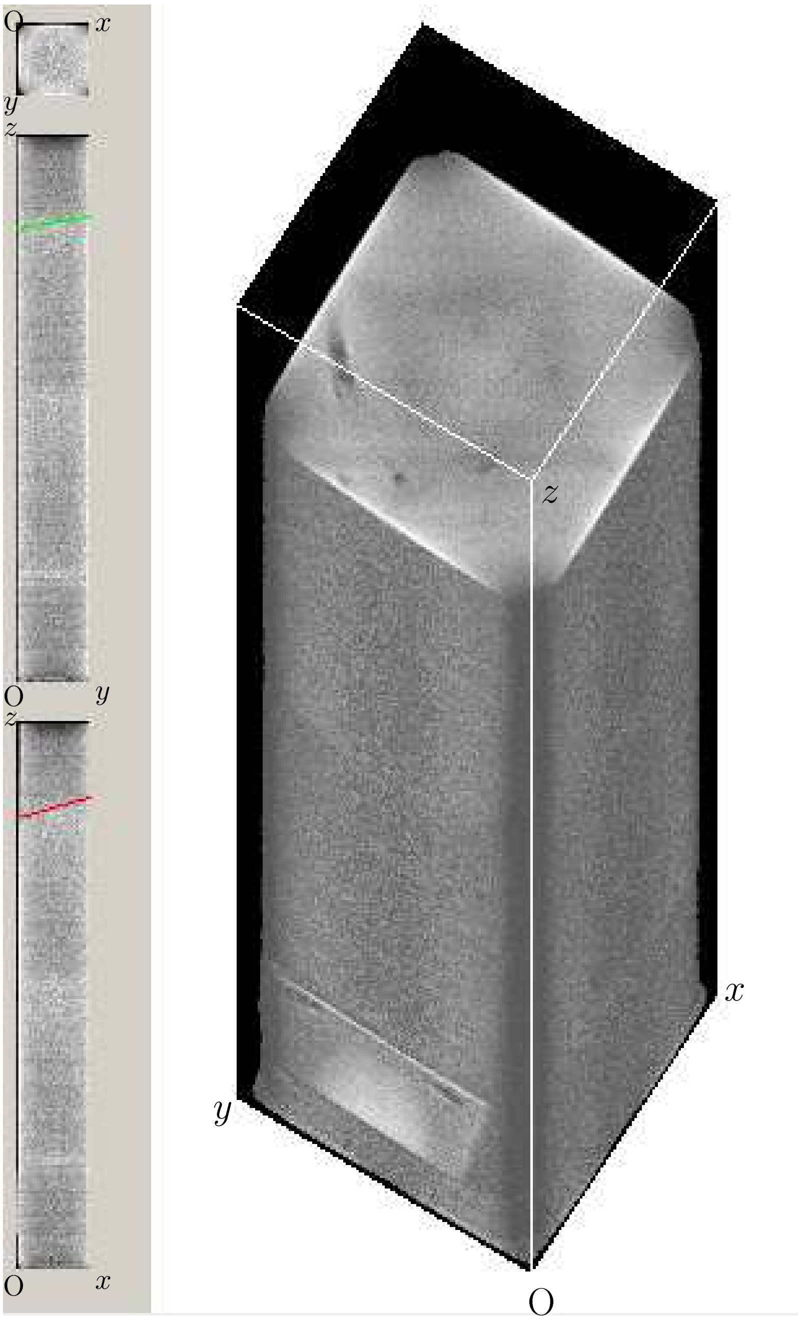

Figure 2.8: Tridimensional raw image of sample AD (steel) obtained using X-ray microtomography, and 2D slices along each spatial direction.

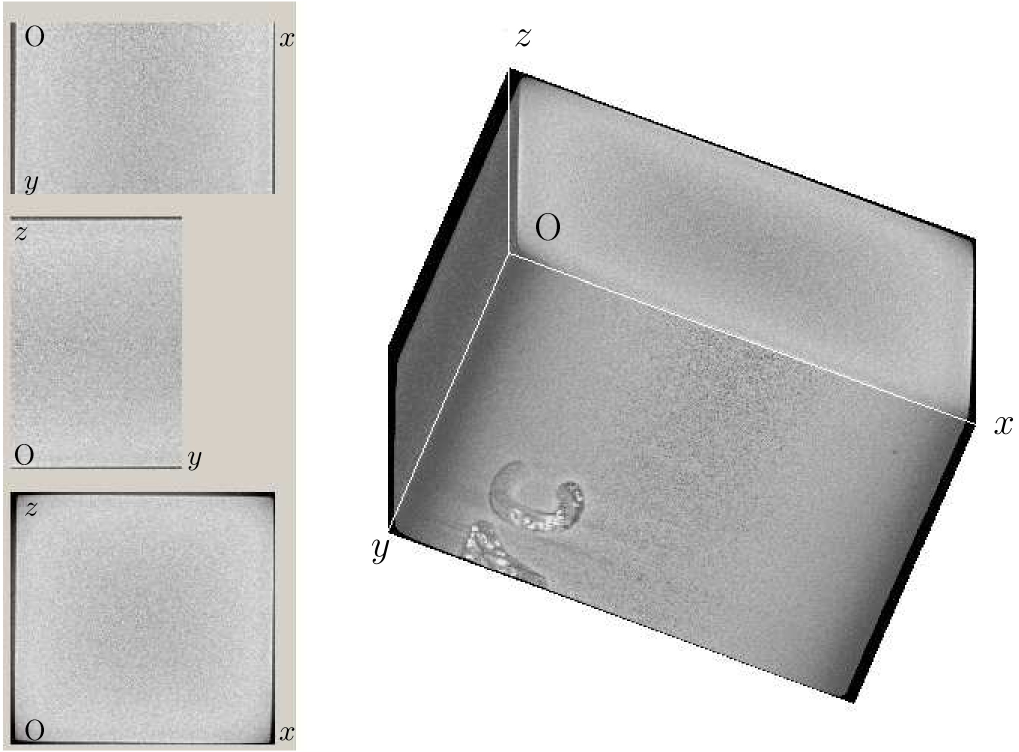

Figure 2.9: Tridimensional raw image of sample T2 (Ti-alloy) obtained using X-ray microtomography, and 2D slices along each spatial direction.

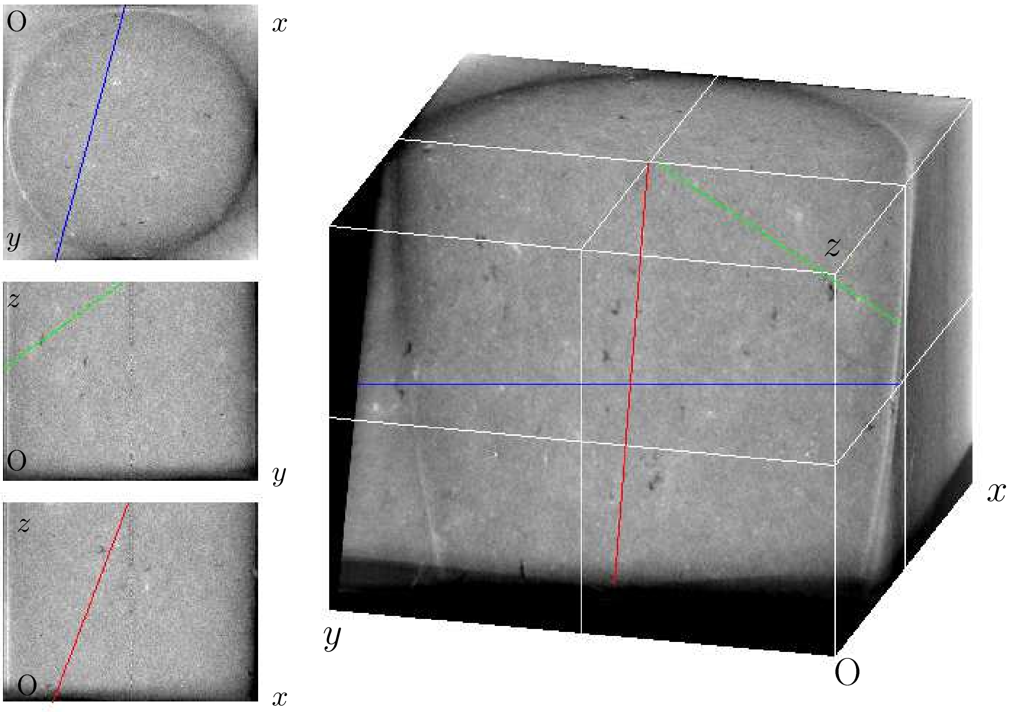

Figure 2.10: Tridimensional raw image of sample C3 (Al-alloy) obtained using X-ray microtomography, and 2D slices along each spatial direction.

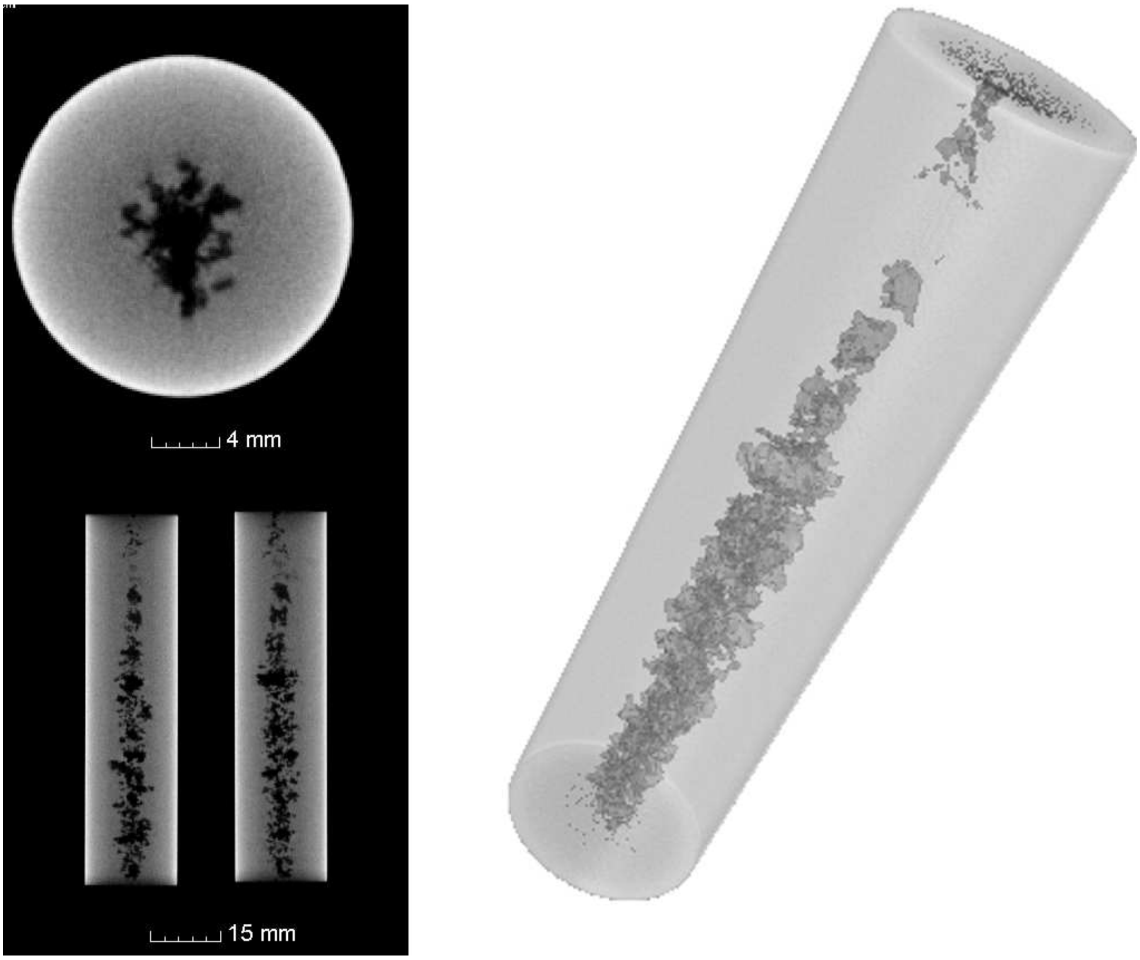

Figure 2.11: Tridimensional raw image of sample JD20 obtained using X-ray microtomography, and 2D slices along each spatial direction.

3D reconstructed image. The interaction of X-rays with the surface of the sample may also involve brighter or darker zones due to beam hardening phenomenon and reflexion at the sample's surface. The objective being to capture the void-matrix interface using a grayscale threshold value, these two artifacts must be eliminated. The free software ImageJ [Rasband, 1997-2012.] is a very powerful software for the analysis of tridimensional images and was thus used within this work for image filtering.

The grayscale tridimensional data is first submitted to a 3D median filter in order to reduce the grayscale noise, (a) → (b) in Fig. 2.12. Compared to other filters (e.g. Gauss, mean value) the median filter presents the advantage of reducing the noise without affecting the image sharpness. This is of great interest, especially at the void-matrix interface.

The presence of brighter and darker zones is reduced by means of a *background subtraction* algorithm. A background image is computed according to the rolling ball algorithm [Sternberg, 1983], which can be briefly described as follows. Let us consider the 2D image Fig. 2.12 (b) and imagine a ball that is rolling at the top of the grayscale profile to generate the background profile. The level of details to be eliminated thus depends on the ball radius. In this case, a ball radius of 20 voxels was chosen to obtain (c). The obtained background image is subtracted to the image to obtain the final treated image (d) = (b) – (c).

3D surface mesh generation

A tridimensional surface mesh of the matrix-void interface was generated from the tridimensional grayscale image using an algorithm that was previously developed at CEMEF by Zaragoci et al. [2012], Zaragoci [2012]. This algorithm is based on the marching-cubes method [Lorensen and Cline, 1987], using extension by Rajon and Bolch [2003] providing a grayscale interpolation to better capture the interface. According to a grayscale threshold value that determines whether a voxel belongs to one phase (bright voxels: matrix) or to the other phase (dark voxels: void), the algorithm generates a tridimensional surface that corresponds to the interface between both phases.

From sample JD20, the void-matrix interface is illustrated in Fig. 2.13. Let us note the particularly high void density of this sample. Three significant isolated voids were named A, B and C (see enlargement in Fig. 2.13b). They will be further used within this work as their features present great interest for the study. Note the presence of smaller voids on the right of the window in (a), and of a continuous cavity along the entire remaining length on the left of the window. This continuous cavity gives an excellent illustration of tortuosity that can be encountered. However, it will not be further studied within this work as it is industrially considered as an extreme case and is not representative of industrial issues.

In Fig. 2.14, the void-matrix interface is illustrated using a perpendicular view, i.e. along the sample's axis. The tridimensional surface mesh is composed of triangles, whose edges are drawn with red segments. Note the periodicity of the nodes that directly depends on the voxel size of the tridimensional image.

A cutting plane was introduced using the same position than the one defined for the slice in Fig 2.12. The intersection between the surface mesh and the cutting plane is drawn using a blue contour.

3D volume mesh generation

This section describes how to generate a tridimensional RVE containing a real void. It is illustrated using void A.

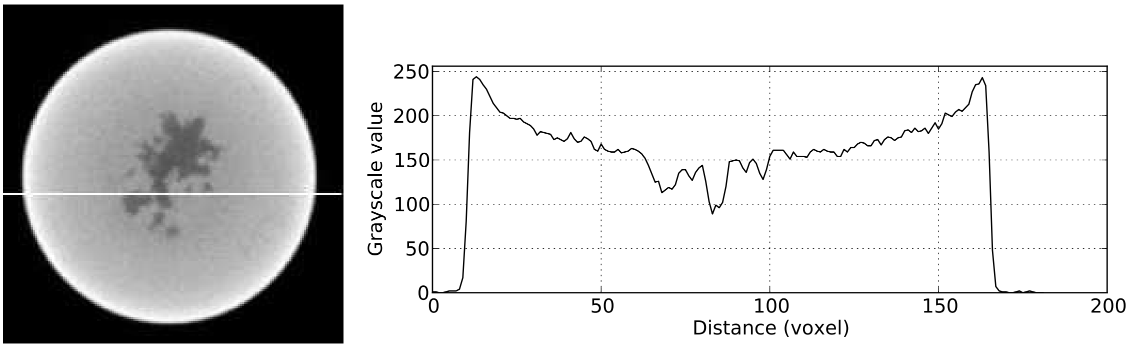

(a) Initial slice

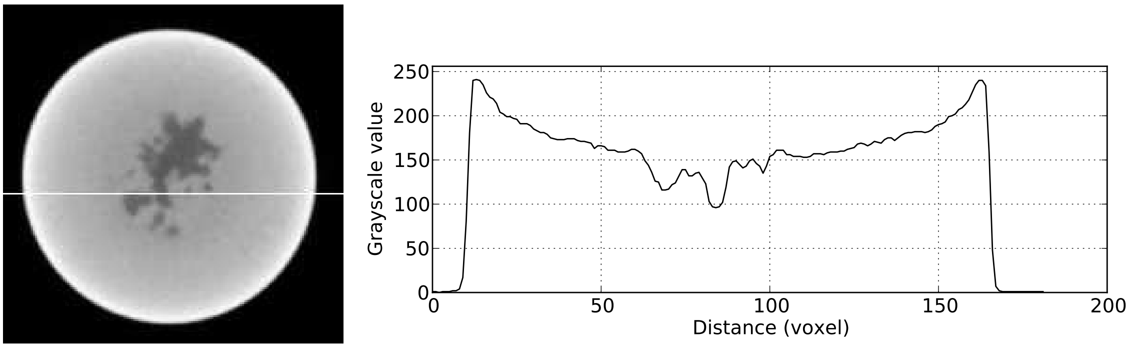

(b) After median filter

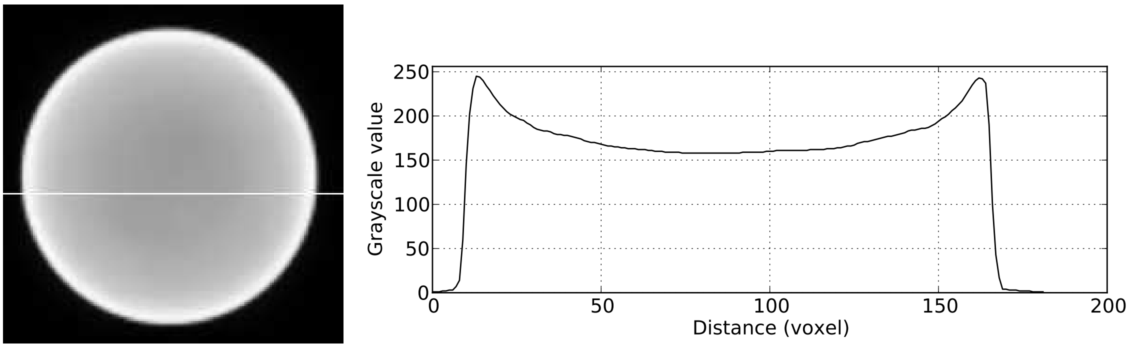

(c) Background image

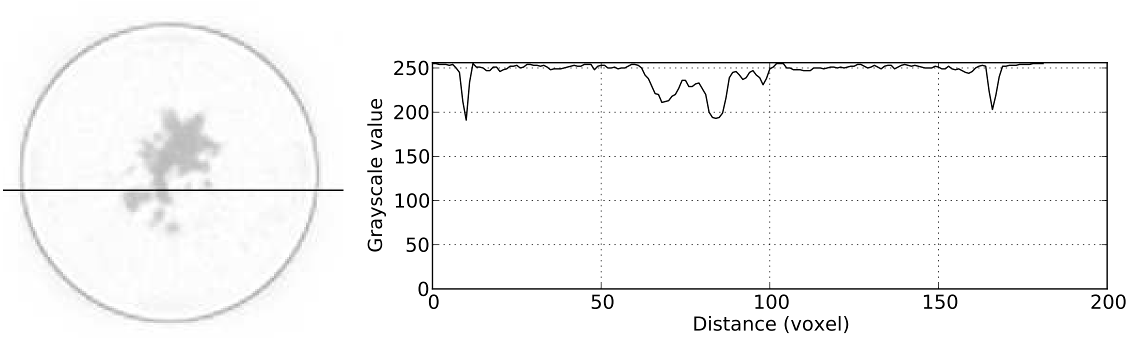

(d) After background subtraction

Figure 2.12: Image filtering, illustrated for each step with a slice of sample JD20, and a profile of grayscale values plotted for the horizontal line.

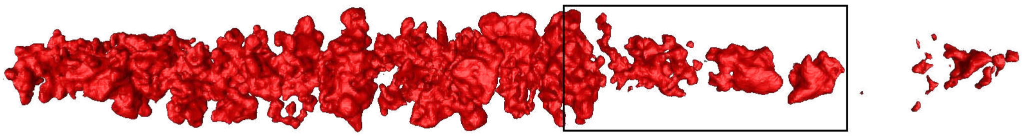

(a) Tridimensional void-matrix interface of the entire sample JD20

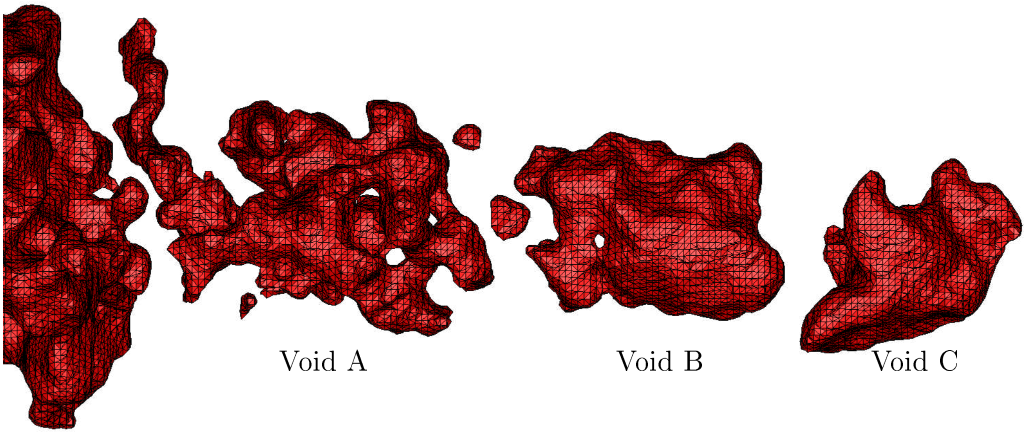

(b) Surface mesh (detail)

Figure 2.13: Tridimensional surface obtained using the marching-cubes algorithm from raw image of JD20.

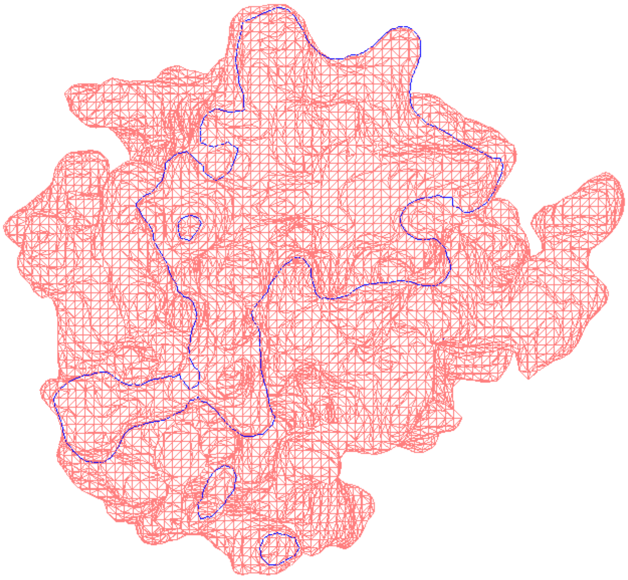

Figure 2.14: Contour (blue line) of the void-matrix interface for the slice that was previously defined in Fig 2.12.

A cuboidal surface mesh is created using the GLPre[1] software according to the dimensions $D_i, \quad i \in \{x, y, z\}$ in order to define the external boundaries of the RVE (see Fig. 2.15). The RVE dimensions D_i are defined according to the void dimensions d_i using a proportionality coefficient η, such as:

$$D_i = \eta . d_i, \qquad i \in \{x, y, z\}, \tag{2.7}$$

where d_i are the dimensions of the void. They are defined as the dimensions of the smallest cuboid in which the void can be contained.

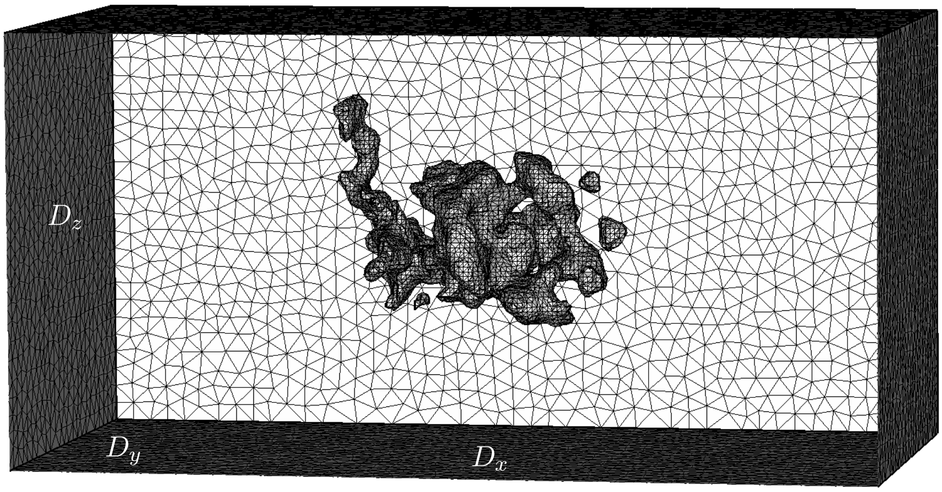

(a) Internal and external surfaces of the RVE mesh, illustrating the surface triangles from the void-matrix interface and the external boundaries of the RVE

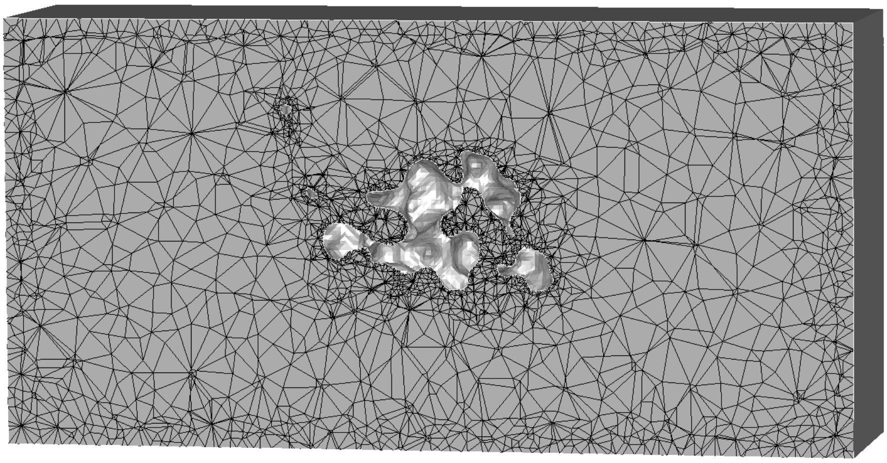

(b) Cutting xz-plane of the volume mesh of the RVE, illustrating the tetrahedral volume elements between internal and external surfaces

Figure 2.15: Initial RVE containing void A, showing the surface elements in the internal surface and the volume elements on the cutting plane.

---

[1] GLPre is the preprocessor used in FORGE® to setup simulations

The relative position of the cuboid is chosen such that the centers of gravity of both meshes coincide. A volume mesh (unstructured tetrahedral elements) is generated between the internal surface mesh of void A and the cuboid's surface using GLPre.

2.4.2 Morphology parameters

The final objective of this work is to obtain a prediction model for void closure accounting for void morphology. A quantification of this morphology is therefore required and is presented in this section. Quantification of tridimensional morphology is often used in image analysis and can be declined in various approaches depending on the desired information to be quantified. Three approaches were defined and discussed by Parra-Denis [2007] to study the morphology of intermetallic particles in aluminum alloys: the parametric characterization, the spectral characterization and an original approach based on the local tridimensional curvature of particles. The first provides a series of parameters that can be physically interpretable. The second and the third provide accurate signatures of the tridimensional morphologies. The parametric characterization shows great interest within this work, as the parameters can be directly used as input data in the prediction model. This approach was thus chosen and the parameters are described in this section.

The number of parameters that can be used to characterize void morphology must be carefully chosen. An excessive number of parameters would substantially hinder the calibration step, as well as the final use of the model.

Void volume is traditionally used to study void closure, notably using the normalized volume V/V_0. A precise knowledge of the current void volume during closure is thus of utmost importance. It can be seen as the first morphology parameter and is presented first. Additionally, tridimensional parameters are introduced using the inertia matrix of the void. The inertia matrix enables principal dimensions and orientations to be computed and will be presented in a second paragraph.

Void volume

Let us consider the closed surface $\partial\mathcal{P} = \bigcup_{\tau\in\mathcal{T}_r} \tau$, where τ is a triangle of the surface mesh $\mathcal{T}_r$ of the void-matrix interface of a void $\mathcal{P}$, as illustrated in Fig. 2.16. Let us introduce the divergence theorem:

$$\iiint_V \operatorname{div}(\vec{F})dV = \oiint_{\partial V} \vec{F}.\vec{n}dS \tag{2.8}$$

where $\vec{F}$ is a vector field, $\vec{n}$ the outward unit normal to the surface ∂V. Let $\vec{F} = \overrightarrow{OX}$, where $\overrightarrow{OX} = \begin{pmatrix} x_1 \\ x_2 \\ x_3 \end{pmatrix}$ the coordinates vector of a point X, such that $\operatorname{div}(\vec{F}) = \operatorname{div}(\overrightarrow{OX}) = 3$. Then Eq. 2.8 can be rewritten as

$$3V = \oiint_{\partial V} \overrightarrow{OX}.\vec{n}dS = \sum_{\tau\in\mathcal{T}_r} \iint_\tau \overrightarrow{OX}.\vec{n}dS, \tag{2.9}$$

By definition, τ being a triangle, it belongs to a plane and $\forall X \in \tau$, $\overrightarrow{OX}.\vec{n} = \text{constant}$. It leads to

$$3V = \sum_{\tau\in\mathcal{T}_r} \overrightarrow{OX}_\tau.\vec{n}_\tau \iint_\tau dS = \sum_{\tau\in\mathcal{T}_r} \operatorname{surf}(\tau)\overrightarrow{OX}_\tau.\vec{n}_\tau, \tag{2.10}$$

where $\overrightarrow{OX}_\tau$ the coordinates vector of a point X_τ of the triangle τ, and $\vec{n}_\tau$ its outwards unit normal. The total volume of the void can thus be obtained by

$$V = \frac{1}{3} \sum_{\tau \in \mathcal{T}_r} \mathrm{surf}(\tau) \overrightarrow{OX}_\tau . \vec{n}_\tau, \qquad \forall X_\tau \in \tau, \tag{2.11}$$

where $\frac{1}{3}\,\mathrm{surf}(\tau)\overrightarrow{OX}_\tau.\vec{n}_\tau$ can be seen as the signed volume $\mathrm{vol}(\mathcal{T}_\tau)$ of the tetrahedron $\mathcal{T}_\tau$ composed by the triangle τ and the vertex O.

In this work, the normal vector is defined by the meshing algorithm in GLPre. This algorithm systematically defines the normal vector outwards the material. In the case of a void, the normal vector is thus oriented towards the void and the final volume of a void is negative. This is coherent as the equation shall be able to be used to compute the volume of any surface mesh. In the case of a meshed domain, the surface's normal will be directed outwards and the computed volume will be positive. On the contrary, in the case of a void (mesh-free domain), a negative volume can thus reasonably be defined as it exhibits the absence of material inside the surface.

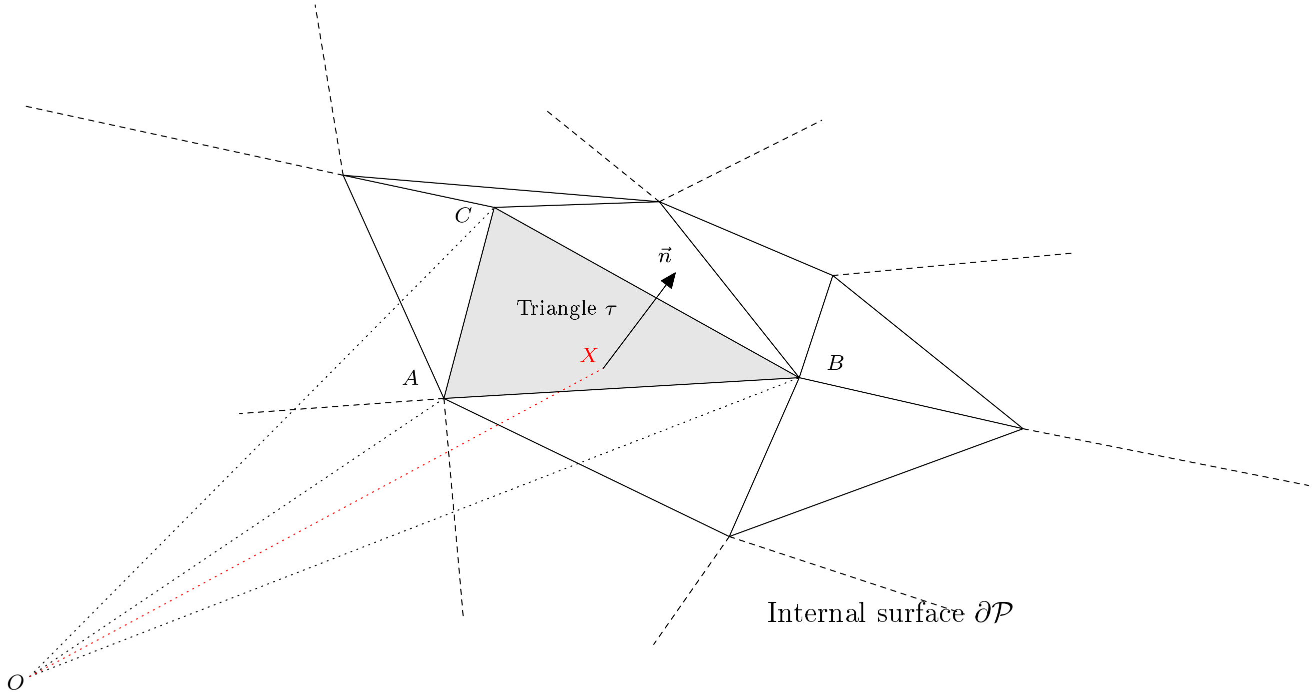

Figure 2.16: Triangle of the internal surface mesh (void–matrix interface).

Tridimensional dimensions and orientation

Equivalent dimensions are obtained by computing the inertia matrix of the initial void. The inertia matrix is expressed by:

$$MI = \begin{pmatrix} MI_1 & MI_4 & MI_5 \\ MI_4 & MI_2 & MI_6 \\ MI_5 & MI_6 & MI_3 \end{pmatrix} \tag{2.12}$$

with

$$\begin{cases} MI_1 = \iiint_{\mathcal{P}} \rho(x_2^2 + x_3^2)dV \\ MI_2 = \iiint_{\mathcal{P}} \rho(x_1^2 + x_3^2)dV \\ MI_3 = \iiint_{\mathcal{P}} \rho(x_1^2 + x_2^2)dV \end{cases} \quad \text{and} \quad \begin{cases} MI_4 = -\iiint_{\mathcal{P}} \rho x_1 x_2 dV \\ MI_5 = -\iiint_{\mathcal{P}} \rho x_2 x_3 dV \\ MI_6 = -\iiint_{\mathcal{P}} \rho x_1 x_3 dV \end{cases}, \tag{2.13}$$

where ρ is the mass density. Within this work, the inertia matrix is used for its morphological features. A homogeneous unitary density $\rho = 1$ is thus considered.

Let $P_{ij} = \iiint_{\mathcal{P}} x_i x_j dV$, such that:

$$\begin{cases} MI_1 = P_{22} + P_{33} \\ MI_2 = P_{11} + P_{33} \\ MI_3 = P_{11} + P_{22} \end{cases} \quad \text{and} \quad \begin{cases} MI_4 = -P_{12} \\ MI_5 = -P_{23} \\ MI_6 = -P_{13} \end{cases}, \tag{2.14}$$

with $(i,j) \in \{1,2,3\}$. Let $\overrightarrow{OX}$ the coordinates vector of a point of the triangle τ, and let $\overrightarrow{V_{ij}} = \frac{1}{5} x_i x_j \overrightarrow{OX}$, such that $\mathrm{div}(\overrightarrow{V_{ij}}) = x_i x_j$. The divergence theorem leads to:

$$P_{ij} = \iiint_{\mathcal{P}} x_i x_j dV = \iiint_{\mathcal{P}} \mathrm{div}\,(\overrightarrow{V_{ij}})dV = \oiint_{\partial\mathcal{P}} \overrightarrow{V_{ij}}.\vec{n}\,dS, \tag{2.15}$$

which can be rewritten as:

$$P_{ij} = \frac{1}{5} \oiint_{\partial\mathcal{P}} x_i x_j (\overrightarrow{OX}.\vec{n})dS \tag{2.16}$$

Using the same remark than for obtaining Eq. 2.10, the scalar product $\overrightarrow{OX}.\vec{n}$ is constant $\forall X \in \tau$ and $\overrightarrow{OX}.\vec{n} = \frac{3\,\mathrm{vol}(\mathcal{T}_\tau)}{\mathrm{surf}(\tau)}$ the equation can be rewritten as:

$$P_{ij} = \frac{1}{5} \sum_{\tau \in \mathcal{T}_r} \left(\overrightarrow{OX}_\tau.\vec{n}_\tau \iint_\tau x_i x_j dS \right) = \frac{3}{5} \sum_{\tau \in \mathcal{T}_r} \left(\frac{\mathrm{vol}(\mathcal{T}_\tau)}{\mathrm{surf}(\tau)} \iint_\tau x_i x_j dS \right). \tag{2.17}$$

To compute the surface integral $\iint_\tau x_i x_j dS$, let us define A, B and C the three vertices of the triangle τ (see Fig. 2.16). The coordinates of the point X can be expressed by:

$$\overrightarrow{OX} = \overrightarrow{OA} + \beta_1 \overrightarrow{AB} + \beta_2 \overrightarrow{AC}, \tag{2.18}$$

where $(\beta_1, \beta_2) \in [0,1]$ the coordinates in the new integration basis $\left(\overrightarrow{AB}, \overrightarrow{AC}\right)$. It comes:

$$dS = \|\overrightarrow{AB} \wedge \overrightarrow{AC}\| d\beta_1 d\beta_2 = 2\,\mathrm{surf}(\tau) d\beta_1 d\beta_2, \tag{2.19}$$

and Eq. 2.17 becomes:

$$P_{ij} = \frac{6}{5} \sum_{\tau \in \mathcal{T}_r} \mathrm{vol}(\mathcal{T}_r) \int\limits_0^1 \int\limits_0^{1-\beta_1} (OA|_i + \beta_1 AB|_i + \beta_2 AC|_i)\,(OA|_j + \beta_1 AB|_j + \beta_2 AC|_j)\, d\beta_2 d\beta_1, \tag{2.20}$$

which can be developed in:

$$\begin{aligned} P_{ij} = \frac{6}{5} \sum_{\tau \in \mathcal{T}_r} \mathrm{vol}(\mathcal{T}_r) \int\limits_0^1 \int\limits_0^{1-\beta_1} & [OA|_i OA|_j + \beta_1^2 AB|_i AB|_j + \beta_2^2 AC|_i AC|_j \\ & + \beta_1(OA|_i AB|_j + OA|_j AB|_i) + \beta_2(OA|_i AC|_j + OA|_j AC|_i) \\ & + \beta_1\beta_2(AB|_i AC|_j + AB|_j AC|_i)] d\beta_2 d\beta_1. \end{aligned} \tag{2.21}$$

Finally, the value of P_{ij} can be computed as

$$\begin{aligned} P_{ij} = \frac{1}{20} \sum_{\tau \in \mathcal{T}_r} \mathrm{vol}(\mathcal{T}_r)[12 OA|_i OA|_j + 2(AB|_i AB|_j + AC|_i AC|_j) \\ + 4(OA|_i AB|_j + OA|_j AB|_i + OA|_i AC|_j + OA|_j AC|_i) \\ + AB|_i AC|_j + AB|_j AC|_i]. \end{aligned} \tag{2.22}$$

Using Eq. 2.22 and Eq. 2.14, the inertia matrix can be computed for any void, knowing the coordinates of the triangles of the surface mesh of the closed surface $\partial\mathcal{P}$.

The inertia matrix is a symmetric positive-definite matrix. It is diagonalizable in an orthonormal basis $\{\vec{u_1}, \vec{u_2}, \vec{u_3}\}$ of eigen-vectors, which correspond to the three principal inertia axes of the void. It also admits strictly positive eigenvalues $\{I_1, I_2, I_3\}$, which correspond to the three principal inertia moments of the void.

The computation of void volume and void's inertia matrix was implemented in the source code of FORGE [2011] as a Fortran *subroutine* in order to provide values at each increment step of the *full-field* simulations.

2.4.3 Morphology-equivalent ellipsoids

For the particular case of an ellipsoid, the principal moments of inertia are given by an analytical expression of the ellipsoid's dimensions (see Fig. 2.17):

$$\begin{aligned} I_1 &= \frac{V}{5}\left(r_2^2 + r_3^2\right), \\ I_2 &= \frac{V}{5}\left(r_1^2 + r_3^2\right), \\ I_3 &= \frac{V}{5}\left(r_1^2 + r_2^2\right), \end{aligned} \tag{2.23}$$

leading to:

$$\begin{aligned} r_1 &= \sqrt{\frac{5}{2V}\left(I_2 + I_3 - I_1\right)}, \\ r_2 &= \sqrt{\frac{5}{2V}\left(I_1 + I_3 - I_1\right)}, \\ r_3 &= \sqrt{\frac{5}{2V}\left(I_1 + I_2 - I_3\right)}. \end{aligned} \tag{2.24}$$

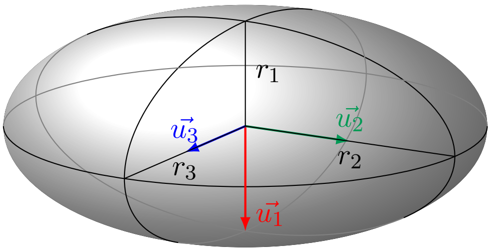

Figure 2.17: Definition of the dimensions and orientation of an ellipsoid.

The void's principal moments of inertia $\{I_1, I_2, I_3\}$ can therefore be used to obtain a set of *morphology-equivalent* dimensions r_1, r_2, r_3 of any void, by analogy with an ellipsoid.

Similarly, the eigen-vectors $\{\vec{u_1}, \vec{u_2}, \vec{u_3}\}$ correspond to the void's principal basis and can also be used to set the orientation of the *morphology-equivalent* ellipsoid.

Fig. 2.18 illustrates a superposition of the surface mesh for void A and its equivalent ellipsoid obtained using the proposed methodology.

In this example, the ellipsoid was generated using data coming from a real case. Naturally, it is also possible to generate ellipsoids with arbitrary dimensions and orientation in order to generate test cases over various ranges of values. This will have great interest to perform the sensitivity study to geometry parameters in Chapter 4. The code to generate the surface mesh of an ellipsoid with given dimensions and orientation was implemented using C++.

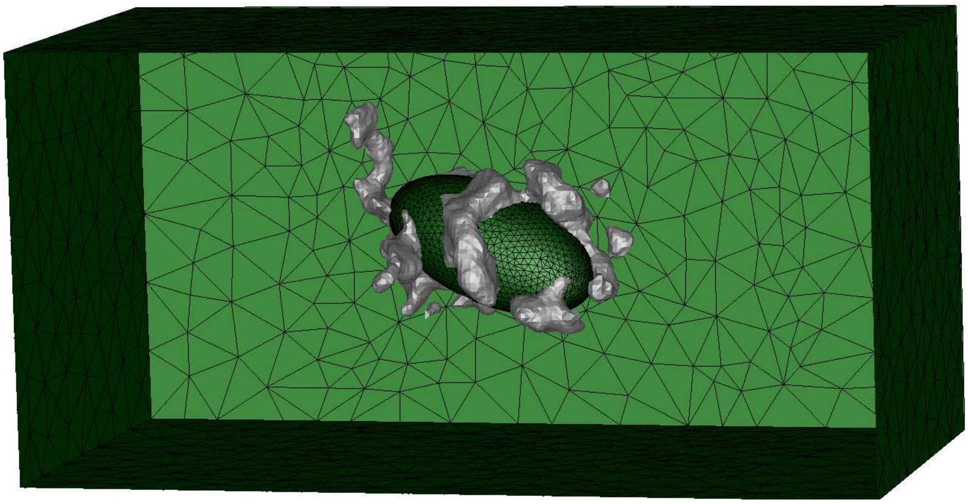

(a) Surface mesh of the RVE containing a *morphology-equivalent* ellipsoid to void A (green), indicatively superimposed with void A (white)

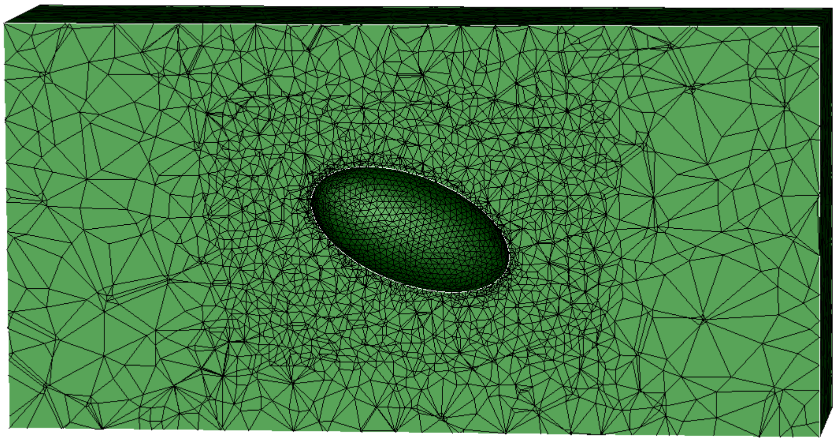

(b) Cutting xz-plane of the volume mesh of the RVE containing the *morphology-equivalent* ellipsoid

Figure 2.18: Initial RVE containing the *morphology-equivalent* ellipsoid, compared to the real morphology of void A.

2.5 Validation of the meso-scale approach

In the proposed meso-scale approach, the use of RVEs is the core of the work and must be carefully defined. The mechanisms of void closure are studied on the basis of a wide campaign of *full-field* simulations at the RVE-scale. The simulations are performed using the finite element software FORGE [2011] (described in Appendix A).

The objective of this section is to identify adequate numerical parameters in order to ensure the validity of the results obtained at the RVE-sale. First, a sensitivity study to numerical features is presented in terms of RVE dimensions and mesh size. The RVE dimensions are defined according to the proportionality coefficient η (defined in Eq. 2.7). The mesh sizes are isotropic and homogeneous by zone in the RVE.

The sensitivity study to numerical features was performed in several steps.

- In a first approach, approximate RVE dimensions were determined using a coarse mesh size. The results will not be detailed in this document.
- Using these approximate RVE dimensions, the dependence to mesh size was studied and an adequate value of mesh size was determined.
- Using the value of mesh size obtained in the previous step, the sensitivity study to RVE dimensions was then repeated for various RVE dimensions.
- The sensitivity study to mesh size was finally repeated using another real void with different boundary conditions.
- Using the adequate values, the results obtained at the RVE-scale for Void A were finally compared to a *full-field* explicit process simulation at the workpiece scale in order to verify the use of a meso-scale approach to study void closure in industrial process conditions.

2.5.1 Dependence to mesh size

According to the first step, the approximate value $\eta = 4$ was obtained using a coarse mesh size $h = 2.5$ mm (in a first approximation). In this paragraph, all RVE simulations are thus performed using the value $\eta = 4$ in Eq. 2.7. Their relative computation times are presented in Table 2.2.

h_{max} (mm)	h_{min} (mm)	Nb nodes	Nb CPUs	CPU time	Total CPU time
2.5	2.5	12 000	2	30 min	1 hour
0.5	0.5	450 000	16	2 days 12 hours	40 days
2.5	1.8	14 000	1	2 hours	2 hours
2.5	1.3	19 000	2	2 hours	4 hours
2.5	1.0	23 000	2	6 hours	12 hours
2.5	0.8	32 000	2	10 hours	20 hours
2.5	0.5	67 000	4	12 hours	2 days
2.5	0.25	400 000	16	2 days 2 hours	33 days 8 hours
2.5	0.13	650 000	16	6 days 21 hours	110 days

Table 2.2: Tested mesh sizes with associated computation features, performed using CPUs at 2.3GHz, 32Go RAM.

Reduction of the required area for h_{min}

In the two first lines of Table 2.2, the mesh size was homogeneous throughout the RVE, respectively $h = 2.5$ mm and $h = 0.5$ mm. By comparing their total CPU times, it can be seen that refining the mesh size homogeneously throughout the RVE involves a significant increase in terms of computation times. This is mainly due to the large increase in the number of nodes of the finite element mesh. Figs. 2.19a and b illustrate the field of equivalent strain for both cases of homogeneous mesh size. It can be seen that the mechanical fields are relatively homogeneous in the zones that are far from the void. It was thus decided to define two areas for the mesh size, such as illustrated in Fig. 2.19c. A fine mesh size h_{min} and a coarse mesh size h_{max} can be set, respectively, close and far from the void. The dimensions of the area close to the void (refinement box) are defined as twice the voids dimensions d_i.

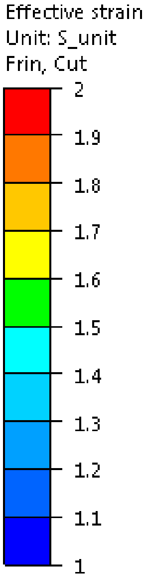

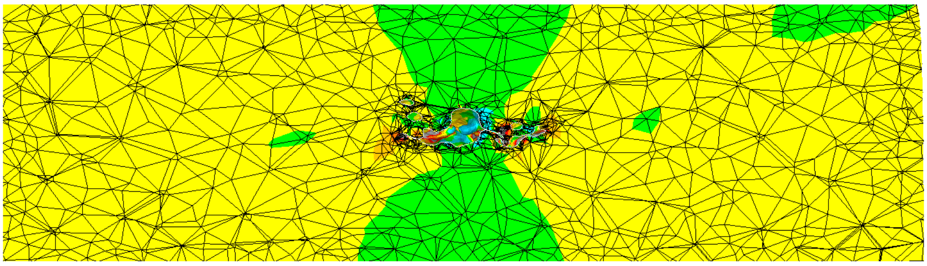

(a) No refinement $h_{min} = h_{min} = 2.5$ mm

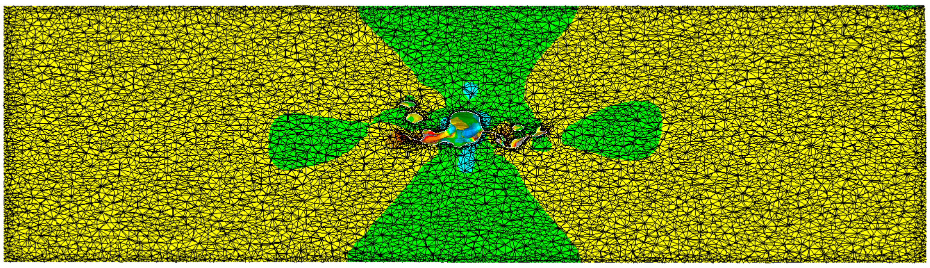

(b) Global refinement $h_{max} = h_{min} = 0.5$ mm

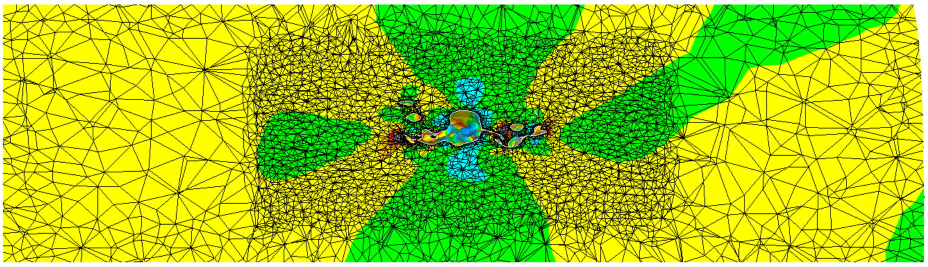

(c) Local refinement $h_{max} = 2.5$ mm; $h_{min} = 0.5$ mm

Figure 2.19: Cutting plane of the RVE containing void A under hot rolling conditions, with various mesh sizes, at $t = 0.1$ s.

It was then verified that the introduction of these two areas had no impact on void closure. The void volume evolutions are plotted in Fig. 2.20. The evolutions that were obtained with the global and local refinement are identical. On the contrary, the evolution that was obtained without refinement ($h_{max} = h_{min} = 2.5$ mm) significantly underestimates void closure.

In the following, the value of the fine mesh size h_{min} will be defined in the refinement box. A coarse mesh size $h_{max} = 2.5$ mm will systematically be defined far from the void. Note that the fact of coarsening the mesh size far from the void induces a significant reduction of total CPU time (by a factor 20) for the same void volume evolution.

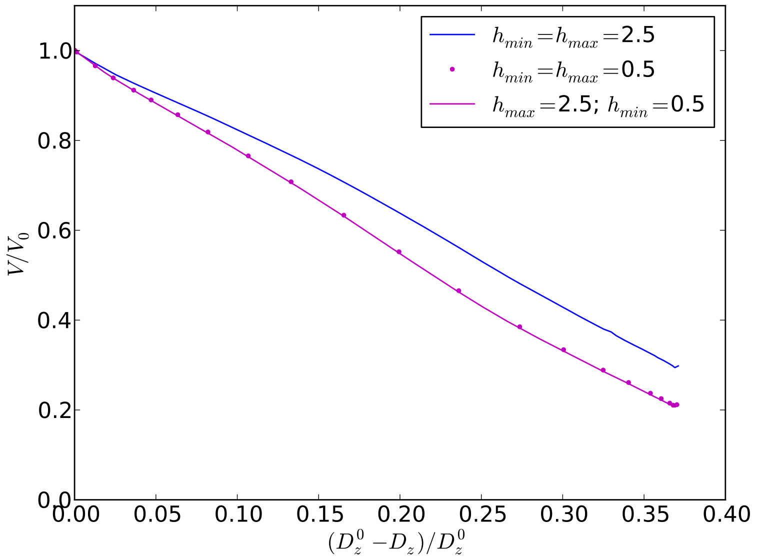

Figure 2.20: Effect of h_{max} (in mm) on void volume evolution of void A under hot rolling conditions.

Influence of h_{min}

Several RVE were generated using various values of h_{min} (see Table 2.2). A few examples are illustrated in Fig. 2.21 on a cutting plane.

Void volume evolution is plotted in Fig. 2.22 for the tested mesh sizes. The figure points out a non negligible sensitivity to mesh size. A maximum difference of about 10% was obtained over the tested range.

In order to understand the origin of this sensitivity, profiles of equivalent strain for a segment length in the RVE are presented in Fig. 2.23 for several mesh sizes. On the two ranges of abscissa [0, 15] mm and [38, 50] mm, homogeneous values are measured. They correspond to the homogeneous deformation zones in the RVE.

In the close neighborhood of the void, i.e. on the ranges [18, 24] mm and [27, 33] mm, strong fluctuations can be observed. The fluctuations are due to the material flow around the void. In fact, void closure involves rather strong gradients of deformation around the void. It is particularly elevated in this case, as the void presents a rather tortuous aspect. The values of equivalent strain obtained with finer meshes show higher amplitude regarding the peaks at 22 mm and at 33 mm. In order to ensure the accuracy of such gradients of mechanical fields, the mesh size must be sufficiently fine. Using coarse mesh sizes involves an underestimation of the void evolution (see Fig. 2.22a and b).

Fig. 2.22 illustrates the influence of h_{min} on the value of void volume at $t = 0.1$ s. The figure mentions a convergence of the values when refining the mesh size. The relative

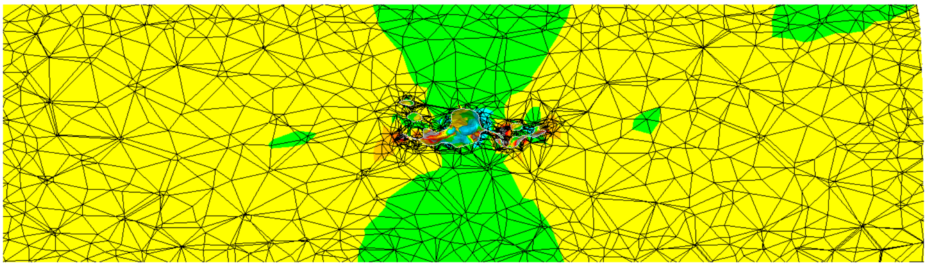

(a) $h_{min} = 2.5$ mm

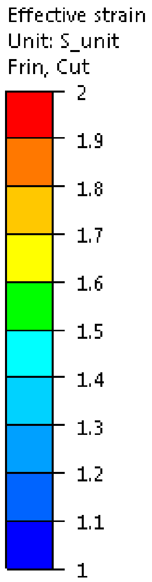

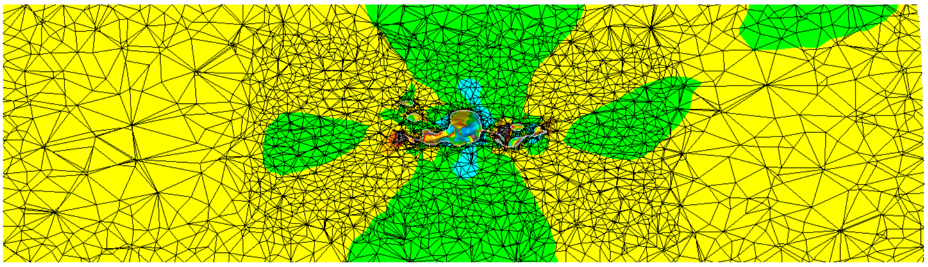

(b) $h_{min} = 0.8$ mm

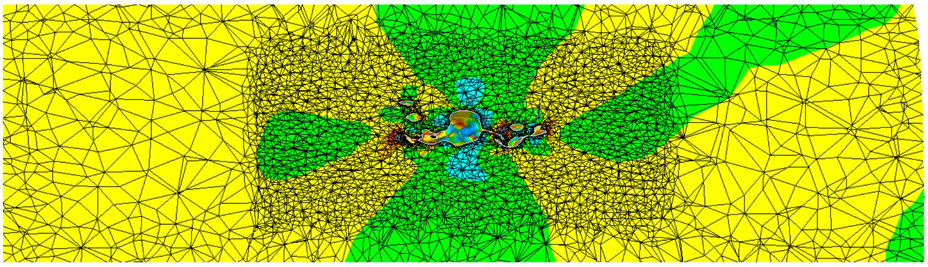

(c) $h_{min} = 0.5$ mm

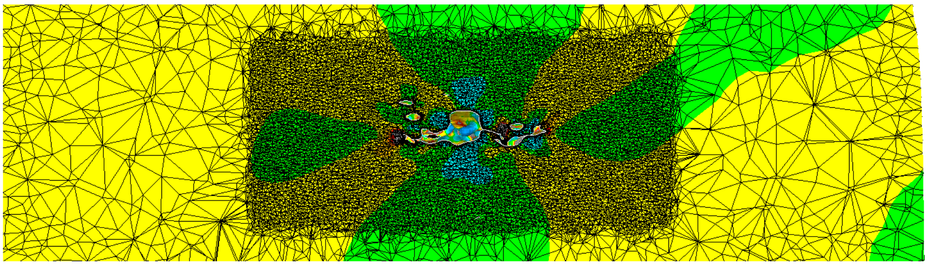

(d) $h_{min} = 0.25$ mm

Figure 2.21: Cutting plane of the RVE containing void A under hot rolling conditions, with various mesh sizes h_{min}, at $t = 0.1$ s.

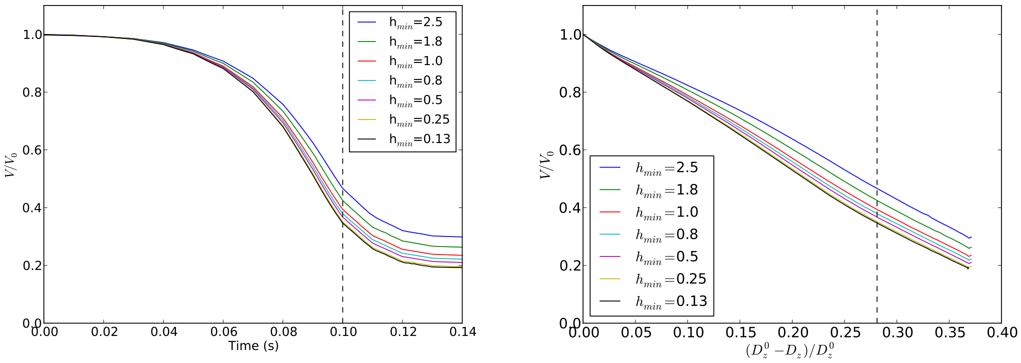

(a) Void volume *vs.* time

(b) Void volume *vs.* height reduction

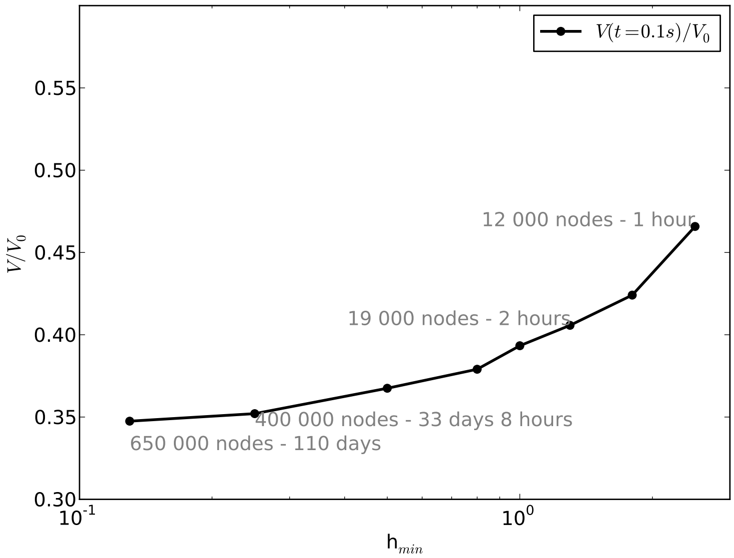

(c) Void volume at $t = 0.1$ s *vs.* mesh size

Figure 2.22: Effect of h_{min} (in mm) on void volume evolution of void A under hot rolling conditions.

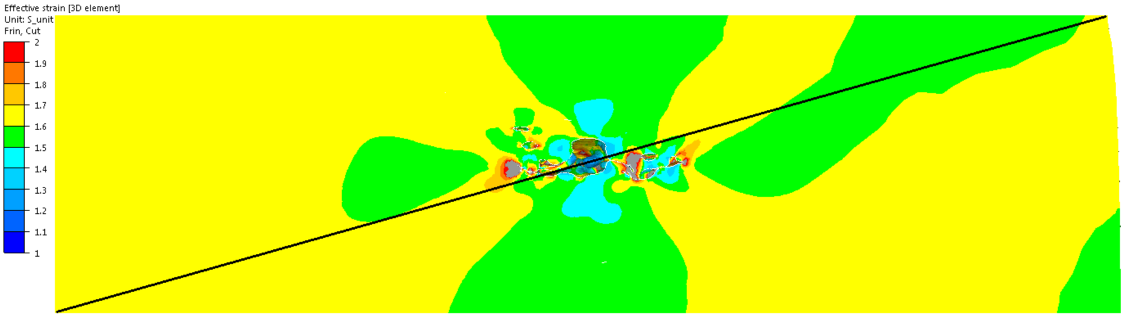

(a) Definition of the line used for the abscissa below

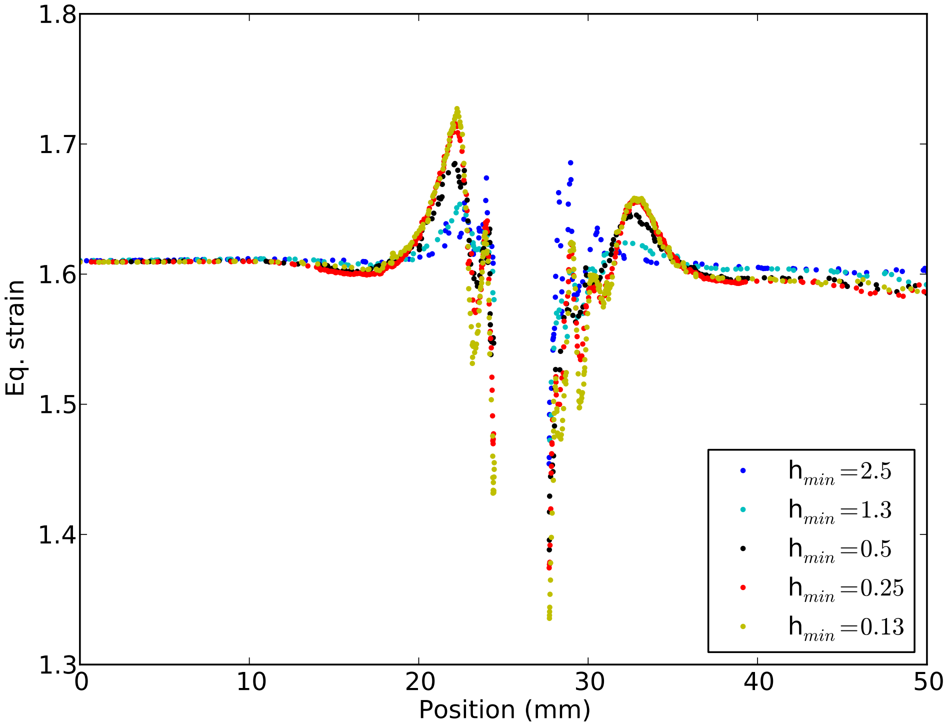

(b) Values of equivalent strain along the diagonal line defined above

Figure 2.23: Profile of equivalent strain along a line, at $t = 0.1$ s, for several values of h_{min} (in mm).

difference in terms of void volume between the results using $h_{min} = 0.25$ mm and those using $h_{min} = 0.13$ mm is lower than 0.5%. However, the total required CPU time is multiplied by a factor greater than 3. The value $h_{min} = 0.25$ mm can thus be considered as an acceptable value and will be used in the forthcoming RVE simulations.

2.5.2 Dimensions of the RVE

In the previous paragraph, the value of $\eta = 4$ had to be used in a first approximation, as the adequate mesh size was not yet defined.

In the present section, the RVE dimensions are studied using the adequate value of mesh size $h_{min} = 0.25$ mm. This value is set throughout the RVE $h_{min} = h_{max} = 0.25$ mm. The number of nodes of the finite element meshes are thus relatively high (see Table 2.3). The total CPU times are consequently very high as well.

The same case as previously was used, considering void A under hot rolling conditions, and is illustrated in Fig. 2.24 for the four RVE dimensions.

η	Nb nodes	Nb CPUs	CPU time	Total CPU time
2	240 000	4	6 days 17 hours	26 days 20 hours
3	400 000	4	10 days 1 hour	40 days 4 hours
4	570 000	8	10 days 16 hours	85 days 8 hours
5	722 000	8	16 days 22 hours	135 days 8 hours

Table 2.3: Tested dimensions for the RVE containing void A, under hot rolling conditions, performed using CPUs at 2.3GHz, 32Go RAM.

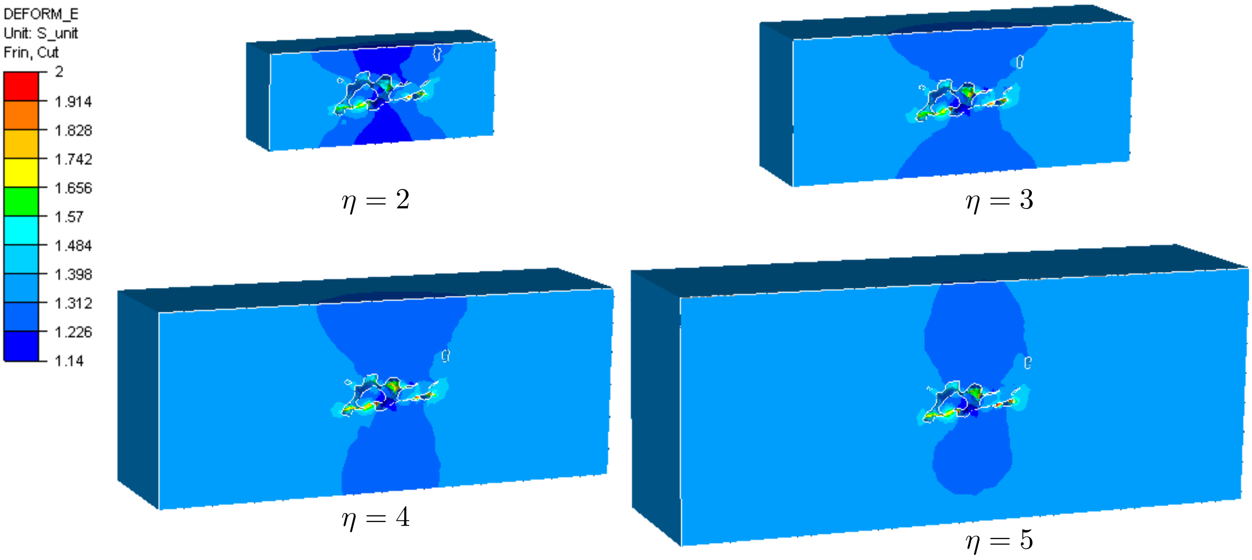

Figure 2.24: Strain field in RVE using various dimensions.

The volume evolutions are given in Fig. 2.25. The values exhibit a convergence for large RVE dimensions. This is coherent with the fact that homogeneous mechanical fields are applied using boundary conditions. In fact, the error obtained when reducing the value of η is due to an interaction of the mechanical fields with the boundaries of the RVE. This interaction can be qualitatively observed in Fig. 2.24, by comparing the strain field for $\eta = 2$ and the three other cases. The presence of boundaries at the close surroundings of the void locally modifies the mechanical fields around the void. The four cases are given for a common remote deformation state. The resulting value of deformation in the homogeneous zones (right and left) is about 1.35. Zones of lower deformation (around 1.25) can be observed above and below the void. It is noteworthy that these zones are truncated by the presence of the boundary, but the resulting field is roughly the same for all cases $\eta \geq 3$. Conversely, the value obtained for the case $\eta = 2$ is lower, around 1.20, due to the excessive proximity of the upper and lower boundaries. This results in an underestimation of void closure. In Fig. 2.25, the volume obtained from the RVE with $\eta = 2$ is about 8% larger than the three values obtained with $\eta \geq 3$.

However, increasing the dimensions of the RVE significantly increases the number of elements of the mesh and thus the required computation time. For the case $\eta = 3$, the difference in void volume is about 1.5% compared to $\eta = 5$, which can be seen as an acceptable compromise between computation time and the obtained value of void volume.

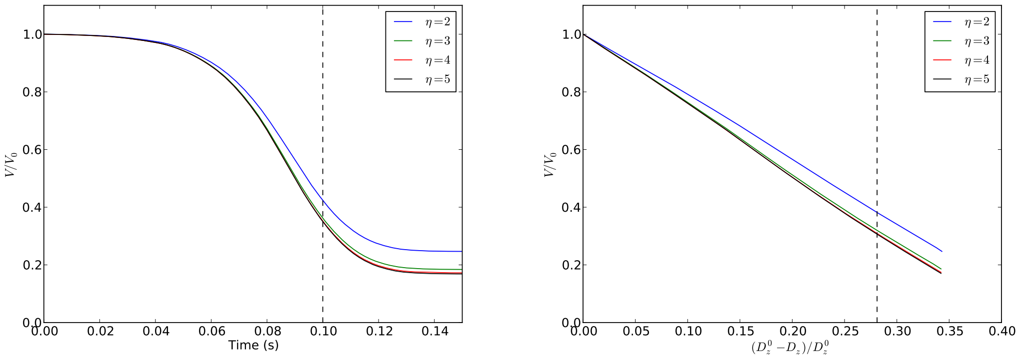

(a) Void volume *vs.* time

(b) Void volume *vs.* height reduction

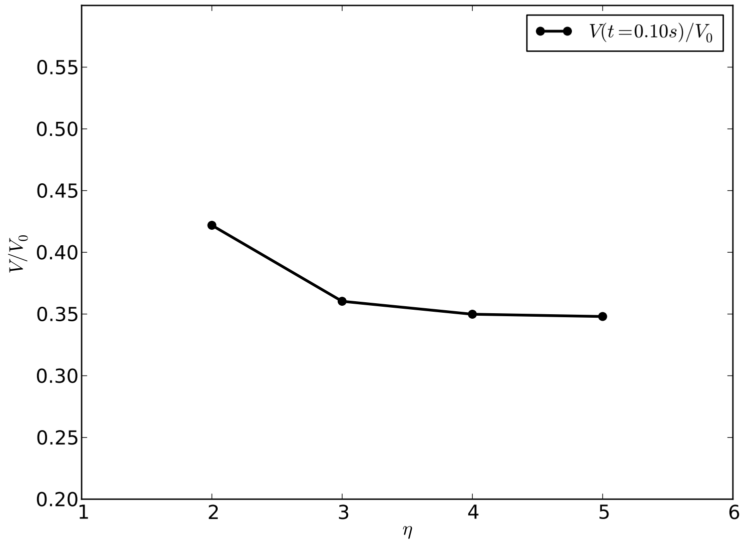

(c) Void volume at $t = 0.1$ s *vs.* η

Figure 2.25: Effect of RVE dimensions on void volume evolution.

2.5.3 Verification of the mesh size using a second case

The previous influence to mesh size was identified using the case of void A under hot rolling condition. The sensitivity to mesh size was then repeated using a second void, and using different boundary conditions. Void AD was extracted from the tridimensional microtomography image of Sample AD. A tridimensional RVE mesh was generated using the value $\eta = 3$ (in Eq. 2.7), and is illustrated in Fig. 2.26. The local refinement box containing the value h_{min} was defined as twice the dimensions of the void, as in the previous case. The values of mesh size are given in Table 2.4. The value $h_{max} = 1$ mm was defined elsewere, as illustrated on the cutting planes in Fig. 2.27.

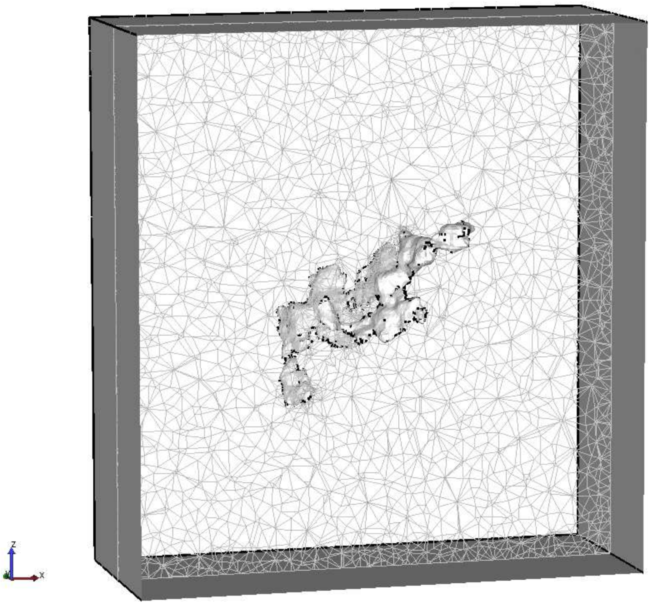

Figure 2.26: Initial geometry of the tridimensional RVE containing void AD.

h_{max} (mm)	h_{min} (mm)	Nb nodes	Nb CPUs	CPU time	Total CPU time
1.0	1.0	31 000	16	4 hours	2 days 16 hours
1.0	0.8	36 000	16	6 hours	4 days
1.0	0.5	64 000	16	18 hours	12 days
1.0	0.38	91 000	16	26 hours	17 days 8 hours
1.0	0.25	182 000	16	106 hours	70 days 16 hours
1.0	0.18	396 000	32	117 hours	156 days

Table 2.4: Tested mesh sizes with associated computation features for void AD, performed using CPUs at 2.3GHz, 32Go RAM.

In this case, more compressive boundary conditions were chosen, in order to obtain a significantly different void volume evolution. As illustrated in Fig. 2.28, this case involves a steep initial slope and a complete final closure. The maximum relative difference obtained over the range of tested mesh sizes was slighter in this case, about 5% at $t = 2.14$ s.

Void volumes *vs.* h_{min} are plotted in Fig. 2.28c and the influence of the mesh size on the void volume can be observed. In the present case, the mesh size of $h_{min} = 0.25$ mm also appears as an adequate compromise between computation time and of the void volume evolution accuracy.

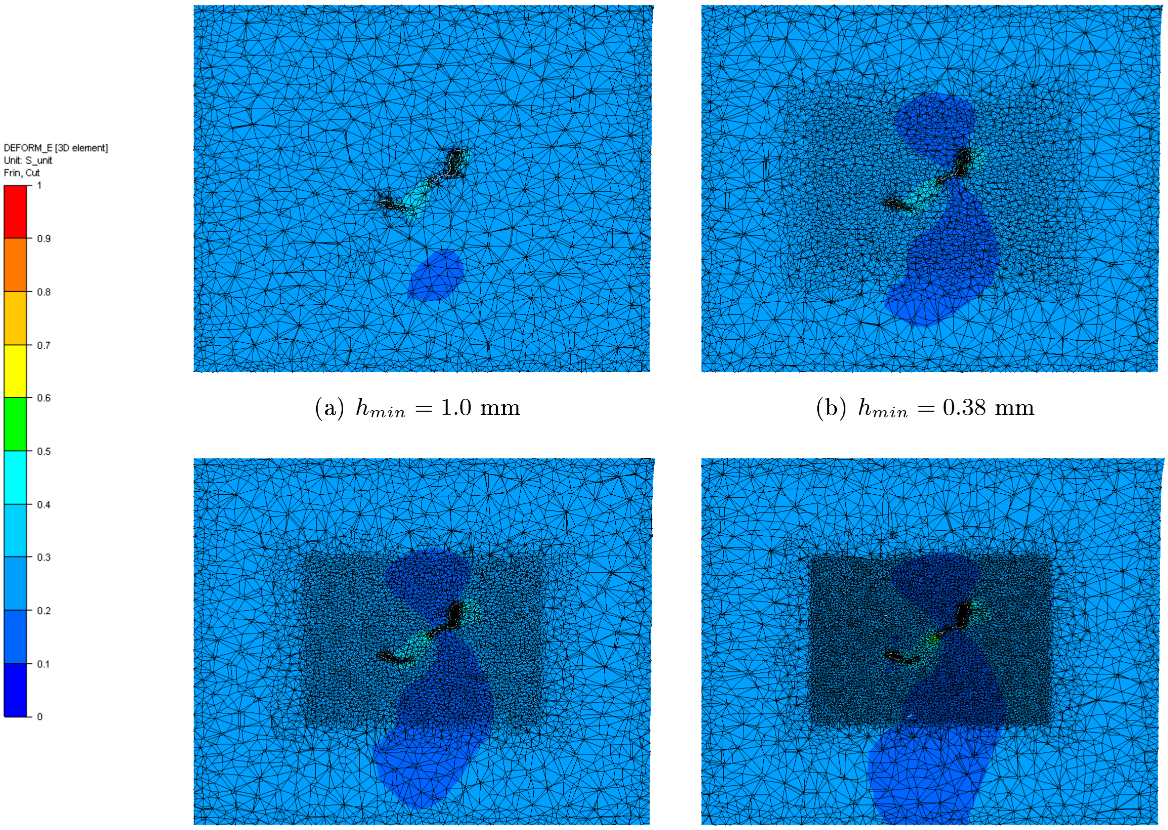

(a) $h_{min} = 1.0$ mm

(b) $h_{min} = 0.38$ mm

(c) $h_{min} = 0.25$ mm

(d) $h_{min} = 0.18$ mm

Figure 2.27: Cutting plane of the RVE containing void AD under constant boundary conditions, for various mesh sizes h_{min} and common $h_{max} = 0.1$ mm, at $t = 2.14$ s.

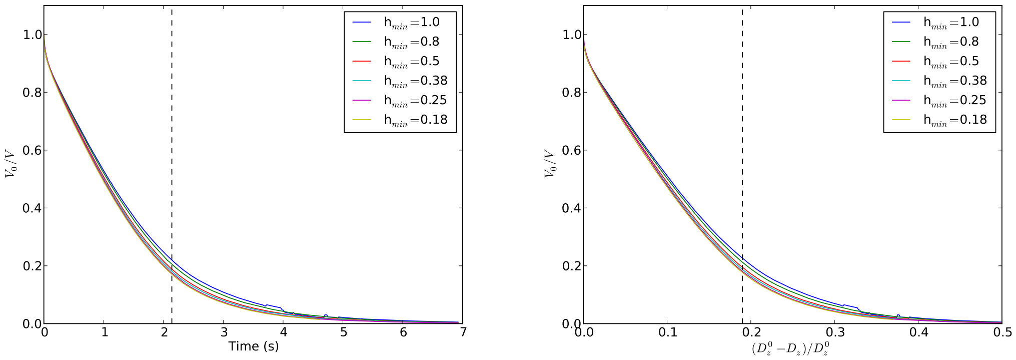

(a) Void volume *vs.* time

(b) Void volume *vs.* height reduction

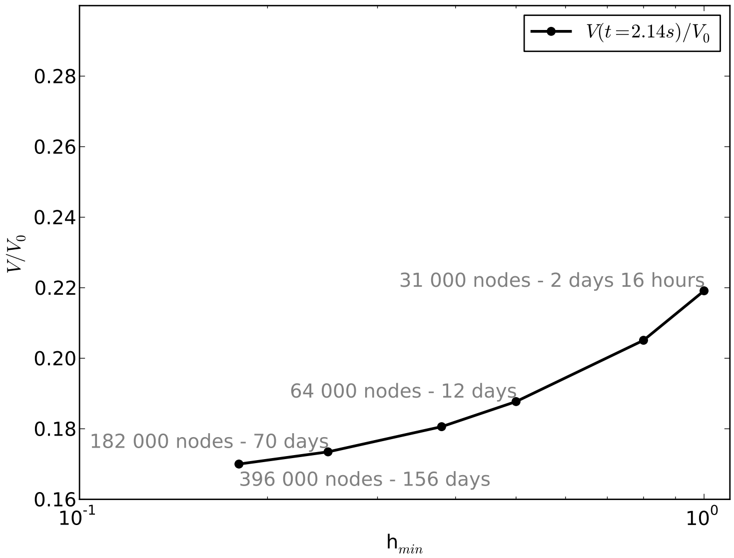

(c) Void volume at t=2 s *vs.* mesh size

Figure 2.28: Effect of h_{min} (in mm) on void volume evolution of void AD under constant boundary conditions.

As a conclusion, the RVE dimensions must be at least three times larger than the void dimensions. If a lower value of η is used, boundary effects might rise and void closure might be underestimated. All forthcoming RVE simulations will thus be defined according to the condition $\eta \geq 3$.

The dimensions of the refinement zone must be about twice the dimensions of the void.

For the two studied real voids A and AD, the value $h_{min} = 0.25$ mm provided a good compromise between the results accuracy and computation times. Larger mesh sizes have the tendency to slightly underestimate of void closure as well.

The two voids A and AD can be considered as representative of the real voids that will be considered within this work, as they were all extracted from comparable steel specimen and exhibit comparable sizes. Within this work, the value of $h_{min} = 0.25$ mm can thus reasonably be chosen for the forthcoming simulations.

2.5.4 Comparison with *full-field* explicit simulation

To finally validate the use of an RVE to study void closure at the micro-scale under real industrial conditions, a comparison was performed with a *full-field* explicit simulation at the workpiece scale and is presented in this section.

The internal void surface of void A (see Fig. 2.13) was embedded in the workpiece defined in the case Pass C1–5, provided by Ascometal. The case of hot rolling was chosen for the following reasons. First, mechanical loadings that were obtained from the process study were successfully applied using boundary conditions on an RVE. Second, the morphology of void A (obtained from Ascometal steel sample) is coherent in terms of dimensions and conditions.

The void position in the workpiece was defined according to the position of the points used to generate boundary conditions. The workpiece mesh is illustrated in Fig. 2.29.

Identical mesh sizes are defined around the void, according to values prescribed in the previous section in order to ensure the accuracy of local mechanical fields. Boundary conditions on the RVE were imposed according to the method presented in section 2.3. The computation features are given in Table 2.5.

The void volume evolutions are compared in Fig. 2.30. Note that in the case of the explicit rolling simulation, mesh degeneration was encountered and was manually corrected in order to pursue the simulation. This explains the discontinuities of the void evolution for the explicit process. Manual mesh correction became impossible after a certain time. The curve is thus incomplete.

However, on the entire range t = [0, 0.11] s, the curves show an excellent agreement. This agreement shows that the volume of a real void can be predicted with excellent accuracy in an RVE, using adequate boundary conditions, adequate meshing features and adequate RVE dimensions. In addition, by substituting the actual complete behaviour of the entire workpiece with simple boundary conditions, the RVE approach enables the computation to be performed with better stability, as mesh degeneration was not encountered in this case. The void volume evolution was obtained over the process duration, while it was interrupted in the case of the explicit process.

Simulation	h_{min}	Nb nodes	Nb CPUs	CPU time	Total CPU time
Full-field explicit	0.25 mm	3 450 000	32	11 days 9 hours	364 days
RVE ($\eta = 3$)	0.25 mm	400 000	4	10 days 1 hour	40 days 4 hours

Table 2.5: Computation features for the explicit macroscopic approach and the RVE approach, performed using CPUs at 2.3GHz, 32Go RAM.

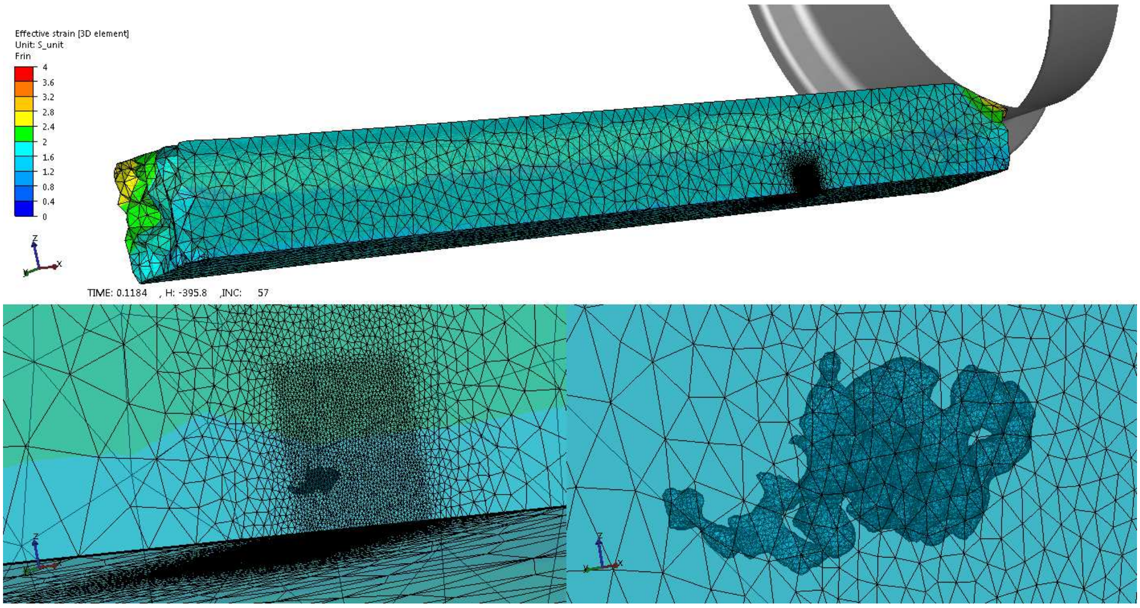

Figure 2.29: *Full-field* explicit description of a bar containing void A, during hot rolling pass.

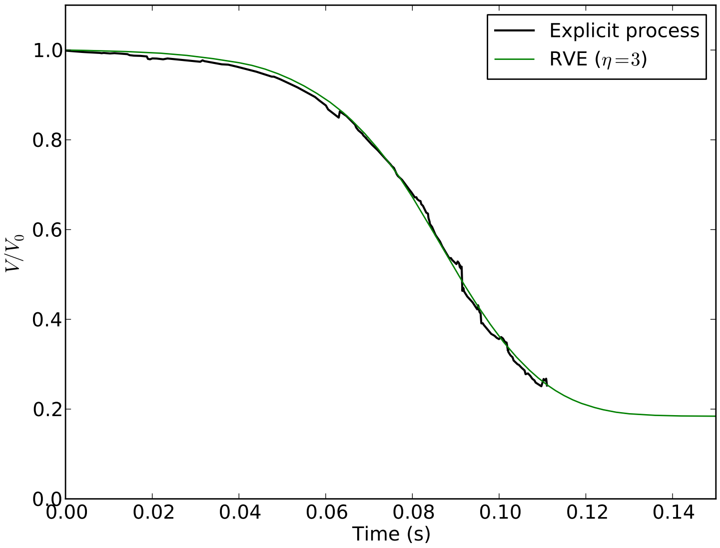

Figure 2.30: Comparison of void volume evolution in the explicit process simulation and in the RVE.

2.6 Conclusions

A meso-scale approach was chosen thanks to its potential accuracy and flexibility for studying void closure in a wide range of conditions.

The accuracy was shown in terms of void description and boundary conditions. Real void morphologies coming from tridimensional microtomography images can be defined with excellent precision. Boundary conditions that respect real industrial loadings can also be applied and were verified. A comparison with a *full-field* explicit process simulation containing a void justified the use of an RVE, and illustrated the benefits in terms of accuracy and computation times.

The flexibility of the approach was also demonstrated by the introduction of *morphology-equivalent* geometries and prescribed boundary conditions. Flexibility is, in fact, a key of the presented approach, as it enables a series of arbitrary geometries and arbitrary boundary conditions to be defined within the ranges defined in Chapter 1. The use of RVEs using such prescribed conditions will enable a parametric study and the construction of the prediction model.

Numerical features were also tested in order to ensure the validity of the RVE simulations. The study showed that attention must be paid to the definition of tridimensional meshes, in terms of dimensions and mesh size. Adequate values of RVE-to-void dimensions ratio η and of mesh size h_{min} were found (regarding the typical voids considered within this work). A good compromise between results accuracy and computation time was obtained.

Chapter 3

Experimental validation of *full-field* simulations

Contents

Résumé français

Ce chapitre présente une validation expérimentale de l'évolution de pores qui peut être prédite par une description explicite en champ complet en utilisant le logiciel éléments finis FORGE [2011]. La description explicite en champ complet est utilisée dans ce manuscrit à deux reprises. A l'échelle du VER, les pores sont décrits de façon explicite, afin d'étudier les mécanismes de refermeture de manière très précise (chapitre 4). A l'échelle macroscopique, le modèle développé sera finalement comparé au chapitre 5 à des simulations explicites en champ complet, pour deux cas de procédés industriels. La simulation en champ complet apparaît donc comme un outil de référence à la construction du modèle et à sa validation. Il convient donc de s'assurer de la validité des calculs obtenus.

L'observation précise de la morphologie 3D des pores a été réalisée sur quatre échantillons d'aciers par microtomographie aux rayons X. Des essais d'écrasement à chaud ont été réalisés afin d'induire un certain taux de refermeture. Ensuite, les échantillons déformés ont été à nouveau observés par microtomographie aux rayons X. Ces essais d'écrasement ont parallèlement été simulés en utilisant une description explicite en champ complet à partir des images initiales, et l'état final des pores prédit par cette simulation a été comparée aux images finales obtenues par microtomographie.

Malgré le peu de littérature existante sur ce type d'observations, la faisabilité de cette validation expérimentale a été démontrée. Le paramètre clé est le rapport entre la taille moyenne des pores et celle de l'échantillon. L'échantillon qui a donné lieu à la meilleure qualité d'image a montré une excellente corrélation avec la simulation éléments finis en champ complet. Ce résultat a donc permis de valider d'utilisation de la description explicite en champ complet comme représentatif du comportement réel des pores dans le cadre de ce travail.

3.1 Introduction

The main objective of the present chapter is to verify the accuracy of the void evolution that can be obtained using a *full-field* explicit simulation in FORGE [2011]. *Full-field* explicit simulations are extremely useful in the present work and are used at two levels. Firstly, *full-field* explicit simulations are used at the RVE-scale to study the local mechanisms of void closure (Chapter 4). Secondly, *full-field* explicit simulations are used at the process-scale with workpieces containing voids for the final validation of the *mean-field* model (Chapter 5). In other words, *full-field* explicit simulations are assumed to faithfully represent the real behaviour of voids during deformation. It is therefore a prerequisite to ensure the validity of such simulations using experimental testing.

Certain assumptions were made regarding the use of FORGE [2011].

- The boundary condition at the void's surface is a free surface (zero-stress). This choice was made according to the assumption that the presence of an internal gas in the void is neglected.
- An algorithm of self-contact also avoids two zones of the void's surface to penetrate each other. This self-contact is handled using a master-slave algorithm based on the penalty method [Fourment et al., 2003]. A normal force is applied on both surfaces to avoid penetration of both parts of the mesh. As a consequence, the algorithm does not allow friction between the two surfaces in contact.
- Fully plastic deformation is only considered and the material obeys the von Mises plasticity theory.

The experimental validation aims to verify these assumptions.

As pointed out in the previous chapter, it is relatively difficult to obtain accurate information regarding voids in workpieces using non-destructive methods.

Ultrasonic testing is generally used at an industrial level as it provides relatively fast information regarding internal defects.

X-ray microtomography rises as the most accurate method to provide non-destructive tridimensional information. Although relatively few studies were found in the literature, this technique shows great potential [Toda et al., 2009, Lee et al., 2011] and was thus chosen in the present work.

Four different samples containing voids were provided by industrial partners. They were deformed using hot compression tests, in various conditions. The initial and final void states were measured using X-ray microtomography. The initial state was used to generate the initial mesh of each sample. The deformation of each sample was then simulated using a *full-field* explicit description with FORGE [2011] and the final computed state was compared to the final measured state obtained using X-ray microtomography.

3.2 Scope of the experimental campaign

Due to the lack of literature regarding such testing and the non-negligible costs of microtomography scans, the experimental procedure had to be carefully defined.

The adequate testing conditions are unknown *a priori*. The conditions had thus to be chosen such that an exploitable final state could be obtained. Indeed, for a better final comparison, the voids must have been significantly deformed. On the other hand the final void volume must also remain sufficiently large to provide significant contrast using X-ray microtomography.

The main adjustable parameter for compression tests is the height reduction. In order to define a prescribed height reduction, preliminary simulations were performed using approximate testing conditions. The results from preliminary simulations were used to define an adequate reduction height for each compression test, exclusively.

Once the tests were conducted, a new *full-field* explicit simulation at the workpiece scale was performed for each sample according to the real testing conditions (e.g. initial sample's temperature, thermal and friction coefficients with the tools).

To summarize, for each sample, the following sequence was performed:

0. US-scan to identify the samples of interest (available industrial data),
1. X-ray microtomography to obtain the initial state,
2. preliminary simulation to define the experimental protocol,
3. experimental compression test,
4. simulation of the compression tests using real conditions,
5. X-ray microtomography to obtain the final state,
6. comparison of results from points 4 and 5.

From all specimen that were examined using X-ray microtomography (Chapter 2), the steel specimens AD and JD20 exhibited the best quality of images. In total, four samples were used. Two samples were extracted from specimen AD and were deformed using upsetting test (between flat dies) at Aubert&Duval. Sample JD20 and an additional sample JD47 (extracted from the same ingot) were used using plane-strain compression (between punch-dies) at Ascometal CREAS. One advantage of performing two different mechanical tests is to impose various thermomechanical states in the samples.

The two upsetting tests were performed first. The results in terms of feasibility were used for a better dimensioning for the second campaign. The two campaigns are thus presented in their chronological order.

3.3 Samples NEZ1 and NEZ2

3.3.1 Initial void state

Two steel samples were extracted from the specimen AD. The extraction was performed according to the initial void state in the specimen AD, which is detailed in Fig. 3.1.

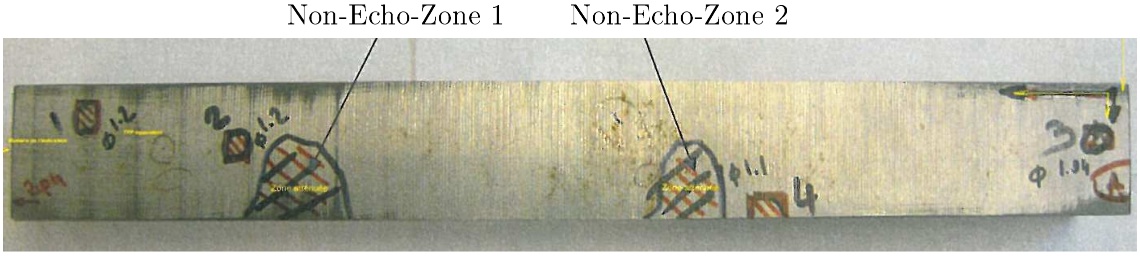

(a) Photograph of initial specimen AD (330 mm× 40 mm × 40 mm), view from Face A

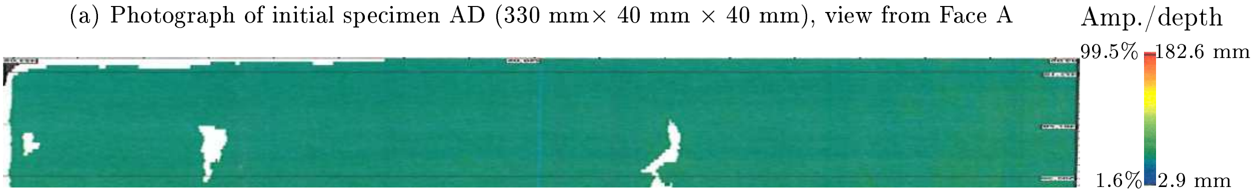

(b) Ultrasonic testing (signal amplitude from Face A)

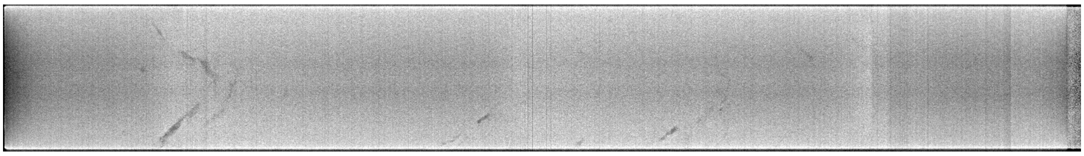

(c) Slice of tridimensional microtomography image (depth from Face A: 12.9 mm)

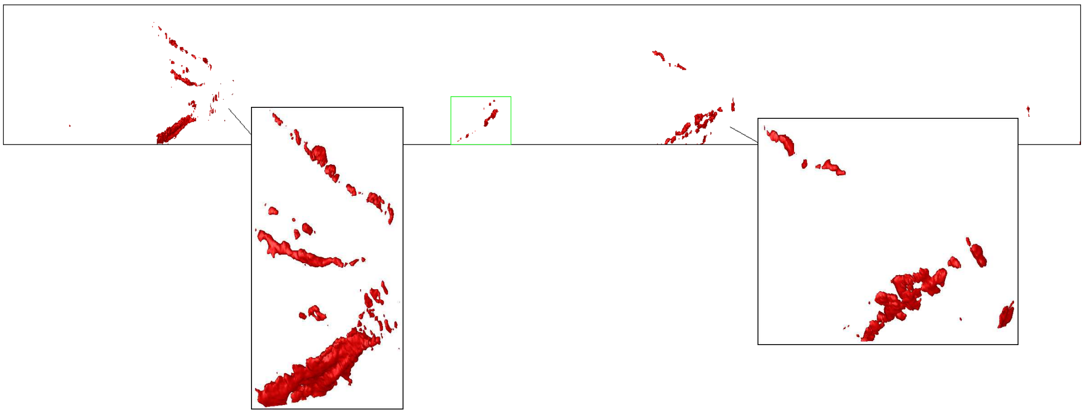

(d) Void-matrix interface, obtained using the marching-cubes algorithm from the tridimensional microtomography image

Figure 3.1: Tridimensional examination of specimen AD.

Indications from ultrasonic testing

The average positions and sizes of the voids were previously assessed using ultrasonic testing at Aubert&Duval. Ultrasonic testing was performed using the immersion technique along the four lateral faces of the squared-based specimen. The results are typically presented using C-scans, which is a 2D representation of the signal amplitude over the samples surface. In Fig. 3.1b, the C-scan is presented for face A, i.e. the visible face on Fig. 3.1a.

The C-scan exhibits a roughly homogeneous signal amplitude of the signal with the green color. This level of amplitude corresponds to a depth of about 40 mm and can thus be attributed to the back echo of the sample's opposite face.

The local presence of a void generates an additional ultrasonic echo that can be analyzed in order to assess its size. This is performed using the classical *flat-bottom hole* equivalence. This empirical technique consists in comparing the measured signal with a series of signals that were previously calibrated using flat-bottom holes. It enables an equivalent diameter and an average depth for the void to be assessed. This technique is rather widely used at an industrial level.

Note that the ultrasonic reflection is implicitly assumed to be identical to the one of a flat-bottom hole, which may be questionable, notably in the case of complex morphologies.

For the specimen AD, the scanning parameters were adjusted in order to detect indications that were greater than a *flat-bottom hole* of 1 mm. The results are given in Table 3.1. Four indications were obtained. Their equivalent diameter and average depth were comparable.

Indication in Fig. 3.1a	1	2	3	4
Equivalent diameter (mm)	1.2	1.2	1.34	1.1
Depth (mm)	10.6	11.1	9.8	10.7

Table 3.1: Ultrasonic indications from Face A using the *flat-bottom hole* equivalence.

On the C-scan in Fig. 3.1b, two white areas can be noticed and are due to the absence of amplitude in the ultrasonic signal. The absence of amplitude results from a total dispersion of the signal and mentions the presence of strong heterogeneities in the sample. It can be the result of the presence of a large void, or a cluster of voids.

These indications were obviously insufficient for an accurate definition of *full-field* explicit simulations. A tridimensional examination using X-ray microtomography was thus performed and is presented in the following.

Indications from X-ray microtomography

As presented in Chapter 2, the initial specimen was entirely scanned using X-ray microtomography (Fig. 2.8). An example of slice of the tridimensional image is given in Fig. 3.1c for an arbitrary depth.

The void-matrix interface was extracted from the tridimensional image according to the method presented in section 2.4.1 involving the marching-cubes algorithm. The void-matrix interface is illustrated in Fig. 3.1d.

Two porous zones were observed in the black frames and were enlarged. It is noteworthy that the positions of these two zones roughly coincide with the non-echo zones from the ultrasonic indications. Between the two zones, note the presence of a smaller void (green frame) that was not detected using the ultrasonic scan.

Interestingly, no contrast heterogeneity was observed using X-ray microtomography at the position of the four indications given in Table 3.1. Two different hypotheses may explain this result. In the first hypothesis, a void is present but is not detectable using X-ray microtomography due to its small size. It is plausible in the case of a flat void, in which the thickness would be lower than the resolution of the tridimensional image. In the second hypothesis, no void is present at these positions. The ultrasonic signal might result from another discontinuity from the material (e.g. grain boundary).

The available information was insufficient to determine which of both hypotheses to consider. The study was therefore rather focused on the two non-echo zones (NEZ), as the presence of voids was unquestionable here.

Two samples with comparable dimensions were thus extracted from specimen AD and were called NEZ1 and NEZ2, see Fig. 3.2.

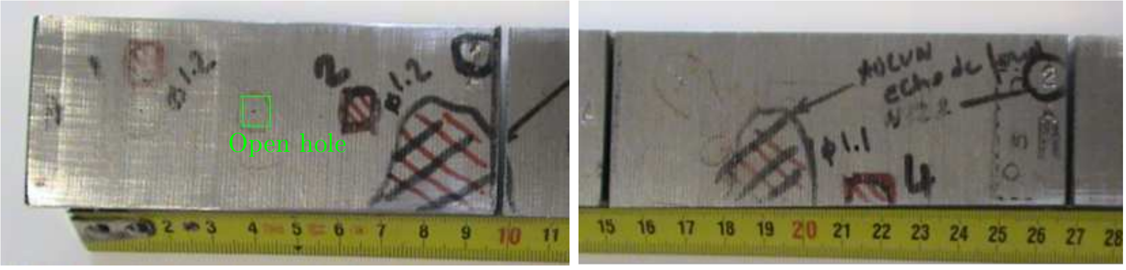

(a) Sample NEZ1 (95 mm× 40 mm × 40 mm) (b) Sample NEZ2 (100 mm× 40 mm × 40 mm)

Figure 3.2: Photograph of samples NEZ1 and NEZ2, after extraction.

3.3.2 Preliminary simulations

Preliminary simulations were performed in order to obtain an approximate closure behaviour of the voids contained in NEZ1 and NEZ2. The main objective was to determine an experimental protocol that might provide the best results. A temperature of 1100°C was chosen according to the range defined in the industrial issues (Chapter 1), typical for forging processes. Thermal exchange and friction coefficients were set according to values that are usually used at Aubert&Duval, but not detailed here for confidentiality reasons.

The meshes for NEZ1 and NEZ2 were generated according to the same method as for the generation of the RVE mesh (Chapter 2). A tridimensional volume mesh was generated between the internal void-matrix surface and the external surface of the sample, as illustrated in Figs. 3.3 and 3.4.

Symmetry planes were defined in order to reduce the computation time. One symmetry plane was defined for NEZ1, as voids were located in one half of the sample (see Fig. 3.3). Three symmetry planes were defined for NEZ2, as the main voids were located in one eighth of the sample, only (see Fig. 3.4). The definition of symmetry planes might be questionable here, as it artificially defines voids in the symmetrical parts of each samples. Yet, the benefit in terms of mesh reduction (i.e. its number of elements) is very attractive and a first-order approximation of the void closure is expected, according to the approximate conditions that are set. Simulations under real conditions will be presented later in this document.

In order to further reduce the number of elements of NEZ1, the mesh size was slightly coarser than the one prescribed by the sensitivity study (section 2.5.1). A slight error is also due to the chosen mesh size h_{min}. According to the sensitivity study, this error in terms of void volume is about a few percents and remains acceptable for a first approximation. The computation features are given in Table 3.2.

Figs. 3.3 and 3.4 also illustrate the field of equivalent strain on the deformed samples, using a cutting plane. The field exhibits two zones of low deformation at the top and the bottom of the cutting plane, which is a typical effect of compression between flat dies. Around the voids, the mechanical fields exhibit rather strong fluctuations, as it can be expected according to the discussion regarding mesh size.

Simulation	h_{min}	Nb elements	CPU time	Total CPU time
Full-field explicit NEZ1	0.5 mm	$2.6\ 10^6$	6 days	192 days
Full-field explicit NEZ2	0.25 mm	$2.3\ 10^6$	4 days 8 hours	139 days

Table 3.2: Computation features for the preliminary simulations for NEZ1 and NEZ2, performed using 32 CPUs at 2.3GHz, 32Go RAM.

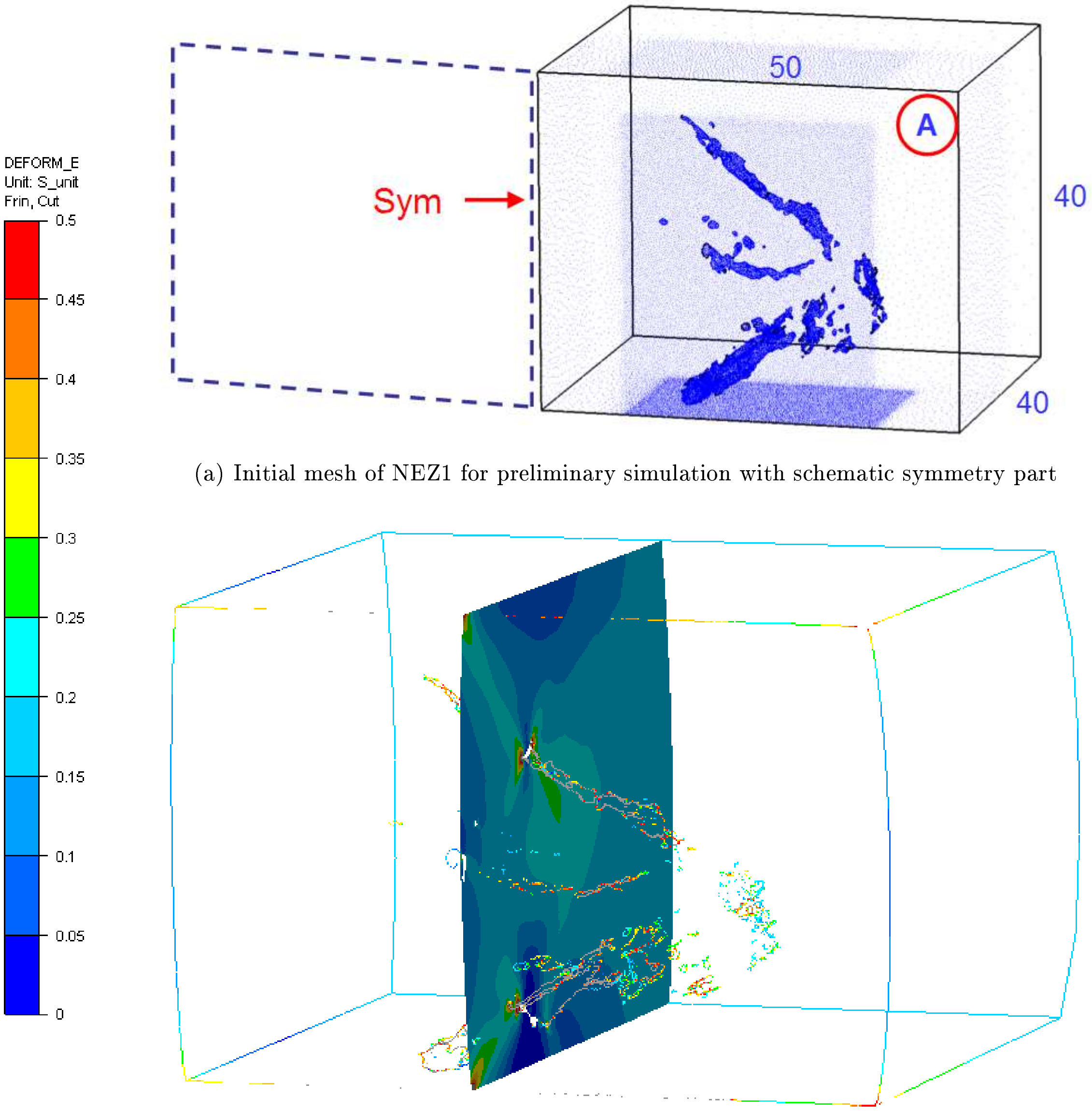

(a) Initial mesh of NEZ1 for preliminary simulation with schematic symmetry part

(b) Cutting plane on deformed mesh of NEZ1, showing equivalent strain field

Figure 3.3: Preliminary simulation of NEZ1 for the definition of experimental protocol.

The volume evolutions of all internal voids are plotted in Fig. 3.5 using color lines. The total volume of voids is plotted using a dashed black line. In both samples, a large disparity in terms of void volumes can be observed. In fact, many small voids were defined, but remain negligible in terms of void volume. The total volume evolution is mainly due to the evolution of the biggest voids.

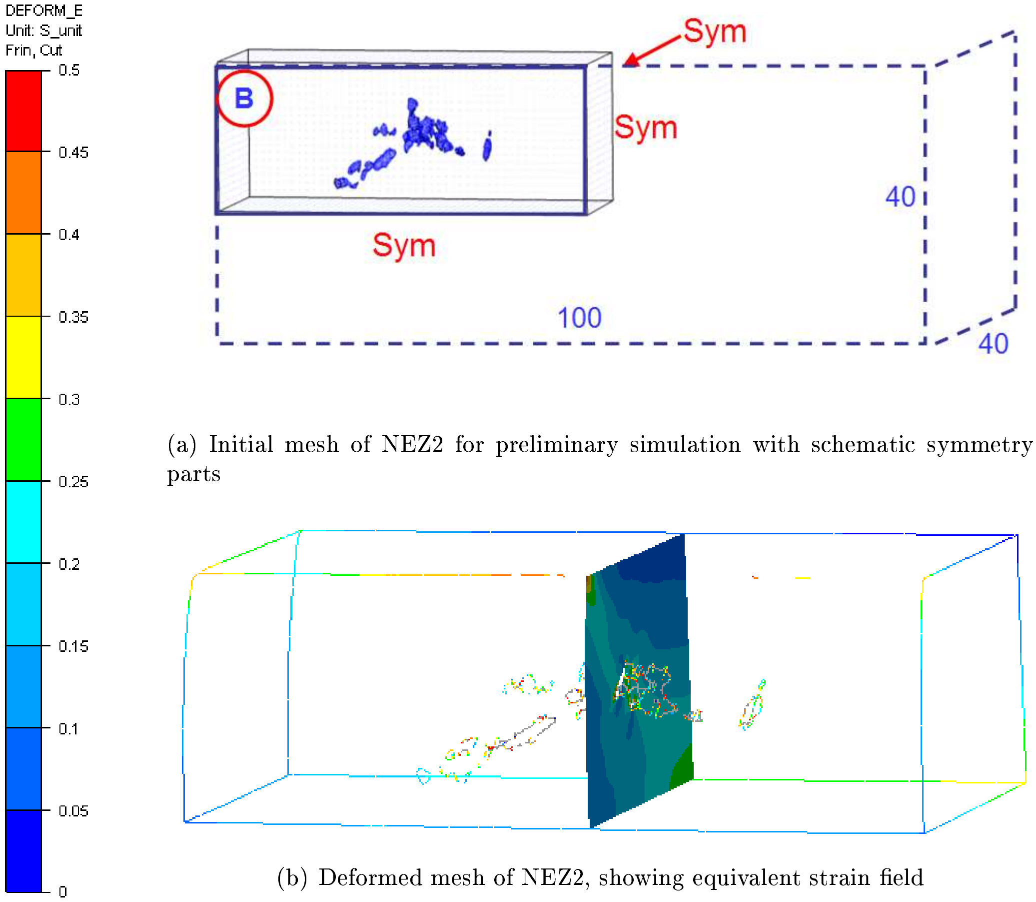

(a) Initial mesh of NEZ2 for preliminary simulation with schematic symmetry parts

(b) Deformed mesh of NEZ2, showing equivalent strain field

Figure 3.4: Cutting plane on deformed mesh of NEZ2 for the definition of experimental protocol.

Note the presence of numerical artifacts (resulting from mesh degeneration of several voids) beyond the height reduction -12mm. The largest artifact can be seen on VOID 19 (red thick line) on NEZ2. It is therefore also visible in the curve for the total volume (dashed black line). Fortunately, this artifact occurs when voids are nearly closed, i.e. at a level of closure that presents low interest for the preliminary study.

In the case of NEZ1, the evolution of VOID 15 clearly drives the total evolution, as its initial volume is much larger than others. Moreover, regarding VOID 18, VOID 1 and VOID 2, it can be seen that their evolutions are significantly different. This is due to a combination of several effects, e.g. the position in the sample, the mechanical state at the considered position and the void's morphology. These results highlight the sensitivity of void closure to all these parameters, and illustrates the great interest in properly defining an adequate reduction height to obtain relevant results in terms of final void states. A too low deformation might involve insignificant reductions of void volume reduction. An excessive value of deformation might lead to complete closure of the voids, or to final volumes that might not be detectable using X-ray microtomography. The final prescribed reduction height is 6 mm for both samples.

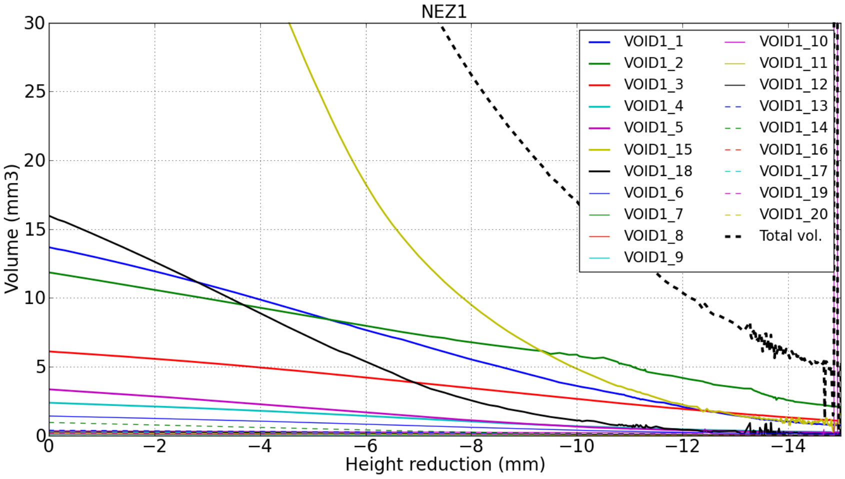

(a) Void volume evolutions for the preliminary simulation of NEZ1

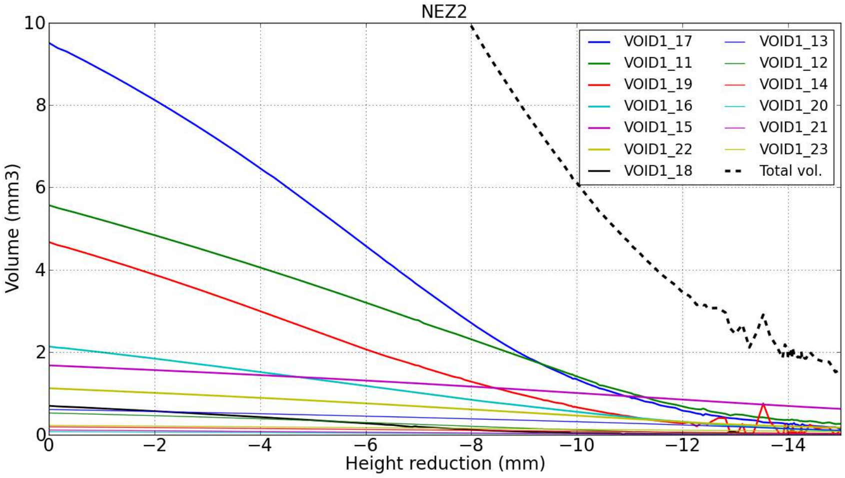

(b) Void volume evolutions for the preliminary simulation of NEZ2

Figure 3.5: Void volume evolutions for the preliminary simulations.

3.3.3 Experimental testing

The experimental compressions of both samples NEZ1 and NEZ2 were performed at Aubert&Duval using a 300-ton press with pre-heated dies (850°C), as illustrated in Fig. 3.6. Samples were heated at 1100°C and held during 1 h 30 min at this temperature.

(a) Sample before compression

(b) Samples after compression (during cooling)

Figure 3.6: Photographs of NEZ1 and NEZ2 during experiment.

Transfer duration from furnace to the lower die was 8 s. Contact duration with the lower die was 7 s and with both dies was 4 s. The die velocity was 0.6 mm/s and the deformation duration was 12 s. The resulting reduction height was thus 7.2 mm. The samples were cooled down and the surface oxidation (about 0.5 – 1 mm thickness) was removed. The final samples are illustrated in Figs. 3.7 and 3.8.

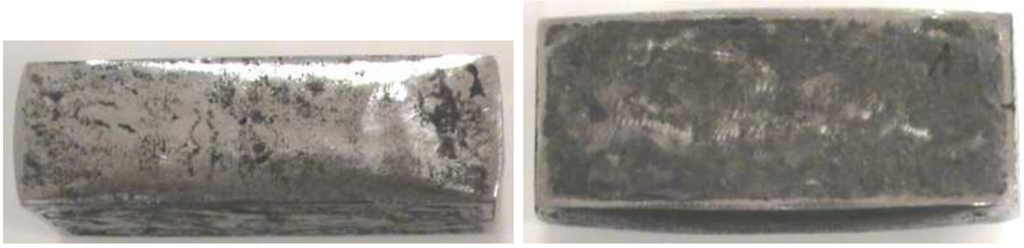

(a) Side view

(b) Upper view

Figure 3.7: Photographs of the deformed sample NEZ1.

(a) Side view

(b) Upper view

Figure 3.8: Photographs of the deformed sample NEZ2.

The samples were then observed using X-ray microtomography at CETIM. A slice of the obtained image after deformation is presented in Fig. 3.9b and is compared to the initial state before compression (Fig. 3.9a). Note that the contrast that was obtained with the deformed sample is even lower than the one from the initial sample, as the voids dimensions were reduced. Nevertheless, the largest void at the bottom right of the initial state can be seen on the deformed state as well (see black frames in Fig. 3.9). At mid-height right position, a rather small initial void remained visible on the deformed state as well (see red frames in Fig. 3.9). On the contrary, a void can be seen at the upper right position on the initial state and is not visible on the deformed state (see white frame in Fig. 3.9a).

From the tridimensional image, the void-matrix interface was extracted according to the method presented in the previous chapter.

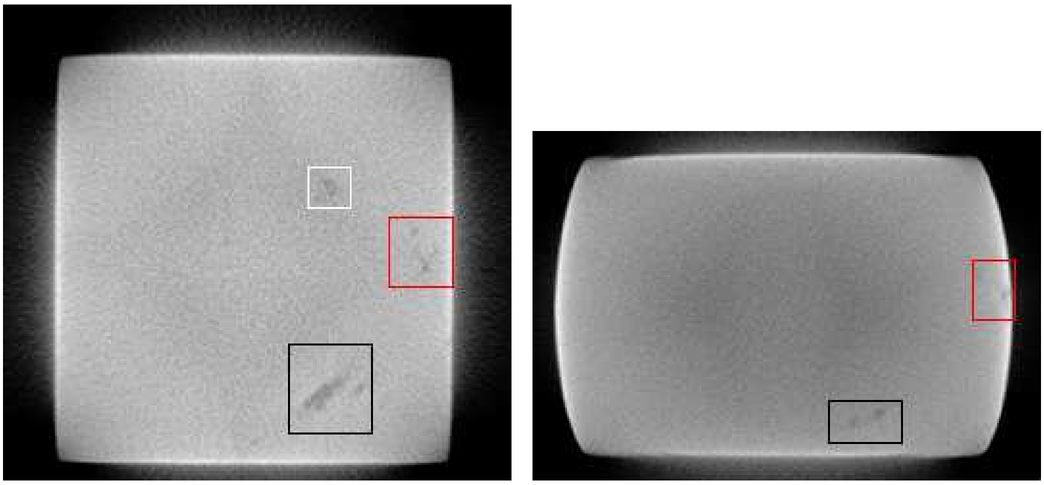

(a) Before compression

(b) After compression

Figure 3.9: Slices obtained from microtomography images (NEZ1).

3.3.4 Simulations under real experimental conditions

New simulations were performed using the real experimental conditions. Both samples were meshed with best level of detail that could be obtained using the initial 3D image. The internal 3D surface mesh of the void-matrix interface (extracted from the raw image using the marching-cubes algorithm) was used, and an external 3D surface mesh was generated using the sample dimensions. The 3D volume meshing of the samples was performed using GLPre.

The thermal path (transfer and contact times) was reproduced, as it was measured during experiment. Thermal coefficients and friction coefficients were adjusted according to the final bulged shape of the samples (also known as *barrel effect*). Several values of friction coefficients and thermal coefficients were imposed and a series of simulations were performed in order to obtain an adequate set of values.

In the case of NEZ1, the entire sample was meshed, as the actual position of the void is rather central (see Fig. 3.10). In the case of NEZ2, a symmetry plane was defined (see Fig. 3.11), thanks to the absence of voids in the right half of the sample. This implicitly assumes that the presence of voids has no impact on the global deformation of the sample. This assumption is reasonable regarding the void-to-sample dimensions ratio, which is about 1/40 to 1/10.

The computation features are given in Table 3.3. The number of elements were very large due to the wide porous zone that required fine mesh size. The computation time of NEZ1 was longer because the time step had to be reduced to avoid mesh degeneration in this case.

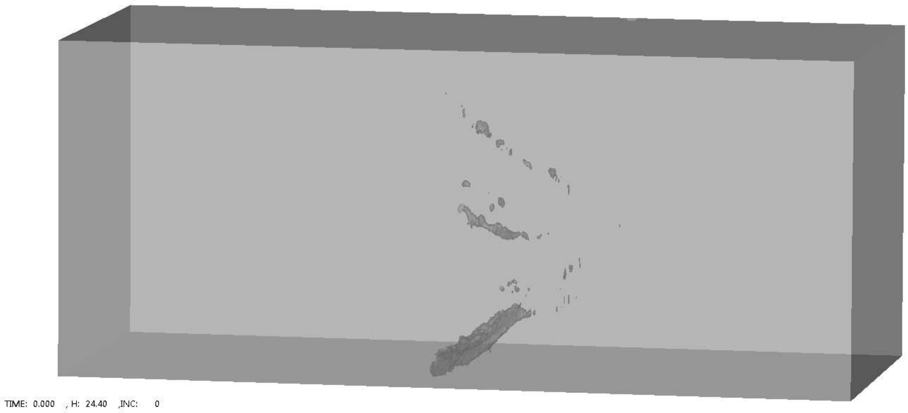

(a) Initial state of NEZ1

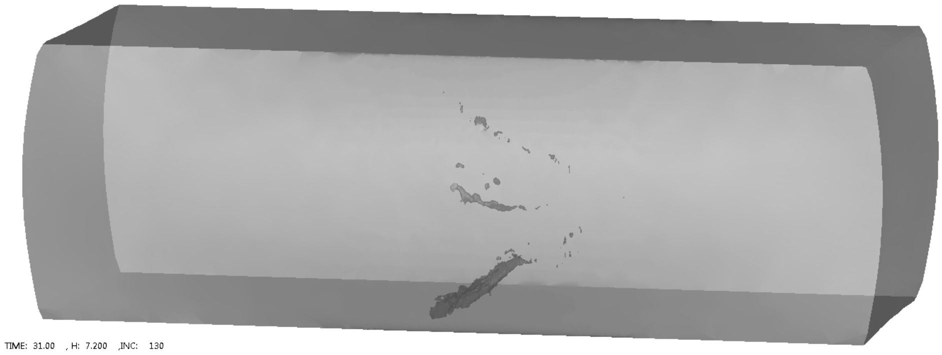

(b) Deformed state of NEZ1

Figure 3.10: Initial and deformed states for NEZ1.

Simulation	h_{min}	Nb elements	CPU time	Total CPU time
Full-field explicit NEZ1	0.25 mm	$4.04\ 10^6$	127 hours	64 days
Full-field explicit NEZ2	0.25 mm	$4.13\ 10^6$	48 hours	24 days

Table 3.3: Computation features for the simulations for NEZ1 and NEZ2 using real experimental conditions, performed using 12 CPUs at 3GHz and 24 Go RAM.

The final deformed states are illustrated in Figs. 3.10b and 3.11b. The results are compared to the deformed state that was obtained from X-ray microtomography and discussed in the two following sections.

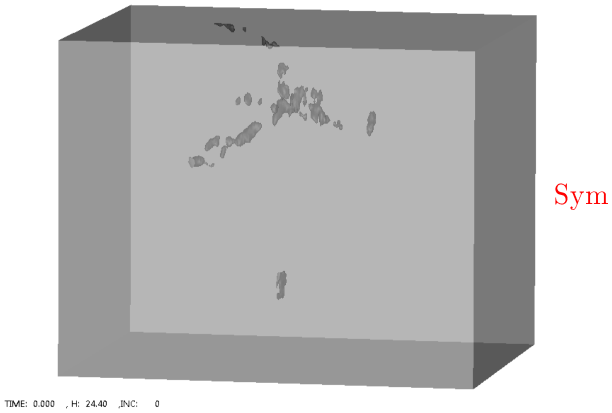

(a) Initial state of NEZ2

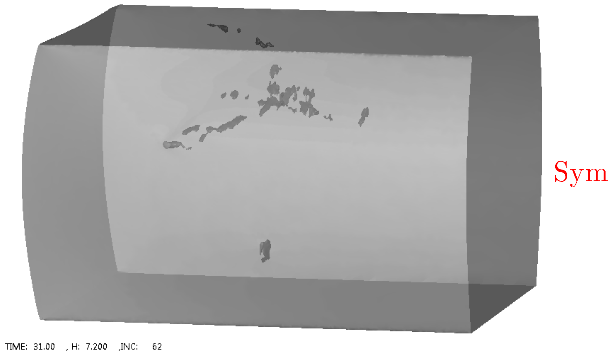

(b) Deformed state of NEZ2

Figure 3.11: Initial and deformed states for NEZ2.

3.3.5 Results regarding NEZ1

The deformed void-matrix interface that was obtained from the simulation of NEZ1 is now compared with the void-matrix interface that was obtained from the X-ray microtomography image in Fig. 3.12. For each surface, a distinction between the *material* side and the *external* side was made.

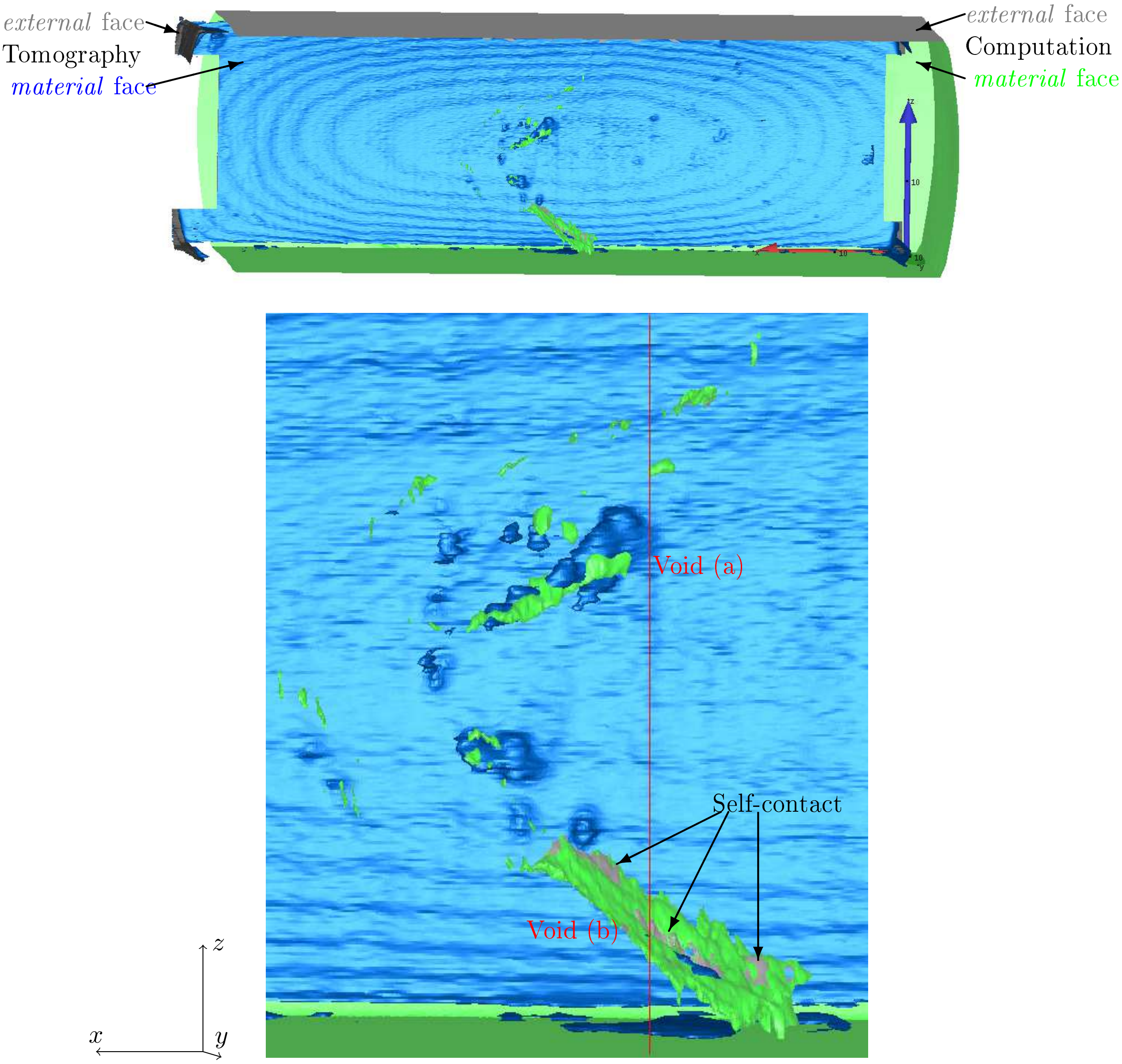

Figure 3.12: Comparison, for NEZ1, of final surfaces obtained from computation and from 3D-image.

The visualization software allows the choice of colors for *one* side of each surface, only. The opposite side must have a gray color. It was preferred to set colors for the *material* sides of each surface.

The *material* side of the surface from simulation is drawn in green color and the *material* side of the surface from tomography is drawn in blue color. The *external* faces of both surfaces are drawn with gray color.

Indicating the *external* side shows interest as the presence of self-contact in the computation surface can be observed. As self-contact is handled using the penalty method, a very small penetration of both *external* surfaces (gray color) can be observed on void (b) (see Fig. 3.12).

Final position of the voids

Regarding the sample's boundaries, a lateral shift of about 4 mm along the sample's axis (x–axis) was observed. This is due to the initial mesh generation for NEZ1. The initial tridimensional void-matrix interface was defined according to the initial image from X-ray microtomography, that had been performed on the entire specimen AD, i.e. before extraction of the samples. As a consequence an incertitude regarding the position along the x-axis was obtained. Nevertheless, relatively to the length of the sample, this shift is about 4% and its potential effect on the comparison was ignored. The relative position of both interfaces was thus manually shifted along the x-axis.

The final void position that was obtained from the simulation shows rather good agreement with the X-ray examination. It is illustrated in Fig. 3.12. A similar comparison is also given in Fig. 3.13 using a yz cutting plane. The x abscissa is indicated using a vertical red line in Fig. 3.12. The agreement is very good regarding the position of the voids in the yz plane as well.

Void (a)

Void (a) has a *vein-like* shape. It is an open hole that is visible on the sample surface as well (see green frame in Fig. 3.2a). The hole's position was verified and shows very good agreement. Unfortunately, the order of magnitude of the thickness of void (a) is submillimetric and is nearly the one of the voxel size of the microtomography image. Due to the rather low contrast of the image, a quantitative analysis would involve a large number of incertitudes. As a consequence, the analysis was not further conducted using this void.

Void (b)

Void (b) is illustrated in Figs. 3.12 and 3.13 as well. It has a slanted *band-like* shape. In Fig. 3.13c an outline of the void-matrix interface is also given on the yz cutting plane. The outline is presented using a red line, and is plotted for both interfaces (from computation in green and from the tridimensional image in blue).

The outline from the tridimensional image exhibits the presence of two voids. The outline from computation exhibits the presence of two residual cavities, that are the result of the partial closure of void (b). The presence of self-contact in the zone located between the two cavities confirms the partial closure of the void.

The two outlines, which were obtained from the tridimensional image and from computation, are roughly concentric. This result illustrates the good agreement regarding the final position of the voids.

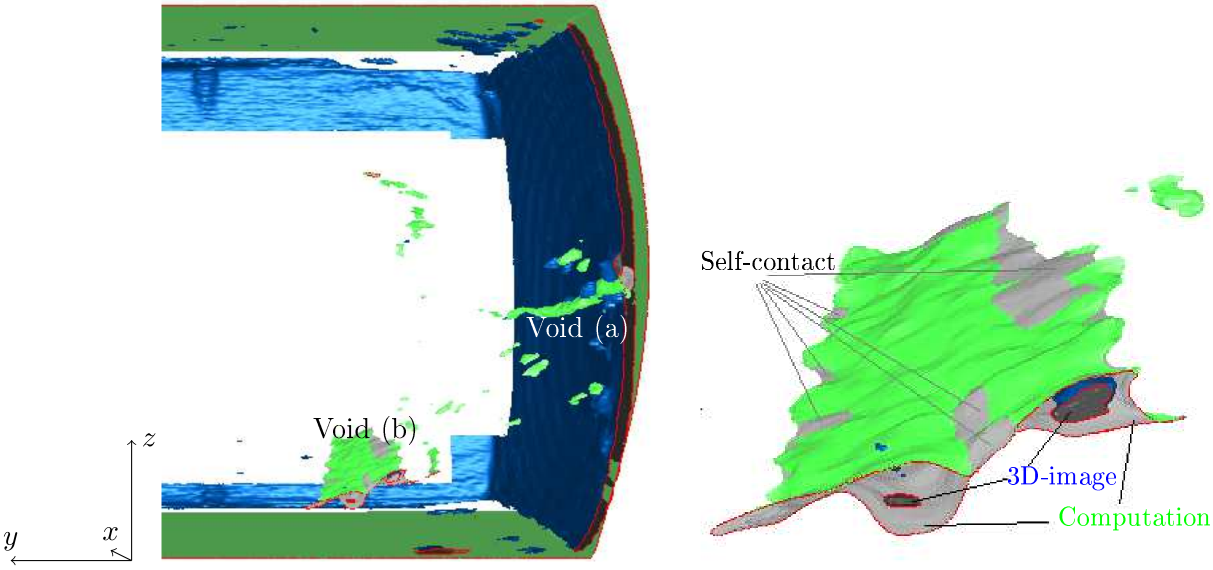

(a) Cutting plane of sample NEZ1

(b) Cutting plane of void (b)

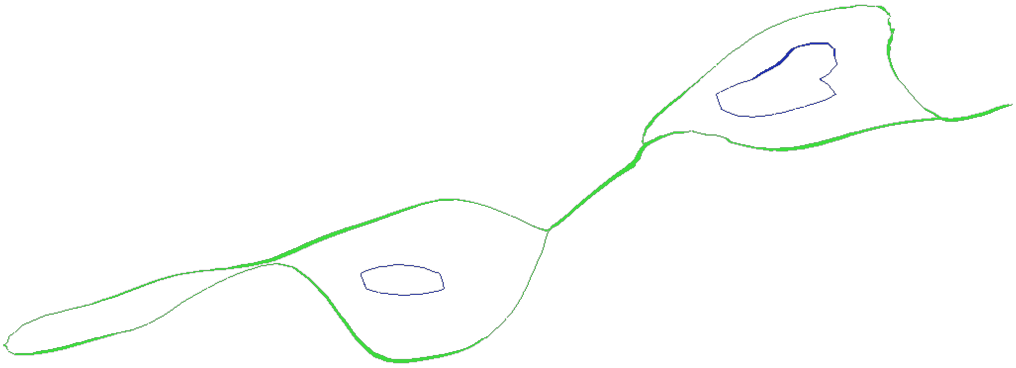

(c) Outline from computation (green) and from 3D-image (blue)

Figure 3.13: Comparison, for NEZ1, of final surfaces obtained from computation and from 3D-image, using a yz cutting plane. The *material* sides are colored with green and blue, respectively, and the *external* sides and contact areas are indicated on the figure to avoid confusion in the gray areas.

3.3.6 Results regarding NEZ2

The same analysis was performed using NEZ2. The comparison between void-matrix interfaces from computation (green) and from tridimensional examination (blue) is presented in Fig. 3.14. In this case, a cluster of tiny voids in zone (a) can be observed at the top of the sample. A larger void (b) can be seen in the lower part of the sample, rather close from the sample's boundary.

The position of boundaries exhibits a slight difference in the x direction due to the initial position of the voids in the sample's mesh. It was manually corrected by a shift along x axis as well.

Zone (a)

The global position of the voids in zone (a) shows rather good agreement. The very small dimensions of the voids in this zone significantly affected the accuracy of the obtained void-matrix interface from microtomography. Their average dimensions exhibit the same order of magnitude as the voxel size. It is therefore difficult to clearly identify the different voids in the porous zone (a). A slight error regarding the position of several voids was measured. It did not exceed 1 mm.

Void (b)

Void (b) exhibits a roughly flat shape and is rather vertically oriented, as illustrated in Fig. 3.15. However, the void is located close to the boundary of the sample. This position unfortunately presents rather low interest in terms of closure, as the thermomechanical state is not well adapted for void closure. The level of deformation is relatively low, due to the "blacksmith cross" effect, see Fig. 3.16a. The stress triaxiality ratio is rather moderate as well in this zone, see Fig. 3.16b. As a consequence, the void volume reduction is about 11% for void (b), according to the computation. On the other hand, the average reduction of the voids that are located in zone (a) is about 80%.

The final global aspect shows good agreement between the void-matrix interfaces from computation and from tridimensional examination.

3.3.7 Conclusions

Generally, a good agreement was obtained between void-matrix interfaces from *full-field* explicit computations and from tridimensional examination. This was verified in terms of position of the voids and their visual aspects.

Unfortunately, the analysis was strongly penalized by the low void-to-sample dimension ratio, inducing small voxel size and very low contrast in the microtomography image. The methodology yet demonstrated great potential in terms of feasibility, regarding the very coherent results that were obtained between the simulation and microtomography images.

It was thus decided to perform a second campaign of compression tests using samples with a greater void-to-sample dimension ratio.

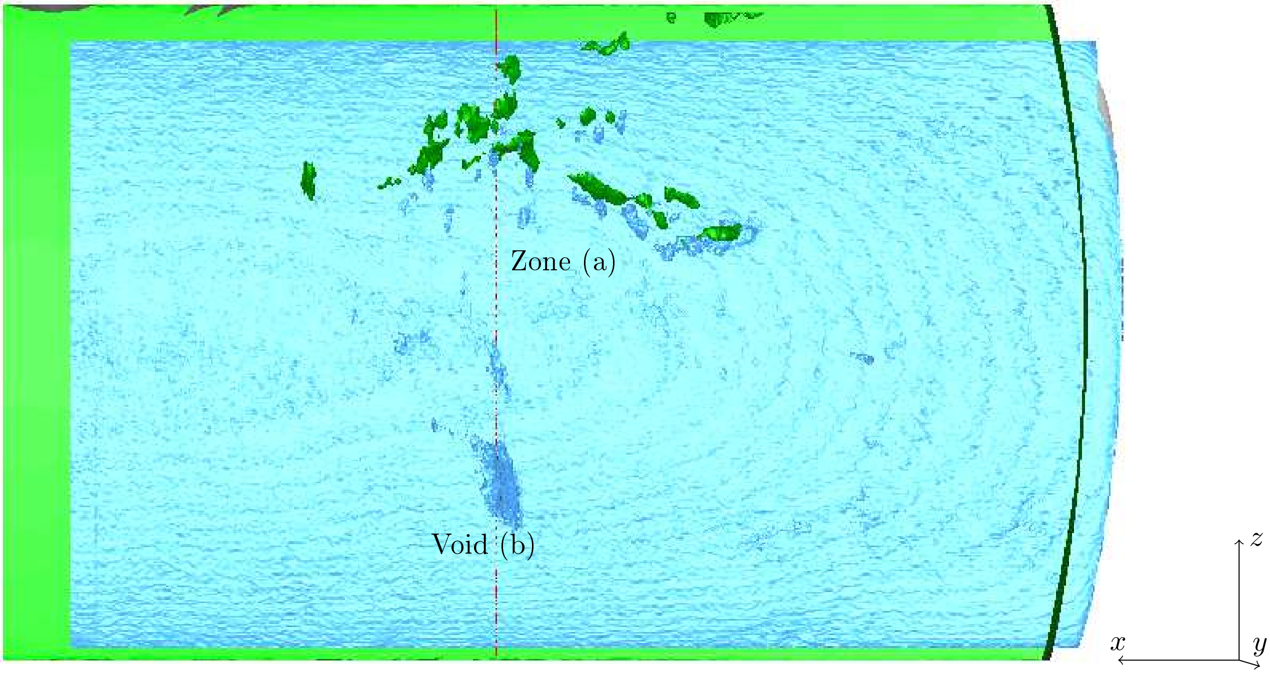

Figure 3.14: Comparison of final void-matrix interfaces obtained from computation (green) and from microtomography (blue) for NEZ2.

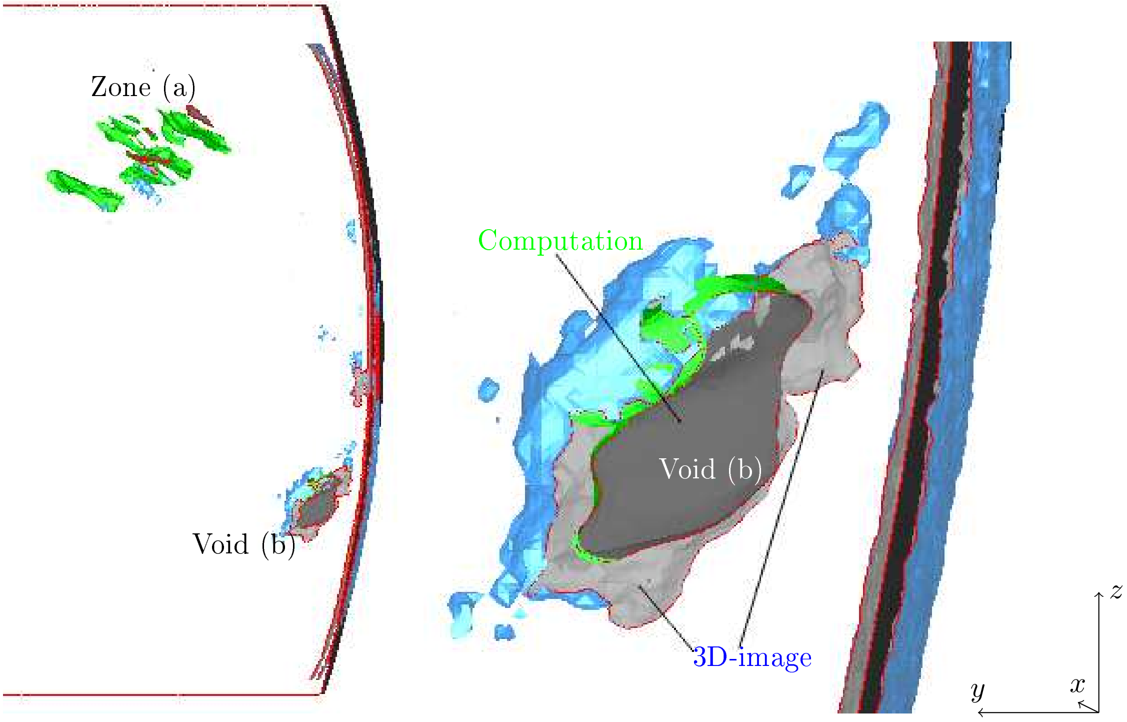

(a) Perpendicular cutting plane

(b) Detail of Void (b)

Figure 3.15: Comparison of final void-matrix interfaces obtained from computation (green) and from microtomography (blue) for NEZ2, using a yz cutting plane.

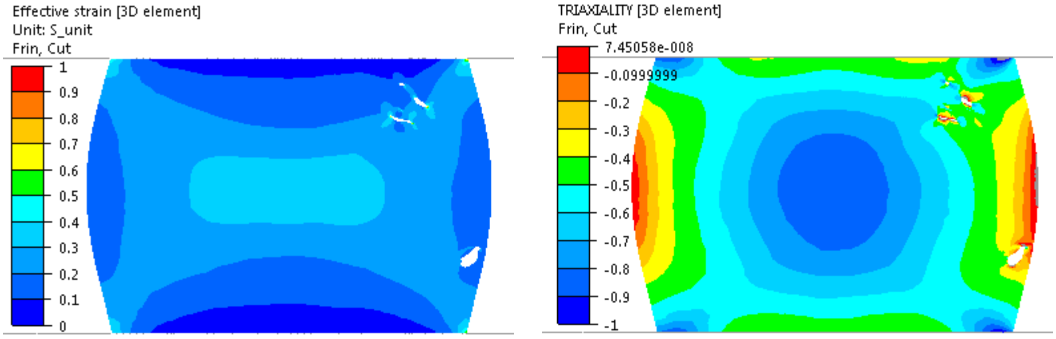

(a) Equivalent strain (b) Stress triaxiality ratio

Figure 3.16: Mechanical fields in the sample NEZ2 at the final state, using a cutting plane yz at the abscissa that is defined with a vertical red line in Fig. 3.14.

3.4 Samples JD20 and JD47

Steel samples JD20 and JD47 were used for experimental validation. These extra-porous samples were collected at Ascometal CREAS (Research center) according to their low density and, therefore, their large interest within this study. They were previously described in Chapter 2, section 2.4.1.

Plane strain compression was chosen as it provides different stress states in the material. It generally provides less compressive stress triaxiality ratio for non-porous samples. Excellent accuracy in terms of height reduction is generally obtained, which is of great interest for samples with small dimensions.

Note that, according to the experimental setup, the sample must have a rectangular shape. The cylindrical sample JD20 was thus machined from ⌀20 mm to a 10 mm × 10 mm square section. These dimensions were defined according to the tomograph capabilities in terms of signal absorption and the available space inside the tomograph. This aspect must obviously be considered for the initial sample, but also for the final deformed sample.

3.4.1 Preliminary simulations

For the first preliminary simulation, only a few voids were defined in the sample's mesh, see Fig 3.17. The void geometries were obtained from the initial tridimensional image of JD20.

As in the previous section, classical friction and thermal conditions were defined in a first approximation and are not detailed here for confidentiality reasons. Mesh size was set to the value $h_{min} = 0.25$ mm around the voids.

The evolution of void volume *vs.* height of reduction is plotted in Fig. 3.18. The curves indicate that a reduction to a final height of 6 mm leads to complete closure of the three voids. Over the range $H = [8, 10]$ mm, the closure rate shows the maximum value and is relatively constant. Beyond the value 8 mm, the void volumes are too small to give adequate contrast using X-ray examination. Thus, the prescribed final height to be reached was fixed to $H_f^* = 8.8 \pm 0.2$ mm.

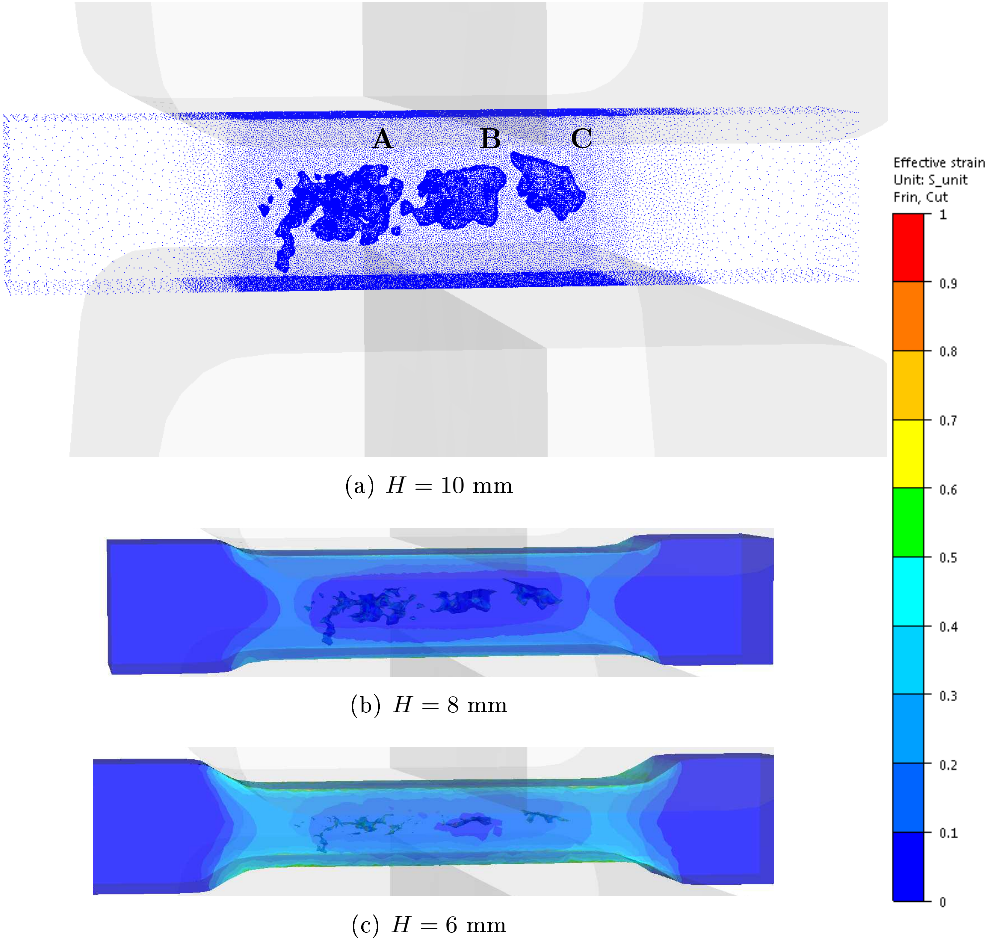

(a) $H = 10$ mm

(b) $H = 8$ mm

(c) $H = 6$ mm

Figure 3.17: Preliminary test simulation of sample JD20 (CPU time of 200 h using 10 CPUs, 3GHz, Windows x64, 24 Go RAM).

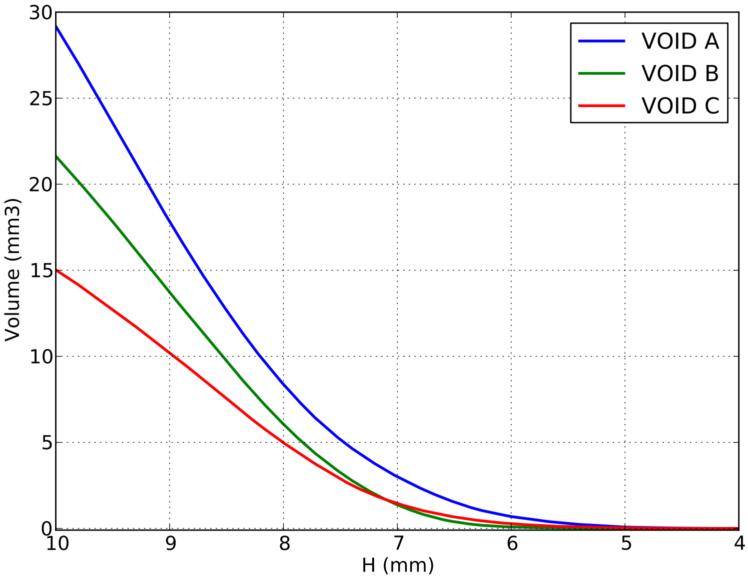

Figure 3.18: Volume evolution for the three voids A, B and C defined in Fig. 3.17.

3.4.2 Compression tests

The tests were performed at Ascometal CREAS. Before performing the compression test on samples JD20 and JD47, preliminary void-free samples were used in order to verify the testing conditions in terms of reduction height and temperature evolution.

The samples are first enclosed in a container and are heated up using an induction furnace to the desired temperature. The container helps maintaining the temperature during transfer between the heating system and the press. Thermocouples (K-type) were used to verify the temperature evolution during induction heating. The temperature drop during transfer to the press was measured and was compensated by setting a slightly higher temperature to the heating step. The temperature accuracy at the deformation's starting instant is therefore better controlled. An infrared camera was also used and the initial temperature homogeneity at sample's surface was verified.

The samples are deformed between the two dies using a screw press (Fig. 3.19) with a die velocity of 400 mm.s^{-1}. After deformation, the samples are placed in an argon atmosphere to avoid oxidation during cooling.

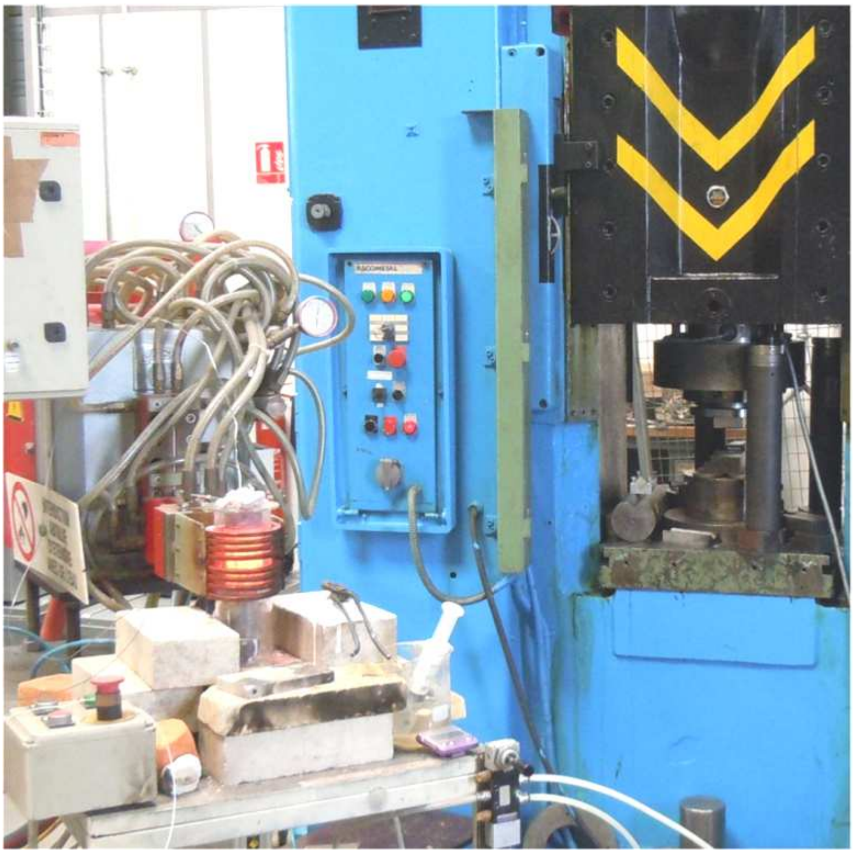

Figure 3.19: Photograph of the induction heating system (left) and screw press with punch-dies (right).

The deformed samples are illustrated in Fig. 3.20. The actual reduction height for each sample was measured at three positions on the deformed zone and was homogeneous. The reduction height for JD20 was 8.70 mm and the one for JD47 was 9.00 mm. The samples were then sent to Fraunhofer for microtomography examination. The resolution provided a voxel size of 102 μm.

The 3D images were filtered using the same methodology as the one presented in the previous chapter, section 2.4.1. For each sample, a 3D surface mesh of the void-matrix interface was extracted.

(a) Side view

(b) Upper view

Figure 3.20: Photographs of the samples JD20 and JD47 after deformation.

3.4.3 Simulations under real experimental conditions

Simulation	h_{min}	Nb elements	CPU time	Total CPU time
Full-field explicit JD20	0.25 mm	$2.9\ 10^6$	12 hours	6 days
Full-field explicit JD47	0.25 mm	$2.6\ 10^6$	10 hours	5 days

Table 3.4: Computation features for the simulations for NEZ1 and NEZ2 using real experimental conditions, using 12 CPUs at 3GHz and 24 Go RAM.

Two simulations were performed in order to obtain results under conditions that are comparable to the experimental ones. Both samples were meshed using the same methodology as in section 3.3. The internal tridimensional surface mesh of the void-matrix interface was obtained from the tridimensional image using the marching-cubes algorithm, and a boundary surface mesh was generated using the sample's dimensions. The 3D volume meshing of the samples is performed using GLPre. They are illustrated in Figs. 3.21 and 3.22.

In the case of JD20, it was decided to ignore the void state in the undeformed part of the sample (left part on Fig. 3.21) in order to reduce the total number of elements in the mesh.

In Figs. 3.21a and 3.22a the contact area is shown using a binary red/blue scale. The blue color represents the contact with the dies. In Figs. 3.21b and 3.22b, the mesh was plotted for a central cutting plane. The mesh size at the internal void surface is given by the voxel size, i.e. about $h_{min} \approx 0.1$ mm. Mesh size at the surface of the sample is set to the value $h_{max} = 0.5$ mm. The strain-rate field is plotted as well. It illustrates the classical deformation profile of the plane-strain compression test. The edges of the dies involve a higher strain zone exhibiting a "V" shape.

Note that the initial raw image was obtained from the (initially) cylindrical sample JD20, as it was done at the beginning of this PhD work. Due to the imaging artefacts at the surface of the sample, the position of the boundaries was approximate and the absolute position of the void-matrix interface is not strictly determined. In addition, the sample had to be machined toward a square-base, according to the microtomography requirements. The voix-matrix interface was thus placed to an arbitrary centerline position (relatively to the sample boundaries).

As illustrated in Fig. 3.20, the position and direction of the die on the sample were slightly different in both cases, due to manual experimentation. An angle of about 22° was measured between the dies and the sample JD47. The actual position and direction of the dies were therefore also properly defined according to visual observation of the deformed samples. The angle can be seen on the contact zone on Fig. 3.22a.

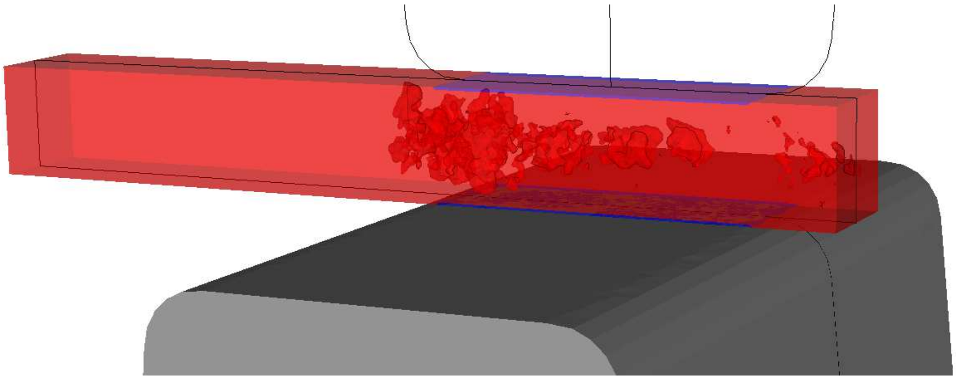

(a) Contact area in blue

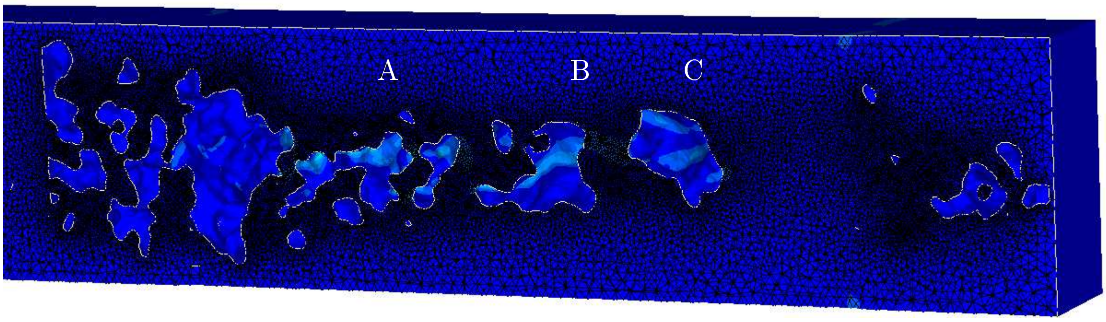

(b) Initial state (after first increment)

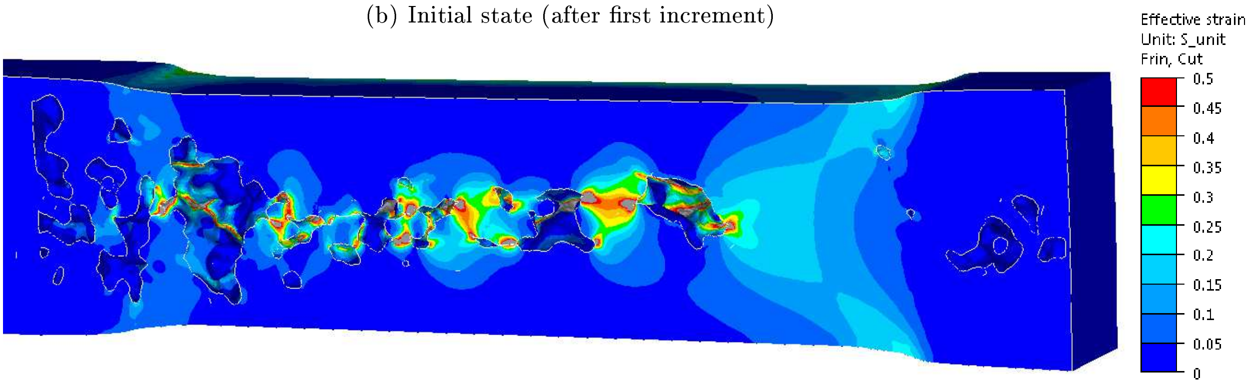

(c) Final state

Figure 3.21: Simulation of JD20 using real testing conditions (2.9 10^6 elements).

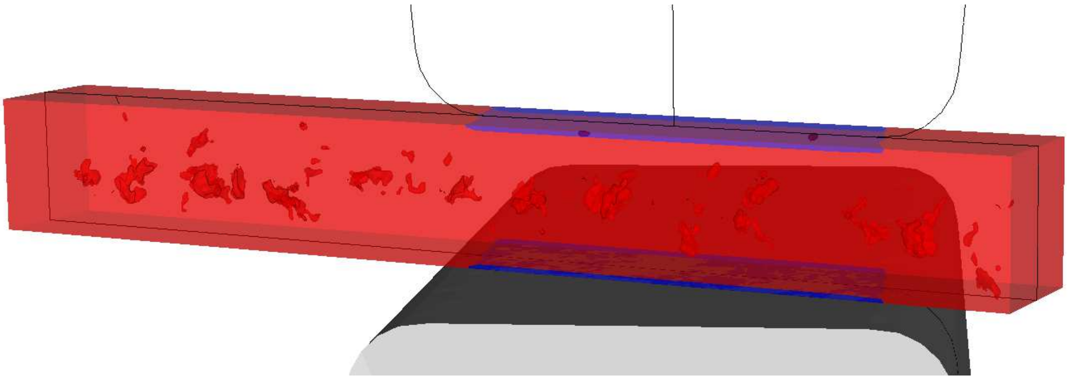

(a) Contact area in blue

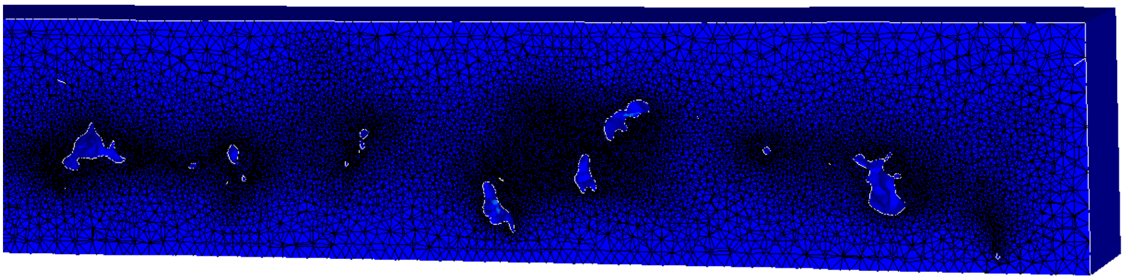

(b) Initial state (after first increment)

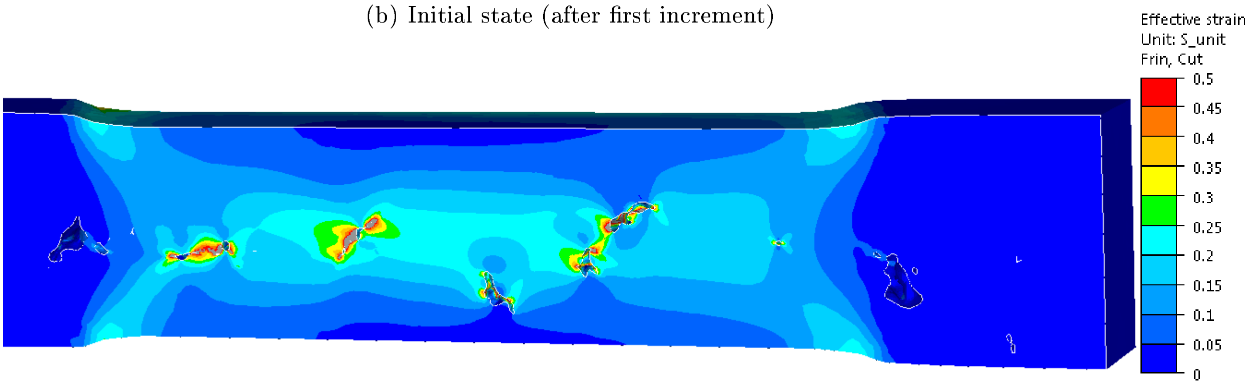

(c) Final state

Figure 3.22: Simulation of JD47 using real testing conditions ($2.5\ 10^6$ elements).

3.4.4 Results regarding JD20

In this section, the final surface obtained from the simulation is compared to the 3D image obtained for each deformed sample. It is worth noticing that the measured volume depends on the chosen value of threshold. For each sample, a common threshold value was chosen in order to fit the prediction results as good as possible.

The void-matrix interface was detected using the marching-cubes algorithm presented in the previous chapter, section 2.4.1. A slice of the 3D image is presented in Fig. 3.23a. For a cutting plane at the same position, a superposition of contours is given in Fig. 3.23b, showing the matrix-void interfaces in both cases. The green line was predicted by the finite element simulation, and the blue line was measured on the 3D image.

The comparison on this cutting plane shows an excellent agreement between the finite element prediction and tridimensional observations. It is true regarding the final shape of voids, as well as their final position.

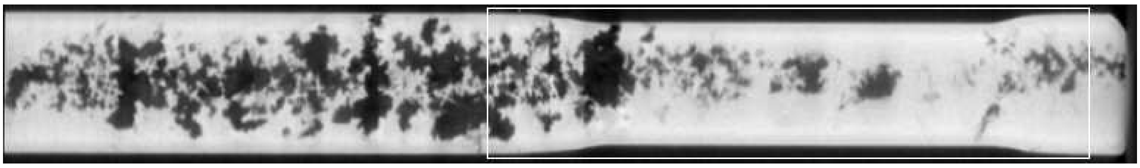

(a) Raw image from microtomography

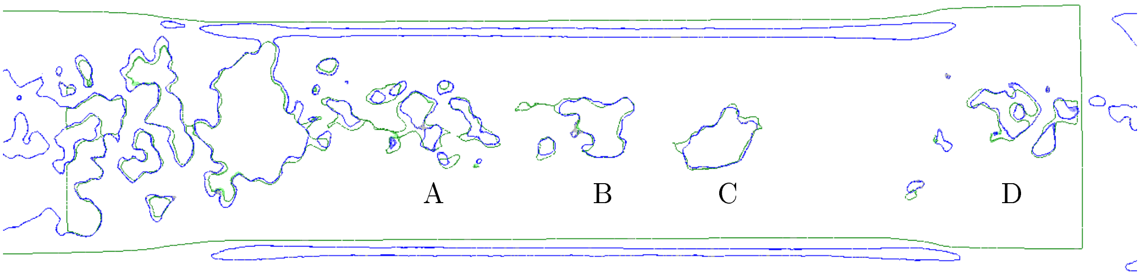

(b) Contour superposition of final mesh (green) and detected void-matrix interface from raw image (blue) (close-up from the right-hand half of (a))

Figure 3.23: Comparison of results using cutting plane of sample JD20.

Void C

Regarding final shapes, void C exhibits the best agreement. It can be seen on Fig. 3.23b, and it is illustrated in Fig. 3.24 as well for a perpendicular cutting plane. The distance between both lines remains in the order of magnitude of the voxel size, i.e. around 100 μm. The prediction of the final void shape seems therefore to be within the range of the accuracy provided by X-ray microtomography measurements.

Void B

On Fig. 3.23b it can be seen that void B exhibits a zone of partial closure around its upper–left part. It is visible on the computation contour (green line), but was not detected on the contour from the raw image (blue line). Interestingly, a small residual void remains on the left part of the contact zone and was not detected on the contour from the raw image neither. Yet, when looking at the grayscale raw image (Fig. 3.23a), a slightly darker zone can be observed at this position, mentioning that this residual void actually exists in the sample but was not detected by the marching-cubes algorithm due to its low contrast and small size.

The contours are also compared for a perpendicular cutting plane in Fig. 3.25. Similarly, the narrowest parts of the void may not have been detected from the tridimensional image.

These remarks confirms the fact that the accuracy of the measure using X-ray microtomography remains a limitation factor, particularly in the case of voids with small dimensions (compared to the size of the sample). In spite of this, the agreement with the prediction is very good. Apart from the undetected zones, the final contours show an excellent agreement for void B, as for void C.

Void A

Similar conclusions can be made regarding void A. Both contours show excellent agreement (Fig. 3.23b), except in the zones of partial closure (involving contact and small residual voids).

Note the relative difference of position for the sample boundaries between simulation data and measured data. This is due to the approximate initial positioning of the boundary in the initial mesh for the simulation, as pointed out above. Fortunately, the samples present a common undeformed zone that was used to manually readjust the relative position of the simulation and the measure. This explains why the boundaries of the samples are relatively different, while the void-matrix interface gives an excellent agreement.

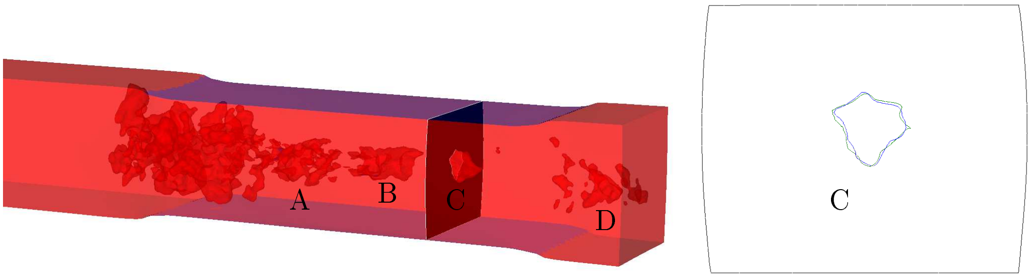

Figure 3.24: Cutting plane showing void C at the final height ($H = 8.7$ mm).

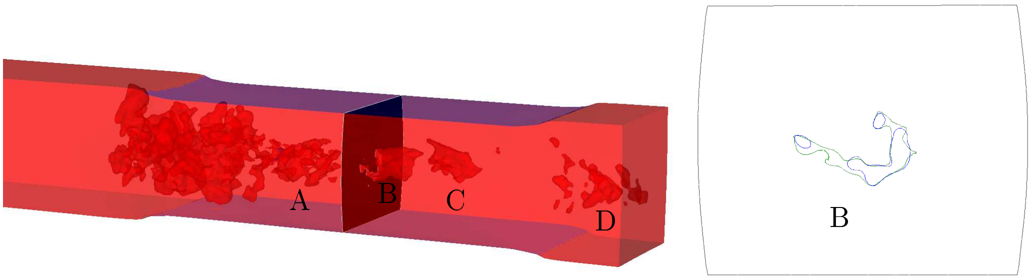

Figure 3.25: Cutting plane showing void B at the final height ($H = 8.7$ mm).

3.4.5 Results regarding JD47

The results for JD47 are presented in a similar manner. A grayscale raw slice is given in Fig. 3.26a, and the comparison is made in Fig. 3.26b using the superimposed contours of void-matrix interfaces obtained from the simulation (green line) and measured from the raw data (blue line). It is noteworthy that the contrast obtained for this sample was lower than the one for the previous sample. This is due to the voids smaller dimensions. The direct consequence is a lower accuracy of the void-matrix interface obtained by the marching-cubes methods, as it is closely linked to the definition of a threshold value. The determination of an adequate threshold value was harder for this sample.

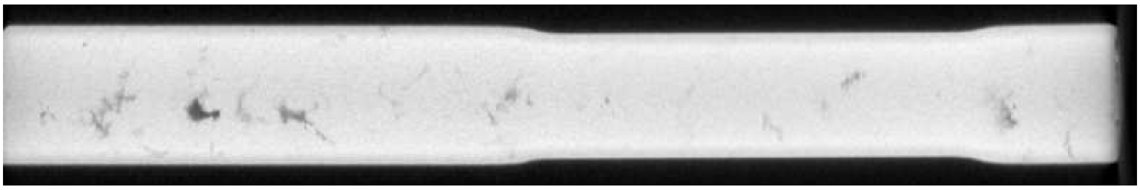

(a) Raw image from microtomography

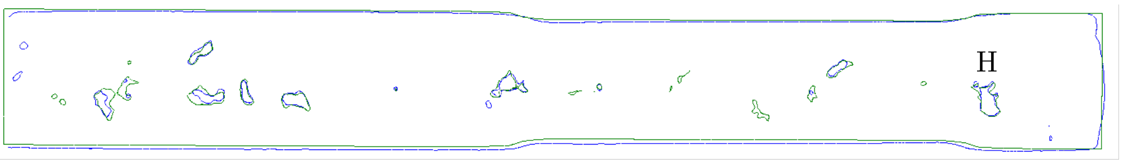

(b) Contour superposition of final mesh (green) and detected void-matrix interface from raw image (blue)

Figure 3.26: Comparison of results using cutting plane of sample JD47.

From a general point of view, the respective positions of the voids show very good agreement. This is true in the deformed zone, as well as in the undeformed zone. For this sample, the position of the sample's boundaries show better agreement than for previous sample. The reason is that the initial void state was obtained from the actual geometry, after the machining step to a square-based bar. The position of the internal voids was thus possible with better accuracy. The small remaining difference may be attributed to the low accuracy of the boundary due to surface contrast artifacts, and to experimental incertitudes (e.g. real thermal exchanges, effect of gravity, or manual positioning of the sample on the die).

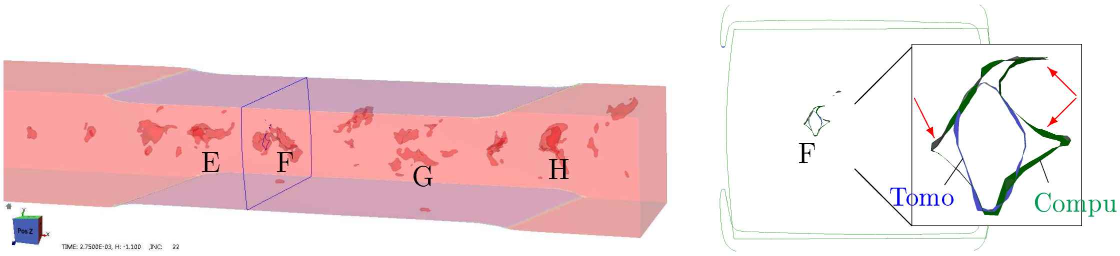

Figure 3.27: Detail of void F in the deformed sample JD47.

When looking at the contours in Fig. 3.27, it can be observed that the predicted shape exhibits three rather narrow peaks (see red arrows in zoom). These peaks result from a partial closure of thin part of the void. Regarding the upper peak, contact was even observed in the contour from computation. These narrow parts might not have been

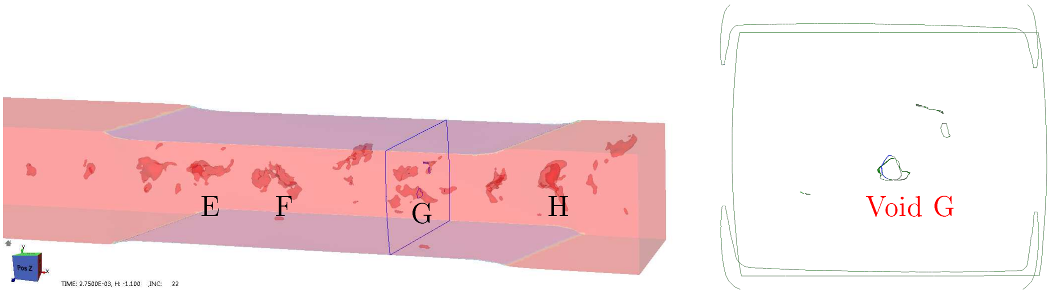

Figure 3.28: Detail of void G in sample JD47.

detected using the tomography-based technique. Nevertheless, let us note that, once the narrow peaks ignored, the final shape is remarkably accurate.

A good agreement was also obtained in Fig. 3.28. The distance between prediction and measured interface remains in the incertitude range of the measure.

3.4.6 Final void volumes

For each sample, the volume evolutions of four voids were studied and are plotted in Fig. 3.29. The lines correspond to the prediction simulation and the dots are values measured on the measured void-matrix interface.

The initial value for the prediction coincides with the volume measured from the initial microtomography image, as it was used to generate the initial mesh. The volumes of the voids were measured from the microtomography images at the final reduction height using the method described in Chapter 2, section 2.4.2.

The measured void volumes show excellent agreement with the prediction for sample JD20 (see Fig. 3.29a). The relative error is about 1% for voids A, C and D, and raises to 13% for void B. The perpendicular cutting plane in Fig. 3.25 illustrates the difference of volume on void B. The difference of contours was discussed above, and pointed out the fact that the narrowest part of the voids may not be detected by the tomography-based technique. However, an excellent agreement was obtained for all other contours and it is now also verified on the final void volumes.

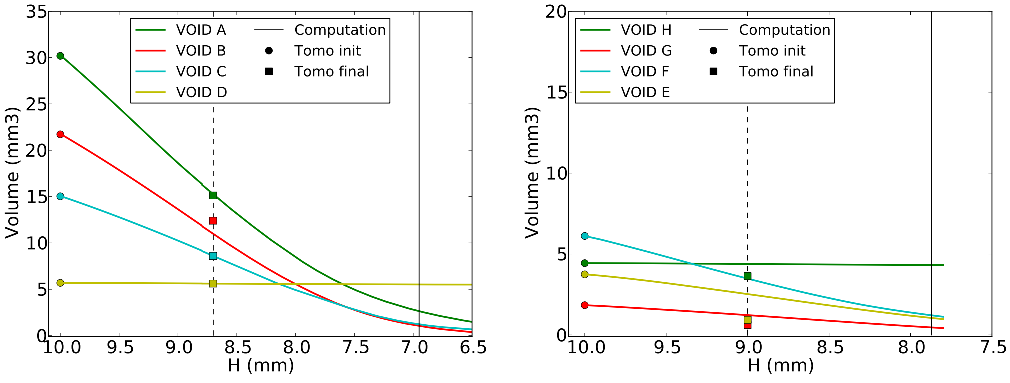

(a) JD20

(b) JD47

Figure 3.29: Volume evolution of four voids in both samples JD20 and JD47.

In the case of sample JD47, the measured values are globally underestimated compared to the prediction value (see Fig. 3.29b). This may be explained by particular small dimensions of the voids. The initial void volumes for sample JD47 were in the range [2, 6] mm^3, while the ones of sample JD20 vary over the range [5, 30] mm^3. The excessively small dimensions may explain the discrepancy in the case of sample JD47.

Due to the low void-to-sample thickness ratio, the contrast obtained from microtomography is rather low. Both sharpness and contrast are consequently lower and the void-matrix interface is detected with less accuracy.

Secondly, some voids (or some part of voids) are nearly equal to the voxel size. These voids might have been detected on the initial image, but not on the final image, as their size reduced during compression. This was the case of void F, for example.

3.4.7 Conclusions

To conclude on both samples JD20 and JD47, the qualitative analysis exhibited excellent agreement in terms of final position of the void-matrix interfaces. The main discrepancies are most likely due to the tridimensional images, due to the small dimensions of the voids.

For the sample JD20, the void-to-sample dimensions ratio was larger and the quantitative analysis exhibited excellent agreement in terms of void volume evolution.

3.5 Conclusions

The experimental campaign that was performed at Ascometal involved two porous samples. The samples exhibited a larger void-to-sample dimensions ratio than the samples used in the previous campaign at Aubert&Duval.

From these compression tests, two main results can be pointed out:

- First, the feasibility of such testing was demonstrated. The combination of X-ray microtomography and compression testing was successfully conducted and provided accurate results. Nevertheless, full attention must be paid regarding the choice of the sample's dimensions. The void-to-sample dimension ratio is a key-parameter for the accuracy of the X-ray imaging. Low values of void-to-sample dimension ratio will significantly enhance the final contrast of the tridimensional image. Low samples dimensions are generally required with respect to the spatial capabilities of the tomograph.

  On the other hand, reducing the sample's dimensions may reduce the accuracy of the compression test itself. It involves stronger gradients of temperature and requires piloting the tools with high accuracy.

  Preliminary simulations were very helpful for the definition of an adequate experimental protocol, notably in terms of final height reduction.

- The final tridimensional examinations showed excellent agreement with the prediction obtained from the *full-field* simulations. This agreement was shown in terms of position, visual aspect and void volume of various voids.

  The use of *full-field* explicit simulations with FORGE [2011] to model the local behaviour of voids was therefore validated.

Full-field explicit simulations will be extensively used in the following chapters. In Chapter 4, a wide campaign of *full-field* explicit simulations at the RVE-scale is performed in order to build and calibrate the new prediction model. In Chapter 5, *full-field* macroscopic simulations of processes containing voids are performed in order to compare and validate the prediction model.

Chapter 4

Construction of a new prediction model for void closure

Contents

Résumé français

Ce chapitre présente l'étude des mécanismes de refermeture de porosité à l'échelle du VER, ainsi que la construction du nouveau modèle de refermeture de porosité. Le modèle doit être construit à partir de grandeurs quantifiables dans un contexte industriel. La morphologie réelle exacte de pores étant une donnée difficile à quantifier, car elle requiert une étude systématique approfondie en microtomographie, l'utilisation de géométries éllipsoïdales équivalentes est proposée pour la construction du modèle. La prise en compte de la géométrie initiale de pore fait partie des avancées principales du nouveau modèle.

La première partie de ce chapitre est donc dédiée à une discussion relative à l'utilisation de ces géométries équivalentes. Il est montré que la taille absolue des pores n'a pas d'impact sur le comportement en referemeture, à l'inverse des rapports de formes qui présentent un impact majeur. L'erreur commise par l'utilisation de géométries équivalentes est discutée à partir de quatre pores réels. Le gain obtenu par l'utilisation d'éllipsoïdes équivalentes est démontré en comparaison à l'utilisation de sphères (systématiquement utilisées dans la littérature).

La seconde partie présente une étude de sensibilité aux différents paramètres identifiés comme potentiellement influents sur la refermeture, afin de sélectionner les paramètres à prendre en compte dans le modèle. Il est montré que les paramètres de géométrie (rapports d'aspect, orientation) ont un impact majeur, au même titre que la triaxialité des contraintes et la déformation équivalente cumulée. Concernant les paramètres matériaux, le coefficient d'écrouissage/adoucissement, ainsi que le coefficient de sensibilité à la vitesse de déformation ont un impact non-négligeable sur le comportement en refermeture. Cependant, leur influence reste de second ordre dans les plages de valeurs definies par la problématique industrielle. Ils ne seront pas pris en compte dans le modèle. La consitance du matériau et la vitesse de déformation n'ont aucune influence sur le comportement en refermeture.

La troisième partie présente la construction du modèle, le choix des expressions analytiques pour chaque dépendance, ainsi que leur calibration par régression. L'ensemble des influences a pu être modélisée par une somme de polynômes d'ordre 2. En utilisant les quatres géométries issues de pores réels, et sous plusieurs conditions mécaniques, il est montré que le nouveau modèle est capable de prédire l'évolution de leur volume avec une précision inférieure 5% dans 90% des cas, et qu'elle reste inférieure à 17% dans le cas le plus extrême.

4.1 Introduction

The first chapter demonstrated the lack of reliable existing model in the literature to predict void closure, notably regarding the influence of initial void geometry. The second chapter showed that the use of RVE simulations at the meso-scale enables an accurate tridimensional description of voids, and that boundary conditions can be accurately controlled. The third chapter showed that the use of FORGE [2011] is capable of providing accurate simulations of the actual behaviour of the voids during deformation.

The present chapter presents the results of a wide campaign of RVE simulations that was performed using FORGE [2011] in order to study the influences of several parameters on void closure. First, the use of geometrical parameters that were introduced in Chapter 2 is discussed. Then, a global parametric sensitivity study is presented in order to qualitatively understand the involved mechanisms and to identify which parameters must be further quantified. In a third section, the quantification of the identified parameters is presented. Semi-analytical equations are proposed to model the observed behaviours. A calibration of the semi-analytical model is then presented using regression analysis. In a last section, the prediction of the semi-analytical model is verified using several geometries coming from real industrial data and the relative error is assessed.

4.2 Use of equivalent geometries

Spherical voids are often used in the literature [Budiansky et al., 1982, Lasne, 2008, Zhang et al., 2009, Tanaka et al., 1986, Nakasaki et al., 2006]. In the present work, the use of equivalent ellipsoids is proposed to additionally consider tridimensional information. In Chapter 2, the use of *morphology-equivalent* ellipsoids was introduced. It was demonstrated that it is possible to generate an equivalent ellipsoid that exhibits the same inertia matrix than a real void. This possibility enables the dimensions and the orientation of a real void to be faithfully represented. The objective of this section is to discuss this representativity.

The effect of the size of a void is first discussed. Then, comparisons in terms of closure behaviours are performed between real voids, spherical voids and *morphology-equivalent* ellipsoids.

4.2.1 Void size

The RVE dimensions are defined using the ratio η, i.e. with respect to the void's dimensions (section 2.5.2). Boundary conditions are imposed in order to apply a prescribed strain-rate and stress triaxiality ratio, which are both dimensionless variables.

Studying a void at the RVE-scale is therefore a dimensionless problem.

Note that in the case of large void-to-workpiece dimensions ratios, the general hypotheses of the meso-scale approach (section 2.2) might not be verified. The separation of scales is no longer possible, neither the use of a *mean-field* model. In these particular cases, the meso-scale may not be used, and the use of explicit *full-field* simulations are required, such as the ones conducted by Chen et al. [2012], Lee et al. [2011], Banaszek et al. [2013]. This is however out of the scope of the present study. Within this work, according to the industrial issues (Chapter 1) the void-to-workpiece dimensions ratio is small and the meso-scale approach can be used.

As a consequence, the *absolute* void dimensions have no importance, neither has the initial void volume V_0. The study is thus performed using a normalized volume V/V_0. On the contrary, the *relative* void dimensions (aspect ratios) and the orientation of the void (with respect to principal deformation direction) are key parameters.

4.2.2 Comparison of closure behaviours

Limitations of the use of a sphere

A comparison was performed between void AD (obtained from X-ray microtomography), the case of a sphere, and the case of the void's *geometry-equivalent* ellipsoid, as previously described in Chapter 2, section 2.4.3. Void volume evolutions are plotted in Fig. 4.1. The volume evolution of the spherical void is clearly not representative of the one obtained using void AD, as the slope of the curve is lower by a factor around two over the range $V/V_0 = [0.2, 1]$. On the contrary, the use of a *geometry-equivalent* ellipsoid shows great interest, as the curve shows very good agreement with the actual closure of void AD.

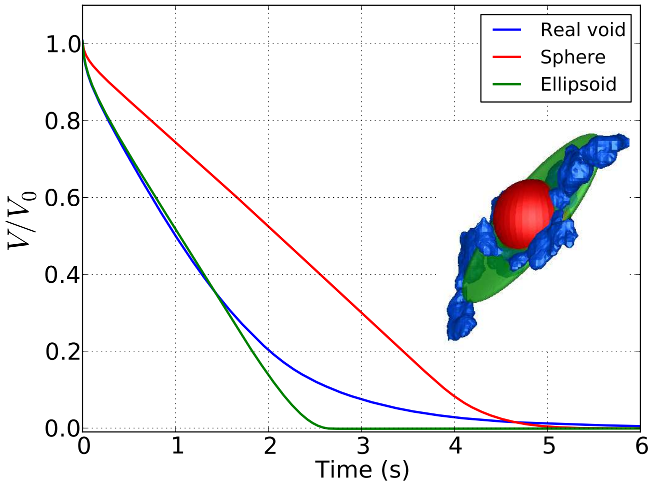

Figure 4.1: Void volume evolution of void AD, compared to a sphere and to its *geometry-equivalent* ellipsoid under arbitrary constant boundary conditions

Evaluation of the use of ***morphology-equivalent*** ellipsoids

In order to better illustrate the ability of an equivalent ellipsoid to model a real void, a comparison was performed using four different cases and are presented in Figs. 4.2 and 4.3. The real voids (obtained from X-ray microtomography) are compared to their *geometry-equivalent* ellipsoid in terms of void volume evolution. Void volume evolution is plotted under three various stress triaxility ratios, covering the range of interest within this work.

Regarding voids 3 and 4, the curves show good agreement on the range $V/V_0 = [0.2, 1]$. The major difference is observed in the final closure stage.

For the case of Void A, the use of an equivalent ellipsoid shows larger discrepancies, due to the extreme tortuosity of the real void. Regarding Void AD, the agreement is better for more compressive stress states. The largest discrepancy occurs for $T_X = 0$. Let us also note a slightly positive slope at the early stage of closure for the ellipsoidal void. This highlights a slight opening of the void. The value $T_X = \frac{\sigma_m}{\bar{\sigma}} = 0$ (i.e. $\sigma_m = p = 0$) indicates that the RVE is submitted to shearing stresses only. The values of boundary conditions $\sigma_{xx} = \sigma_{yy} = -\frac{\sigma_{zz}}{2}$ thus impose tensile stresses on the faces perpendicular to the main deformation direction z. A maximum value of void volume of $V/V_0 = 1.021$ is reached around $\bar{\varepsilon} = 0.1$. The opening behaviour thus remains very low and closure occurs after $\bar{\varepsilon} > 0.1$. This observation can be attributed to the particular geometry of the void, as it is very elongated and its orientation is very different from the three other voids.

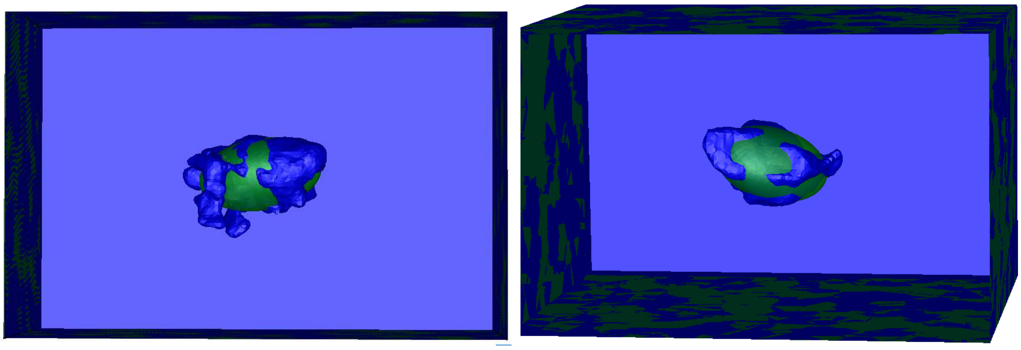

(a) Void 3 (b) Void 4

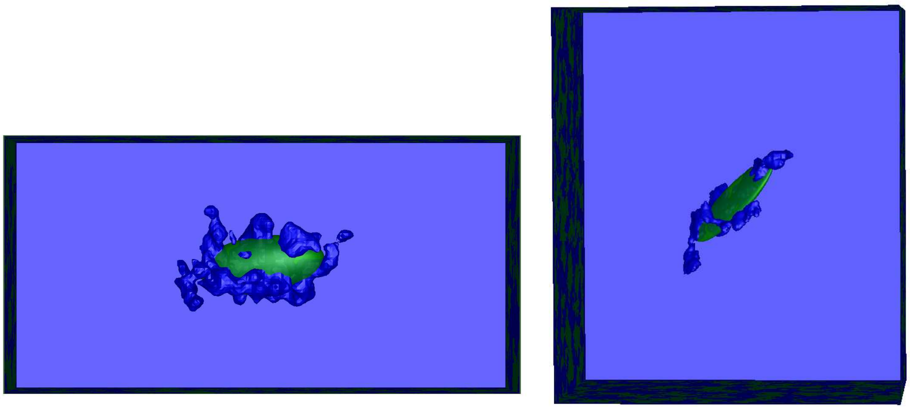

(c) Void A (d) Void AD

Figure 4.2: Initial RVEs containing real voids, superimposed with their *geometry-equivalent* ellipsoids.

Nevertheless, the observed discrepancy remains relatively low compared to the variation range of the curves over the range of interest $T_X = [-1, 0]$. The agreement for high compressive states is excellent.

Comparison of closure states of Void 3

In order to better understand the differences of closure behaviour between a real void and its equivalent ellipsoid, various void states are illustrated in Fig. 4.4 for Void 3 and its equivalent ellipsoid under $T_X = -0.4$. The field of equivalent strain is plotted at various stages of the closure, $\bar{\varepsilon}$ =0, 0.2, 0.4 and 0.5.

First, the presence of local contact can be observed at earlier stages in the case of the real void than for the ellipsoidal void. Contact can be already seen at $\bar{\varepsilon} = 0.2$ with a red arrow in Fig. 4.4c, while no contact has occurred at this instant in the case of the ellipsoid. At $\bar{\varepsilon} = 0.4$, contact can be observed at the periphery of the ellipsoidal void (red arrows in Fig. 4.4f). Note that, at $\bar{\varepsilon} = 0.4$, the ellipsoidal void is nearly closed and its volume V/V_0 is lower than 0.1 in Fig. 4.3a. At $\bar{\varepsilon} = 0.5$, the ellipsoidal void is completely closed (see Fig. 4.4h) and its volume is equal to zero.

It is noteworthy that the change of slope due to contact occurs around $\bar{\varepsilon} = 0.4$, i.e. when contact starts to occur at the periphery of the void.

In the case of real void 3, the change of slope occurs ealier. This result is the consequence

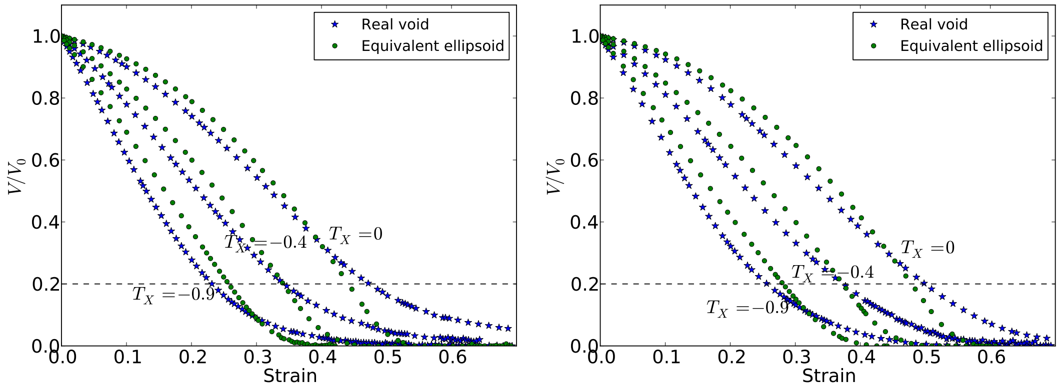

(a) Void 3 (b) Void 4

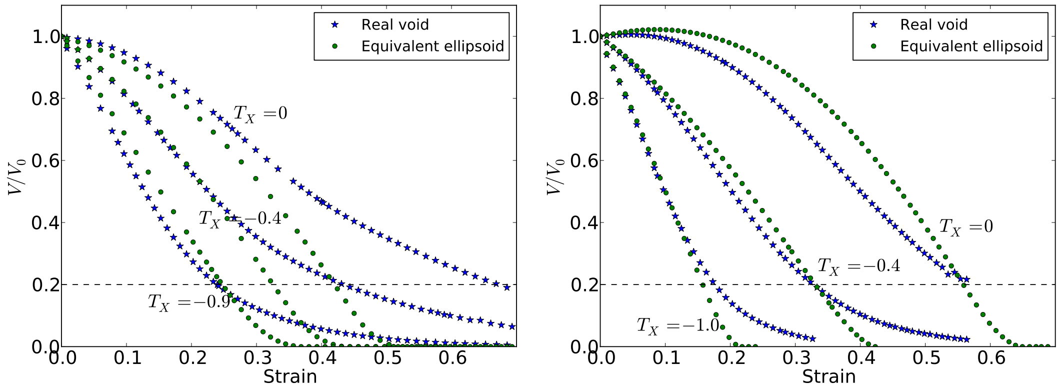

(c) Void A (d) Void AD

Figure 4.3: Void volume evolution of real voids and of their *geometry-equivalent* ellipsoids, under various stress triaxiality ratios.

of two phenomena. First, contact occurs earlier, and therefore slows down the closure rate. Secondly, as the void deforms, its shape changes due to the deformation, and the geometry-equivalence of the ellipsoid may be affected.

This effect is illustrated in the case of Void 3, with the presence of a residual cavity at the final stage. This residual cavity can be observed in Fig. 4.4g (indicated with a red circle).

In fact, this residual cavity results from an incomplete closure of a particular sub-part of the void that can be seen on the initial void (red circle in Fig. 4.4a). According to its particularly elongated and vertical aspect, the volume evolution of this sub-part is significantly lower than the rest of the void. The consequence is a decrease of the total closure rate of the void. At the final stages, as the rest of the void is quasi-entirely closed, the contribution of the sub-part is more important and becomes the main contribution to the total closure rate of the void. The slope of the void volume evolution thus drops. The change of slope is smoother than in the case of the ellipsoidal void, and occurs before $\bar{\varepsilon} = 0.4$, i.e. when the rest of the void is quasi-completely closed (green circle in Fig. 4.4e).

To better represent the real void using simple geometries, it would be possible to replace the equivalent ellipsoid by a series of several equivalent ellipsoids. Each ellipsoid could be generated using the inertia matrix of several segmented parts of the initial complex void. However, the definition of several ellipsoidal voids involves the problem of proximity of

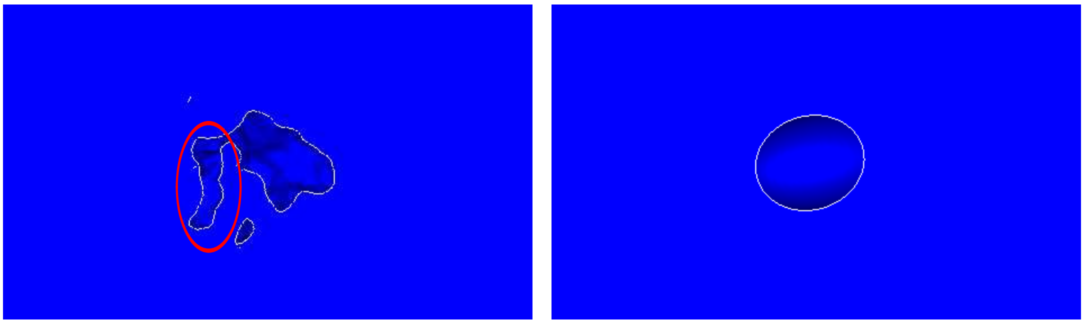

(a) Void 3 at $\bar{\varepsilon} = 0$ (b) Equivalent ellipsoid 3 at $\bar{\varepsilon} = 0$

(c) Void 3 at $\bar{\varepsilon} = 0.2$ (d) Equivalent ellipsoid 3 at $\bar{\varepsilon} = 0.2$

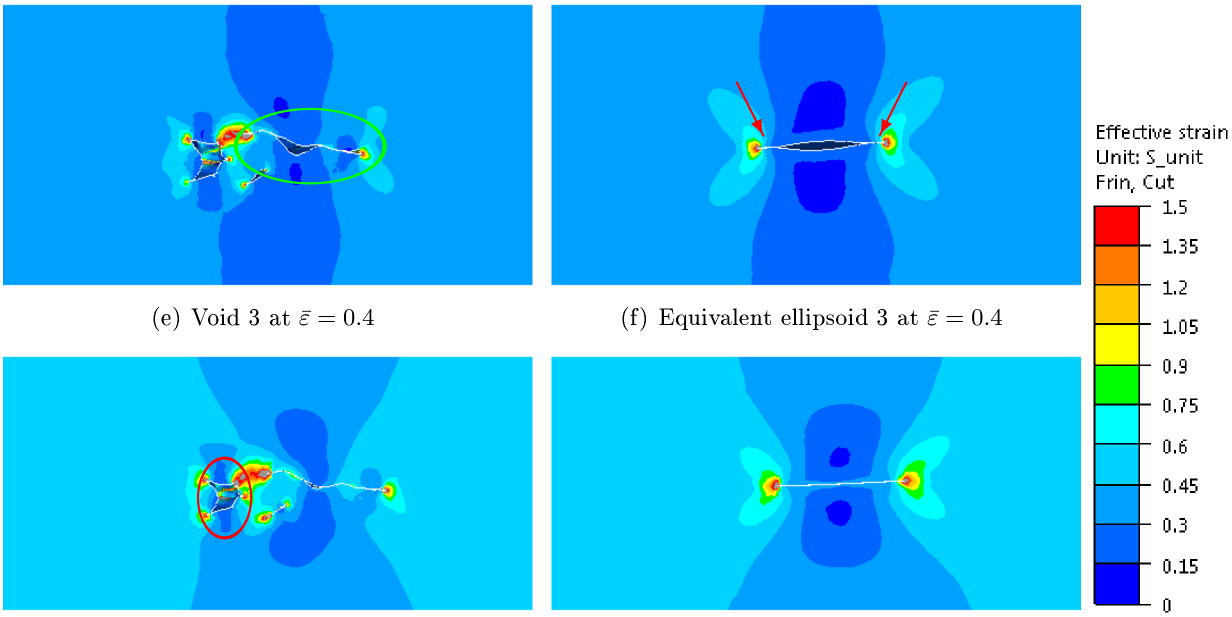

(e) Void 3 at $\bar{\varepsilon} = 0.4$ (f) Equivalent ellipsoid 3 at $\bar{\varepsilon} = 0.4$

(g) Void 3 at $\bar{\varepsilon} = 0.5$ (h) Equivalent ellipsoid 3 at $\bar{\varepsilon} = 0.5$

Figure 4.4: Field of equivalent strain around Void 3 and around its equivalent ellipsoid at various stages of deformation, under $T_X = -0.4$ and $\dot{\bar{\varepsilon}} = 1$ s^{-1}.

the voids to be considered. Within this work, using the meso-scale approach and by the choice of the value $\eta = 3$ (the RVE-to-void dimensions ratio), the case of isolated voids are exclusively considered.

In addition, the main goal of using equivalent geometries is to identify simple geometry parameters in order to supply a *mean-field* prediction model. The definition of several ellipsoids for a void would significantly complicate the quantification using geometry parameters. It would also naturally require an advanced knowledge of the actual void state. A tridimensional measurement of actual void state would systematically be required when using the model during simulation of any industrial process. Yet, it was shown that there is at present a lack of technique to systematically obtain a sufficiently accurate description of voids in large workpieces.

The definition of one equivalent ellipsoid (including aspect ratios and orientation) thus appeared as the most reasonable way to consider void morphology. It represents a good compromise between its ability to describe real voids behaviour, and its ability to be implemented in a *mean-field* model.

4.3 Parametric sensitivity study

The objective of this section is to identify the parameters that exhibit an influence on void closure and that might be considered for the prediction model. According to literature, void volume evolution is systematically presented as a function of equivalent strain [Budiansky et al., 1982, Tanaka et al., 1986, Ragab, 2004, Lasne, 2008, Zhang et al., 2009]. It is explained by the fact that plastic deformation is naturally required in order to obtain deformation of the void, and thus a possible volume evolution.

Some other parameters can be added to characterize the ability of a void to close under various conditions. Stress triaxiality ratio is often considered as a major parameter regarding void growth [e.g. Rice and Tracey, 1969, Lemaitre, 1992]. Stress triaxiality ratio is also taken into account in all existing models for void closure [Budiansky et al., 1982, Tanaka et al., 1986, Lasne, 2008, Zhang et al., 2009]. Material parameters were studied by several authors [Budiansky et al., 1982, Duva and Hutchinson, 1984] according to various hypotheses that were detailed in Chapter 1, and are considered in the model of Zhang et al. [2009].

According to literature [Lee and Mear, 1994, Kakimoto et al., 2010, Chen et al., 2010, Chen and Lin, 2013] and to previous work [Saby et al., 2013b], void morphology also appears as a key parameter in void closure mechanisms. Yet, there is at present a lack of studies regarding quantitative influence of void morphology in the literature. In this work, tridimensional morphology is studied in terms of orientation and dimensions of voids.

The influence of material parameters is first studied in terms of strain hardening and strain-rate sensitivity. Then, using an ellipsoid with arbitrary dimensions, thirteen various orientations are defined and the effect of spatial orientation is studied. Seven various ellipsoidal geometries are then defined using various aspect ratios in order to study the effect of geometry. Finally the effect of mechanical state is studied within the ranges of interest defined in Chapter 1. For each geometrical case, eight different stress triaxiality ratios are successively applied on the RVE over the range $T_X = [-1, 0]$.

4.3.1 Sensitivity to material parameters

A dependence to material behaviour was pointed out in the literature. For visco-plastic materials, Budiansky et al. [1982] and Duva and Hutchinson [1984] studied the effect of strain-rate sensitivity coefficient using various stress triaxiality conditions for the evolution of a spherical void. They used a power-law matrix without strain hardening $\sigma_0 = A\dot{\bar{\varepsilon}}^m$ and proposed an analytical dependence of void evolution to strain-rate sensitivity coefficient m. Duva and Hutchinson [1984] and Lee and Mear [1992] stated that the effect of strain-rate sensitivity for such materials can also be applied for the case of strain hardening materials obeying $\sigma_0 = A\bar{\varepsilon}^n$. In fact, the involved mechanisms are the same and the same analysis can be conducted by simply replacing $\dot{\bar{\varepsilon}}$ by $\bar{\varepsilon}$.

Li et al. [2003] and Ragab [2004] studied the effect of strain hardening on void opening, dealing with damage prediction. They found out that strain hardening mainly affects the coalescence phenomenon. A slight effect was observed on void evolution (in this case, growth) as well. This results is in good agreement with the remark from Duva and Hutchinson [1984] and Lee and Mear [1992].

In this section, the effect of strain-rate sensitivity and the effect of strain hardening are assessed using the RVE containing a sphere. The first objective is to verify the results from literature regarding the methodology of the present work. Then, as most material laws depend on both strain hardening and strain-rate sensitivity, the combined effect of both coefficients n and m is assessed as well.

A power-law equation is used, the so-called Hansel-Spittel law:

$$\sigma_0 = A\left(\bar{\varepsilon} + \varepsilon_0\right)^n \dot{\bar{\varepsilon}}^m e^{m_4/(\bar{\varepsilon}+\varepsilon_0)}, \tag{4.1}$$

where A is the material consistency (in MPa), m the strain-rate sensitivity, (n, m_4) the strain hardening and softening coefficients, and ε_0 a regularization term that enables initial rigidity of the material. This law is widely used in the field of hot metal forming. In addition, it presents the advantage of being coherent with the law used in Budiansky et al. [1982] and Tvergaard [1984] when $n = m_4 = \varepsilon_0 = 0$, as it reduces to $\sigma_0 = A\dot{\bar{\varepsilon}}^m$.

Influence of material consistency

The influence of material consistency A, was first studied. The void volume evolution was plotted for several values of A. Using an arbitrary strain hardening coefficient ($n = 1$), material laws with different values of A were compared. The stress-strain curves are illustrated in Fig. 4.5a. These curves illustrate the wide range of stresses that are obtained. The resulting void volume evolution is plotted in Fig. 4.5b. In spite of the wide range of stresses that are obtained, the closure behaviour is identical in all cases.

A second case was thus defined using another value of strain hardening coefficient $n = 0.1$. The stress-strain curves and the resulting void volume evolution are plotted in Fig. 4.5c and Fig. 4.5d, respectively. As both void volume evolutions are superimposed, the same conclusion can be made. The material consistency A has no influence on void closure. An arbitrary value $A = 1$ MPa is thus set for the following analyses.

Note that a difference can be observed in terms of void volume evolution between the cases $n = 1$ and $n = 0.1$. The influence of n is studied in a forthcoming paragraph.

Pure effect of m

First, the results of Zhang et al. [2009] in terms of void volume evolution of a spherical void were reproduced. The behaviour law that is used in the work of Zhang et al. [2009] is viscoplastic without strain hardening, given by $\sigma_0 = A\dot{\bar{\varepsilon}}^m$. As already pointed out, this law can be obtained using the Hansel-Spittel law by setting the parameters $n = m_4 = \varepsilon_0 = 0$. However, due to convergence difficulties when using rigid perfectly plastic behaviour ($n = 0$), the value $n = 0.01$ was used instead.

Several values of m were defined on the range [0.01, 1] and the resulting void volume evolutions are plotted in Fig. 4.6. The curves show very good agreement with the values obtained by Zhang et al. [2009].

The influence of m is thus verified using the present approach. The effect is rather significant on the tested range $m = [0.01, 1]$. Nevertheless, values of strain-rate sensitivities for hot metals rarely exceeds the value $m = 0.25$. Over the range $m = [0.01, 0.2]$, the influence of m on void volume evolution is moderate.

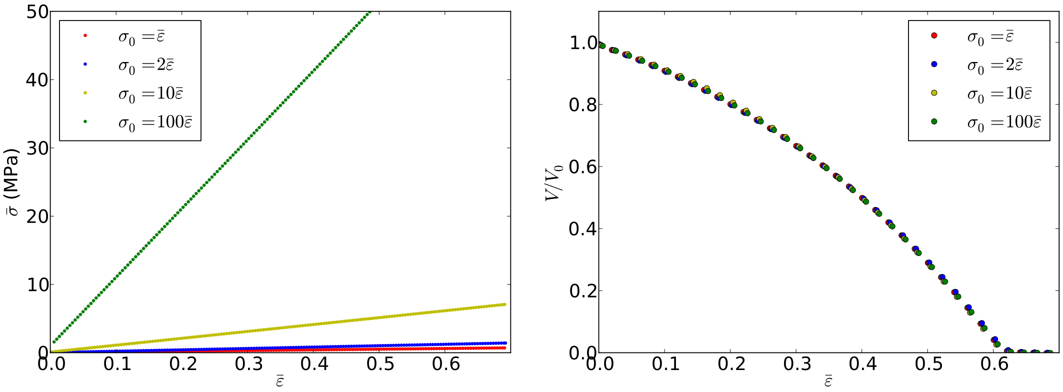

(a) Stress *vs.* strain curves, for $n = 1$ (b) Void volume evolution, for $n = 1$

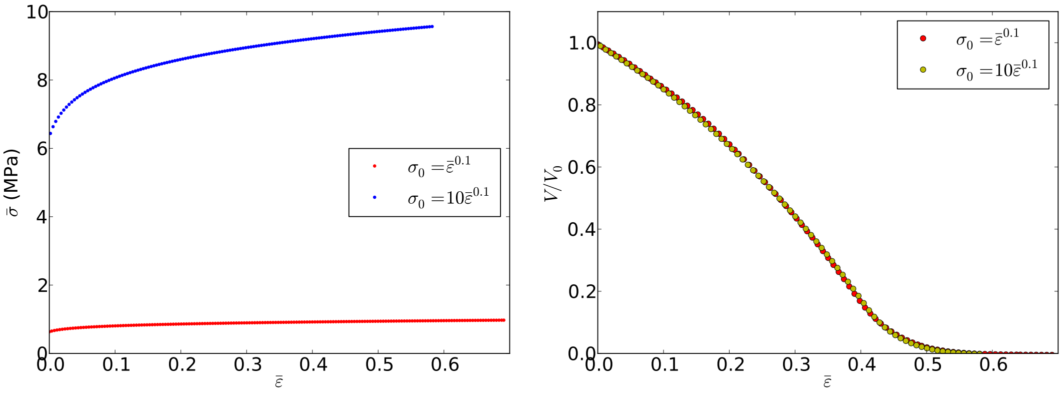

(c) Stress *vs.* strain curves, for $n = 0.1$ (d) Void volume evolution, for $n = 0.1$

Figure 4.5: Effect of material consistency A on void volume evolution, under $\dot{\bar{\varepsilon}} = 1\text{s}^{-1}$ and $T_X = -1/3$, for different values $A = \{1, 2, 10, 100\}$ MPa, using $n = 1$ in (a,b) and using $n = 0.1$ in (c,d).

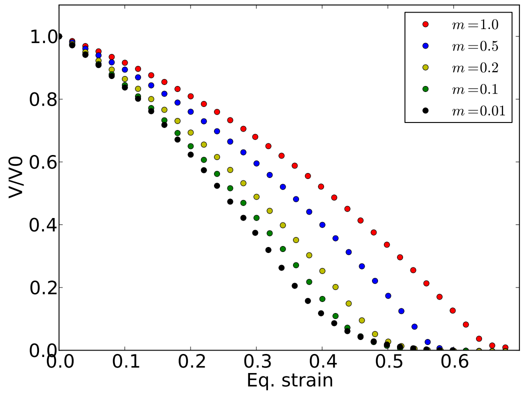

(a) Void volume evolution

Figure 4.6: Effect of strain-rate sensitivity m on void volume evolution, using $n = 0.01$ under $\dot{\bar{\varepsilon}} = 1\text{s}^{-1}$ and $T_X = -1/3$.

Pure effect of n

The pure effect of strain hardening n is now studied. The range $n = [0.01, 1]$ was initially defined to cover a large variety of material behaviours.

Yet, hot metals often exhibit softening behaviours. Softening can be introduced in the Hansel-Spittel law using negative values of n. An additional case with the values $(n, m_4) = (-0.1, -0.001)$ was thus introduced in order to qualitatively represent a material with softening behaviour. Note that in that special case, a non-zero value of m_4 was used in order to avoid the presence of an infinite value of σ_0 at $\bar{\varepsilon} = 0$. (It was verified that the introduction of the non-zero value of m_4 has no significant impact on the material behaviour.) Although this special case may not physically represent a typical behaviour (see Fig. 4.8), it is a simple qualitative example exhibiting a negative slope of the stress–strain curve and is comparable to the other cases.

Throughout this paragraph, the effect of strain-rate sensitivity is ignored by setting the value $m = 0$. The behaviour law is thus reduced to $\sigma_0 = \bar{\varepsilon}^n$.

The stress-strain curves are presented in Fig. 4.7a and illustrate the large variety of material behaviours that is considered. The resulting void volume evolutions are plotted in Fig. 4.7b.

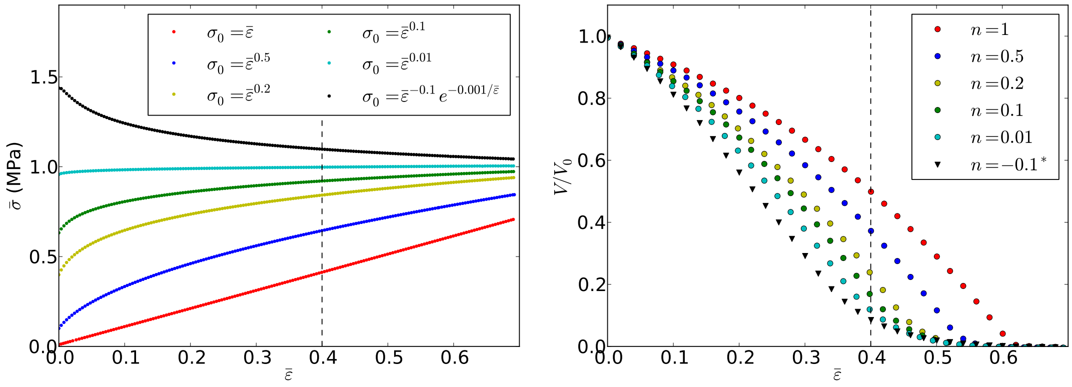

(a) Stress *vs.* strain curves

(b) Void volume evolution

Figure 4.7: Effect of strain hardening on the evolution of a spherical void, using strain-rate sensitivities $m = 0$ under $\dot{\bar{\varepsilon}} = 1\text{s}^{-1}$ and $T_X = -1/3$ (*For negative strain hardening values, the value $m_4 = -0.001$).

The curves indicate that strain hardening has a non-negligible effect on void volume evolution on the tested range $n = [-0.1, 1]$. Void volumes were measured at $\bar{\varepsilon} = 0.4$ for the boundary cases $n = -0.1$ and $n = 1$. They exhibit a difference of about 40% on void closure. This difference tends to decrease at the final stages, as the slope drops due to internal contact.

The effect of internal contact is illustrated in Fig. 4.8. In the case of a linear material $n = 1$, the shape remains ellipsoidal throughout the deformation. When reducing strain hardening n, the curvature is changed and contact between internal surfaces appears earlier. This effect induces a faster void closure at the beginning, and, on the contrary, reduces the final slope to complete closure.

However, it is noteworthy that the required deformation for complete closure is comparable for all cases. The value of strain hardening for hot metal rarely exceed the value $n = 0.2$. The difference reduces to about 15% over the range $n = [-0.1, 0.2]$.

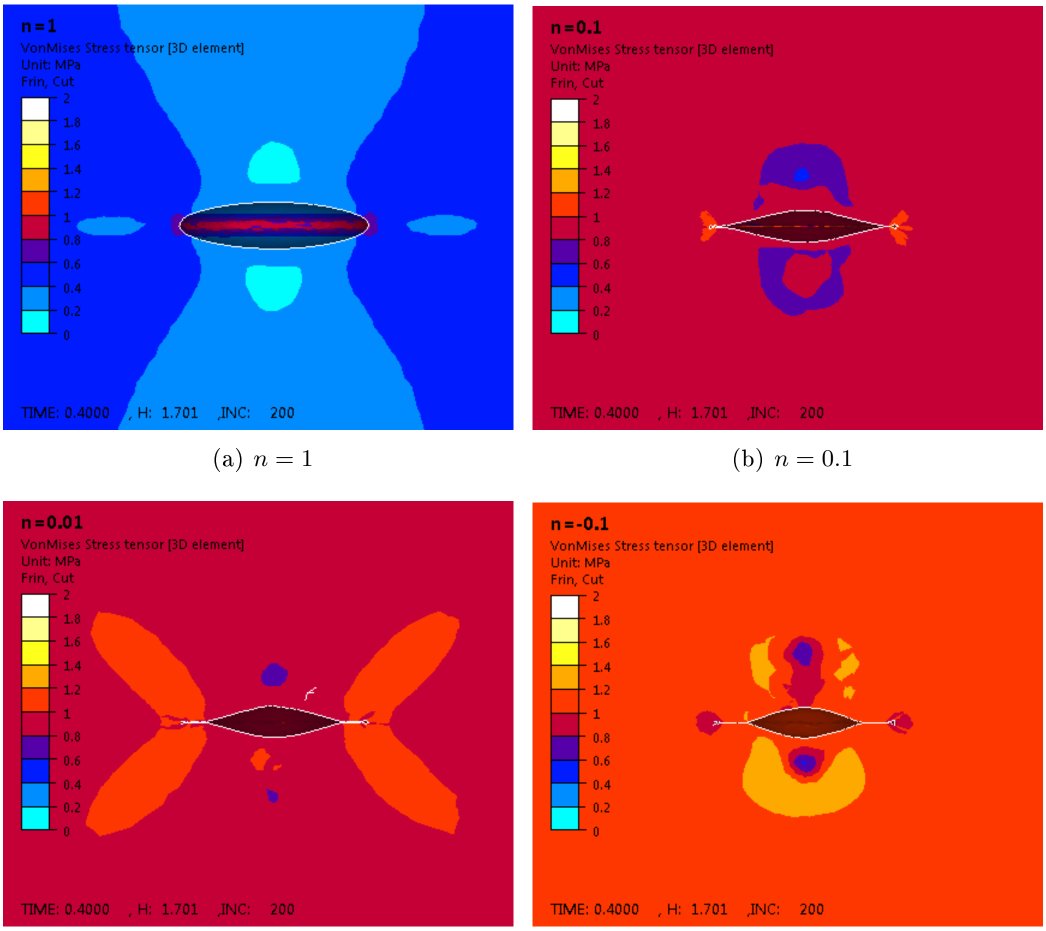

(a) $n = 1$

(b) $n = 0.1$

(c) $n = 0.01$

(d) $n = -0.1$

Figure 4.8: Cutting plane illustrating the von Mises equivalent stress field, for an initially spherical void at $\bar{\varepsilon} = 0.4$, under $\dot{\bar{\varepsilon}} = 1\text{s}^{-1}$, $T_X = -1/3$ and for different values of strain hardening coefficient n.

When comparing this effect to the ones described later regarding void morphology or stress triaxiality ratio, the influence of strain hardening can be considered as second order within the considered range $n = [0.01, 0.2]$.

The result regarding the negative value $n = -0.1$ also suggests that the general tendency that is obtained for the influence of n seems coherent over negative values. Similarly, the curve using $n = -0.1$ shows a relative difference around 5% with the case $n = 0.01$, and the required deformation for complete closure remains similar.

As mentioned by Lee and Mear [1992], the effect of strain hardening and the effect of strain-rate sensitivity are driven by the same mechanisms. The resulting influence of n can therefore be used for the one of m and vice-versa.

Combined effects of n and m

The analysis was further conducted to the case of materials that present both strain hardening and strain-rate sensitivity ($n \neq 0$ and $m \neq 0$). Let us now consider the value of the sum $n+m$. Three values for the sum were chosen: $n+m = 1$, $n+m = 0.5$ and $n+m \approx 0$. The results of simulations are plotted in Fig. 4.9. For each value of $n + m$, two different combinations were used and are indicated in the plot.

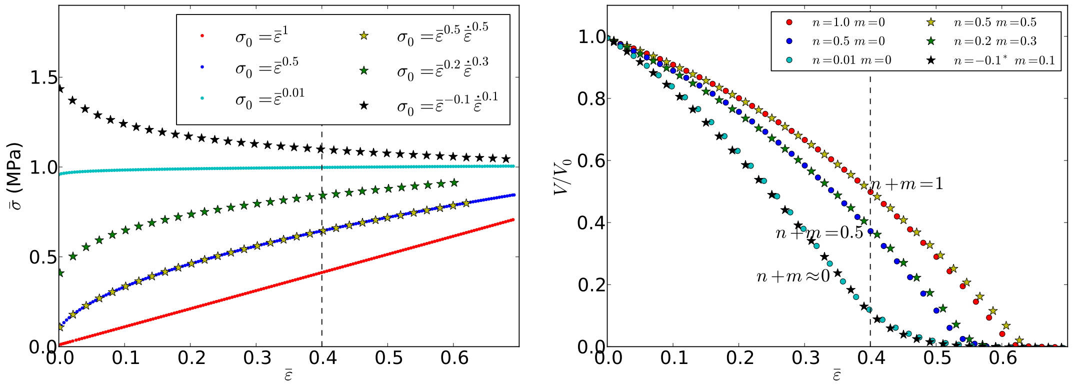

(a) Stress *vs.* strain curves

(b) Void volume evolution

Figure 4.9: Effect of the sum $m+n$, under $\dot{\bar{\varepsilon}} = 1\text{s}^{-1}$ and $T_X = -1/3$ (*For negative strain hardening values, the value $m_4 = -0.001$).

The superimposed curves suggest that the effects of n and m are in fact additive. For each value of $n+m$, both void volume evolutions are identical, although the stress-strain curves are significantly different. This is due to the fact that the effect of strain hardening is visible on the stress-strain curve, whereas the effect of strain-rate sensitivity is not visible as all curves are plotted for a common value of strain-rate $\dot{\bar{\varepsilon}} = 1\text{s}^{-1}$. Note that the void volume evolution for the case $(n, m) = (0.01, 0)$ that was used in first approximation for a quasi-perfectly plastic material, is identical to the evolution in the case $(n, m) = (-0.1, 0.1)$, as the sum $m+n$ is approximately equal to zero. This remark illustrates the validity of the observed additivity of the effects, even at the bounds of the range of tested values.

The value of $n+m$ might thus be seen as a single material parameter regarding its influence on void closure.

4.3.2 Sensitivity to void morphology

In this section, the Hansel-Spittel law (Eq. 4.1) is used with constants that are typical for the behaviour of hot steel:

- $A = 31.23$ MPa is the material consistency at the given temperature,
- $m = 0.153$ the strain-rate sensitivity,
- $n = -0.135, m_4 = -0.055$ the strain hardening/softening coefficients, and
- $\varepsilon_0 = 0.025$ a regularization term that enables initial rigidity of the material.

The stress–strain curve is illustrated in Fig. 4.10.

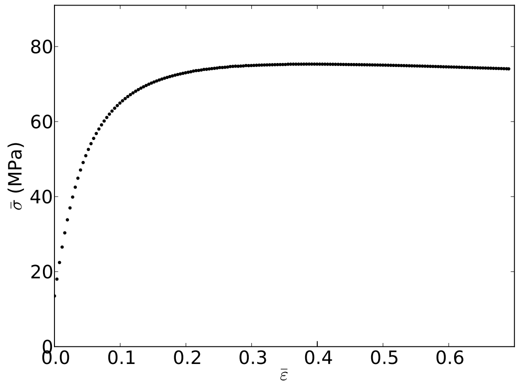

Figure 4.10: Stress-strain curve of the the material used for the calibration (Eq. 4.1).

Sensitivity to void orientation

Let us define the canonical basis $(\vec{e_x}, \vec{e_y}, \vec{e_z})$. The three principal vectors of deformation $(\vec{e_1}, \vec{e_2}, \vec{e_3})$ can be obtained by diagonalizing the strain-rate tensor. Similarly, the three principal vectors for the void can be obtained by diagonalization of the inertia matrix, and the principal vectors are called $(\vec{u_1}, \vec{u_2}, \vec{u_3})$. An example is given in Fig. 4.11 for the particular case $(\vec{e_1}, \vec{e_2}, \vec{e_3}) = (-\vec{e_z}, \vec{e_y}, \vec{e_x})$.

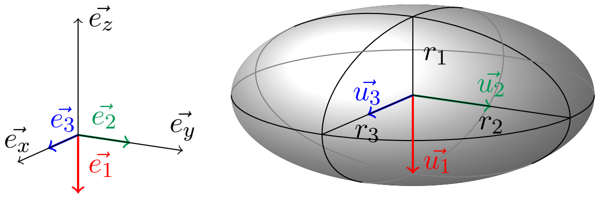

Figure 4.11: Definition of the orientation using void's principal axes $(\vec{u_1}, \vec{u_2}, \vec{u_3})$.

According to the current methodology (that was defined in Chapter 2), void closure is studied at the RVE-scale. Let us recall that the mechanical state at the RVE-scale is imposed using a vertical velocity $\vec{V_z}$ and lateral stresses σ_{xx} and σ_{yy}. As a consequence, the main deformation direction remains constant during all RVE simulations and $\vec{e_1} = -\vec{e_z}$, as it is illustrated in Fig. 4.11. Vertical axisymmetry is also assumed by the choice of $\sigma_{xx} = \sigma_{yy}$ (defined in Chapter 2). This assumption will be discussed later in Chapter 5. The obtained results are therefore invariant by rotation around the z-axis, i.e. around $\vec{e_1}$.

Yet, in real process conditions, the main deformation direction may vary during process, and the final prediction model must be able to take into account this effect. It is thus chosen to define the orientation of a void with respect to the main deformation direction $\overrightarrow{e_1}$, using parameters (p_1, p_2, p_3) such as:

$$\begin{aligned} p_1 &= (\vec{u_1}.\vec{e_1})^2, \\ p_2 &= (\vec{u_2}.\vec{e_1})^2, \\ p_3 &= (\vec{u_3}.\vec{e_1})^2, \end{aligned} \tag{4.2}$$

This definition verifies $p_1 + p_2 + p_3 = 1$.

When using the final *mean-field* prediction model, it will thus be possible (at each integration point) to update the orientation parameter according to the local current deformation state.

In Fig. 4.11, the particular configuration $(1, 0, 0)$ is illustrated, meaning that the principal direction $\vec{u_1}$ of the ellipsoid is colinear with the principal deformation direction $\vec{e_1}$.

Orientation cases Several orientations were defined in order to study the influence of orientation on void closure. A given ellipsoid of dimensions $r_2/r_1 = 2$ and $r_3/r_1 = 1.5$ was used. The cases presented in Fig. 4.12 and 4.13 were obtained by rotating the void around the $\vec{e_y}$ axis and the $\vec{e_x}$ axis, respectively.

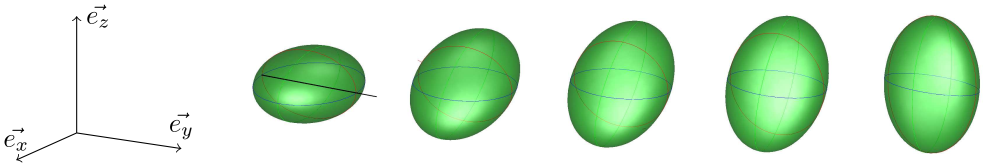

Angle (degrees)	0	30	45	60	90
Parameters (p_1, p_2, p_3)	(1, 0, 0)	(0.75, 0, 0.25)	(0.5, 0, 0.5)	(0.25, 0, 0.75)	(0, 0, 1)

Figure 4.12: Various ellipsoids, obtained by rotation around $\vec{e_y}$.

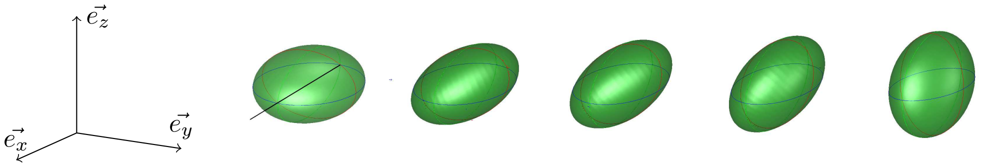

Angle (degrees)	0	30	45	60	90
Parameters (p_1, p_2, p_3)	(1, 0, 0)	(0.75, 0.25, 0)	(0.5, 0.5, 0)	(0.25, 0.75, 0)	(0, 1, 0)

Figure 4.13: Various ellipsoids, obtained by rotation around $\vec{e_x}$.

Void volume evolutions The void volume evolutions for each series of cases are presented in Fig. 4.14. The orientation is given using the couple of values (p_1, p_2), as p_3 can be deduced from $p_3 = 1 - p_1 - p_2$. From the curves, it can be seen that orientation has a significant influence on void volume evolution. Three particular cases can be pointed out: the case $(p_1, p_2) = (1, 0)$, the case $(p_1, p_2) = (0, 1)$ and the case $(p_1, p_2) = (0, 0)$. Each case corresponds to a compression along $\vec{u_1}$, $\vec{u_2}$ and $\vec{u_3}$, respectively. The curves indicate that compression along $\vec{u_1}$ involves the fastest void closure, as the void is compressed along its smallest dimension r_1. On the contrary, compression along $\vec{u_3}$ involves the slowest void closure, as compression is made along the void's longest dimension r_3. These two cases can be seen as upper and lower bounds for this ellipsoid. Void evolution under compression along $\vec{u_2}$ is naturally between both boundaries, as well as for any other orientation.

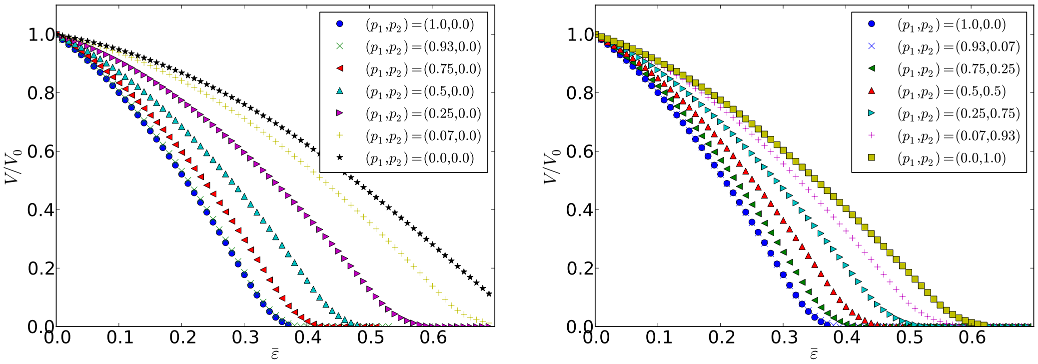

(a) Rotation around $\vec{e_y}$ $(p_2 = 0)$

(b) Rotation around $\vec{e_x}$ $(p_3 = 0)$

Figure 4.14: Influence of orientation parameters.

Sensitivity to void's aspect ratios

The upper and lower bounds obtained previously using a given ellipsoid evidently depends on the initial geometry. In order to assess the influence of geometry on these bounds, several ellipsoids were defined according to various aspect ratios. The aspect ratios are defined by $\left(\frac{r_3}{r_1}, \frac{r_2}{r_1}\right)$.

Ellipsoids cases using various aspect ratios Various aspect ratios were used and are presented in Fig. 4.15 (using the orientation $(p_1, p_2) = (1, 0)$). Ellipsoids A and B are prolate, as $r_1 = r_2 < r_3$. Ellipsoids C and D are oblate, as $r_1 < r_2 = r_3$. Ellipsoids E and F are defined such as $r_1 < r_2 < r_3$. For each ellipsoid, the RVE was generated and identical deformation conditions were applied in order to obtain void volume evolutions along the three principal directions of each ellipsoid.

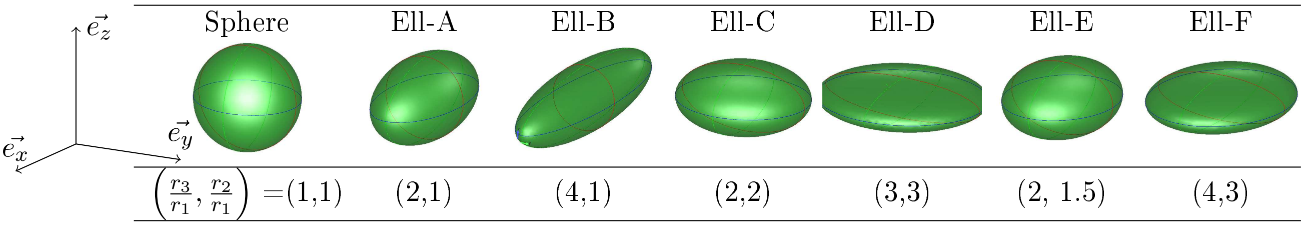

Figure 4.15: Various ellipsoids with given aspect ratio $\left(\frac{r_3}{r_1}, \frac{r_2}{r_1}\right)$, for $(p_1, p_2) = (1, 0)$.

Void volume evolutions The void volume evolutions are given in Fig. 4.16. In the case of ellipsoids A, B, C and D, two of the three curves are superimposed. This is due to the particular symmetry of such geometries. For the prolate ellipsoid A, identical behaviours are obtained for compressions along the $\vec{u_1}$ and $\vec{u_2}$ axes. This result is observed for the prolate ellipsoid B as well. For the oblate ellipsoids C, identical behaviours are obtained for compressions along the $\vec{u_2}$ and $\vec{u_3}$ axes. It is also is observed for the oblate ellipsoid D. For ellipsoids E and F, the closure rates along one direction depends on the geometry.

By comparing the pairs of ellipsoids (A, B), (C, D) and (E, F), it is observed that larger aspects ratios tend to increase the difference in terms of closure rate between the minor axis and the major axis.

By comparing the triplet of ellipsoids (A, C, E) in the orientation $(1, 0)$, different closure rates are observed, although their first aspect ratio are identical $\frac{r_3}{r_1} = 2$. This remark shows that void closure not only depends on one aspect ratio but also on the tridimensional morphology.

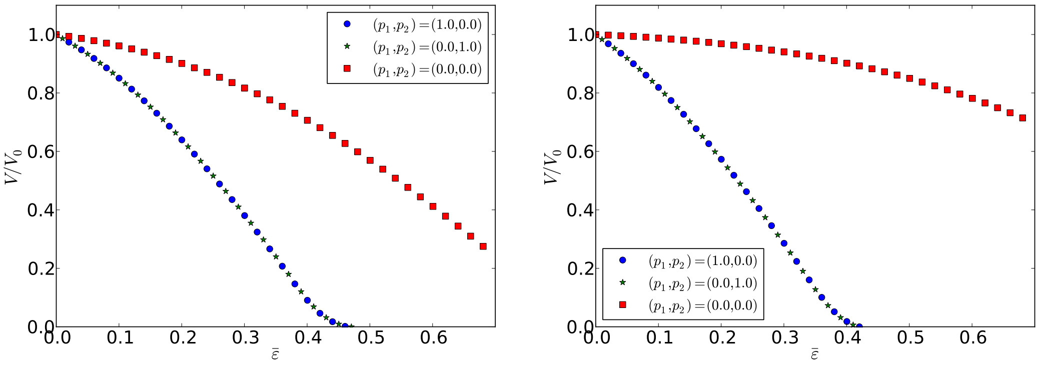

(a) Ellipsoid A (b) Ellipsoid B

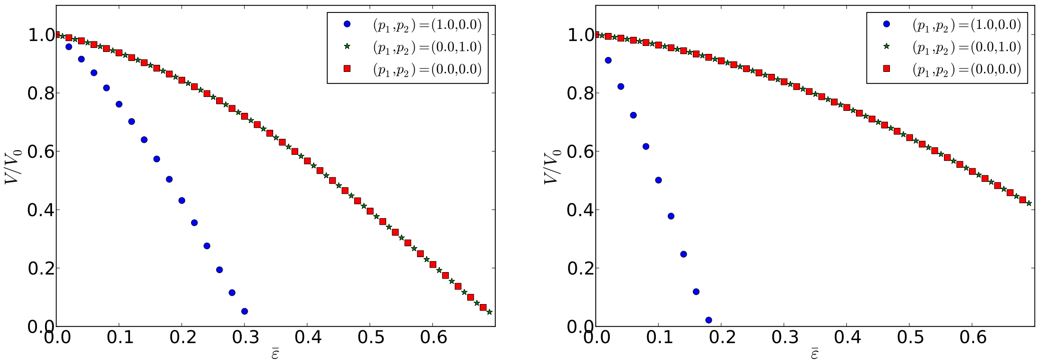

(c) Ellipsoid C (d) Ellipsoid D

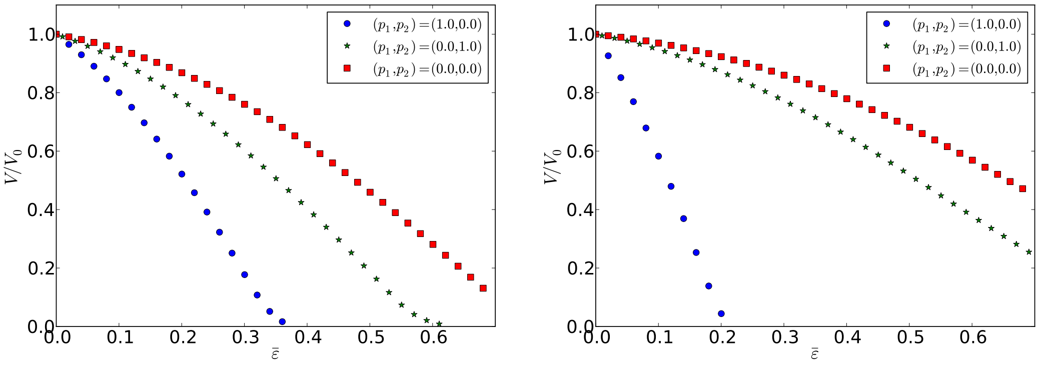

(e) Ellipsoid E (f) Ellipsoid F

Figure 4.16: Void volume evolution for various initial geometries, and for three different orientations.

Final stages of closure When looking at the curves in Fig. 4.14, 4.16 and 4.18, it can be observed that void volume generally exhibits a slight change of slope at final stages. This phenomenon was already observed in section 4.2, and is due to the presence of contact between internal void surfaces at the final stage of closure, as shown in Fig. 4.17. This phenomenon was also observed by Zhang et al. [2009] for spherical voids.

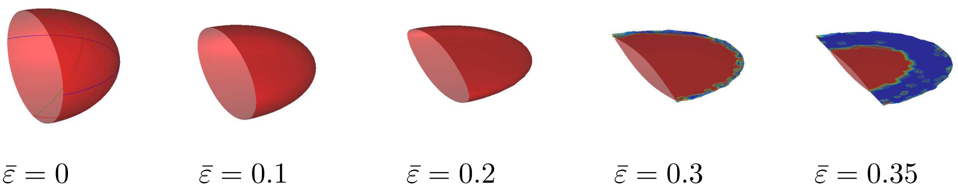

Figure 4.17: Evolution of the void Ell-E during closure for the orientation $(p_1, p_2) = (1, 0)$ under $T_X = -1/3$. The blue color shows the contact between internal surfaces.

4.3.3 Sensitivity to mechanical state

Influence of stress triaxiality ratio on the closure of Ellipsoid E

As described in section 2.3, boundary conditions are applied in order to impose a constant stress triaxiality ratio. Void closure was studied under various stress triaxiality ratios and the curves are presented in Fig. 4.18.

The curves confirm that compressive stress states have a favorable effect on void closure. This result is in good agreement with the conclusions obtained in Chapter 1 regarding the bibliographic state-of-the-art. The studies using a macroscopic approach concluded that process conditions (e.g. die shapes, temperature gradients, friction) must be chosen in order to induce more compressive states in the material. Empirical models, as well as analytical and semi-analytical models that are described in Chapter 1, systematically include a dependence to stress triaxiality ratio. It is thus verified here, and the value of T_X will be considered in the prediction model within the present work.

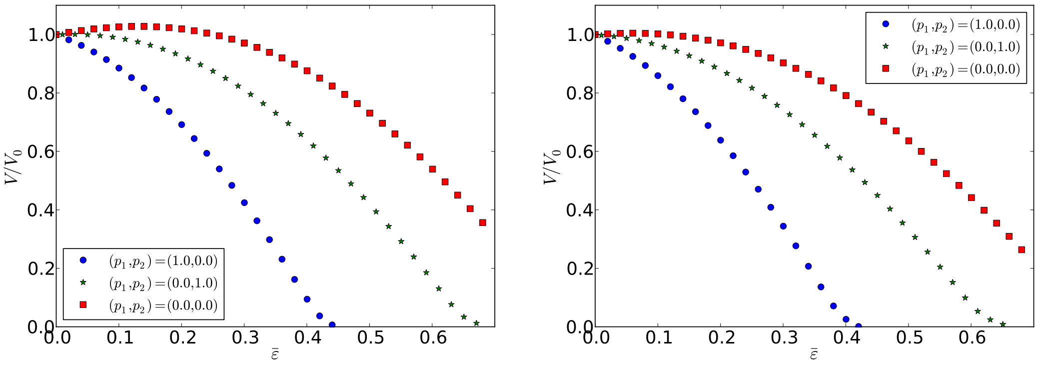

(a) $T_X = 0$ (b) $T_X = -0.1$

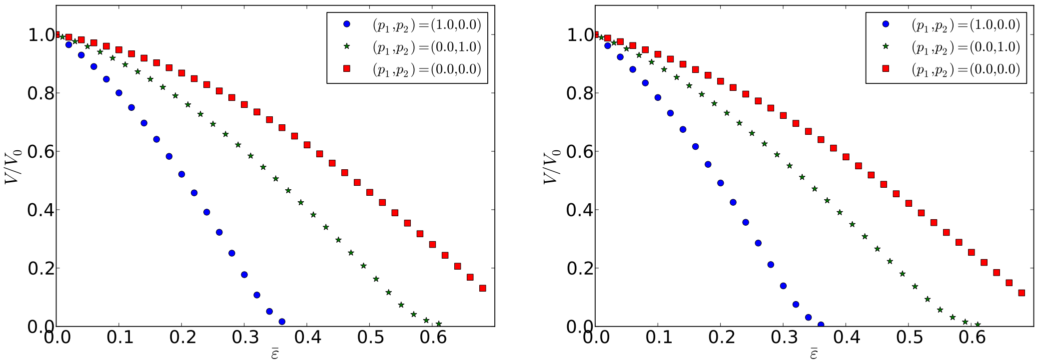

(c) $T_X = -1/3$ (d) $T_X = -0.4$

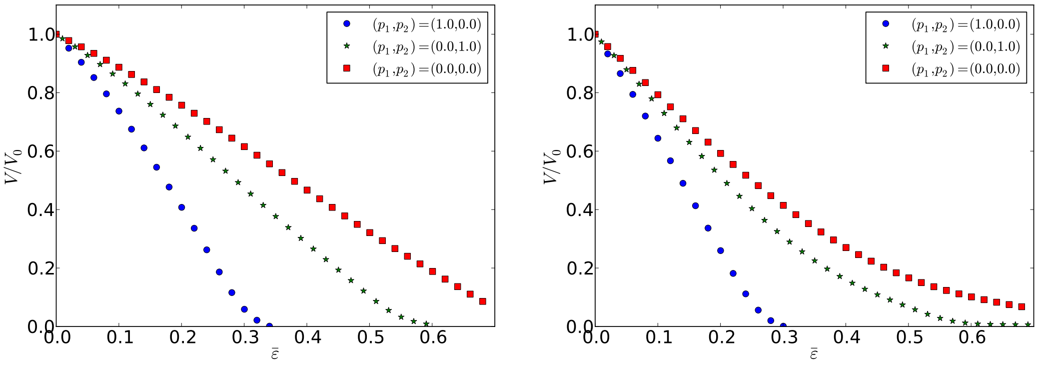

(e) $T_X = -0.6$ (f) $T_X = -1.0$

Figure 4.18: Void volume evolutions of Ell-E, under various values of stress triaxiality ratios.

Influence of remote strain-rate and stress triaxiality ratio on a real void

The notion of remote strain-rate deals with the velocity boundary condition that is vertically applied on the RVE, as it is described in section 2.3.2. The influence of remote strain-rate was tested in the case of real void coming from X-ray microtomography (defined in Chapter 2). More details about this configuration can be found in Saby et al. [2013b].

Description of the cases The RVE containing the real void A (obtained from X-ray microtomography from the steel sample JD20, previously described in section 2.5.1) was used to perform a sensitivity study to both strain-rate and stress triaxiality ratio. Similarly, a constant strain-rate was applied and the stress triaxiality ratio was controlled during deformation. Different values of stress triaxiality ratios over the range [-0.82, -0.15] and various values of strain-rate over the range [0.001, 100] s^{-1} were used.

Void volume evolutions Void volume evolutions are plotted in Fig. 4.19 for three values of T_X and three values of $\dot{\bar{\varepsilon}}$. The curves confirms the strong influence of stress triaxiality ratio on void closure. This result is verified for all tested strain rates.

For each value of stress triaxiality ratio, the quasi-perfect superposition of the curves at various strain-rates indicates that strain-rate has no influence on void closure.

Local mechanical state around the void To explain this result, the field of equivalent stress around the voids is illustrated in Fig. 4.20 for several tested values of strain-rate. Due to the strain-rate sensitivity of the material (m=0.153 in the present case), the global flow stress varies from about 24 MPa to 140 MPa over the range of tested strain-rates. These values were measured at a position that is sufficiently far from the void to be considered as homogeneous. The positions are indicated in Fig. 4.20, for each case, at the bottom-right corner. This measured value is approximately equal to the remote value, as it is not affected by the local modifications of the mechanical field around the void.

Fig. 4.20 also illustrates the shape of the void at $\bar{\varepsilon} = 0.24$. For the four presented cases, the shape is identical. This result is coherent with the identical void volume evolution of the different cases.

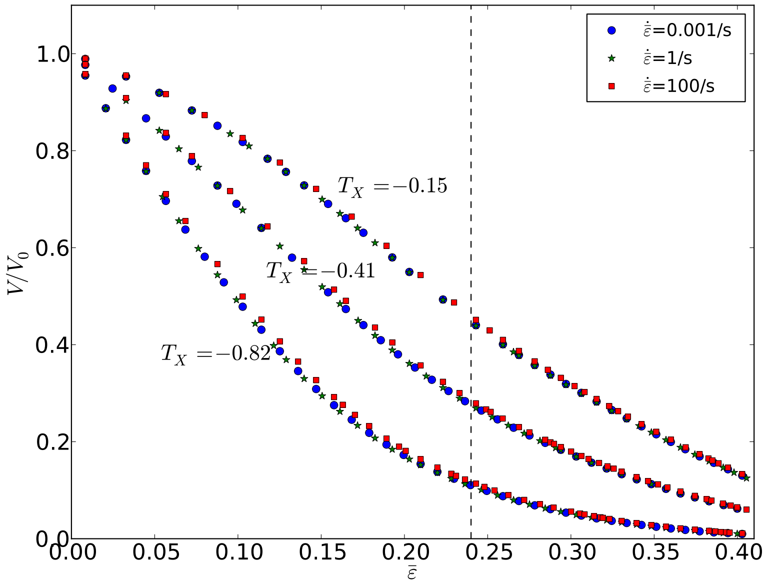

Figure 4.19: Void volume evolution of void A under five constant stress triaxiality ratios, and for six values of strain-rate.

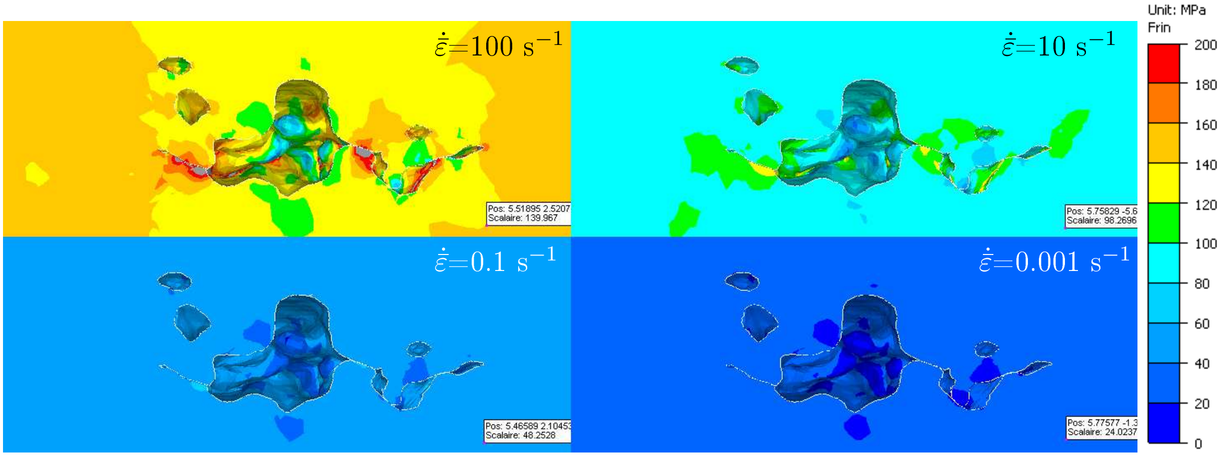

Figure 4.20: Von Mises equivalent stress around void A at $\bar{\varepsilon} = 0.24$ under $T_X = -0.41$, for various strain-rate values.

4.4 Prediction model for void closure

This section presents the construction steps for the new prediction model for void closure. First, the choice of an analytical function that is able to model void closure as a function of equivalent strain is presented. Then the dependence to void orientation is quantitatively studied in order to extend the analytical function to any orientation of ellipsoid (for a given ellipsoid). The dependence to aspect ratios is then quantitatively studied in order to extend the analytical function to any ellipsoid (geometry and orientation). Finally, the dependence to stress triaxiality ratio is quantitatively studied in order to extend the analytical function to any ellipsoid and to any stress triaxiality ratio. The final equation is verified using the four *geometry-equivalent* ellipsoids (from real observations) that were presented in the previous section.

The analytical functions are calibrated using the RVE simulations presented in the previous section using regression analysis. The quality of the regressions is systematically illustrated using the R^2–correlation coefficient. The final difference that is obtained between the calibrated prediction model and the reference states (from RVE simulations) is given using the L^2–norm.

4.4.1 Choice of an analytical function

A relationship between void volume and equivalent strain is sought here. According to the parabolic aspects of the curves obtained in the previous section for various geometries and under various conditions, a second order polynomial function is proposed. The analytical function can be expressed as:

$$V/V_0 = A + B\bar{\varepsilon} + C\bar{\varepsilon}^2. \tag{4.3}$$

where A, B and C are fitting parameters. The initial condition leads to $A = 1$. This expression can be reduced to a linear expression:

$$\frac{V/V_0 - 1}{\bar{\varepsilon}} = B + C\bar{\varepsilon}, \tag{4.4}$$

in which the two coefficients B and C can be fitted using linear regression analysis. This is of great interest regarding the large quantity of parameters to be assessed within this study.

As pointed out in the previous section, the final void evolution may not be representative of void closure in the general case, as it is driven by the particular ellipsoidal shape. As a consequence, interest is rather focused on the range $V/V_0 = [0.2, 1]$. Values below the threshold value 0.2 will therefore be ignored in the regression analysis (see example in Fig. 4.21). The first 10 increment steps are ignored as well due to the presence of a vertical asymptote at $\bar{\varepsilon} = 0$ on the linearized curves, and in order to accurately capture the linear evolution using linear regression analysis.

4.4.2 Dependence to orientation

For all orientation cases, the curves of void volume were fitted using linear regression analysis. It is illustrated for several particular orientations in Fig. 4.21. Values of B and C coefficients were obtained with very good correlation (using R^2-correlation coefficients). The values for B and C are plotted with dots in Fig. 4.22 versus orientation parameters p_1 and p_2. Each coefficient exhibits a linear dependence to orientation parameters. Linear regression is thus used to fit this dependence and R^2−correlation showed very good values as well. As a consequence, the following expression is proposed:

$$\begin{aligned} B &= p_1 B^{\vec{u_1}} + p_2 B^{\vec{u_2}} + p_3 B^{\vec{u_3}} \\ C &= p_1 C^{\vec{u_1}} + p_2 C^{\vec{u_2}} + p_3 C^{\vec{u_3}} \end{aligned} . \tag{4.5}$$

In this equation, $B^{\vec{u_i}}$ and $C^{\vec{u_i}}$ are geometry-dependent parameters that correspond to void evolution under compression along $\vec{u_i}$. They can be obtained using the three particular cases $(p_1, p_2) = (1, 0)$, $(p_1, p_2) = (0, 1)$ and $(p_1, p_2) = (0, 0)$, respectively. According to the analytical expression in Eq. 4.5, for a given ellipsoid, knowing its volume evolution along its three principal directions is sufficient for predicting its volume evolution in any random orientation. The values of $B^{\vec{u_i}}$ and $C^{\vec{u_i}}$ are thus obtained from the regression shown in Fig. 4.21.

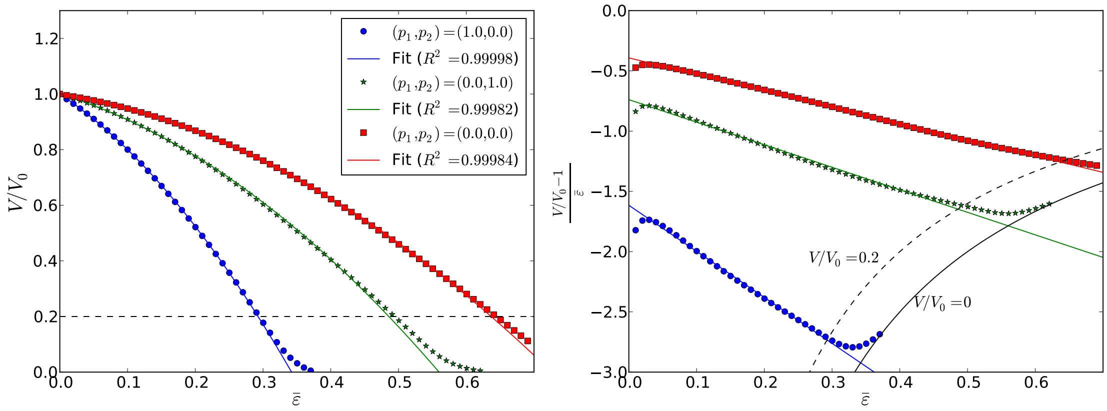

Figure 4.21: Curve fitting (with R^2−correlation factor) performed on RVE results (Ell-E for the three principal orientations) by linear regression using the linearized expression (Eq. 4.4).

Based on $B^{\vec{u_i}}$ and $C^{\vec{u_i}}$ coefficients that were obtained with Ell-E for $(p_1, p_2) = \{(1, 0); (0, 1); (0, 0)\}$, the validity of Eq. 4.5 was checked using randomly oriented ellipsoids. Four orientations were defined using successive rotations around $\vec{e_x}$ and $\vec{e_y}$. The resulting pairs of orientation parameters (p_1, p_2) are $(0.56, 0.19)$, $(0.19, 0.56)$, $(0.19, 0.06)$ and $(0.06, 0.19)$. The model was computed using Eqs. 4.3 and 4.5 for each orientation. A comparison is given in Fig. 4.23, together with bound cases $(1, 0)$ and $(0, 0)$. For the six curves, a very good agreement was obtained between the model and the values obtained from RVE simulations. The average L^2–norm error was computed over the whole deformation, between the RVE-values and the model in Eq. 4.5, and remains under 3% for all cases. As a consequence, the model is suitable to take into account the effect of orientation. Together with Eq. 4.3 the model is suitable for predicting void evolution for any orientation.

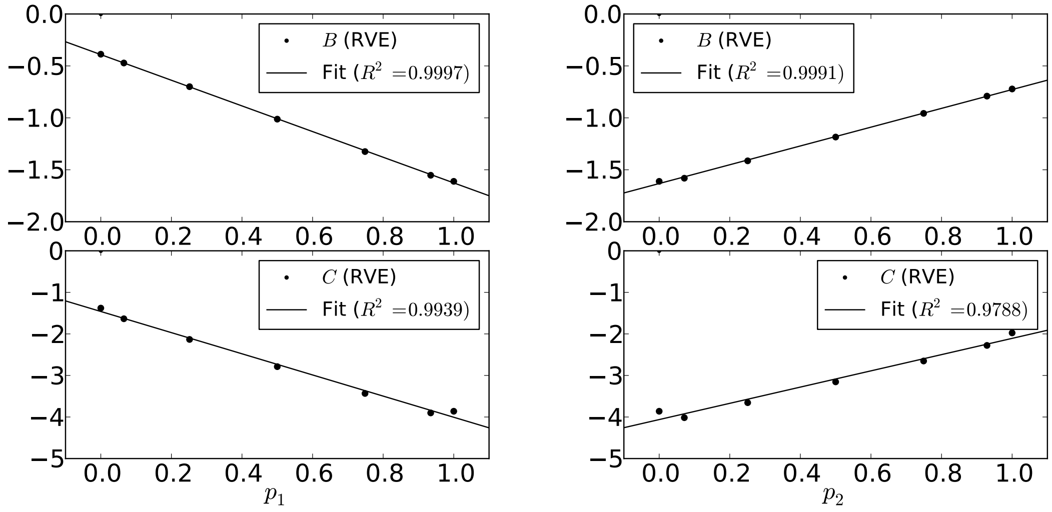

(a) $p_2 = 0$ (b) $p_3 = 0$

Figure 4.22: Influence of orientation parameters on B and C coefficients.

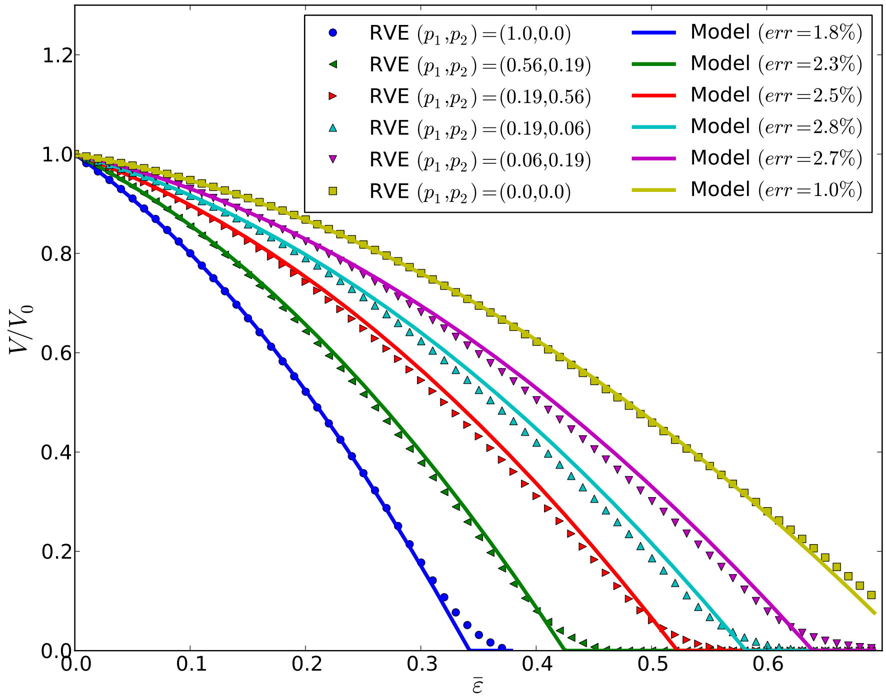

Figure 4.23: Void volume evolution obtained using RVE simulations (dots) and model predictions (lines) given by Eqs. 4.3 and 4.5, for various orientations, with average L^2-norm error.

4.4.3 Dependence to geometry

The dependence to aspect ratios is now studied using the same methodology as described above. Void evolution coefficients B and C are obtained from curves in Fig. 4.16 using linear regression analysis. The linearized form of void volume evolution is used as well, such as shown in Fig 4.24. The R^2-correlation coefficient was excellent again, meaning that Eq. 4.3 is suitable to model closure of ellipsoidal voids.

For each ellipsoid, three coefficients $B^{\vec{u_i}}$ (and $C^{\vec{u_i}}$) were obtained, respectively along their three principal directions $i = \{1, 2, 3\}$. The values obtained for $B^{\vec{u_i}}$ (and $C^{\vec{u_i}}$) are plotted in Fig. 4.25 versus a geometry parameter defined as

$$\gamma_i = \frac{\sqrt[3]{V_0}}{r_i}. \tag{4.6}$$

This parameter represents an apparent geometry parameter according to the $\vec{u_i}$ direction. It is a non-dimension parameter that considers tridimensional features of the geometry with respect to each principal direction. For example, in the case of the first principal direction $\vec{u_1}$, the parameter can be expressed as:

$$\gamma_1 = \frac{\sqrt[3]{V_0}}{r_1} = \frac{\sqrt[3]{\frac{4\pi}{3} r_1 r_2 r_3}}{r_1} = \sqrt[3]{\frac{\frac{4\pi}{3} r_1 r_2 r_3}{r_1^3}} = \sqrt[3]{\frac{4\pi}{3} \frac{r_2}{r_1} \frac{r_3}{r_1}}. \tag{4.7}$$

The γ_1 parameter is proportional to the cubic root of the product of aspect ratios. In this manner, this parameter contains the information relative to tridimensional geometry. This parameter was chosen as it provided a bijective relation with the $B^{\vec{u_i}}$ and $C^{\vec{u_i}}$ coefficients, regardless of the value of i.

As expected, due to axisymmetrical features, it is verified that for prolate ellipsoids, $B^{\vec{u_1}} = B^{\vec{u_2}}$ and $C^{\vec{u_1}} = C^{\vec{u_2}}$. Regarding oblate ellipsoids it is found that $B^{\vec{u_2}} = B^{\vec{u_3}}$ and $C^{\vec{u_2}} = C^{\vec{u_3}}$. Finally, for the spherical void $B^{\vec{u_1}} = B^{\vec{u_2}} = B^{\vec{u_3}}$ and $C^{\vec{u_1}} = C^{\vec{u_2}} = C^{\vec{u_3}}$.

On Fig. 4.25, all cases are presented on the same plot in order to establish a unique relationship $b(\gamma_i)$ (and $c(\gamma_i)$) between void closure and the apparent geometry parameter. This is done because, for a given apparent geometry parameter, the same mechanisms are involved whether the apparent geometry corresponds to the first, the second or the third principal direction. Eq. 4.5 thus becomes:

$$\begin{aligned} B &= b(\gamma_1)p_1 + b(\gamma_2)p_2 + b(\gamma_3)p_3 \\ C &= c(\gamma_1)p_1 + c(\gamma_2)p_2 + c(\gamma_3)p_3. \end{aligned} \tag{4.8}$$

From Fig. 4.25, a bijective monotonously decreasing evolution was observed. A quadratic polynomial function is proposed such that:

$$\begin{aligned} b(\gamma_i) &= b_0 + b_1\gamma_i + b_2\gamma_i^2 \\ c(\gamma_i) &= c_0 + c_1\gamma_i + c_2\gamma_i^2. \end{aligned} \tag{4.9}$$

The values plotted in Fig. 4.25 were used to identify coefficients b_0, b_1 and b_2 (and c_0, c_1 and c_2) using polynomial regression analysis. The R^2-correlation factor is very good again.

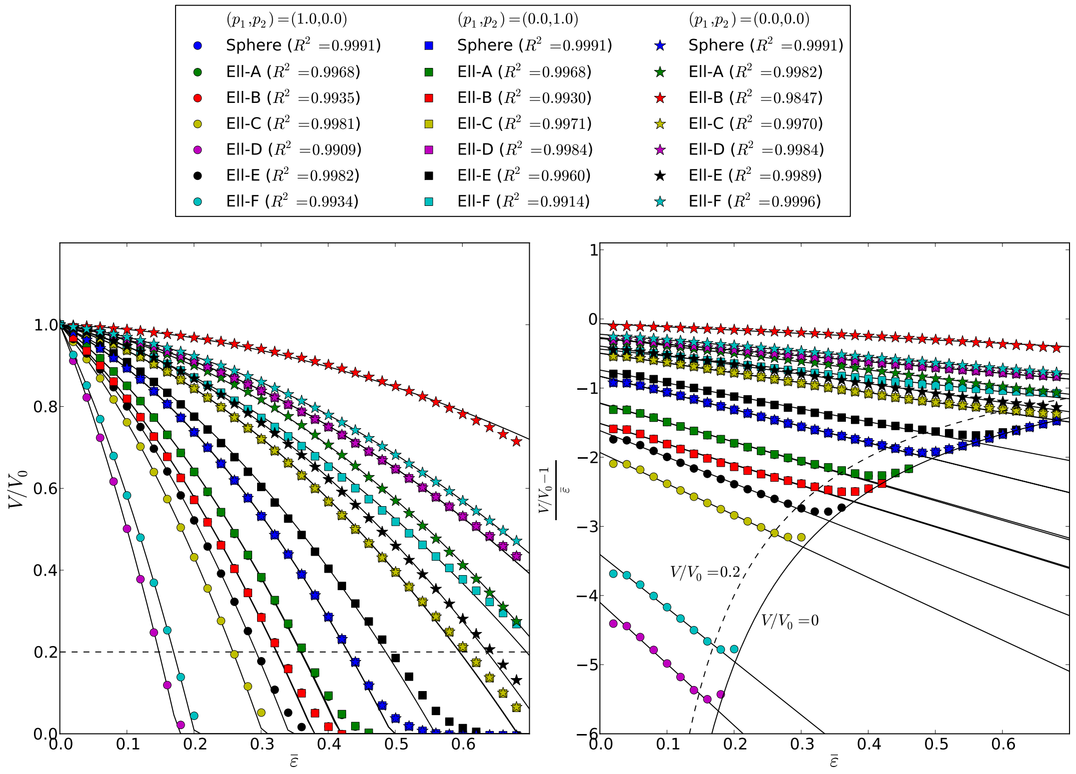

Figure 4.24: Curve fitting (with R^2−correlation factor) performed using RVE results for various geometries and orientations (given in Fig. 4.16), by linear regression using the linearized expression (Eq. 4.4).

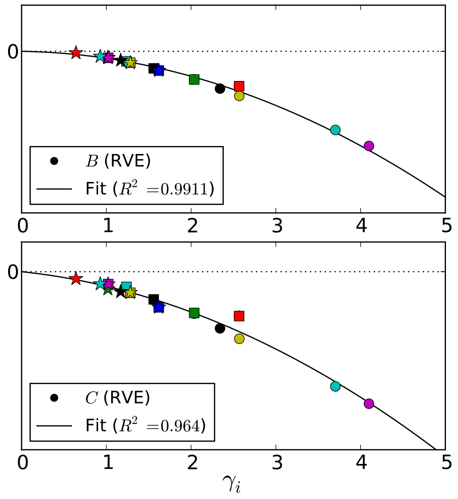

Figure 4.25: Influence of the geometry parameter γ_i on B and C coefficients, obtained from fitting for all cases given in Fig. 4.24 (common legend).

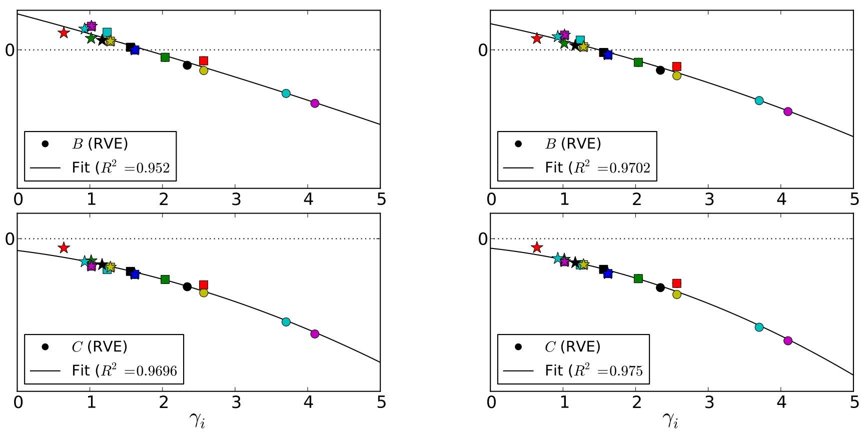

(a) $T_X = -0.04$ (b) $T_X = -0.13$

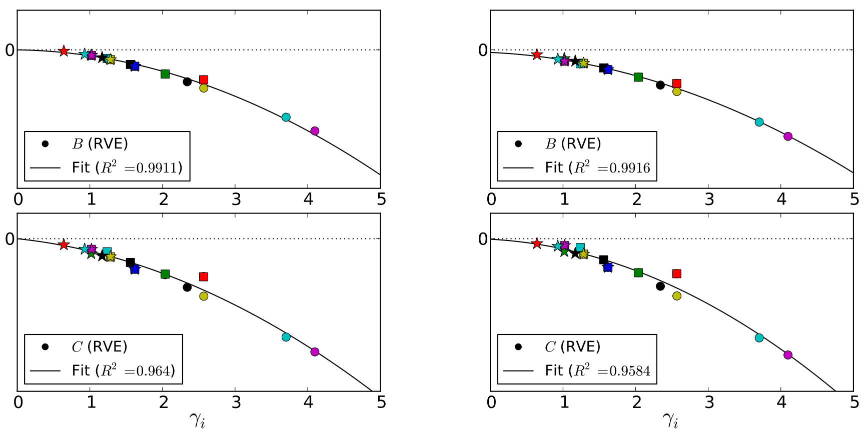

(c) $T_X = -0.33$ (d) $T_X = -0.39$

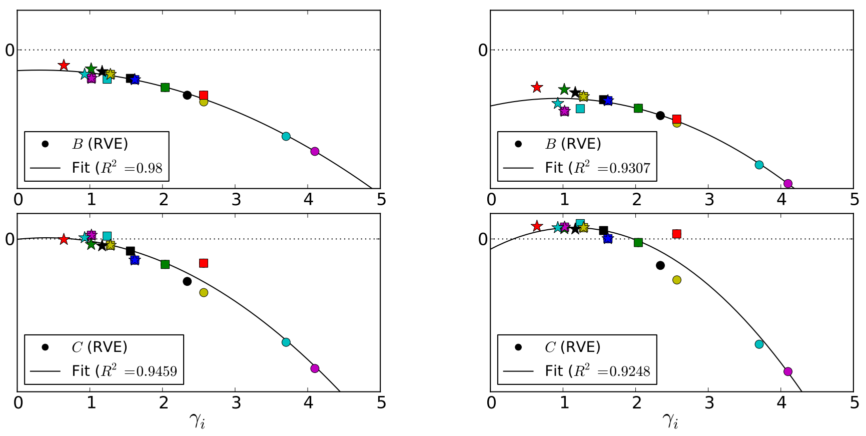

(e) $T_X = -0.57$ (f) $T_X = -0.94$

Figure 4.26: Comparison, for several values of stress triaxiality ratio T_X, of the influence of the geometry parameter γ_i on B and C coefficients, obtained from curve fitting (see legend for the dots in Fig. 4.24).

4.4.4 Dependence to stress triaxiality ratio

All expressions in this section up to Eq. 4.9 were obtained for the particular value $T_X = -1/3$, i.e. under uniaxial compression (using the boundary conditions $\sigma_x = \sigma_y = 0$).

In order to quantitatively assess the influence of stress triaxiality ratio and to extend Eq. 4.9, the analysis was repeated under various stress triaxiality ratios over the range $T_X = [-1, 0]$. The evolution of $b(\gamma_i)$ and $c(\gamma_i)$ (i.e. the dependence to geometry) is plotted for various stress triaxiality ratios in Fig. 4.26. The curves exhibit a rather linear dependence to the geometry parameter γ_i for low compressive stress states. Non-linearity occurs when decreasing the value of T_X.

In Fig. 4.26, it can be seen that the fitting accuracy also decreases for compressive stress triaxiality ratios. The case that is plotted using a red square exhibits rather large discrepancy. It corresponds to Ellipsoid B when it is deformed perpendicularly to its longest direction (see Fig. 4.15).

The coefficients b_i and c_i ($i \in \{0, 1, 2\}$) were obtained using polynomial regression analysis for each case and are plotted in Fig. 4.27.

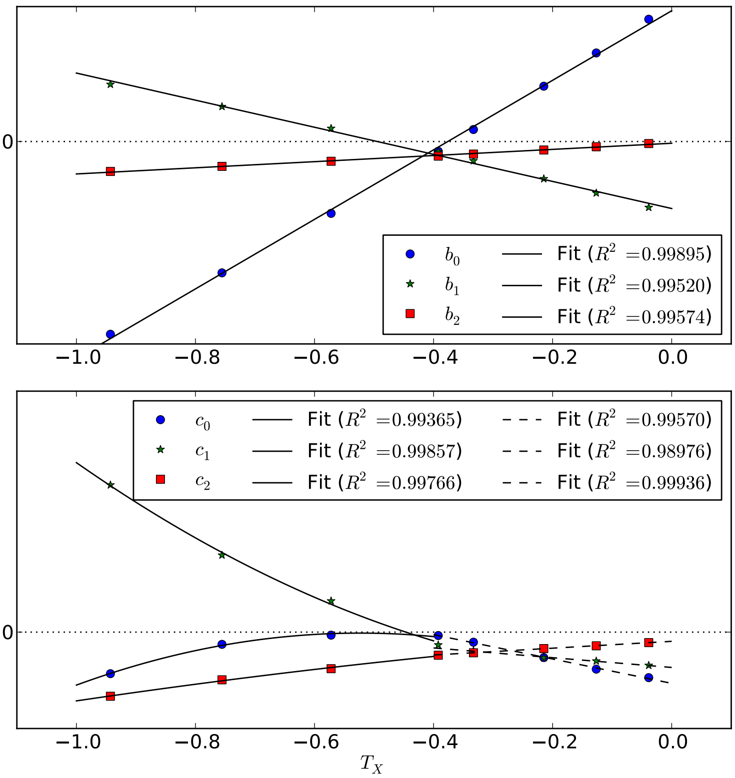

Figure 4.27: Influence of stress triaxiality on the b_i and c_i coefficients ($i \in \{0, 1, 2\}$) from Eq. 4.9.

A linear dependence is observed for the b_i coefficients over the whole range of T_X. For the c_i coefficients, a linear dependence is observed as well on the range $-0.4 \leq T_X \leq 0$, and a quadratic dependence is observed on the range $-1 \leq T_X \leq -0.4$. The regression was therefore split and two batches of calibration constants were obtained, one for each range of T_X. The good values of R^2–correlation coefficients indicate that the chosen analytical functions are suitable to model these dependences.

The final dependence to γ_i and to stress triaxiality ratio T_X can be written as:

$$\begin{aligned} b(\gamma_i) &= b_{00} + b_{10}\gamma_i + b_{20}\gamma_i^2 \quad + T_X\left(b_{01} + b_{11}\gamma_i + b_{21}\gamma_i^2\right) \\ c(\gamma_i) &= c_{00} + c_{10}\gamma_i + c_{20}\gamma_i^2 \quad + T_X\left(c_{01} + c_{11}\gamma_i + c_{21}\gamma_i^2\right) + T_X^2 \quad \left(c_{02} + c_{12}\gamma_i + c_{22}\gamma_i^2\right) \end{aligned} \tag{4.10}$$

The values of constants are given in the confidential Appendix D.1. The coefficients B and C are called *closure coefficients*. In fact, B can be seen as the *initial closure* coefficient, providing the initial slope of the void volume evolution at $\varepsilon = 0$. The coefficient C can be seen as a *deformation-dependent* coefficient, translating the change of shape during deformation. This is in good agreement with the results of Lee and Mear [1994]. The authors pointed out the necessity to consider the change of shape of a void during deformation.

In the present work, the coefficient is calibrated under constant loadings. The value of C thus contains the information of the change of shape during a uniform loading.

For a better prediction, the current evolution of the void must be known throughout the deformation. For a given pass, it is correct as the material is generally loaded along one main axis.

4.4.5 Final expression of the prediction model

Finally, the crossed dependences to orientation, to geometry and to stress triaxiality ratio can be summarized in a single expression:

$$\frac{V}{V_0} = 1 + B\bar{\varepsilon} + C\bar{\varepsilon}^2 \qquad \text{with} \begin{cases} B = \displaystyle\sum_{i=1}^{3}\sum_{j=0}^{2}\sum_{k=0}^{1} b_{jk}(T_X)^k(\gamma_i)^j p_i \\ C = \displaystyle\sum_{i=1}^{3}\sum_{j=0}^{2}\sum_{k=0}^{2} c_{jk}(T_X)^k(\gamma_i)^j p_i \end{cases} \tag{4.11}$$

where the numerical values of the six constants b_{jk} and the nine constants c_{jk} are given in the confidential Appendix D.1.

4.5 Validation of the prediction model

In order to verify the reliability of the proposed model, predicted evolutions are compared to the void volume evolutions that were measured for several ellipsoidal voids, under various mechanical conditions. The four morphology-equivalent ellipsoids that were presented in section 4.2 are used. The RVEs containing these ellipsoidal voids are illustrated in Fig. 4.28. Various stress triaxiality values are imposed on the range $T_X = [-1, 0]$.

	Dimensions (mm)			Orientation		
	r_1	r_2	r_3	p_1	p_2	p_3
Ellipsoid 3	1.35	1.62	2.36	0.97	0.01	0.02
Ellipsoid 4	1.20	1.42	2.10	0.67	0.10	0.23
Ellipsoid A	1.34	1.63	3.17	0.88	0.21	0.01
Ellipsoid AD	0.47	1.61	3.97	0.20	0.22	0.58

Table 4.1: Geometrical features of the ellipsoids used for the validation of the calibration.

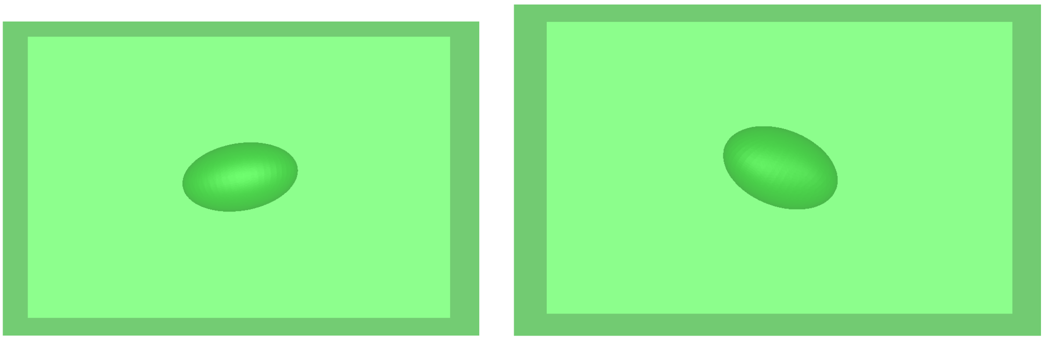

(a) Ellipsoid 3 (b) Ellipsoid 4

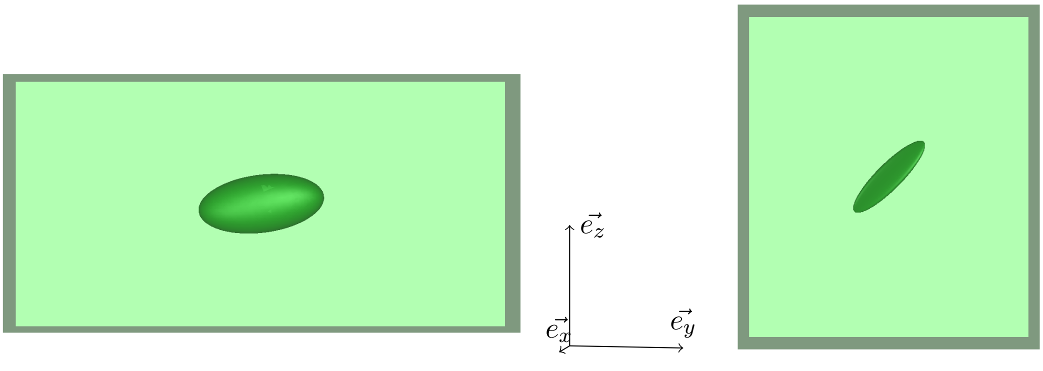

(c) Ellipsoid A (d) Ellipsoid AD

Figure 4.28: Initial RVEs containing *morphology-equivalent* ellipsoids.

Void volume evolution is thus plotted for each ellipsoid in Fig. 4.29. For each plot, the predicted volume evolution is plotted as well. It is computed using Eq. 4.11, according to the geometrical features given in Table. 4.1 and the prescribed stress triaxiality ratio T_X.

The objective here is to assess the ability of the model to predict the behaviour of ellipsoids. This is directly related to the efficiency of the chosen model, as well as the calibration step.

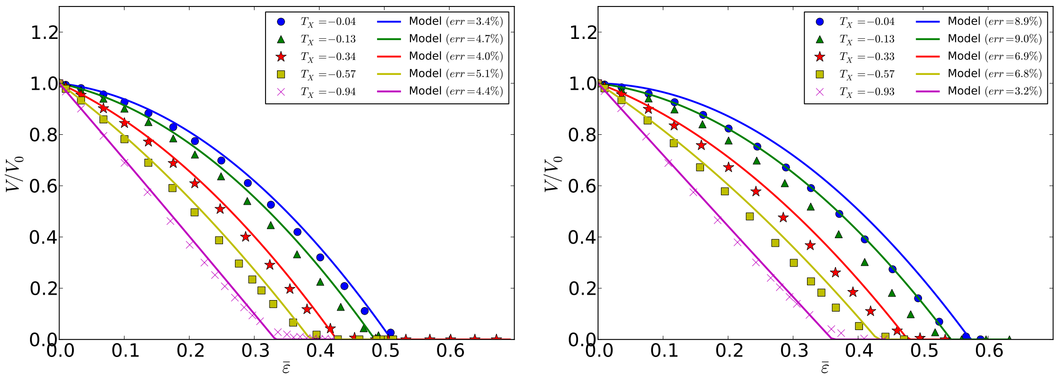

(a) Ellipsoid 3 (b) Ellipsoid 4

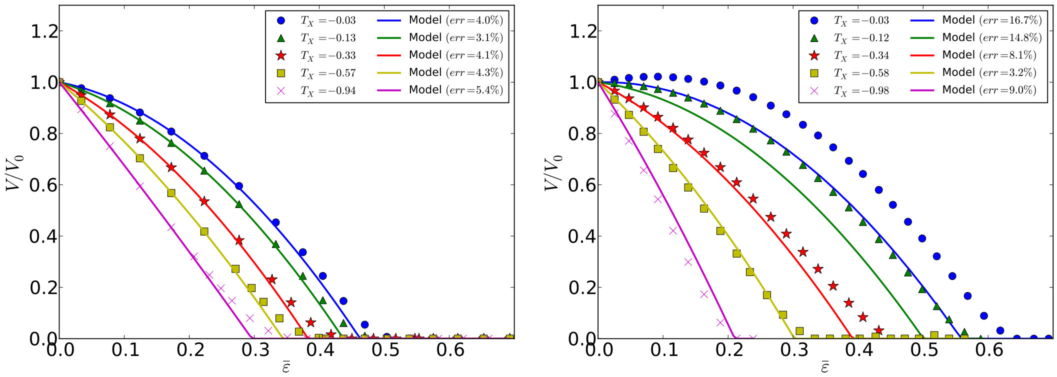

(c) Ellipsoid A (d) Ellipsoid AD

Figure 4.29: Illustration of the L^2–norm error made by the prediction model on the actual closure of an ellipsoidal void.

Ellipsoid 3

The aspects ratios of ellipsoid 3 can be obtained from its dimensions and are $(r_3/r_1) = 1.75$ and $(r_2/r_1) = 1.20$. The orientation parameter p_1 is close to unity and $p_2 \approx p_3 \approx 0$. These values of orientation indicate that the principal vector of the void $\vec{u_1}$ is colinear with the main deformation direction $\vec{e_1}$. In other words, the void is mainly deformed along its smallest dimension r_1. As a consequence, according to Eq. 4.8, the closure coefficients b and c are respectively equal to $b(\gamma_1)$ and $c(\gamma_1)$.

The L^2–norm error was computed between the model and the result from RVE simulation. For all tested values of stress triaxiality ratio, the error remains lower than 5%. In the case of Ellipsoid 3, the model is capable of predicting its void volume with very good accuracy.

Ellipsoid 4

The aspect ratios of ellipsoid 4 are $(r_3/r_1) = 1.75$ and $(r_2/r_1) = 1.18$. Note that, by chance, the values are roughly identical to the ones of ellipsoid 3. Regarding its orientation, ellipsoid 4 is slightly tilted compared to ellipsoid 3. As a consequence, the values of closure coefficients B (respectively coefficients C) are given by a linear combination of $b(\gamma_1)$, $b(\gamma_2)$ and $b(\gamma_3)$ (respectively $c(\gamma_1)$, $c(\gamma_2)$ and $c(\gamma_3)$), according to Eq. 4.8.

For the lowest triaxiality ratios, the prediction is excellent, with a L^2–norm error about 3%. When increasing the value of stress triaxiality, the prediction slightly underestimates void closure, the L^2–norm error remaining lower than 9% over the whole range of T_X. The obtained error is mainly due to the fact that the closure rates are relatively small for low compressive states. When looking at Fig. 4.26, the relative error that is made by regression for the value of B is higher for the value $T_X = -0.04$ than for the value $T_X = -0.94$, due to the fact that the values are close to zero when T_X tends to zero. As a consequence, the error made on the value of B is visible on the initial slope of the volume evolutions in Fig. 4.29. Nevertheless, since the error remains lower than 9%, the prediction can be reasonably considered as good.

Ellipsoid A

The aspect ratios of ellipsoid A are $(r_3/r_1) = 2.37$ and $(r_2/r_1) = 1.22$. In this case, the second aspect ratio is relatively similar to the previous ones as well. However, the first aspect ratio is larger, indicating that the void is more elongated along its third principal direction. Its orientation parameters exhibit the particular value of $p_3 \approx 0$, meaning that the third principal direction is perpendicular to the z-axis (the deformation axis). The behaviour of the void is thus driven by a combination of the closure coefficients $b(\gamma_1)$ and $b(\gamma_2)$ (and $c(\gamma_1)$ and $c(\gamma_2)$), only.

The L^2–norm error remains lower than 5%. The accuracy of the prediction for ellipsoid A is as good as the one obtained for ellipsoid 3.

Ellipsoid AD

The aspect ratios of ellipsoid AD are $(r_3/r_1) = 8.45$ and $(r_2/r_1) = 3.43$. The orientation parameters indicate that the void does not show any particular orientation.

Regarding Eq. 4.10, the apparent geometrical parameters $\gamma_1 = 4.95$ and $\gamma_3 = 0.59$ of ellipsoid AD are situated at the boundaries of the range of tested values for the calibration (see Fig. 4.26). The accuracy of the regression is therefore lower for such values, and the resulting error is visible on the final prediction of void volume in Fig. 4.29d. This case can therefore be considered as an extreme case for the validation of the model.

The same comment can be made regarding the fact that the maximum discrepancy is obtained for low compressive values of stress triaxiality ratio. The L^2–norm error rises to 17% in the case $T_X = 0$. For more compressive triaxiality ratios, the error remains rather low, with the best prediction obtained for the value $T_X = -0.58$, with an error of about 3%.

4.6 Conclusions

Based on a wide campaign of numerical simulations at the RVE-scale, a parametric sensitivity study has demonstrated the following statements.

- Material parameters exhibit a certain influence on void closure. Both the strain hardening and the strain-rate sensitivity parameters have a comparable influence on void closure, as comparable mechanisms are involved. The main effect is observed in the shape evolution of the void during deformation. The deformation that is required for complete closure remains rather comparable though. Finally, in the case of materials with both stain hardening and strain-rate sensitivity dependences, the effect on void closure can be deducted from the sum of the effects of both parameters. Nevertheless, the influence remains moderate in the range of values for hot metal behaviours and was thus not considered in the proposed model.
- Voids orientation and dimensions have a first order influence on void closure.
- Stress triaxiality ratio also has a first order influence on void closure. On the contrary, void closure is not influenced by the remote strain-rate.
- The use of equivalent ellipsoids shows great interest to model the closure of a real void, by comparison to the use of a sphere. The main discrepancies are obtained at the final stages due to the presence of contact at the internal faces of the void. This effect is accentuated by tortuosity and is not addressed within the present work. The use of an equivalent ellipsoid faithfully represents the behaviour of a real void until contact is encountered, i.e. over about at least 80% of the closure process.

The prediction model was built based on the wide campaign of simulations at the RVE-scale. A quadratic polynomial function is proposed to model void volume evolution. The dependence of void orientation, void dimensions and stress triaxiality ratio were successfully modeled using analytical functions and calibrated using regression analysis. The capability of the model to predict void volume evolution was tested using geometry parameters obtained from real voids that were previously observed using X-ray microtomography. For the four tested cases, the prediction was excellent. A maximum error of 17% was observed for the extreme case, and generally remained lower than 5%. This result indicates that the proposed model is suitable to predict void closure according to void's initial orientations and dimensions, and under various stress triaxiality ratios.

Chapter 5

Application of the new prediction model

Contents

Résumé français

Ce chapitre présente une validation du nouveau modèle présenté au chapitre précédent. Ce modèle à champ moyen est d'abord implémenté dans le logiciel de simulation par éléments finis FORGE [2011] en tant que routine utilisateur. De la même façon que le modèle basé uniquement sur la triaxialité des contraintes (STB) existant dans la version commerciale du logiciel, le modèle est implémenté sous une forme différentielle par un schéma explicite en temps. Un champ initial de volume de pore est donc actualisé à chaque incrément de la résolution éléments finis au moyen du modèle de prédiction en fonction des variables mécaniques et des paramètres initiaux du modèle. Le modèle de Zhang est également implémenté suivant la même méthodologie.

Les trois modèles sont confrontés à des simulations explicites en champ complet pour deux procédés industriels : un cas de forgeage libre et un cas de laminage. Les évolutions du volume de pore prédites par les trois modèles sont comparées et discutées à plusieurs positions, et pour plusieurs géométries initiales de pores. Il est montré que les évolutions prédites par le nouveau modèle sont bonnes dans l'ensemble. Les bénéfices apportés par le nouveau modèle par rapport aux modèles existants sont : la prise en compte de la géométrie initiale (rapports d'aspect et orientation) des pores ; l'expression analytique permettant de prédire l'évolution du volume avec meilleure précision que les modèles actuels. Certaines différences sont malgré tout observées et les hypothèses sont discutées afin de les évaluer. Des pistes d'amélioration concrètes au modèle sont proposées afin de lever les limitations actuelles.

5.1 Introduction

In Chapter 1, it was demonstrated that although explicit macroscopic descriptions might be particularly accurate, they remain rather costly as heavy meshes are required. In addition, they provide results for particular cases, exclusively. Using *mean-field* models, the prediction of void closure can be directly obtained at every position in the workpiece without requiring any specific mesh refinement. In this chapter, the new prediction model is implemented as a *mean-field* model, and is compared for several particular cases to macroscopic explicit simulations.

Prediction models are implemented in the finite-element computation software FORGE [2011], as post-processing subroutines. The computed field is the normalized void volume V/V_0. During computation, at each increment step, the value of the field V/V_0 is evaluated at every integration point of the finite element mesh using the prediction model according to the current mechanical fields and the initial parameters.

Several assumptions are implicitly made when using *mean-field* models. They are recalled for the forthcoming discussion.

- First, general assumptions are made using the meso-scale approach (section 2.2) regarding the separation of scales. It is considered that the presence of voids has a negligible impact on the global behaviour of a workpiece. Note that this assumption enables prediction models to be implemented as post-processing subroutines, as they do not modify the current mechanical fields.

- The second main assumption considers that the *local* (i.e. at the RVE-scale) behaviour of the void is subjected to homogeneous mechanical conditions.

- The method used to impose boundary conditions at the RVE-scale also assumes axisymmetry around the main deformation axis.

- The use of morphology parameters also involves certain assumptions regarding the actual morphology of voids. In Chapter 4, it was shown that the use of geometrical parameters of the voids (dimensions and orientation) enables a good representation of the behaviour of real voids, and that an error of about 5% is generally made. It was also shown that this error might significantly rise in the case of extremely tortuous voids. Nevertheless, by comparing with the use of spherical voids that is generally made in the literature, the use of morphology-equivalent ellipsoids shows great advantage in terms of void volume evolution. In addition, a systematical tridimensional examination of void state is hardly conceivable at an industrial level. The use of equivalent ellipsoids emerges as a reasonable choice as it provides a good compromise between the required information and the available information. For example, statistical industrial studies might provide sufficient information in terms of geometrical parameters.

First, the implementation of the *mean-field* models as subroutines in the finite element software FORGE [2011] is described. The second section presents an evaluation of the model for a case of open die forging. The third section presents an evaluation of the model for a case of hot rolling. For both simulation cases, the new prediction model is systematically compared to existing models from the literature (the STB model, the Zhang model [Zhang et al., 2009]) and to the explicit simulations at the workpiece scale. The discrepancies are measured at the end of a pass (or blow). Their values are given in percent, and are computed by $\frac{V_{\text{model}}-V_{\text{explicit}}}{V_0}$.

5.2 Implementation of the prediction models in a finite element code

The STB model currently exists in the commercial version of FORGE [2011] and its implementation is briefly recalled first. For comparison purposes, the Zhang model was implemented as well and is presented in a second paragraph. Finally, the implementation of the new model Cicaporo is detailed.

The models are implemented using a differential form ΔV. The void volume V^t at the time increment t is obtained using an explicit scheme

$$V^t = V^{t-1} + \Delta V^t, \tag{5.1}$$

in which ΔV^t is the predicted variation of volume that is given by the prediction model, and V^{t-1} is the void volume at previous time increment $t-1$. At each time increment t of the finite element resolution, the variation of volume ΔV^t is evaluated at every integration point of the mesh.

As the volume evolution is expressed using a differential form, an initial value is required. The initial variable field $(V/V_0)^{t=0} = 1$ can be defined throughout the mesh. It is also possible to load a previous field (e.g. incoming from previous simulation), or to manually define different values of $(V/V_0)^{t=0}$ per spatial areas.

The models also require a set of initial parameters, that are fixed at the beginning of simulation.

5.2.1 Stress triaxiality-based (STB) models

In FORGE [2011], the existing prediction model for void closure is based on the integral of the stress triaxiality ratio over the cumulated equivalent strain, such as described in Chapter 1, section 1.3.1. A proportionality coefficient is given such as:

$$\frac{\Delta V^t}{V_0} = K_C {T_X}^t \Delta\bar{\varepsilon}^t \qquad \forall \quad T_X < 0, \tag{5.2}$$

where the value of K_C is an initial parameter and can be user-defined. A default value $K_C = 5$ was proposed by Lasne [2008]. This value was obtained by a calibration using simple compression cases of a billet containing an initially spherical void. An extension was proposed for positive triaxiality ratios by replacing the value K_C by $K_T = 5/3$, obtained by a calibration using tension cases.

It was shown that Eq. 5.2 with $K_C = 5$ is roughly equivalent to the criterion of Kakimoto et al. [2010]. This criterion states that void closure is reached when the value $Q = \int_0^{\bar{\varepsilon}} (-T_X) d\bar{\varepsilon} \geq 0.21$.

In these models, void closure depends on the evolution of stress triaxiality, only. They will be called stress triaxiality-based (STB) models in the following, and the example of the existing model in FORGE [2011] will be used.

The algorithm for the STB model is given in appendix B.1.

5.2.2 Zhang model

The prediction model proposed by Zhang et al. [2009] was identified as the currently most accurate existing model in the literature. The model is based on micro-analytical solutions that were obtained by Duva and Hutchinson [1984] for the volume evolution of a sphere in a viscoplastic material (without considering the change of shape of the void during deformation). Corrective terms were added by Zhang et al. [2009] using a polynomial function with four parameters q_1, q_2, q_3 and q_4 in order to consider the change of shape of the sphere during deformation. The model assumes that the change of void shape during deformation depends on the cumulated equivalent strain, only. The parameters were calibrated using finite element simulations in an RVE containing an initially spherical void. The incremental volume change is expressed as:

$$\frac{\Delta V}{V} = -\left[f(m^*, T_X) - q_1 T_X + 3q_2\bar{\varepsilon}^2 + 5q_3\bar{\varepsilon}^4 + q_4\right]\Delta\bar{\varepsilon}. \tag{5.3}$$

where q_1, q_2, q_3 and q_4 are corrective terms and are tabulated for several values of m^* in Zhang et al. [2009], and $f(m^*, T_X)$ is an analytical function given by:

$$f(m^*, T_X) = \frac{3}{2}\left(-\frac{3}{2n^*}T_X + \frac{(n^*-1)(5n^*+2)}{5(n^*)^2}\right)^{n^*} \quad \text{with } n^* = \frac{1}{m^*}. \tag{5.4}$$

The algorithm for the Zhang model is given in appendix B.2.

The model takes into account a dependence to a material parameter m^*. This material parameter corresponds to the strain-rate sensitivity coefficient in the case of a visco-plastic material without strain hardening.

In the case of materials with strain hardening, softening, or further mechanical behaviours, the Zhang model is undefined. Further work, as the one regarding the effect of strain hardening (section 4.3.1) is required in order to accurately predict the quantitative dependence to material parameters. This was not pursued within this work as the qualitative influence was second order with respect to the morphology and mechanical state.

Nevertheless, according to the qualitative results obtained with strain hardening, the influence of material parameters seemed comparable to the influence of m^* that is considered in the Zhang model. As a consequence, an arbitrary value of m^* may reasonably be chosen in order to assess the capabilities of the Zhang model, in a first-order approximation. The choice of the arbitrary value will be made and discussed in section 5.3.1.

Note that the incremental volume change is expressed as $\Delta V/V$, whereas the incremental volume change of the STB model is expressed as V/V_0. When integrating both models under constant boundary conditions (T_X = constant), the Zhang model exhibits an exponential equation, whereas the STB model exhibits a linear evolution.

5.2.3 New void closure model Cicaporo

According to previous discussion, the absolute value of the volume of a void V has no influence on its closure behaviour. On the contrary, the geometry of the void exhibits a first-order influence. In the Zhang model, the corrective terms are calibrated in order to contain the information of the effect of shape change during deformation. However, according to Eq. 5.3 the model also depends on the current absolute volume V of the void.

In the proposed new model Cicaporo, the use of V/V_0 was preferred. The information regarding the change of shape during deformation is contained in the value of the closure coefficient C.

The differential form is expressed as:

$$\frac{\Delta V}{V_0} = \left[B + 2C\bar{\varepsilon}\right]\Delta\bar{\varepsilon}, \qquad \text{with} \quad \begin{cases} B = \displaystyle\sum_{i=1}^{3}\sum_{j=0}^{2}\sum_{k=0}^{1} b_{jk}(T_X)^k(\gamma_i)^j p_i \\ C = \displaystyle\sum_{i=1}^{3}\sum_{j=0}^{2}\sum_{k=0}^{2} c_{jk}(T_X)^k(\gamma_i)^j p_i, \end{cases} \tag{5.5}$$

with T_X the stress triaxiality ratio, $\gamma_i = \sqrt[3]{V_0}/r_i$ the geometry parameters, and p_i the orientation parameters. The values of the calibration constants b_{jk} and c_{jk} are given in the confidential appendix D.1. The value of stress triaxiality T_X^t is considered at each integration point and increment time.

Initial dimensions The geometry parameters γ_i are obtained using the three initial dimensions r_1, r_2 and r_3. The values of r_1, r_2 and r_3 are set by the user as input parameters in the subroutine. They are defined at the beginning of computation.

Initial orientation Void orientation is also defined at the beginning of computation in the canonical basis using the initial principal vectors $(\overrightarrow{u_1}, \overrightarrow{u_2}, \overrightarrow{u_3})$ of the void. These vectors correspond to the eigen-vectors of the inertia matrix of the void, as previously defined in Chapter 2. Several methods may be used to define these three vectors.

The use of three rotations angles θ_X, θ_Y and θ_Z is proposed here. From the canonical basis $(\overrightarrow{e_x}, \overrightarrow{e_y}, \overrightarrow{e_z})$, the void can be oriented towards any spatial direction by imposing successive rotations around the $\overrightarrow{e_x}$, $\overrightarrow{e_y}$ and $\overrightarrow{e_z}$ directions. The three vectors $(\overrightarrow{u_1}, \overrightarrow{u_2}, \overrightarrow{u_3})$ can be directly obtained by the product of three rotation matrices. Note that the proposed method might be easily modified according to users' preference. Different conventions regarding the successive rotations can be used, such as the Euler convention, for example. It is also possible to set directly the coordinates of two of the three vectors $(\overrightarrow{u_1}, \overrightarrow{u_2}, \overrightarrow{u_3})$. In the latter, attention must be paid on orthogonality of the vectors when setting the coordinates.

According to the meso-scale approach, the definition of the orientation parameters p_1, p_2, p_3 is defined between the void's principal vectors and the main compression direction. Yet, the latter may vary in time and space during computation.

The main compression direction is computed for each increment t and at each integration point of the mesh. By diagonalizing the strain-rate tensor, the eigen-vectors $(\overrightarrow{e_1}^t, \overrightarrow{e_2}^t, \overrightarrow{e_3}^t)$ and eigen-values $\varepsilon_1^t, \varepsilon_2^t, \varepsilon_3^t$ are obtained. They are sorted such that $\varepsilon_1^t \leq \varepsilon_2^t \leq \varepsilon_3^t$.

According to the incompressibility of the plastic material, $\varepsilon_1^t + \varepsilon_2^t + \varepsilon_3^t = 0$. The lowest eigen-value is thus negative $\varepsilon_1^t \leq -(\varepsilon_2^t + \varepsilon_3^t) \leq 0$, and can be seen as the main compression. As a consequence, the direction $\overrightarrow{e_1}^t$ is defined as the main compression direction.

The three orientation parameters can thus be obtained at each integration point by:

$$\begin{aligned} p_1^t &= (\overrightarrow{u_1}.\overrightarrow{e_1}^t)^2, \\ p_2^t &= (\overrightarrow{u_2}.\overrightarrow{e_1}^t)^2, \\ p_3^t &= (\overrightarrow{u_3}.\overrightarrow{e_1}^t)^2, \end{aligned} \tag{5.6}$$

where $\overrightarrow{u_i}$ are the eigen-vectors of the initial void.

Change of void shape during deformation As the *mean-field* models predict the evolution of the volume only, the evolution of geometry and orientation of the void are not known in the void-free simulations. In the new prediction model Cicaporo, the information regarding the change of shape of the initial void is contained by the term $C\bar{\varepsilon}$ of Eq. 5.5. It is thus a function of cumulated equivalent strain, initial geometry, and current stress triaxiality ratio. In the Zhang model, the change of shape is assumed to depend on the equivalent strain only. The STB model does not consider this information.

However the value of C is determined with the constants c_{jk} that were calibrated under uniform deformation (the deformation direction being constant in the RVE simulations). As a consequence, it is rather good approximation in the case of processes with almost uniform deformation, but might become a limitation in the case of multi-pass processes, as the deformation direction may significantly vary.

In order to better consider the change of shape during non-uniform deformation, it would be necessary to predict the tridimensional evolution of the void. This is one of the main perspectives to this work and will be discussed in the general conclusion of this document.

The algorithm is given in appendix B.3.

5.3 Case of open die forging

This section gives several validation cases regarding the new prediction model. The process simulation is a case of multi-blow open die forging and was provided by Industeel.

The workpiece is a bottom-cast ingot and is deformed between a vertical hammer-die and a flat-die, see Fig. 5.1. The total sequence is composed of several passes. Each pass has a proper height reduction ratio $\Delta H/H_0$, and is divided into several blows at different positions of the workpiece.

The first pass is an equalization pass, which involves very low deformation in the material. As a consequence, it shows rather low interest for studying void closure, and will not be discussed. On the contrary, the second pass is defined with a significant reduction ratio ($\Delta H/H_0 = 0.27$). It is divided in three blows at different positions of the ingot. Two of the three blows are considered in the present section and are noted blow 1 and blow 2 in the following figures. The deformation of the workpiece during blow 1 and blow 2 is illustrated in Fig. 5.2.

Various initial void states were defined and are described in Table. 5.1. Four different explicit meshes containing voids were generated.

- Explicit case 1 contains three spherical voids. Spherical voids are studied in order to verify the reliability of the new model Cicaporo with respect to the STB and the Zhang model, as both STB and Zhang models were developed for spherical voids. Then, ellipsoidal voids are inserted at various locations in the ingot in the explicit cases 2, 3 and 4.

- In case 2, all ellipsoids are oriented such that their principal vectors coincide with the canonical basis $(\vec{u_1}, \vec{u_2}, \vec{u_3}) = (\vec{e_x}, \vec{e_y}, \vec{e_z})$.

- In case 3, all ellipsoids are oriented such that their principal vectors are defined as $(\vec{u_1}, \vec{u_2}, \vec{u_3}) = (\vec{e_z}, \vec{e_y}, -\vec{e_x})$, i.e. obtained by a rotation of 90° around $\vec{e_y}$.

- In case 4, various orientations are defined and will be detailed in the discussion. Note that the required computation time for the explicit cases are rather high (see Table 5.1).

The prediction models are evaluated using a void-free simulation. The explicit cases naturally require longer computation times, as the number of elements in the mesh is larger. Handling of self-contact also involves additional computation time.

The benefit in terms of computation time rose up to a factor 23 between the void-free simulation and the explicit case 2.

The predicted values of V/V_0 are collected from the void-free simulations using sensors at the positions that correspond to the center of the voids in the explicit simulations. It is illustrated in Fig. 5.1 for the case containing spherical voids.

Simulation	Voids	Orientation	Nb elements	CPU time	Total CPU time
Explicit case 1	3 spheres	–	180 000	3 hours 30 min	1 day 18 hours
Explicit case 2	5 ellipsoids	$(\vec{e_x}, \vec{e_y}, \vec{e_z})$	266 000	15 hours 20 min	7 days 16 hours
Explicit case 3	5 ellipsoids	$(\vec{e_z}, \vec{e_y}, -\vec{e_x})$	256 000	12 hours 50 min	6 days 10 hours
Explicit case 4	5 ellipsoids	various	259 000	5 hours 20 min	2 days 16 hours
Void-free	–	–	70 000	40 min	8 hours

Table 5.1: Performed simulations for the validation case of open die forging, performed using 12 CPUs (3GHz, 24Go RAM).

In this chapter, the material behaviour is the same as the one used in the previous chapter for the model calibration. It is given by the Hansel-Spittel law which is recalled here:

$$\sigma_0 = A\left(\bar{\varepsilon} + \varepsilon_0\right)^n \dot{\bar{\varepsilon}}^m e^{m_4/(\bar{\varepsilon}+\varepsilon_0)}, \tag{5.7}$$

where $A = 31.23$ MPa is the material consistency at the given temperature, $m = 0.153$ the strain-rate sensitivity, $n = -0.135, m_4 = -0.055$ the strain hardening/softening coefficients, and $\varepsilon_0 = 0.025$ a regularization term that enables initial rigidity of the material.

5.3.1 Case of spherical voids

The workpiece containing three explicit spherical voids is illustrated in Fig. 5.1a. It is compared to the void-free simulation in Fig. 5.1b. As defined in the previous chapter, void closure prediction is made at each integration point of the workpiece, providing fields of predicted void volume at any point of the mesh (by interpolation). The values obtained from the prediction models will be compared for a few positions only. The positions are defined using sensors (indicated using red points in Fig. 5.1b), and correspond to the position of the explicit voids center that are defined in Fig. 5.1a.

Regarding the x abscissa, position 1 is approximately located under the hammer-die during the first blow, whereas position 3 is roughly located under the hammer-die during the second blow. Finally, position 2 is located between these two positions. Position 1 and Position 2 have the same vertical location, whereas position 3 is located slightly lower. Dimensions are expressly not given for confidentiality reasons of the presented data.

Results

The results in terms of void volume evolution are plotted in Fig. 5.3. The values that were measured from the explicit simulations are plotted using dots. The prediction that was obtained from each model is plotted with lines. The STB model is plotted using a black continuous line. The Zhang model is plotted using dashed black lines, for three various virtual values of material parameter $m^* = 0.1$, $m^* = 0.3$ and $m^* = 0.5$. The new prediction model Cicaporo is plotted using a red line.

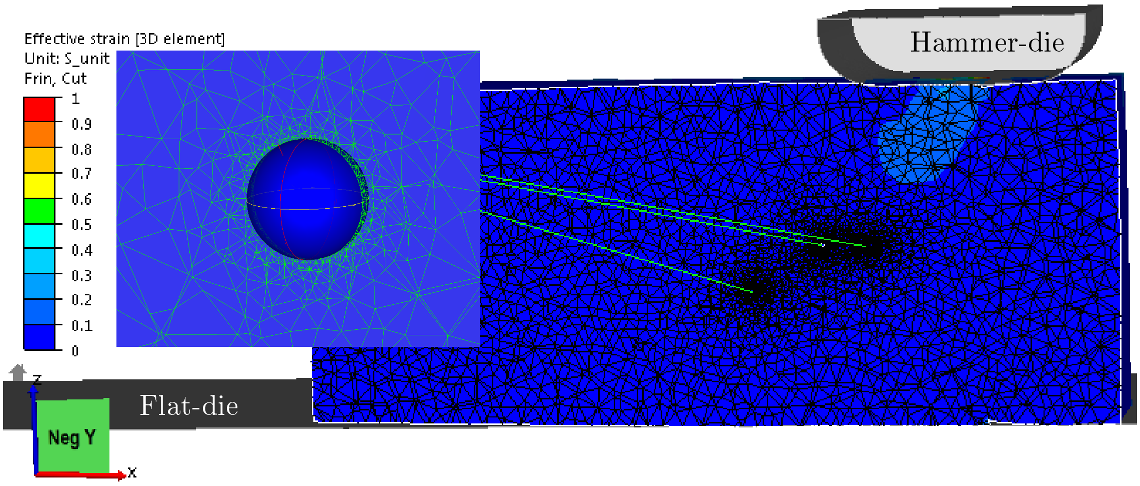

(a) Explicit case containing 3 spherical voids

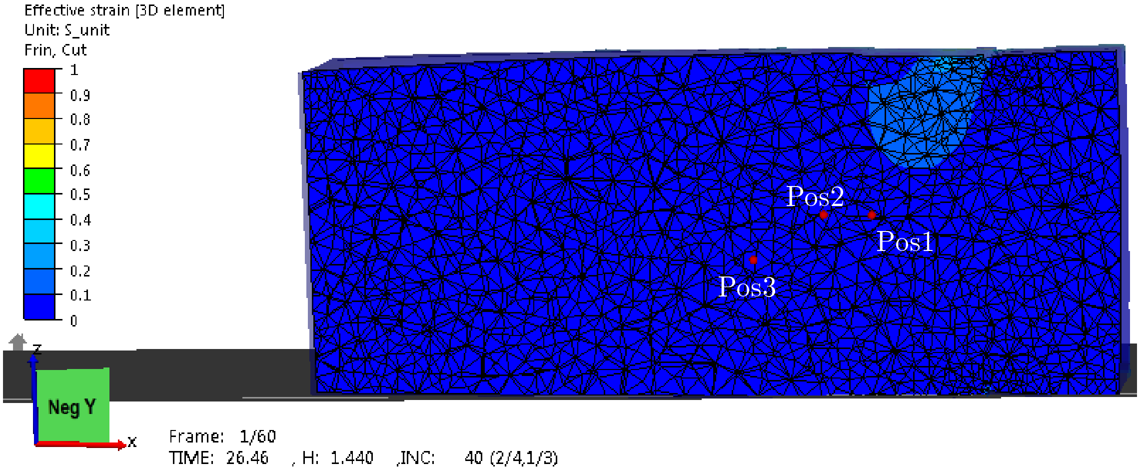

(b) Void-free case with *mean-field* prediction models

Figure 5.1: Cutting planes from the two simulations at beginning of PASS2 – blow 1.

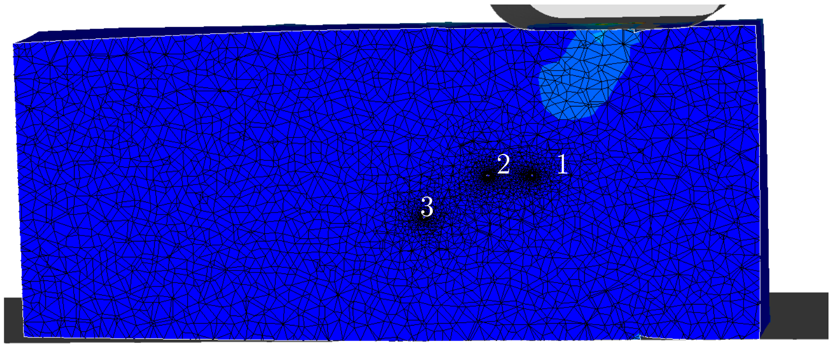

(a) Pass 2 – Beginning of blow 1

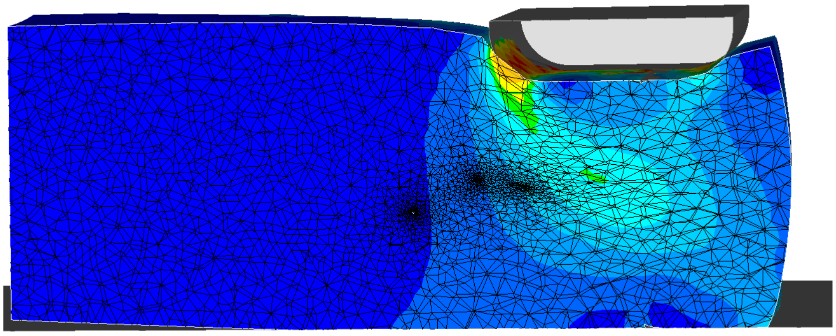

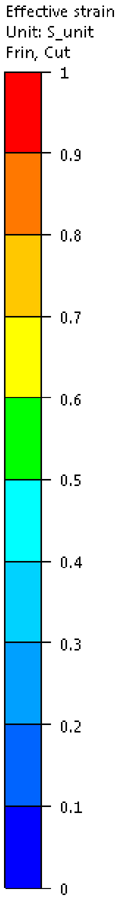

(b) Pass 2 – End of blow 1

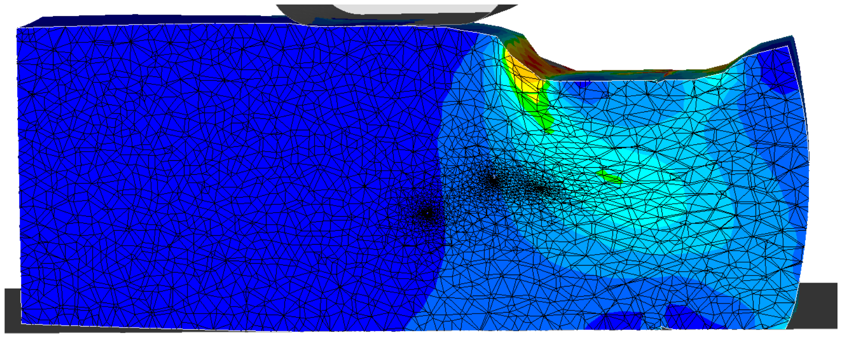

(c) Pass 2 – Beginning of blow 2

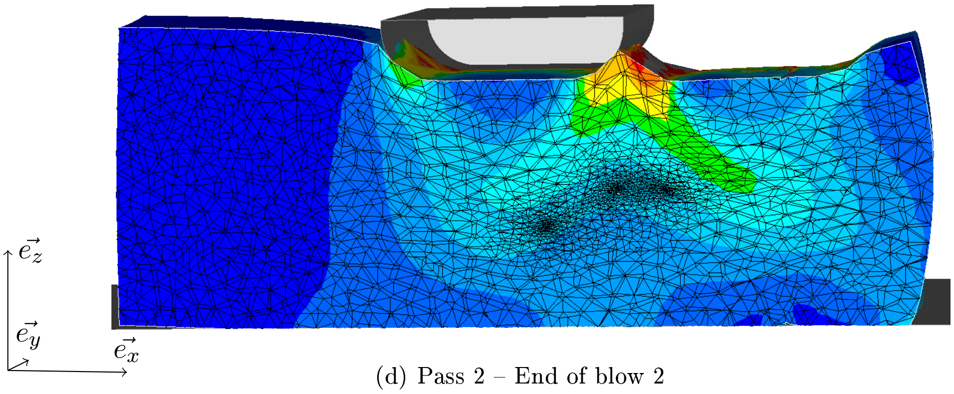

(d) Pass 2 – End of blow 2

Figure 5.2: Equivalent strain in the workpiece containing spherical voids during PASS 2.

According to its definition, the Zhang model is undefined for the present material, as its behaviour contains strain-rate sensitivity, strain hardening and strain softening. However, as pointed out above, a virtual value m^* can reasonably be found in order to provide a first-order approximation of the model according to the qualitative results obtained regarding material influence. Thus, several arbitrary virtual values were defined $m^* = 0.1$, $m^* = 0.3$ and $m^* = 0.5$ in order to observe whether it is possible to find out a suitable value for this case.

Explicit volume evolutions Let us first focus on the values that were measured from the explicit simulation and plotted using black dots in Fig. 5.3. At the end of the equalization pass (PASS1), a very low reduction of void volume is obtained. The main contribution to void closure occurs during PASS2. The following analysis is thus focused on PASS2, blows 1 and 2, i.e. in the interval $t = 26 - 85$ s. The transition between blow 1 and blow 2 occurs at $t = 57$ s.

The main reduction of void volume at position 1 occurs during blow 1. The main reduction in void volume at position 3 occurs during blow 2. At position 2, blow 1 and blow 2 roughly bring the same contribution to void closure. This result is directly due to the position in the workpiece, whether the void is placed in a deformed zone or not. Deformed zones are located under the hammer-die during each blow (see Fig. 5.2).

The mechanical loading paths are given for the three positions in Fig. 5.4. The evolutions of equivalent strain confirm the previous remarks. At position 1 the main deformation occurs during blow 1. At position 3, the main deformation occurs during blow 2. At position 2, a comparable deformation is obtained during blows 1 and 2. Note that the profile of stress triaxiality ratio systematically decreases during each blow. The most compressive values are thus obtained at the end of each blow, whereas the less compressive values are obtained at the beginning of each blow, especially at the beginning of blow 2. This is in good agreement with the change of slope of the void volume evolution in Fig. 5.3 at the beginning of blow 2.

Finally, due to the mesh size that was defined around the voids, a slight underestimation of void closure may be observed. Nevertheless, according to the sensitivity study that was presented in Chapter 2, section 2.5.1, the underestimation might not exceed a few percent.

Choice of a virtual parameter m^* for the Zhang model As discussed above, the value of m^* cannot be strictly defined according to the present material. The several virtual values of m^* that were used within this case are discussed now.

Very good agreement is observed between the new model Cicaporo and the Zhang model using the virtual value $m^* = 0.3$ (see Fig. 5.3). The final discrepancy relative to the explicit case is about 23%. This common disrepancy can be explained by the fact that both models are based on similar assumptions relative to their common approach at the meso-scale.

It is worth noticing that the virtual value $m^* = 0.5$ provides a lower discrepancy. Nevertheless, the gain in terms of final volume prediction is rather moderate, as it reduces the discrepancy of about 5% compared to the new model Cicaporo. On the other hand, the choice of a value $m^* = 0.1$ increases the discrepancy of about 15%.

These remarks suggest that, for this given case, an adequate value of m^* might eventually be determined in order to reduce the discrepancy with the explicit case. However, the determination of such a value would require additional explicit cases in order to ensure its accuracy, and thus might become costly.

In the following, the value of $m^* = 0.3$ will be considered only. This choice was made as the obtained prediction is coherent with the model Cicaporo for a sphere.

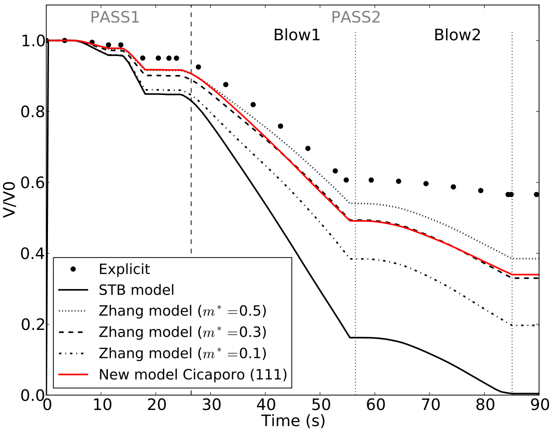

(a) Position 1

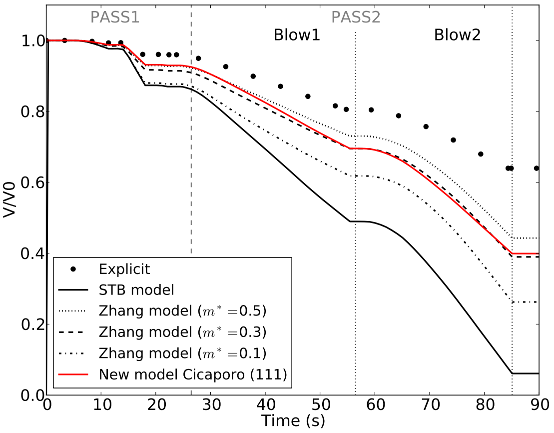

(b) Position 2

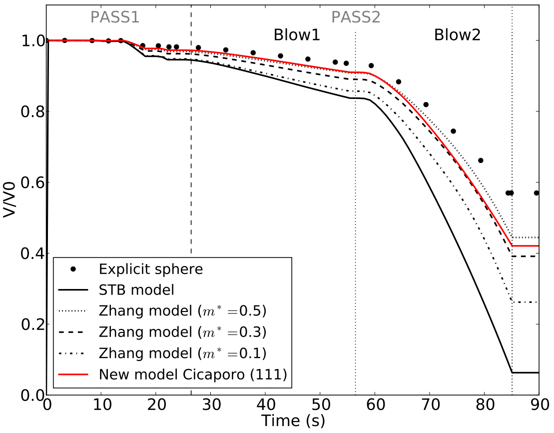

(c) Position 3

Figure 5.3: Void volume prediction for an initially spherical void, compared to STB and Zhang models, and the values measured in the explicit simulation, given for several positions in the workpiece.

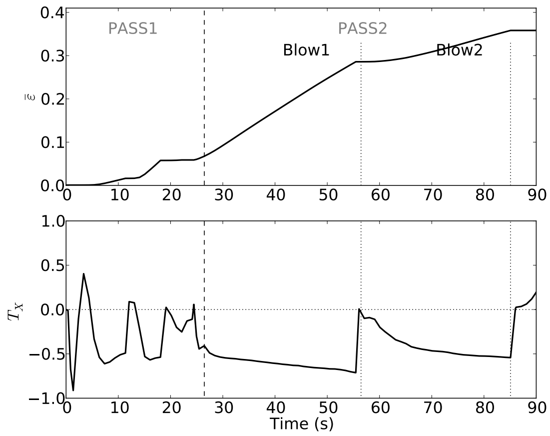

(a) Position 1

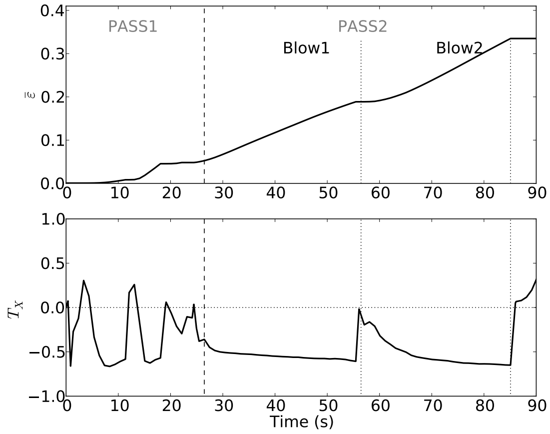

(b) Position 2

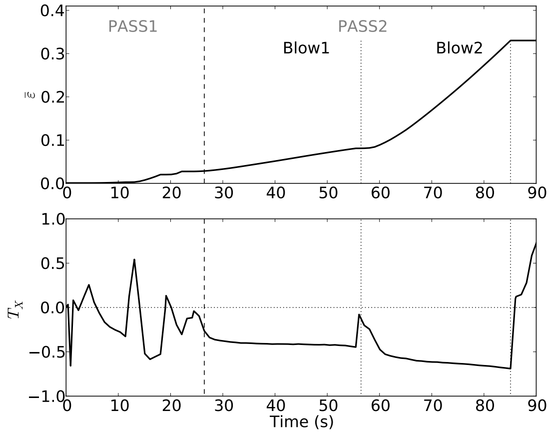

(c) Position 3

Figure 5.4: Evolution of equivalent strain and stress triaxiality ratio for the three different positions in the workpiece.

Change of shape of the voids The prediction that is obtained by the STB model shows rather large discrepancies with the measured actual volume in the explicit simulation. The STB model predicts a quasi-complete closure for the three positions. Void closure is therefore significantly overestimated by the STB model (about 57%), although this model was calibrated using spherical voids. This result can be explained by the fact that the STB model does not consider the change of shape of the voids during deformation. The discrepancy thus increases with cumulated equivalent strain.

Both the Zhang model and the new model Cicaporo take into account the change of shape of the void during deformation. They are expressed as functions of equivalent strain and were calibrated using homogeneous and uniform deformation cases at the RVE-scale.

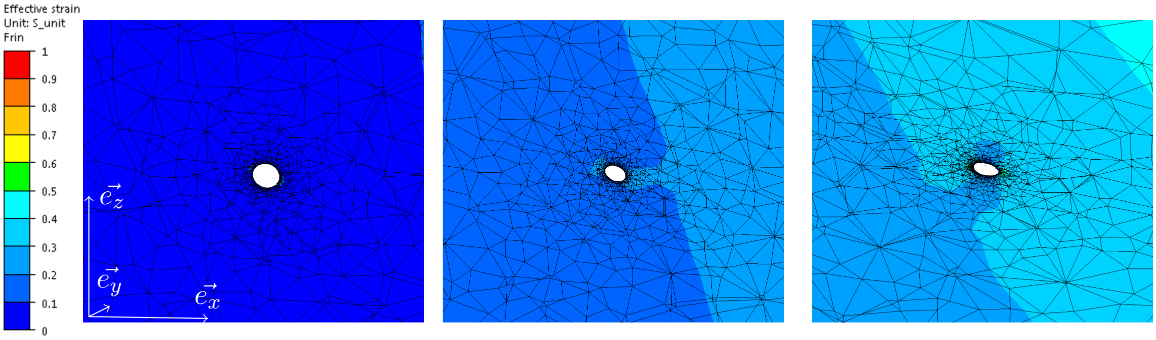

(a) Position 3 (b) Position 2 (c) Position 1

Figure 5.5: Enlargement of Fig. 5.2 at the end of blow1.

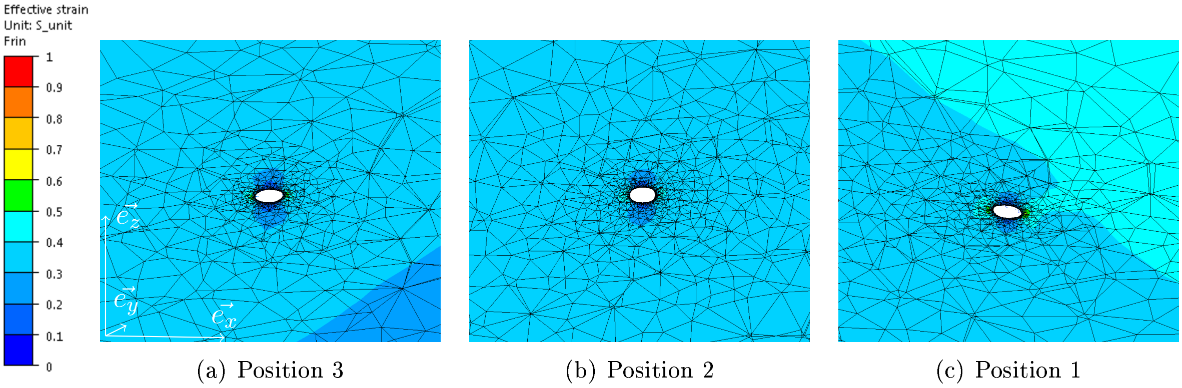

(a) Position 3 (b) Position 2 (c) Position 1

Figure 5.6: Enlargement of Fig. 5.2 at the end of blow2.

Change of compression direction In the new prediction model Cicaporo and in the Zhang model, the effect of the change of shape of the void was calibrated using RVEs that were uniformly deformed. As a consequence, it might present certain limitations in the case of non-uniform loadings. In the case of position 3, the main deformation axis remains rather colinear to $\vec{e_z}$, as it is located under the hammer-die (during blow 2). In the case of position 1, and particularly in the case of position 2, the main deformation axis might exhibit a rather non-uniform evolution during PASS2. When looking at positions 1 and 2 (in Fig. 5.5), the current shape of the void at the end of blow 1 suggests that the deformation axis was not perfectly vertical, but rather tilted. This is coherent with the fact that the void is located on the left of the main deformed zone of blow 1.

During blow 2, the main deformation direction that is induced by the hammer-die seemed to have erased the previous tilted shape, as it is observed in Fig. 5.6. This mentions that the main deformation direction has changed between the end of blow 1 and blow 2. The change of shape that is predicted by the models is therefore slightly different than the explicit case, and contributes to the obtained discrepancy.

This effect is illustrated in Appendix C using several extreme non-uniform loadings on a spherical void. The fact of switching perpendicularly the compression direction significantly modifies the void evolution, due to a different shape change evolution. This effect cannot be considered within the present model, as the current evolution is not strictly known during deformation. The effect of shape change is empirically considered using the coefficient C of the model, which was obtained using uniform compression cases (RVE simulations).

Homogeneity of the mechanical fields In Fig. 5.5, it can be observed that the level of equivalent strain around position 1 is higher than the one of position 2, which is higher than the one of position 3. This result is coherent with the values of equivalent strain that were measured at the three sensors in the void-free simulation (see Fig. 5.4). Nevertheless, a certain gradient of equivalent strain can be locally observed around the void. The whole void is therefore not completely submitted to a homogeneous mechanical field. This gradient is ignored by the models, as homogeneity of the mechanical fields is assumed at the RVE-scale.

Axisymmetry of the stress state The calibration using RVE simulations was performed using axisymmetrical boundary conditions around the main compression direction ($\sigma_x = \sigma_y$ in the case of compression along the z-axis). This choice was made in a first approach for the imposition of boundary conditions. It was made by Zhang et al. [2009] as well.

Yet, the use of T_X only may obviously be insufficient to fully represent the tridimensional stress state. Several recent studies dedicated to ductile damage showed that the stress state can be fully described by the use of the Lode parameter (function of the third stress invariant), in addition to the stress triaxiality ratio [Bai and Wierzbicki, 2008]. The choice of axisymmetrical boundary conditions may thus also contribute to the observed discrepancy. Taking into account the Lode angle as an additional parameter for the prediction of void closure is another perspective to this work and is discussed in the general conclusion.

Conclusions

Finally, it can be concluded that the new model Cicaporo is capable of predicting the evolution of a sphere with a similar accuracy than the most advanced model from literature, as similar assumptions are used.

The obtained discrepancy with the explicit simulation in terms of final void volume is reduced from 57% (STB model) to 23% (Zhang model and new model Cicaporo). The greatest advantage is taken from the fact that both the Zhang model and the new model Cicaporo consider the change of shape of the void during deformation, whereas the STB model does not. The final discrepancy that is observed with both the Zhang model and the new model Cicaporo may be attributed to the assumptions that were used at the mesoscale to calibrate each model, such that the homogeneity of mechanical fields, axisymmetry of the imposed boundary conditions, or the change of compression direction.

Finally, the use of the Zhang model requires the determination of a virtual material parameter, as it is not strictly defined in the case of materials with strain hardening and/or softening behaviours. The final obtained prediction exhibited a variation of about 20% over the tested range of values for the presented case. Special attention must therefore be paid on the determination of m^* when using the Zhang model in further process simulations.

On the contrary, the new model Cicaporo does not require the choice of a material parameter. The calibration was performed using one typical material behaviour, according to the small influence of material parameters within the range of interest regarding hot metal forming processes.

5.3.2 Case of ellipsoidal voids

The reliability of the proposed model is now assessed regarding its dependence to the voids' initial geometry. In this section, five positions in the workpiece are studied. They are illustrated in Fig. 5.7 on the void-free workpiece.

Positions 1, 2 and 3 are identical to the ones defined in the previous section. Two additional positions 4 and 5 were introduced in order to extend the current study to other positions that are located further from the centerline.

Three explicit simulations were performed. Numerical features are given above in Table 5.1. For each explicit simulation, five ellipsoidal voids are placed according to the five positions. All ellipsoids have the same dimensions $(r_1, r_2, r_3) = (4, 3, 2)$. Various orientations are introduced and are summarized in Table 5.2.

In the first explicit case, the ellipsoids are all oriented along the canonical basis such that $(\overrightarrow{u_1}, \overrightarrow{u_2}, \overrightarrow{u_3}) = (\overrightarrow{e_x}, \overrightarrow{e_y}, \overrightarrow{e_z})$. The three rotation angles are equal to zero. In the second explicit case, the ellipsoids are all oriented such that $(\overrightarrow{u_1}, \overrightarrow{u_2}, \overrightarrow{u_3}) = (\overrightarrow{e_z}, \overrightarrow{e_y}, -\overrightarrow{e_x})$, i.e. using a rotation angle around the y-axis $\theta_Y{=}90^\circ$. In the third explicit case further orientations are defined using several rotations around x and y-axes.

A few ellipsoidal voids are illustrated in Fig. 5.8. As the displacement of the hammer die occurs along the $\overrightarrow{e_z}$ direction, the first orientation case can be seen as a rather favorable case in terms of void closure. It is expected that the voids are mainly deformed along their smallest dimension r_3. On the contrary, the second case may be seen as a rather unfavorable case, since the voids are expected to be mainly deformed along their longest dimension r_1.

Position	Dimensions $(r_1,\ r_2,\ r_3)$	Successive rotation angles (°) $\theta_X,\ \theta_Y,\ \theta_Z$
Position 1	(4, 3, 2)	0, 0, 0
	(4, 3, 2)	0, 90, 0
	(4, 3, 2)	0, 30, 0
Position 2	(4, 3, 2)	0, 0, 0
	(4, 3, 2)	0, 90, 0
	(4, 3, 2)	30, 0, 0
Position 3	(4, 3, 2)	0, 0, 0
	(4, 3, 2)	0, 90, 0
	(4, 3, 2)	45, 30, 0
Position 4	(4, 3, 2)	0, 0, 0
	(4, 3, 2)	0, 90, 0
	(4, 3, 2)	45, 60, 0
Position 5	(4, 3, 2)	0, 0, 0
	(4, 3, 2)	0, 90, 0
	(4, 3, 2)	60, 60, 0

Table 5.2: Initial definition of dimensions and orientation of the ellipsoids at the five positions in the workpiece.

Although the STB model and the Zhang model might not be adapted in the case of non-spherical voids, they will be plotted for comparison purposes, in order to highlight the benefits that are obtained using the new model Cicaporo, with respect to existing models.

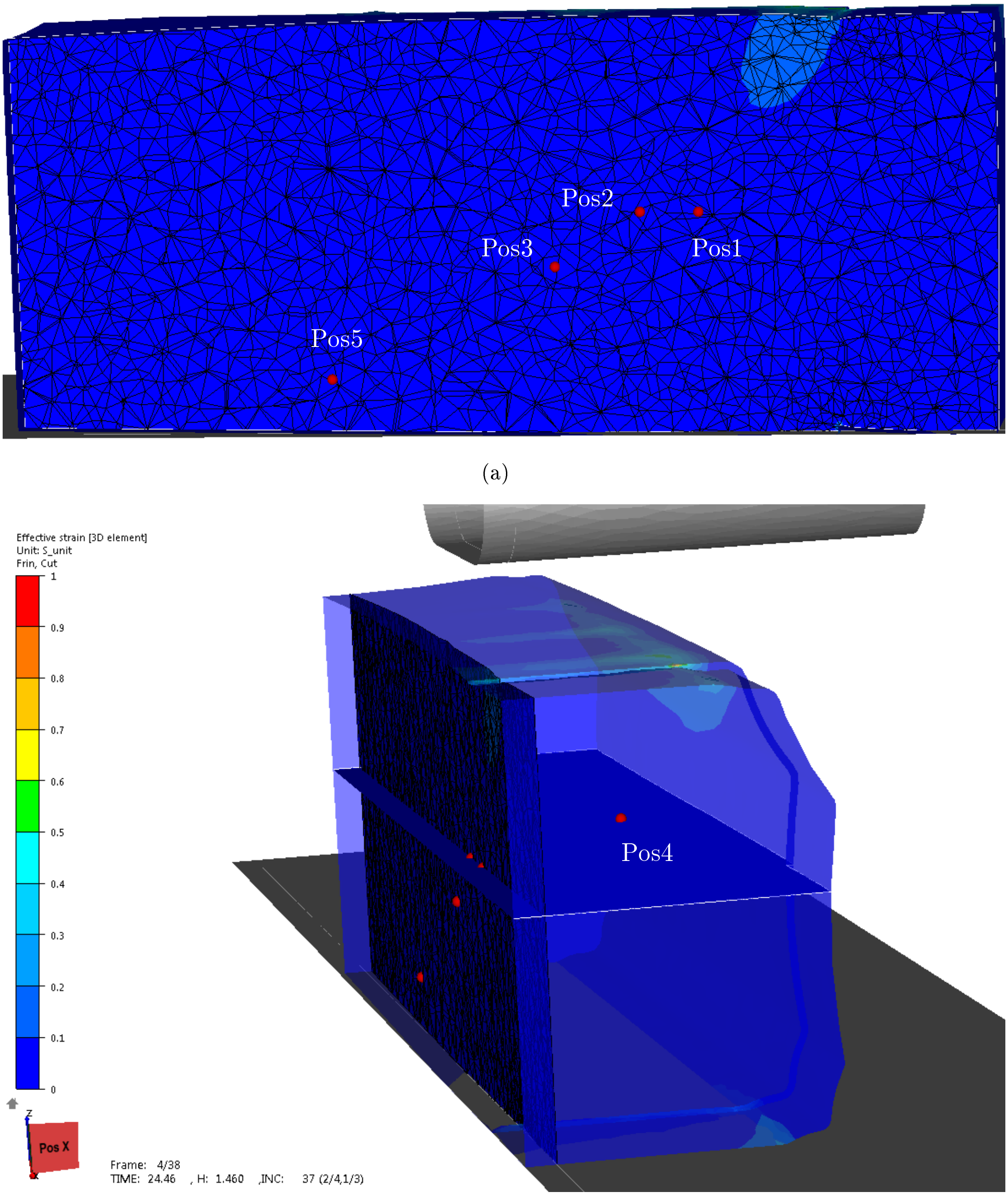

(a)

(b)

Figure 5.7: Definition of the five positions of interest in the process case of open die forging at beginning of PASS2 – blow 1.

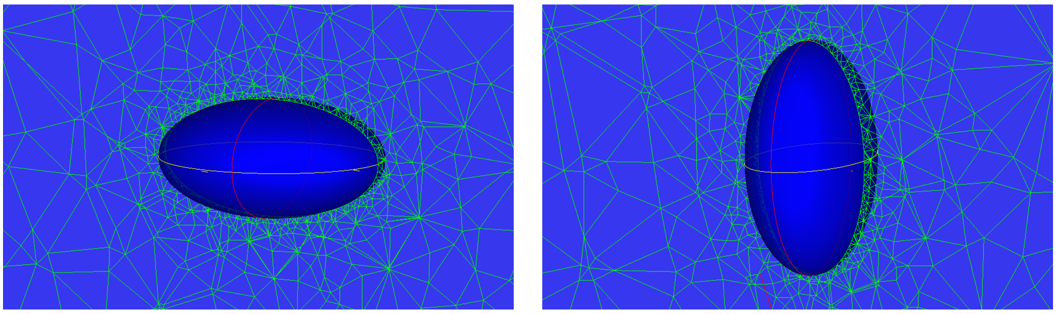

(a) $\theta_X = \theta_Y = \theta_Z = 0$ (b) $\theta_X = 0, \theta_Y = 90^{\circ}, \theta_Z = 0$

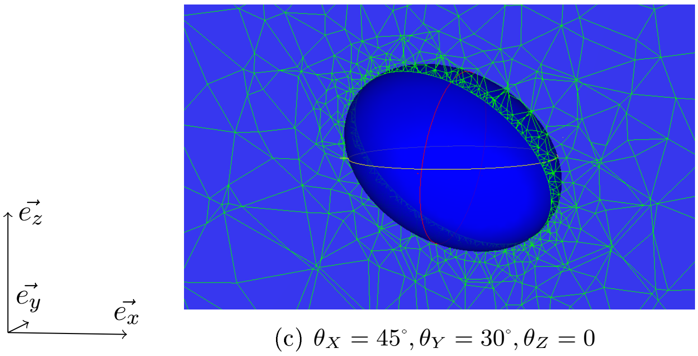

(c) $\theta_X = 45^{\circ}, \theta_Y = 30^{\circ}, \theta_Z = 0$

Figure 5.8: Detail of explicit ellipsoidal shapes of dimensions $(4, 3, 2)$, using various rotation angles.

Position 1

Void volume evolution for position 1 is plotted in Fig 5.9a. Two orientation cases are plotted using blue and red dots, respectively. The STB model is plotted using a black solid line. The Zhang model is plotted using a black dashed line. The new model Cicaporo is plotted using blue and red solid lines, for each orientation respectively.

Void volumes for the two orientation cases exhibit a significant difference in their evolution. This difference can thus be mainly attributed to the difference of initial orientation. The prediction that is provided by the Zhang model is located between both cases. This is coherent with the fact that this model was defined based on a spherical void.

The prediction that is provided by the STB model appears rather similar to the evolution of the ellipsoid in its first orientation case (red curve). This is the result of a coincidence, as the STB model is calibrated based on the evolution of a spherical void. On the other hand, the STB model is unable to predict the behaviour of the void in the second orientation case (blue dots).

Effect of initial orientation The new model Cicaporo gives a good prediction of void evolutions for both orientations. At the end of blow 1, discrepancies of about 7–8% are obtained for both orientation cases (see Fig 5.9b). The final discrepancy at the end of blow 2 is slightly higher for the blue line (about 19%).

This discrepancy is very similar to the one obtained in the case of the spherical voids and that was discussed in the previous section. It can thus also be mainly attributed to the assumptions that were used at the meso-scale.

At the end of blow 2, the predicted difference of final volumes between both orientation cases is 0.43, while the difference obtained in the explicit cases is 0.57. The effect of initial orientation is thus predicted with an accuracy of 14%, while none of other models is capable of predicting this effect.

The void volume evolution in the third orientation case is plotted with yellow color in Fig 5.9b. It is rather similar to the evolution in the first orientation case (red curves). This is due to the fact that the rotation angle of the third orientation case was too low to induce a significant effect on void closure. It is verified with the explicit values, as well as with the predicted values, over the whole duration of blow 1.

The difference that is observed at the beginning of blow 2 is probably due to the steep slope of the curve at end of blow 1, inducing a rather high sensitivity to the value of equivalent strain.

The predicted evolution during blow 2 mainly suffers from the assumption of uniform deformation direction that is made by the model.

Finally, in spite of the global overestimation of the model, the final tendency of the three cases at the end of blow 2 is very well respected.

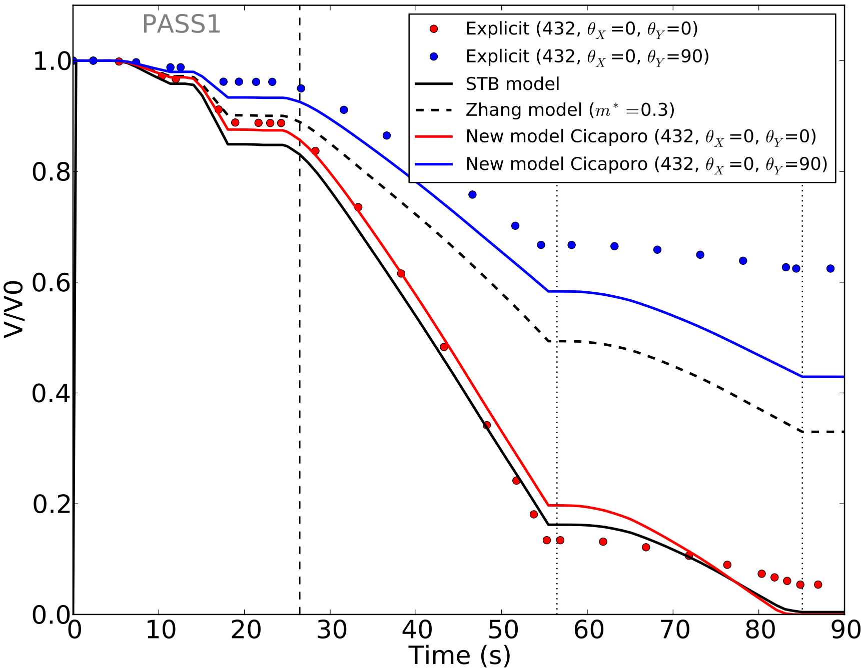

(a) Comparison with existing models

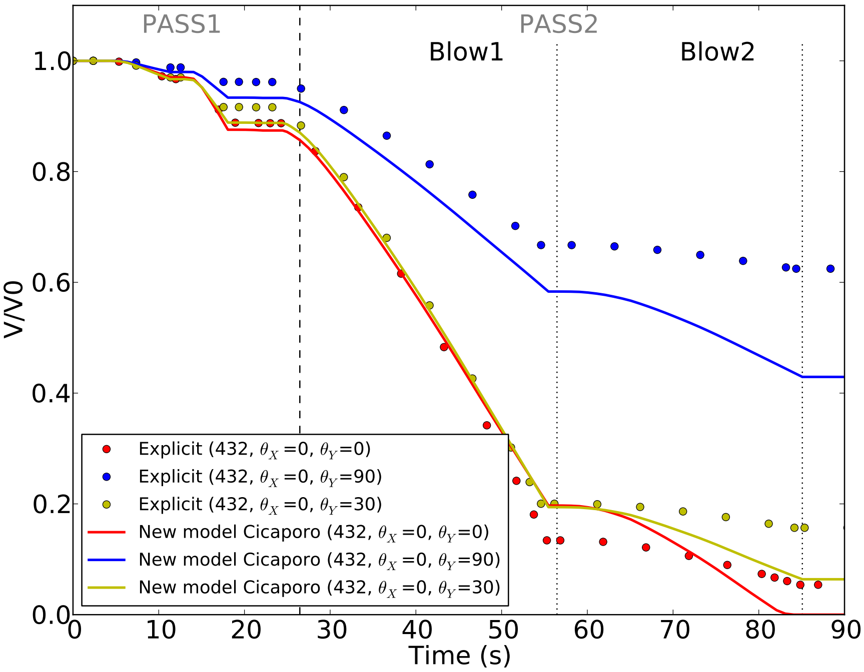

(b) Dependence to initial orientation

Figure 5.9: Void volume evolution for ellipsoidal void, measured at position 1 (explicit simulation), compared to the STB model, the Zhang model and the new prediction model Cicaporo.

Position 2

The results regarding the ellipsoids at position 2 are presented using the same methodology than the one for position 1. In Fig. 5.10a, the prediction of the Zhang model is located between the explicit values of the two orientation cases of the ellipsoidal void. The STB model significantly overestimates the closure about 23% compared to the first orientation case (blue dots), and up to 60% for the second orientation case (red dots). In other words, the use of the STB model indicates that the void is nearly closed at the end of blow 2 (V_f/V_0=0.06), while the final measured void volume varies from $V_f/V_0 = 0.29 - 0.65$ depending on initial orientation.

The new model Cicaporo overestimates void closure at position 2 as well. This might be again explained by the assumptions that are made using the meso-scale.

At this position, the STB model predicts a final void volume that is even lower than the prediction that is made by the new prediction model, considering the initial orientation that is rather favorable for void closure.

The predicted difference in terms of final void volume between both orientation cases is 0.53. It shows that the effect of initial orientation is predicted with excellent accuracy in this case, as this difference is 0.54 in the explicit cases. The dependence to orientation is thus predicted with very good accuracy, despite the global overestimation of closure around 20%.

This result is verified using the comparison of the three orientations presented in Fig. 5.10b. The final overestimation at the end of blow 2 is about 20% with respect to the explicit simulation.

As for the case of spherical voids, the largest overestimation is obtained at position 2 for ellipsoidal voids using several orientations. The discrepancy is therefore most likely due to the assumptions made at the meso-scale. Position 2 is located in a particular zone that is affected by both blows (see Fig. 5.2). The significant change of main deformation direction is thus particularly important in this zone. It might thus significantly contribute to the discrepancy, as the model was calibrated using uniform deformation cases.

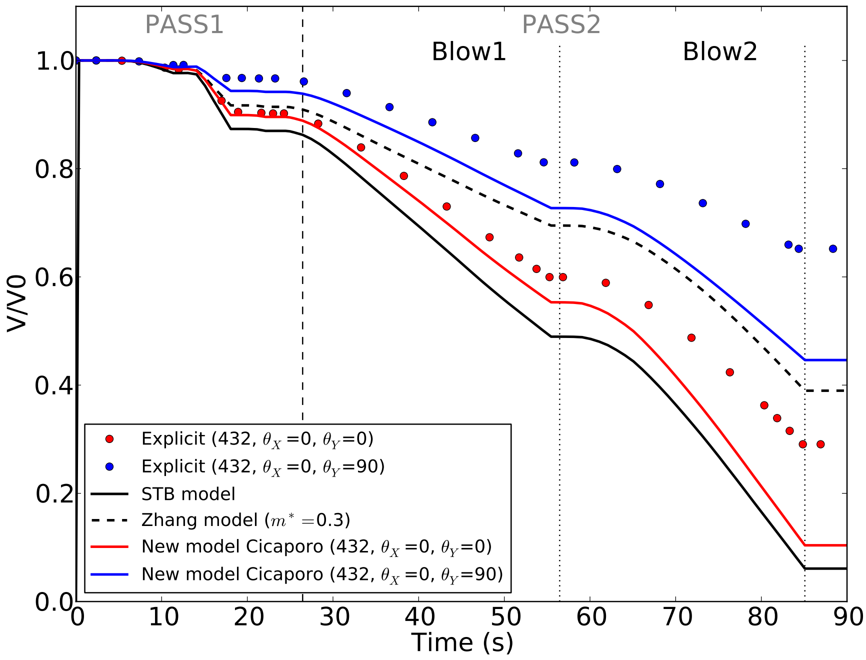

(a) Comparison with existing models

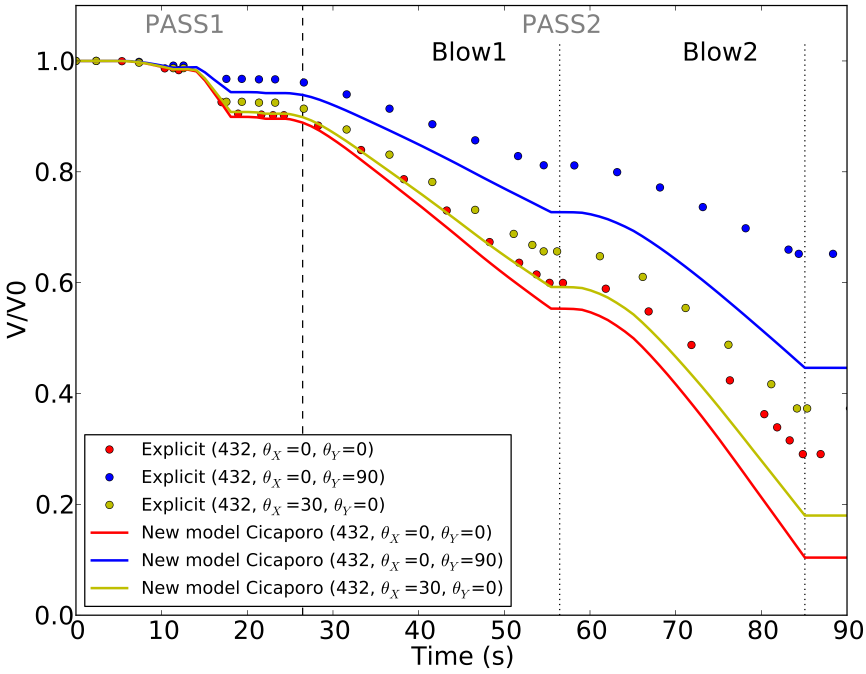

(b) Dependence to initial orientation

Figure 5.10: Void volume evolution for ellipsoidal void, measured at position 2 (explicit simulation), compared to the STB model, the Zhang model and the new prediction model Cicaporo.

Position 3

Position 3 is vertically located under the hammer-die of blow 2 (see Fig. 5.2). The main deformation is therefore rather uniformly orientated along the z-axis during the whole deformation. The main contribution to void closure is coming from the second blow. The curves are plotted in Fig. 5.11.

Again, the Zhang model predicts a void evolution that is between both explicit cases in each orientation with relatively large discrepancies with explicit cases.

As for position 1, the evolution that is predicted by the STB model is rather similar to the explicit measure in the first orientation case (red dots), and overestimates the closure about 0.6 compared to the explicit measure in the second orientation case (blue dots).

On the contrary, the new model Cicaporo provides an excellent prediction, as it remains lower than 10% for all presented orientations at the end of blow 2, and does not generally exceed 2%. It is also verified for the third orientation case that is presebted in Fig. 5.11b. The discrepancy slightly increases at the end of blow 2, as the slope of void volume is relatively elevated at this instant.

The low discrepancies that are obtained can be explained by the fact that the assumptions are better verified at this position. First, as pointed out above, the position is located in a zone where the deformation occurs rather uniformly and homogeneously.

Second, blow 1 has a relatively low effect on void closure, due to the low level of equivalent strain that comes from blow 1 (see Fig. 5.4c). The resulting change of shape of the void is relatively moderate at position 3, compared to the one observed for the previous studied positions 1 and 2.

These remarks are thus very coherent with the discussion regarding the assumptions in the case of spherical voids.

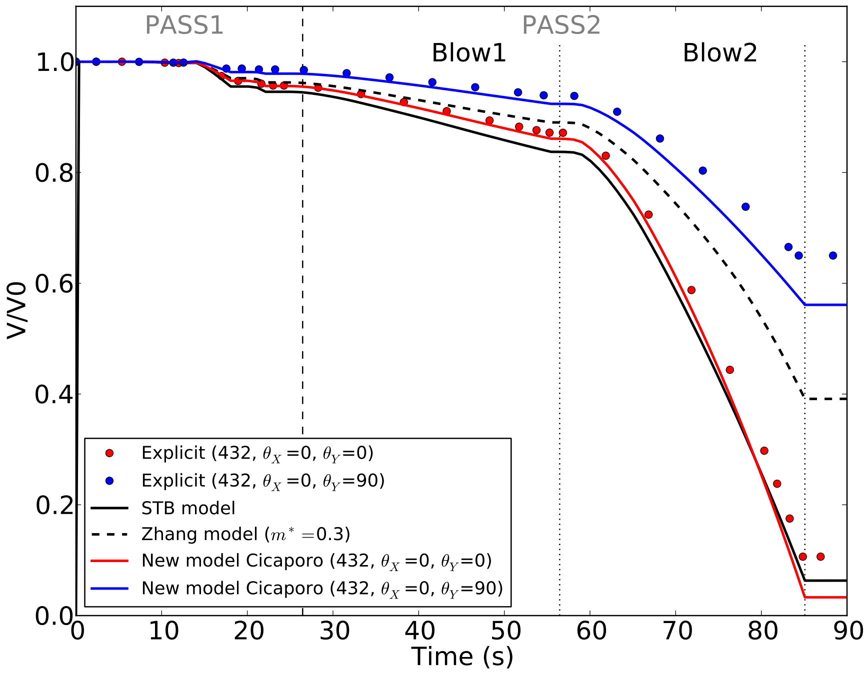

(a) Comparison with existing models

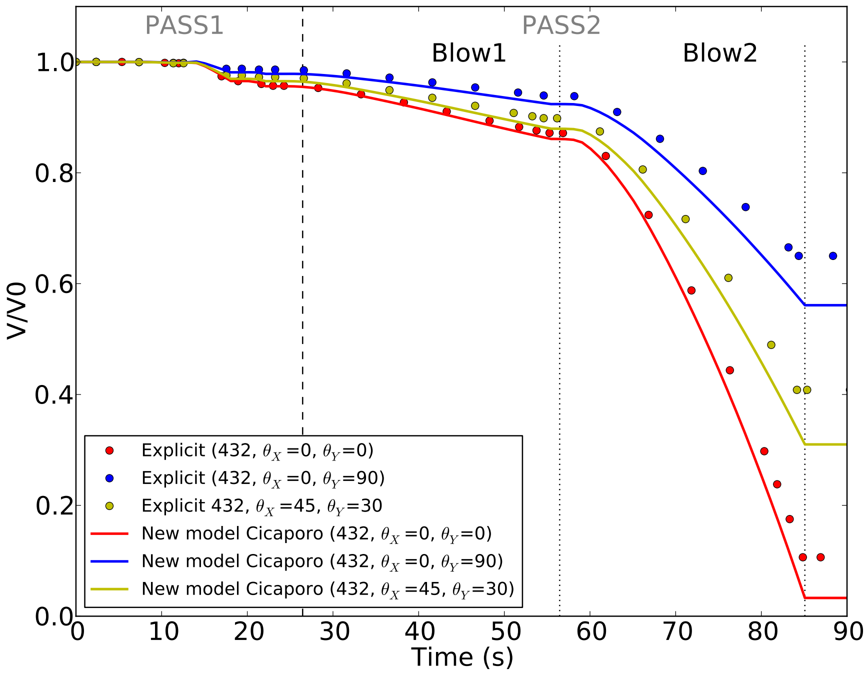

(b) Dependence to initial orientation

Figure 5.11: Void volume evolution for ellipsoidal void, measured at position 3 (explicit simulation), compared to the STB model, the Zhang model and the new prediction model Cicaporo.

Positions 4 and 5

Previous positions 1, 2 and 3 were defined close to the centerline of the workpiece. Two additional positions were also defined further from the centerline, i.e. in areas that are closer to the edges of the workpiece. This enables verifying the reliability of the model for different mechanical conditions. The mechanical loadings at positions 4 and 5 are given in Fig. 5.12. The loading path at position 4 is roughly similar to the one at position 3 in terms of equivalent strain, although the final equivalent strain at the end of blow 2 is lower at position 4 than at the three centerline positions. At position 5, the final value of equivalent strain is significantly lower.

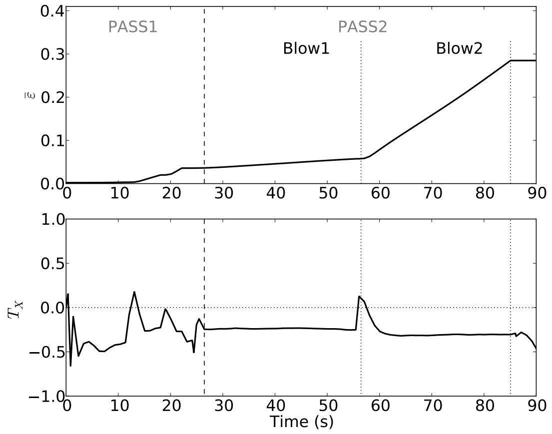

(a) Position 4

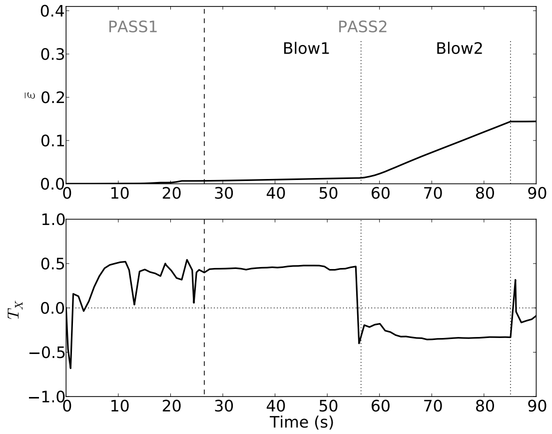

(b) Position 5

Figure 5.12: Evolution of equivalent strain and stress triaxiality ratio for positions 4 and 5 in the workpiece.

In terms of stress triaxiality ratio, the values are less compressive than the ones obtained at previous centerline positions. It is remarkable in the case of position 5, as the stress triaxiality ratio is even positive during blow 1.

These observations have a direct consequence on void volume evolution, according to the dependence of void closure to the stress triaxiality ratio, as illustrated in Figs. 5.13 and 5.14. Regarding position 4, the void volume reduction is globally lower than for the previous positions 1, 2 and 3. This tendency is predicted by all models, as the effect of stress triaxiality is considered in all of them. The final discrepancies thus remain low as well.

At position 4, the STB model predicts a void volume evolution that is comparable to the one predicted by the Zhang model (see Fig. 5.13a). It can be explained by the fact that the level of equivalent strain remains lower that previous positions. The effect due to the change of shape of the void is thus moderate in this case. The discrepancy of the STB model that is mainly due to the non-consideration of this effect is therefore lower at this position than at the previous ones. Yet, both models predict the evolution of a spherical void and the final predicted volumes exhibit rather large discrepancies with both orientation cases.

On the contrary, the new model provides a reliable prediction, as the maximum discrepancy that is obtained remains lower than 10% for both orientation cases.

At position 5, the stress triaxiality ratio exhibits positive values during blow 1 (see Fig. 5.12). Since these values are not combined with a large deformation rate, the resulting effect on void closure remains very low (see Fig. 5.13a)). Nevertheless, the void volume evolution exhibits a slight increase during blow 1. This increase of volume is predicted by the prediction models. The accuracy of the prediction is rather good, as the void deformation is very low.

The effect of initial orientation is predicted with excellent accuracy using the new prediction model Cicaporo. This result can be verified in Figs. 5.13b and 5.14b, in which the additional orientation cases are plotted. For positions 4 and 5, the initial orientation of the third void is significantly different, as the greater angles were used to set the initial ellipsoids.

The void volume predictions now demonstrate the reliability of the model for the case of multiple orientations, and under very different mechanical loadings.

5.3.3 Conclusions

The slight overestimation that is generally observed among all orientation cases is most likely due to the general assumptions that were made for the calibration of the model at the meso-scale. The overestimation has the same order than for the case of spheres. In spite of this, the effect of initial orientation is predicted with excellent accuracy using the new prediction model Cicaporo. For various mechanical loading paths, it was verified that the difference in terms of void volume that is due to initial orientation shows very good agreement with the explicit simulations.

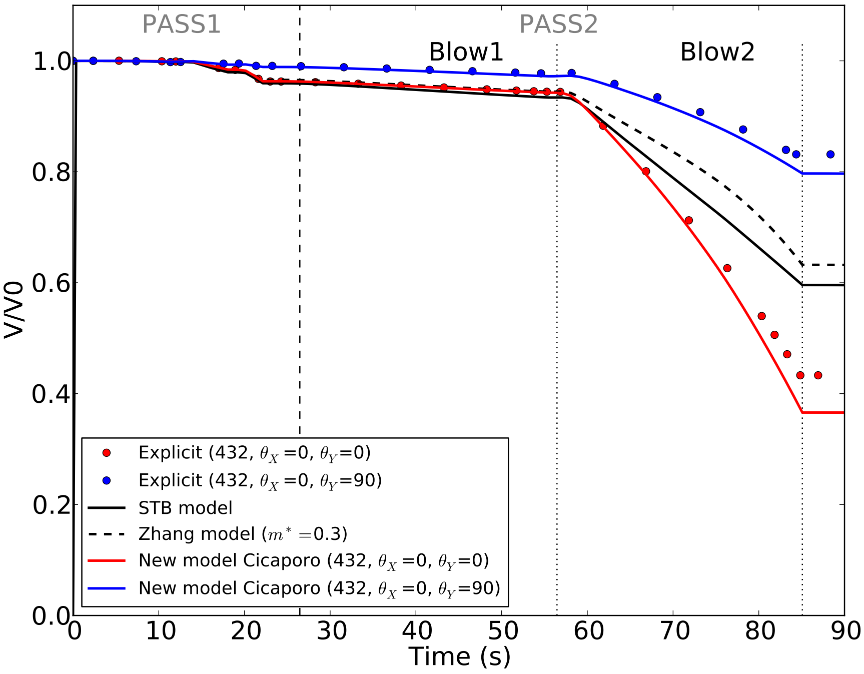

(a) Comparison with existing models

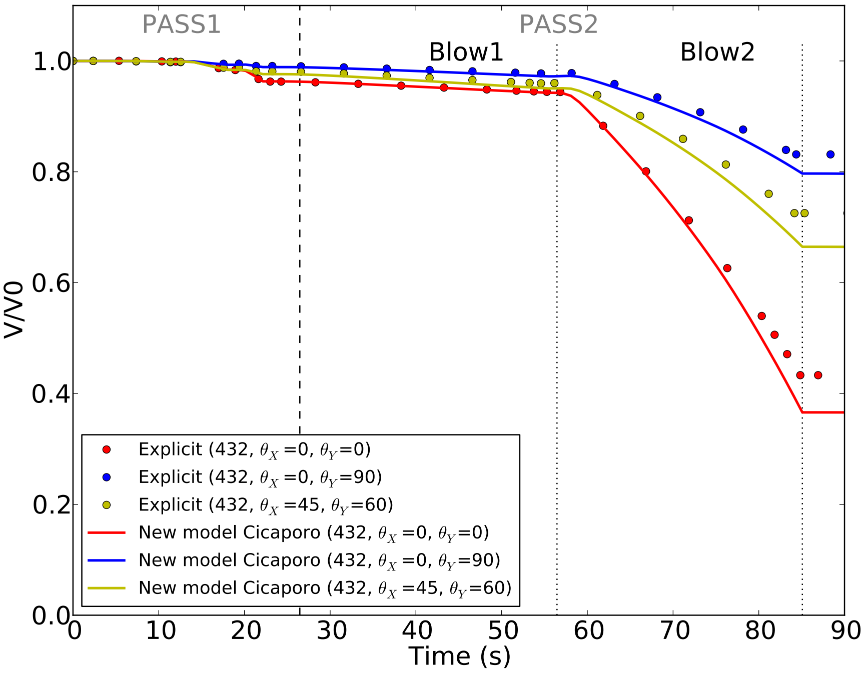

(b) Dependence to initial orientation

Figure 5.13: Void volume evolution for ellipsoidal void, measured at position 4 (explicit simulation), compared to the STB model, the Zhang model and the new prediction model Cicaporo.

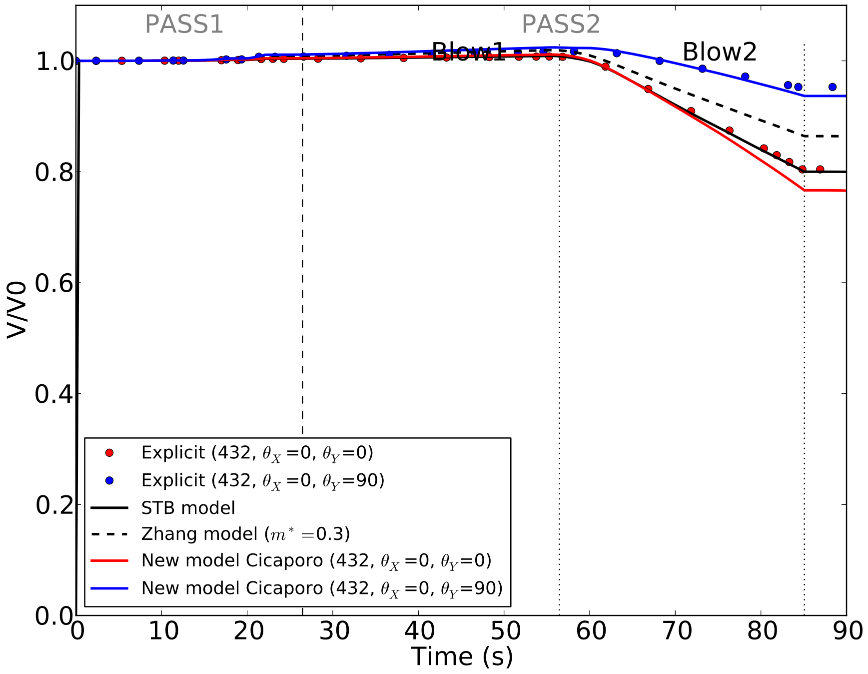

(a) Comparison with existing models

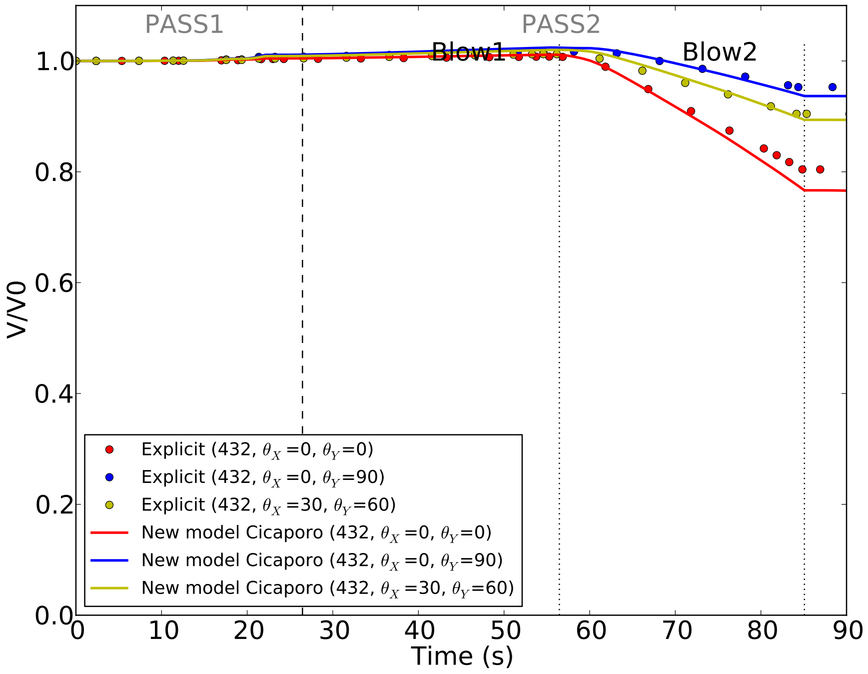

(b) Dependence to initial orientation

Figure 5.14: Void volume evolution for ellipsoidal void, measured at position 5 (explicit simulation), compared to the STB model, the Zhang model and the new prediction model Cicaporo.

5.4 Case of hot rolling

A second validation case was performed using a simulation of hot rolling. The process simulation was provided by Ascometal. Using a similar methodology as in the previous section, two simulations were performed: an explicit simulation, and a void-free simulation.

The explicit simulation contains a series of 9 ellipsoids that are located close to the centerline position. It is illustrated in Fig. 5.15. Although the use of symmetry planes for the definition of the voids might significantly reduce the required number of elements of the mesh, this was not done because the contact between voids' internal faces during computation would be impossible in this case.

Numerical features are given in Table 5.3. The void-free simulation was about 60 times faster than the explicit simulation.

Simulation	Voids	Nb elements	CPU time	Total CPU time
Explicit	9 ellipsoids	3 865 000	5 days 13 hours	66 days 12h
Void-free	–	59 000	2 hours	1 day

Table 5.3: Simulations for the validation case of hot rolling, performed using 12 CPUs (3GHz, 24Go RAM).

Various geometries and orientations were defined at several positions and are described in Table 5.4. The geometries are identical to the ellipsoidal voids that were previously defined in Chapter 4. Two orientations are defined using the rotation angle θ_Y. The other rotation angles θ_X and θ_Z are equal to zero. For each ellipsoid, two cases are thus obtained: the case $(\vec{u_1}, \vec{u_2}, \vec{u_3}) = (\vec{e_x}, \vec{e_y}, \vec{e_z})$, for $\theta_Y = 0$ and the case $(\vec{u_1}, \vec{u_2}, \vec{u_3}) = (\vec{e_z}, \vec{e_y}, -\vec{e_x})$, for $\theta_Y = 90^\circ$.

Positions	Dimensions	Rotation angles (°)
	$(r_1, \quad r_2, \quad r_3)$	$\theta_X, \quad \theta_Y, \quad \theta_Z$
Position 1	Sphere (1, 1, 1)	0, 0, 0
Position 2	Ell-A (2, 1, 1)	0, 0, 0
Position 3	Ell-A (2, 1, 1)	0, 90, 0
Position 4	Ell-B (4, 1, 1)	0, 0, 0
Position 5	Ell-B (4, 1, 1)	0, 90, 0
Position 6	Ell-C (2, 2, 1)	0, 0, 0
Position 7	Ell-C (2, 2, 1)	0, 90, 0
Position 8	Ell-E (4, 3, 2)	0, 0, 0
Position 9	Ell-E (4, 3, 2)	0, 90, 0

Table 5.4: Initial dimensions and orientation of the ellipsoids placed at the 9 positions in the workpiece.

The mechanical loading paths for the first position and for all positions are presented in Fig. 5.16. The values are obtained by point tracking using sensors at the 9 positions in the void-free simulation.

The evolutions of equivalent strain and stress triaxiality ratio are comparable for all positions, with a slight shift in the time-scale. This shift is due to the displacement of the workpiece along the x-axis. A slight difference is obtained in the values of final strain at the end of the pass, between the different positions. The final strain is larger for the positions that are following from the extremity of the workpiece. This difference is due to the fact that the positions were defined relatively close to the extremity of the workpiece.

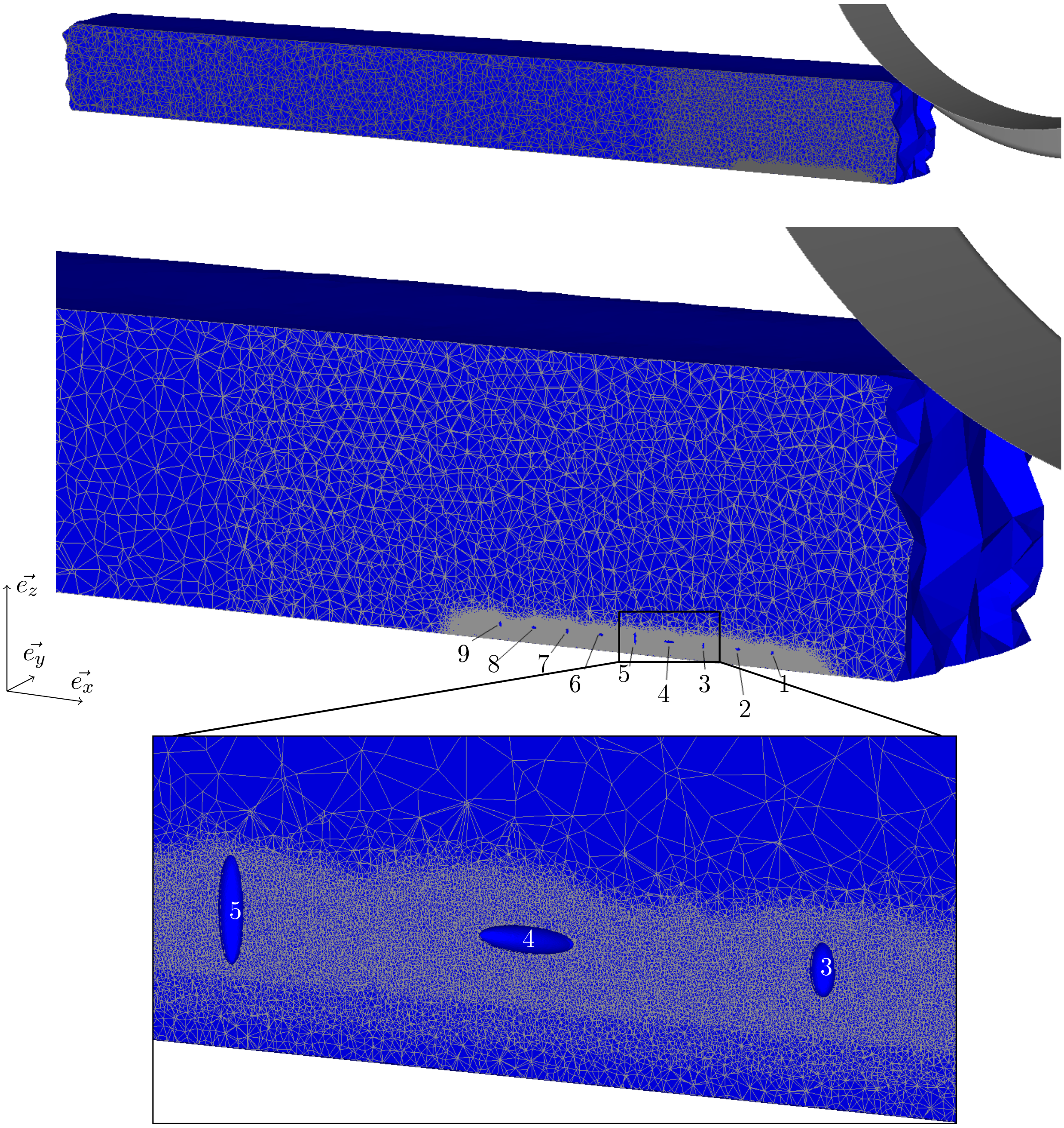

Figure 5.15: Initial explicit mesh of the hot rolling case.

The typical steady state that is classically obtained in rolling processes was not reached yet. Yet, this remark will not hinder the further analysis, as the two compared cases (explicit/void-free) are observed in identical conditions.

An illustration of the strain field is given in Fig. 5.17. Let us note that, conversely to the case of open die forging, the maximum strain values are obtained at the edges of the workpiece. The core is a zone where the equivalent strain remains rather low.

Regarding the values of stress triaxiality ratio in Fig. 5.16a, it is verified that the value remains in the range of validity of the model ($T_X = [-1, 0]$) when deformation occurs, i.e. over $t = 0.05 - 0.19$ s. Lower and higher values can also be observed, but as they are not related to deformation rate, these values have no impact on void closure.

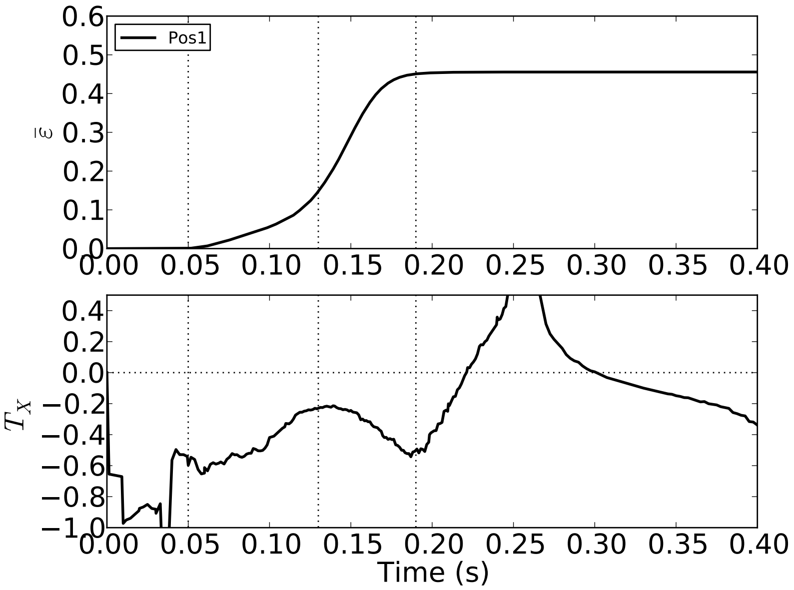

(a) Position 1

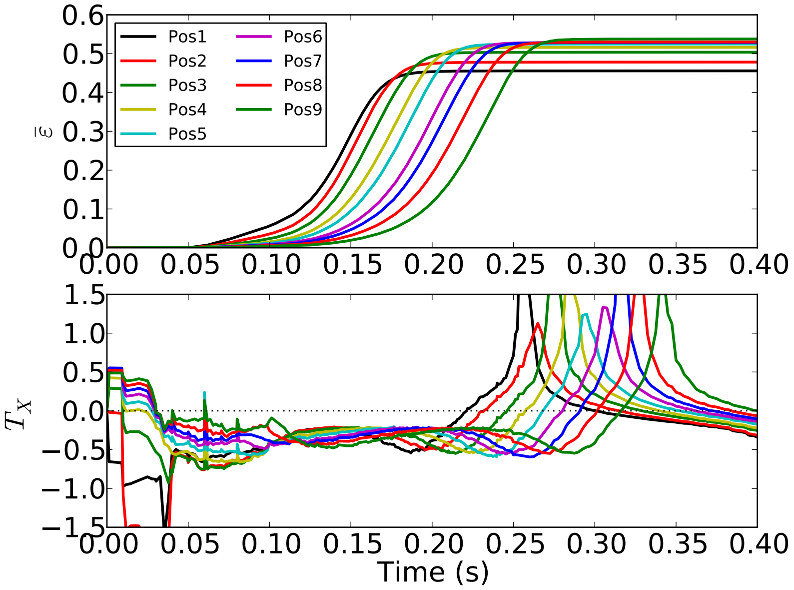

(b) All positions

Figure 5.16: Evolution of equivalent strain and stress triaxiality ratio for the 9 different positions in the workpiece, (a) for position 1 and (b) for all positions (superimposed).

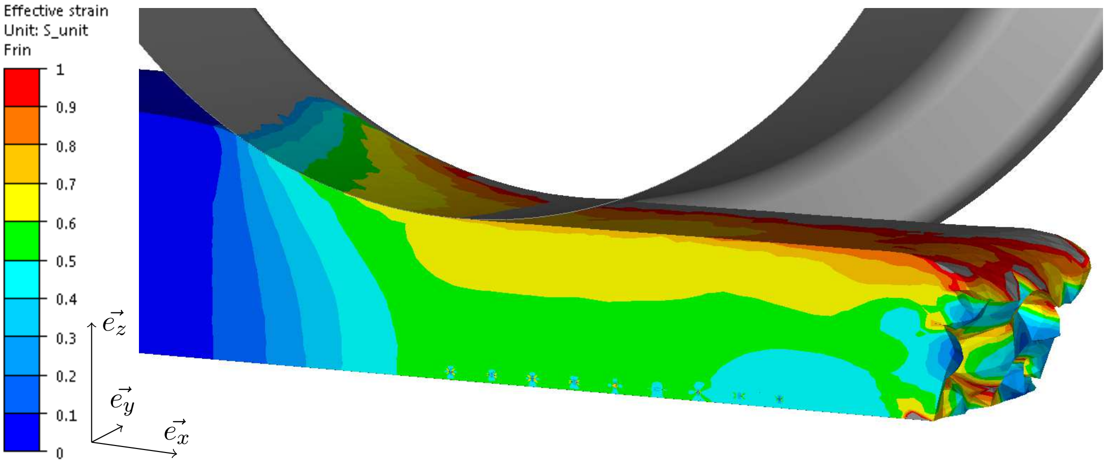

Figure 5.17: Equivalent strain at t=0.28 s for the explicit case of hot rolling.

5.4.1 Spherical void

Void volume evolution of the spherical void (position 1) is plotted in Fig. 5.18 for the explicit simulation, the STB model, the Zhang model and the new prediction model Cicaporo. The closure behaviour exhibits a change of slope around $t = 0.13$ s, which is a direct consequence of the change of slope in the strain evolution (Fig. 5.16a). When the main deformation occurs, (over $t = 0.13 - 0.19$ s), stress triaxiality ratio varies from -0.2 to -0.5.

The general tendency of all models is a slight overestimation of the closure with respect to the values from the explicit simulation This was already observed in the previous case of open die forging. Similar reasons are pointed out.

Underestimation of void closure in the explicit cases First, the void closure in the explicit simulation might be slightly underestimated due to the mesh size that is set in the surrounding of the void. Due to memory limitations, difficulties were encountered when meshing the workpiece according to the prescribed value $h_{min} = 0.25$ mm (Chapter 2, section 2.5.1). For several voids (e.g. ellipsoid 5 in Fig. 5.15), coarse elements are relatively close to the upper part of the void. However, the resulting error regarding the measured volume shall not exceed 2%, according to the sensitivity study in Chapter 2.

The general assumptions on which are based the prediction models may also be pointed out and are discussed now.

Homogeneity of the mechanical fields Let us focus first on the assumption of homogeneous mechanical fields around the voids. In Fig. 5.19a, the field of equivalent strain at $t = 0.13$ s is presented. The gradient is illustrated by plotting the equivalent strain values *vs.* a segment length in Fig. 5.19c. The values of equivalent strain exhibits a certain gradient in the x direction, about 0.025 over the whole segment length. The boundary conditions that are used at the RVE-scale do not consider this gradient, as a vertical displacement is homogeneously applied along the z direction. The final shape can be observed in Fig. 5.19b. Contact between internal faces was obtained at the left part of the void, while the right part of the void was not completely closed up. This effect was not taken into account in the simulation at the RVE-scale using homogeneous boundary conditions.

Presence of voids in the macroscopic explicit simulation The assumption regarding the absence of impact of the presence of voids on the macroscopic mechanical fields is also discussed now. The evolution of equivalent strain is plotted for the void-free simulation and the explicit simulation in Fig. 5.20. For the explicit simulation, the mechanical fields are unknown at the exact position of the void, as the voids are not meshed (see Fig. 5.19). The value was thus assessed at the center of the void using a linear interpolation of the gradient, in a first approximation.

Note that the explicit simulation was interrupted when the level of equivalent strain reached a constant value (after $t = 0.23$ s in Fig. 5.20), as void closure already reached its final state at this instant. In the range of interest $t = 0.05 - 0.19$ s for void closure, the evolution of mechanical fields exhibit a non-negligible difference. A shift is observed for both values (equivalent strain and stress triaxiality ratio). This indicates that the assumption is not strictly verified in this case. Note however that the tendencies of both curves, as well as the minimum and maximum values, are nearly identical in both cases. The observed shift in the mechanical fields can consequently be observed in the predicted evolutions, as they are based on the mechanical fields of the void-free simulation. This can be observed in Fig. 5.18a. The predicted closure is thus overestimated for all models.

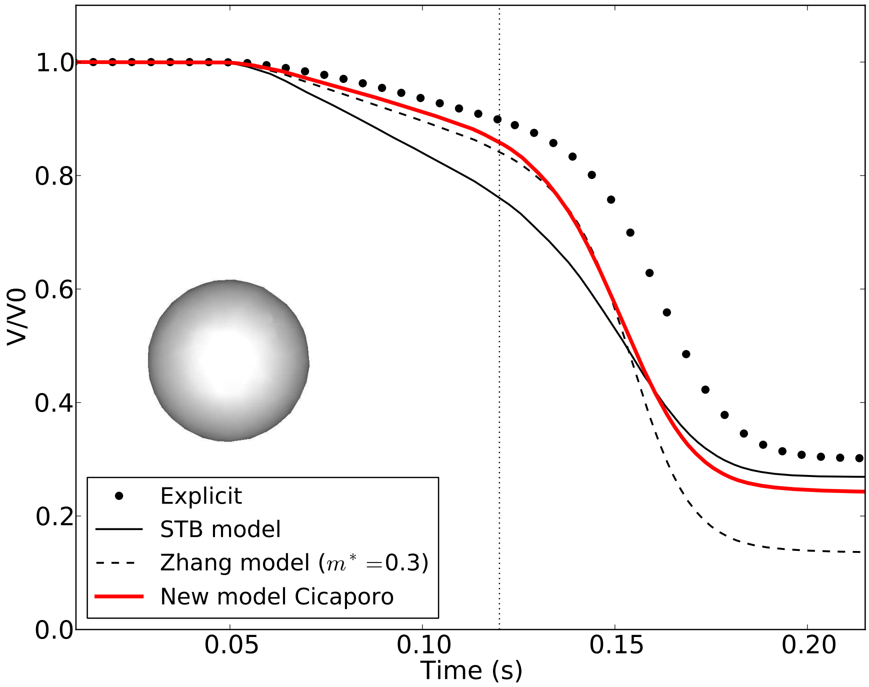

(a) Void volume evolution in time

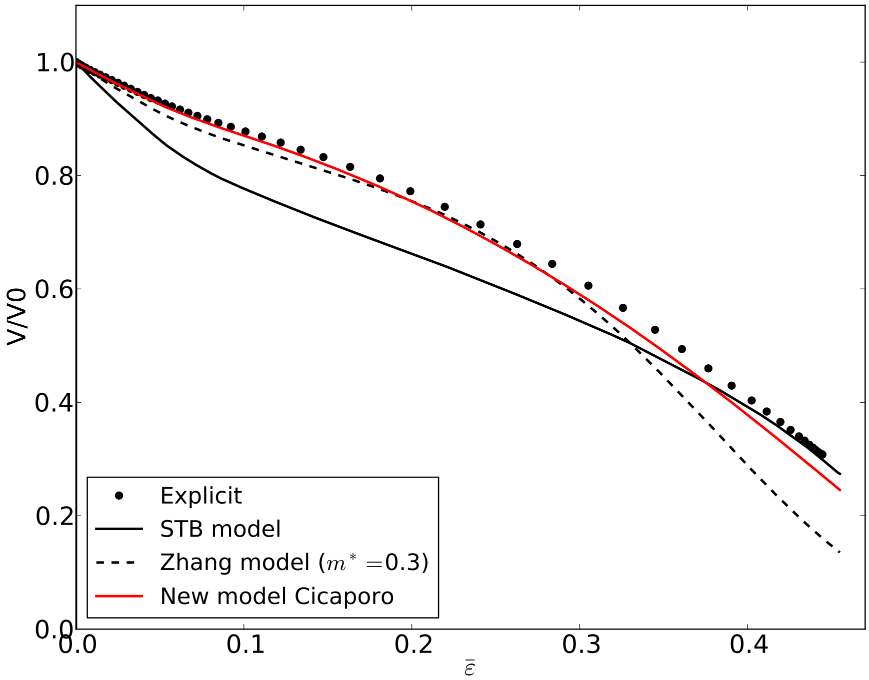

(b) Void volume evolution *vs.* equivalent strain

Figure 5.18: Void volume prediction for a spherical void compared to the STB model, the Zhang model, and to the values measured in the explicit simulations.

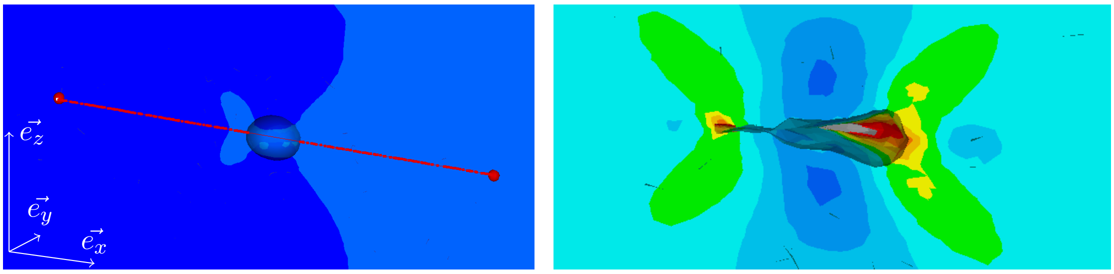

(a) $t = 0.13$ s (b) Final state $t = 0.28$ s (zoom)

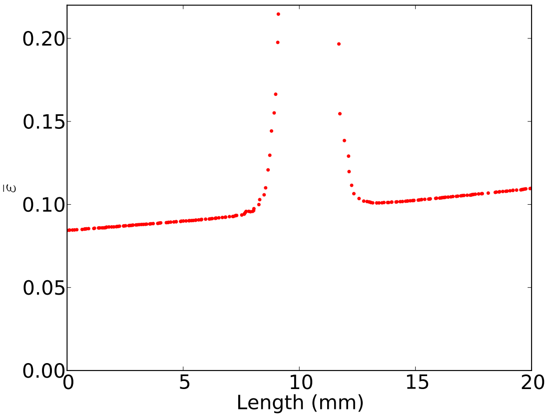

(c) Strain *vs.* length at $t = 0.13$ s

Figure 5.19: Detail of equivalent strain field around the spherical void at various instants of deformation.

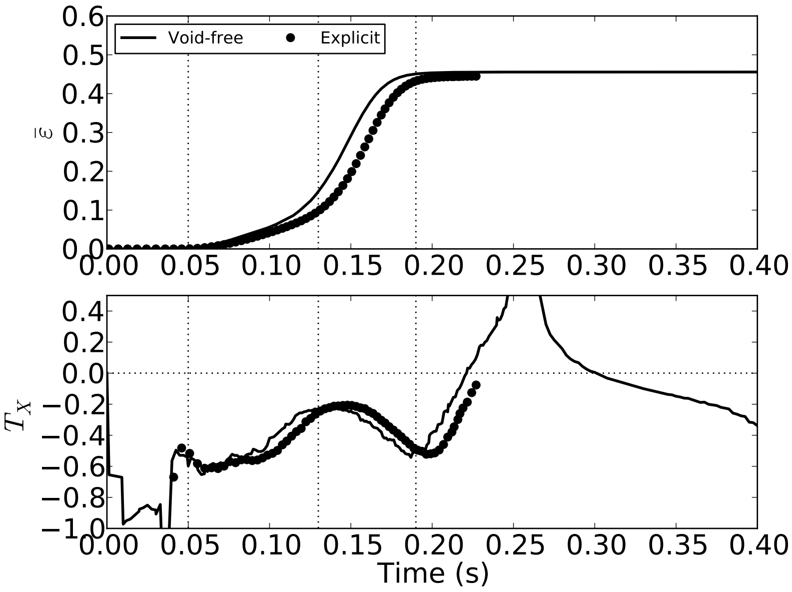

Figure 5.20: Comparison of mechanical fields obtained from the void-free simulation, and the extrapolated value from the explicit simulation, for position 1.

In Fig. 5.18b, the void volume is plotted *vs.* equivalent strain in order to hide the time shift. The value of equivalent strain in the explicit case is obtained by the spatial interpolation, as presented above. As expected, the predicted evolution of closure with respect to the equivalent strain shows better agreement than the evolution in time. This remark indicates that the main difference that is observed on the evolution in time is due to the time shift of the values, but that the mechanical loading path is nearly identical.

Finally, note that the final change of slope in the evolution in time is due to the slope of equivalent strain. It is not due to the final closure stages as it was described in the previous chapter, regarding the presence of contact at the internal faces of the void. In the cases presented in the previous chapter, the change of slope was observed on the evolution in equivalent strain, and occurred when the void volume was very low (typically $V/V_0 < 0.2$). In Fig. 5.18b, the final void volume is greater than 0.2, and the change of slope is not observed regarding the evolution in equivalent strain. As a consequence, the final value of void volume can be obtained from both plots (evolution in time or evolution in equivalent strain).

Closure prediction for the spherical void In Fig. 5.18, both the new model Cicaporo and the Zhang model provide the best prediction of void closure at the beginning of deformation ($t = 0.05 - 0.13$ s). This is due to the fact that both models are based on RVE simulations using similar assumptions. The difference that is obtained at the end of deformation (further than $t = 0.13$ s) is explained by the different analytical functions that are used to model void volume evolution, especially regarding the final stages.

Note that the void volume that is predicted using the STB model shows relatively good accuracy at the end of deformation. This is most likely the result of a compensation between overestimation and underestimation during the loading path. The STB model generally overestimates void closure for low-compressive triaxiality ratios and generally underestimates void closure for large equivalent strain values, as it does not consider the change of void shape.

Over the whole deformation range, the new prediction model Cicaporo predicts void closure with excellent accuracy (lower than 6%) in spite of the assumptions that were discussed above.

5.4.2 Prolate ellipsoid A

In the case of ellipsoid A, the void evolution is studied for the two orientation cases. The shapes of voids during deformation are illustrated in Figs. 5.21 and 5.22. In the first orientation case, the initial void is oriented such that its longer dimension is colinear to x-axis, i.e. the principal displacement direction of the workpiece in the rolling process. The main deformation direction is roughly applied along z, i.e. perpendicular to the longest dimensions of the void. Its volume evolution is plotted in Fig. 5.23a. In the second orientation case, the void is oriented such that its longer dimension is almost colinear to z-axis, i.e. the main deformation direction. Its volume evolution is plotted in Fig. 5.23b.

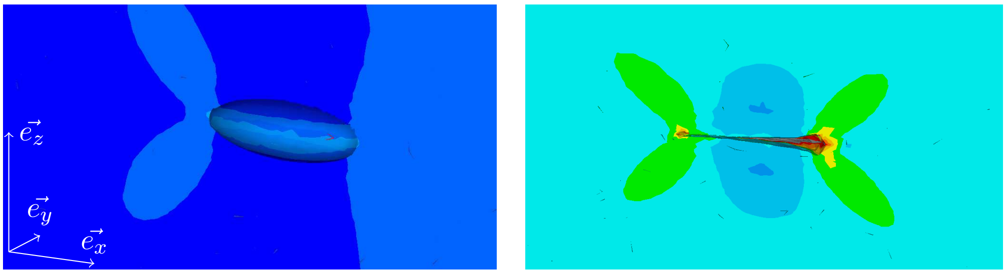

(a) $t = 0.14$ s (b) Final state $t = 0.28$ s

Figure 5.21: Detail of equivalent strain field around ellipsoid A ($\theta_Y = 0$) at various instants of deformation.

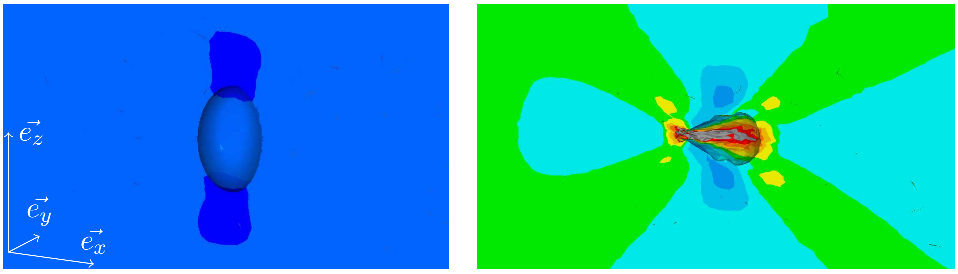

(a) $t = 0.15$ s (b) Final state $t = 0.28$ s

Figure 5.22: Detail of equivalent strain field around ellipsoid A ($\theta_Y = 90^{\circ}$) at various instants of deformation.

Effect of initial orientation A significant difference in terms of final closure is observed for the explicit simulation, between the two orientation cases. The final void volume for the first orientation (Fig. 5.23a) is $V_f/V_0 = 0.19$ and is much larger in the second orientation case (Fig. 5.23b) with $V_f/V_0 = 0.65$. The difference is 0.46 and directly results from the effect of initial orientation.

This difference is not considered by the STB model, neither by the Zhang model. As a consequence, the prediction of each model is independent on the initial orientation. The resulting discrepancies are thus rather large, especially for the second orientation case (Fig. 5.23b). The STB and the Zhang models overestimate final closure of about 35% and 60%, respectively. The overestimation by the new model Cicaporo is about 3% for the second orientation case.

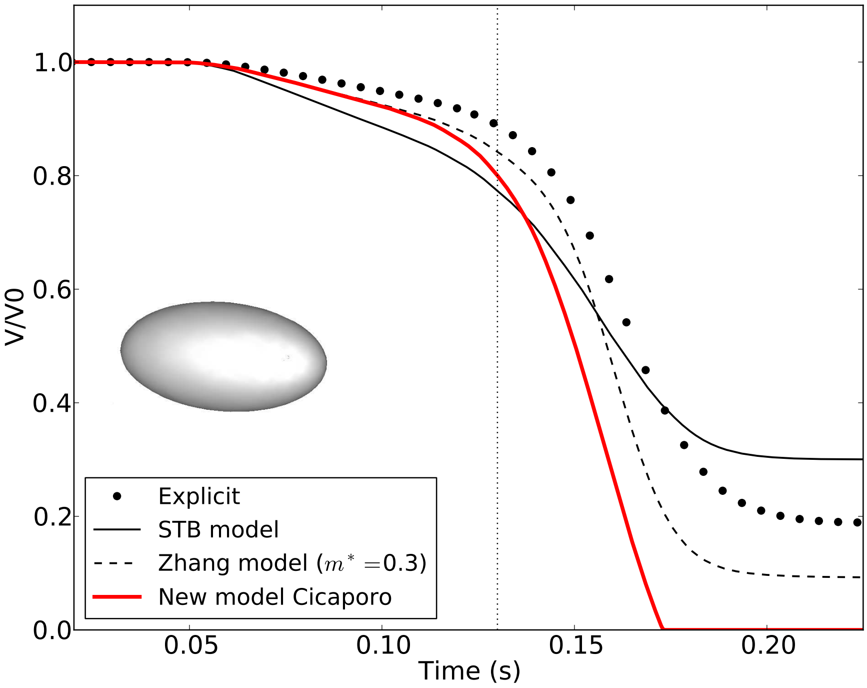

(a) Ell-A $(2,1,1)$ $\theta_Y = 0$

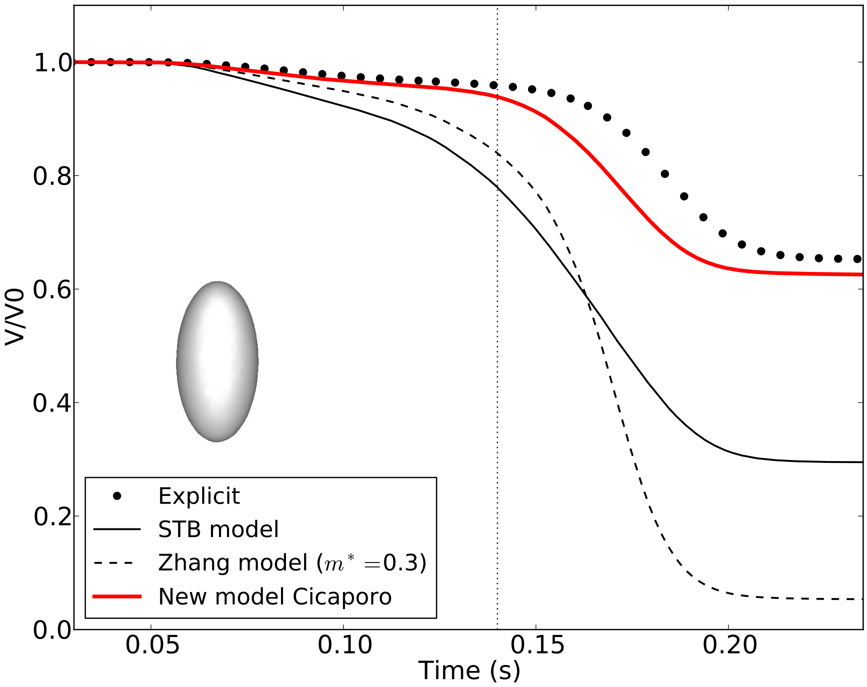

(b) Ell-A $(2,1,1)$ $\theta_Y = 90^{\circ}$

Figure 5.23: Void volume prediction for a prolate ellipsoidal void $(r_1, r_2, r_3) = (2, 1, 1)$ with two different orientations, compared to the STB model, the Zhang model, and to the values measured in the explicit simulations.

Assumptions The new model Cicaporo predicts complete closure in the first orientation case Fig. 5.23a, while the explicit final volume is $V_f/V_0 = 0.19$. Fig. 5.21b illustrates the final shape of this void. In fact, a similar tendency is observed as for the case of the spherical void: the left part of the void is completely closed, while a residual cavity remains on the right part of the void. The discrepancy is thus mainly due to the assumptions of the model in terms of homogeneity of the mechanical fields.

Regarding the beginning of the curves, the overestimation is significant for all models. This was already observed for the spherical case. The same explanation can be given, relatively to the time shift that was observed in the mechanical loading paths (Fig. 5.20).

The final discrepancy that is obtained by the new prediction model is 19%.

5.4.3 Prolate ellipsoid B

The case of the prolate ellipsoid B is very similar to the previous one. The aspect ratio r_1/r_3 of ellipsoid B is twice the one of ellipsoid A. The shapes of voids during deformation are illustrated in Figs. 5.24 and 5.25.

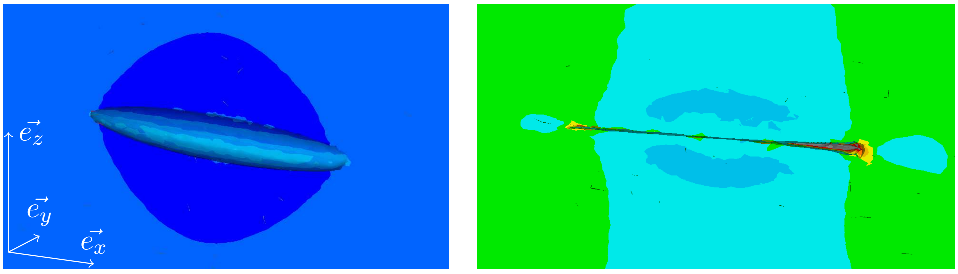

(a) $t = 0.16$ s

(b) Final state $t = 0.28$ s

Figure 5.24: Detail of equivalent strain field around ellipsoid B ($\theta_Y = 0$) at various instants of deformation.

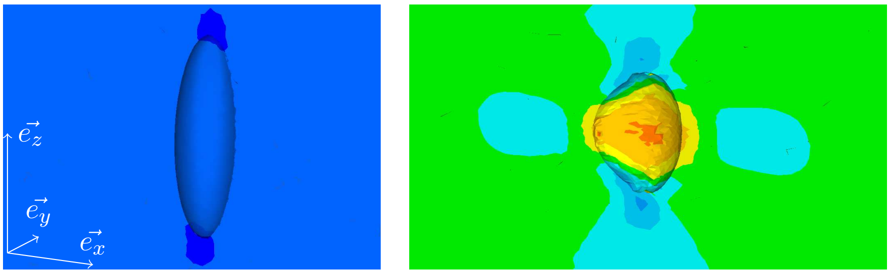

(a) $t = 0.17$ s

(b) Final state $t = 0.28$

Figure 5.25: Detail of equivalent strain field around ellipsoid B ($\theta_Y = 90^{\circ}$) at various instants of deformation.

As the initial void geometry is comparable to the previous case, the results in terms of void volume evolution is very similar to the ones presented above.

Due to the fact that the aspect ratio is larger, the effect of orientation is emphasized. As a result, the difference in terms of final void volumes between both orientation cases is greater. For ellipsoid B, the difference due to initial orientation is 0.84.

The explicit simulation predicts a nearly complete closure in the case of Fig. 5.26a, as the final volume is very low $V_f/V_0 = 0.07$. This overestimation is coherent with the

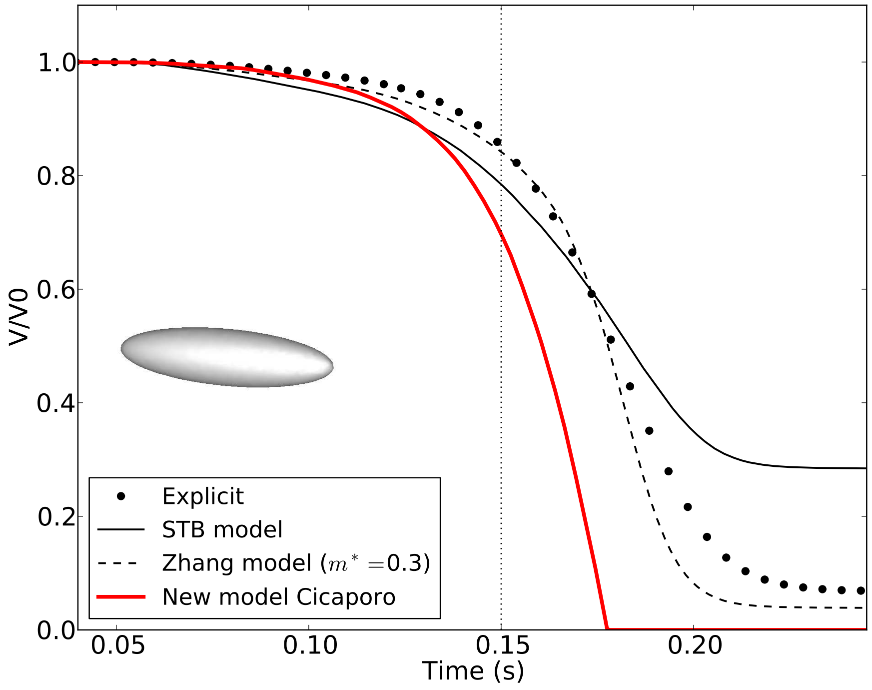

(a) Ell-B $(4, 1, 1)$ $\theta_Y = 0$

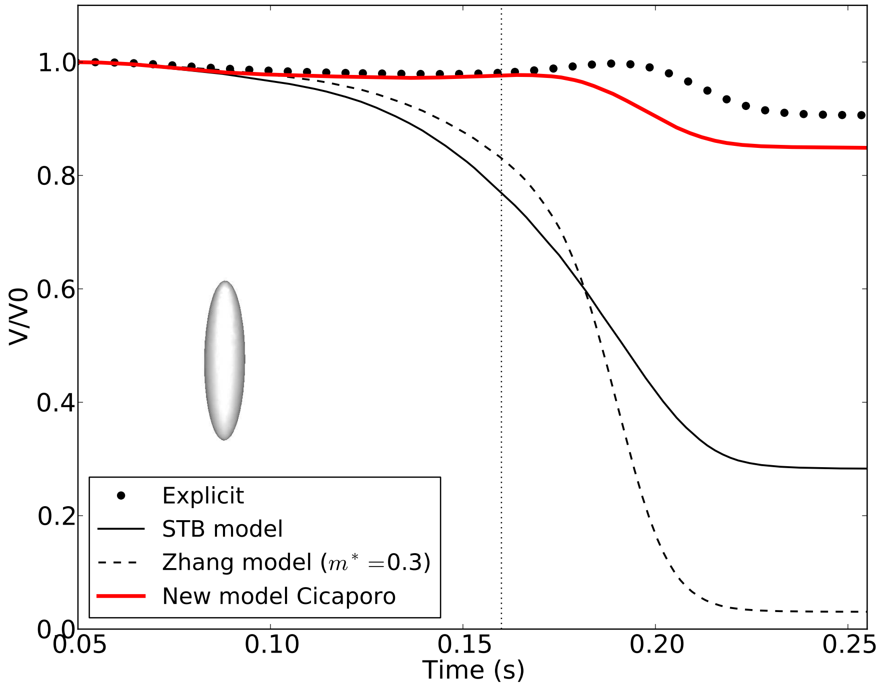

(b) Ell-B $(4, 1, 1)$ $\theta_Y = 90^{\circ}$

Figure 5.26: Void volume prediction for a prolate ellipsoidal void $(r_1, r_2, r_3) = (4, 1, 1)$ with two different orientations, compared to the STB model, the Zhang model, and to the values measured in the explicit simulations.

general overestimation that was observe in previous cases, which is explained by the general assumptions of the meso-scale approach.

In addition, according to the calibration that was made in the previous chapter (section 4.4.4), the case of ellipsoid B was the case in which the fitting exhibited the largest overestimation of closure coefficients. The values of closure coefficient may also contribute to the overestimation in this case.

For the same reasons as previously described, the STB model and the Zhang model show rather large discrepancies with the explicit case, as none of both considers the effect of initial orientation. On the contrary the new model Cicaporo is able to predict this dependence, as the predicted final void volume difference is 0.85.

For each orientation cases, the final void volume is predicted with 0.05 discrepancy with each explicit case.

It is noteworthy that for this ellipsoid, a slight increase of the void volume can be observed for the second orientation case in Fig. 5.26b. This effect was not predicted by any model. This particular behaviour may be explained by the actual mechanical conditions that a void undergoes. The particularly non-symmetric shape of the final void in Fig. 5.25b indicates that the deformation of the void did not occur in the same conditions than in the RVE simulations.

5.4.4 Oblate ellipsoid C

In the case of the oblate ellipsoid C, two orientation cases are studied as well. The same methodology is used as for previous voids.

The shapes of voids during deformation are illustrated in Figs. 5.27 and 5.29. In the first case, the void is oriented such that its shortest dimension is colinear to the main deformation axis z. Void volume evolutions are presented in Fig. 5.28a. In the second case, the void is oriented such that its shortest dimension is perpendicular to the main deformation axis z. The main deformation thus roughly occurs along one of the longest dimensions of the ellipsoidal void. Void volume evolutions are presented in Fig. 5.28b.

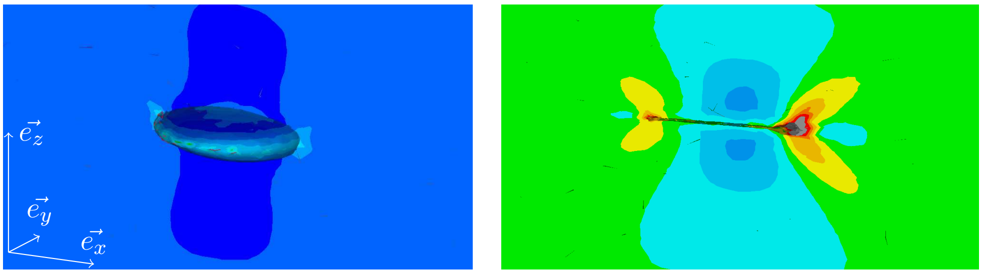

(a) $t = 0.18$ s

(b) Final state $t = 0.28$ s

Figure 5.27: Detail of equivalent strain field around ellipsoid C ($\theta_Y = 0$) at various instants of deformation.

In the first orientation case, the closure is particularly efficient, and the final volume is nearly equal to zero. The final shape of the void is illustrated in Fig. 5.27b and shows that contact was encountered over almost the entire internal surfaces of the void. This is in very good agreement with the new model, as complete closure is predicted.

In the second orientation case, the final void volume is predicted with an excellent accuracy.

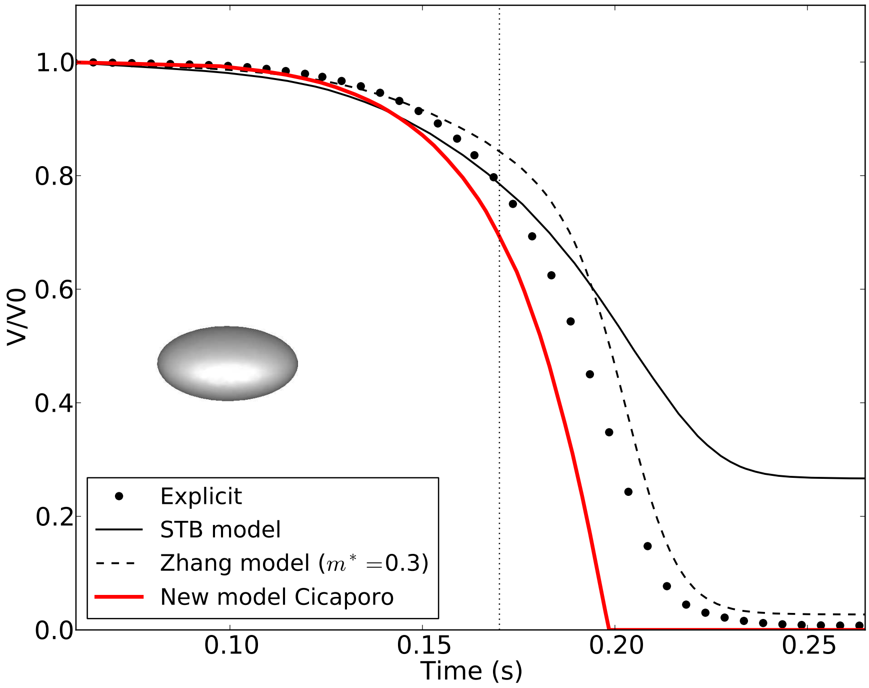

(a) Ell-C $(2, 2, 1)$ $\theta_Y = 0$

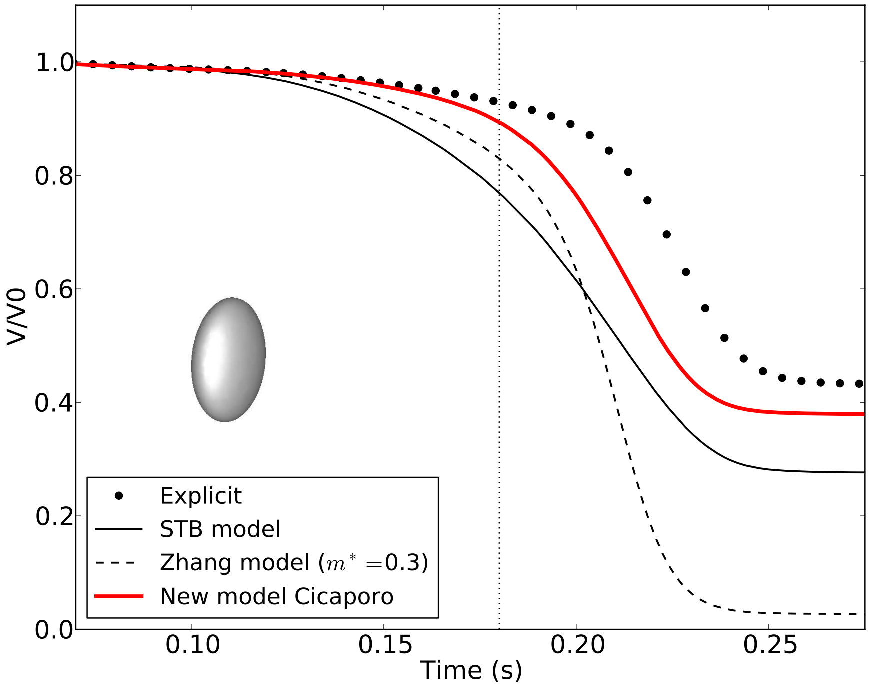

(b) Ell-C $(2, 2, 1)$ $\theta_Y = 90^\circ$

Figure 5.28: Void volume prediction for an oblate ellipsoidal void $(r_1, r_2, r_3) = (2, 2, 1)$ with two different orientations, compared to the STB model, the Zhang model, and to the values measured in the explicit simulations.

Due to the strong dependence to initial void morphology, the STB model and the Zhang model exhibit relatively large discrepancies. Note that for the first orientation case, the Zhang model shows rather good agreement with the explicit case, although the model supposedly predicts the evolution of a spherical void. On the other hand, its prediction gives a discrepancy of 41% with the explicit case for the second orientation.

The prediction of final void volume given by the new model Cicaporo shows a discrepancy lower than 5% for both orientation cases.

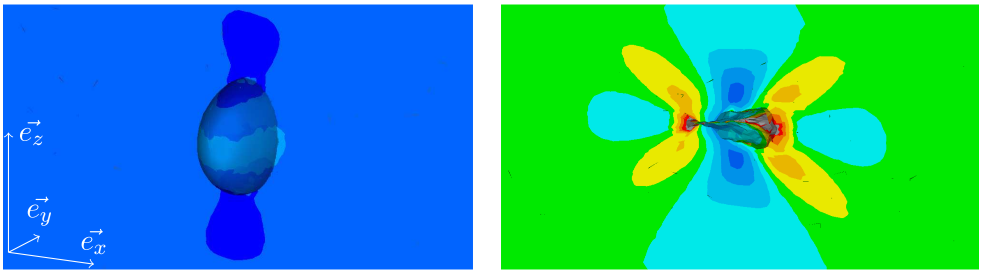

(a) $t = 0.19$ s (b) Final state $t = 0.28$ s

Figure 5.29: Detail of equivalent strain field around ellipsoid C ($\theta_Y = 90^\circ$) at various instants of deformation.

5.4.5 Ellipsoid E

The ellipsoidal void E is defined such that $r_1 \geq r_2 \geq r_3$. As for previous ellipsoids, two orientation cases are studied for this void. The shapes of voids during deformation are illustrated in Figs. 5.30 and 5.32.

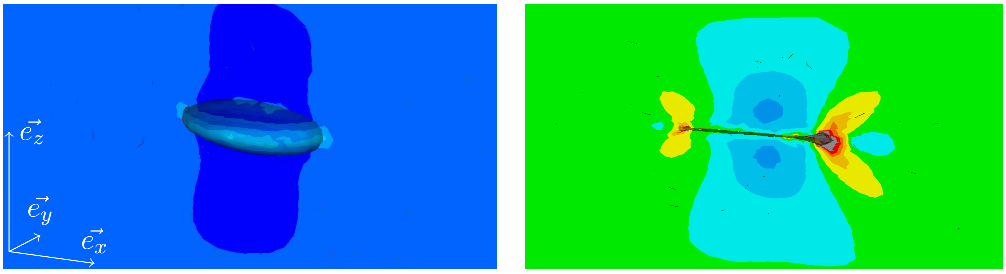

(a) $t = 0.20$ s (b) Final state $t = 0.28$ s

Figure 5.30: Detail of equivalent strain field around ellipsoid E ($\theta_Y = 0$) at various instants of deformation.

The first case is oriented such that its shortest dimension is colinear to the main deformation axis z, and the results are given in Fig. 5.31a. The second case is oriented such that its longest dimension is colinear to the main deformation axis z, and the results are given in Fig. 5.31b.

Very similar comments can be made as for the previous prolate and oblate ellipsoids.

The Zhang model shows a very good agreement with the explicit case for the first orientation Fig. 5.31a, although it is calibrated using a spherical void. The prediction of the Zhang model exhibits a discrepancy of 50% on the final void volume for the second orientation.

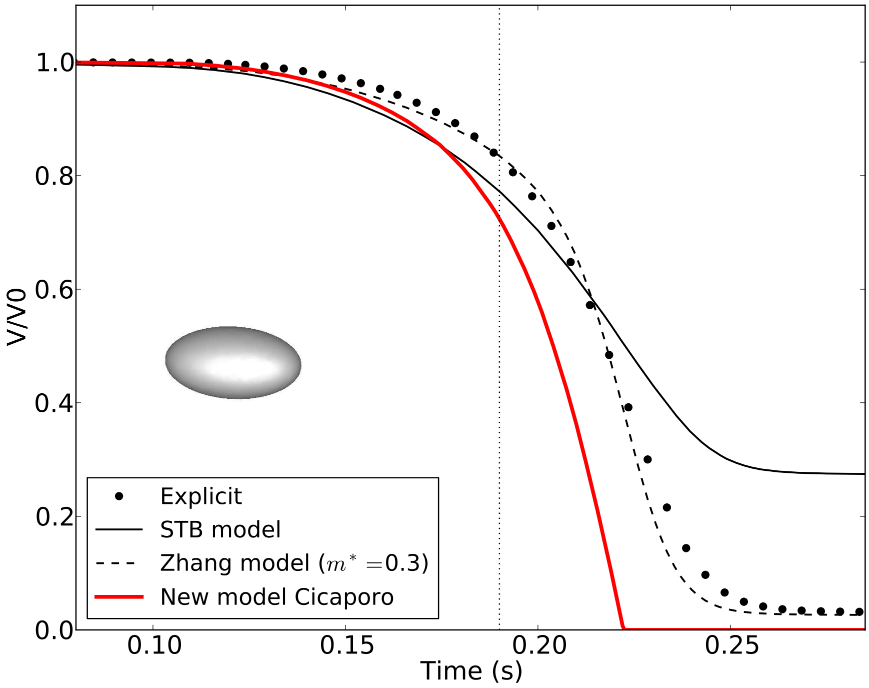

(a) Ell-E $(4,3,2)$ $\theta_Y = 0$

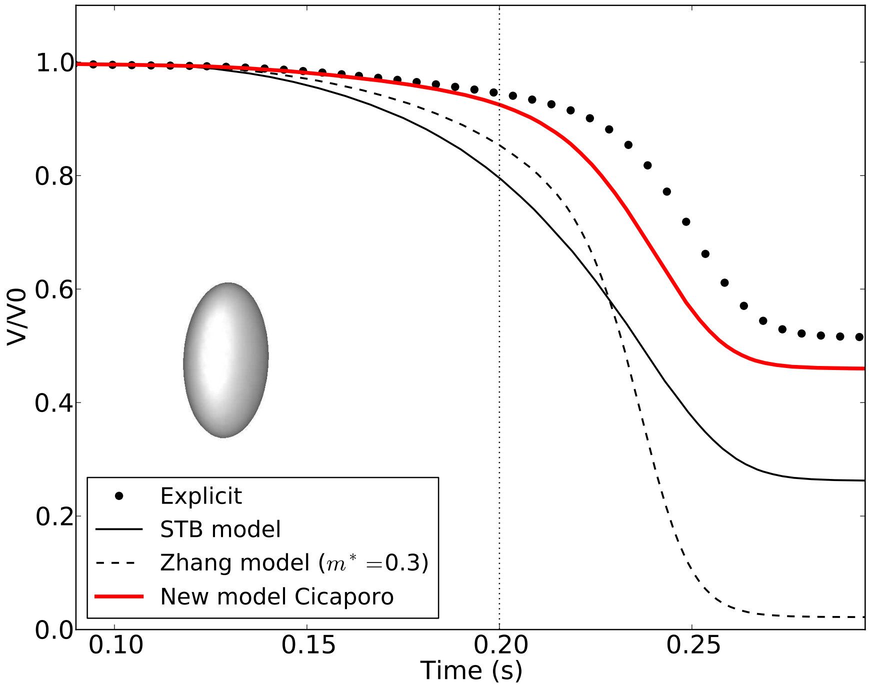

(b) Ell-E $(4,3,2)$ $\theta_Y = 90^{\circ}$

Figure 5.31: Void volume prediction for an ellipsoidal void $(r_1, r_2, r_3) = (4,3,2)$ with two different orientations, compared to the STB model, the Zhang model, and to the values measured in the explicit simulations.

The STB model underestimates final void closure with respect to the first orientation case, and overestimates the value with respect to the second orientation case. The discrepancy is 25% in both cases.

Although the new model Cicaporo overestimates void closure in both cases, the final void volume is predicted with very good accuracy, as the final discrepancy remains lower than 6%.

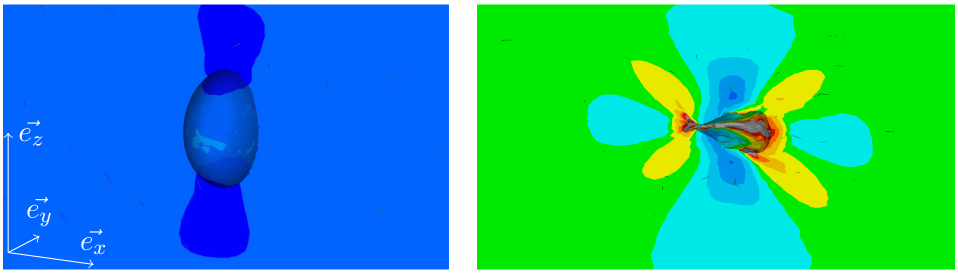

(a) $t = 0.21$ s

(b) Final state $t = 0.28$ s

Figure 5.32: Detail of equivalent strain field around ellipsoid E ($\theta_Y = 90^{\circ}$) at various instants of deformation.

5.4.6 Conclusions

The discrepancies that were obtained in terms of final void volume are synthetized in Fig. 5.33. The discrepancies are given for each prediction model, and for all presented void cases. Negative values indicate that a model overestimates void closure compared to the explicit simulation, as the predicted volume is lower than the explicit one. Positive values indicate that the model underestimates void closure.

The STB model significantly overestimates void closure for the second cases of orientation (A2, B2, C2, E2), while it underestimates void closure for the first cases of orientation (A1, B1, C1, E1). The discrepancies are larger for larger aspect ratios. The lowest discrepancy is obtained for the spherical case.

The largest discrepancies were obtained for the Zhang model. From all presented cases, the Zhang model generally exhibits a stronger overestimation of void closure. The second orientation cases (A2, B2, C2, E2) lead to very high discrepancies, between 40% to 88% overestimation. On the other hand the first orientation cases (A1, B1, C1, E1) were predicted with rather good accuracy, as the discrepancy does not exceed 10%.

Since the new model Cicaporo was built according to similar assumptions as the Zhang model, this general tendency is observed as well. The new model Cicaporo generally overestimates the final void volume. From all tested voids, the model did not exhibit any underestimation of void closure.

Nevertheless, the largest discrepancy was obtained for the ellipsoid A in its first orientation case (A1), with about 19% difference with respect to the explicit simulation. In all other cases, the discrepancy remained lower than 7%. This remark demonstrates the ability of the new model Cicaporo to take into account the effect of initial geometry of the void.

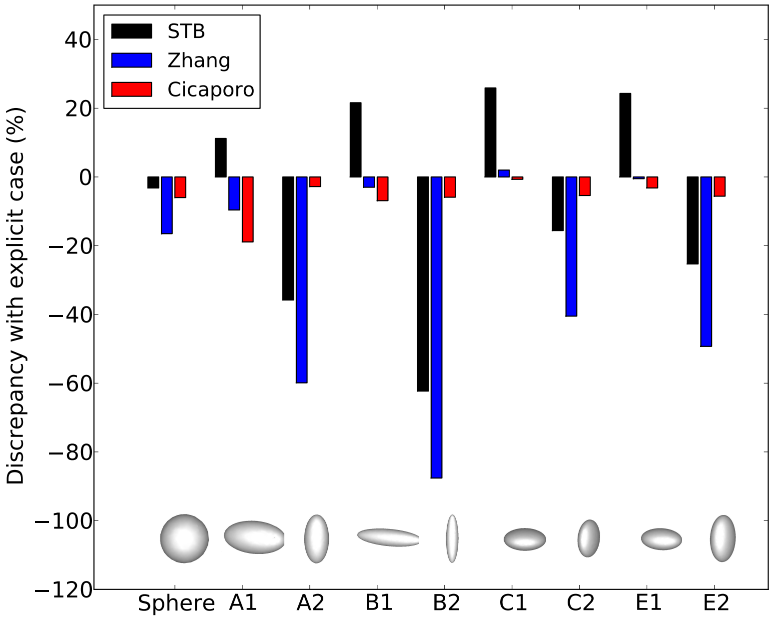

Figure 5.33: Final discrepancies in terms of void volume obtained with the STB model, the Zhang model and the new model Cicaporo for the hot rolling case (the nomenclature relates to the name of the ellipsoid A–E and its orientation case 1–2).

5.5 Conclusions

The new void closure model Cicaporo was implemented in the finite element software FORGE [2011] as a post-processing subroutine, and was compared to the existing STB model proposed by Lasne [2008], and to the model of Zhang et al. [2009]. The models were confronted to explicit simulations. The comparisons were performed for two different industrial processes: a case of open die forging, and a case of hot forging. Various ellipsoidal voids were used, using different dimensions and different orientations, and were submitted to different mechanical loading paths.

The benefits of the new model Cicaporo were demonstrated regarding the dependence to initial geometry (initial dimensions and orientation). The effect of initial geometry of a void is significant on its volume evolution. The STB model and the Zhang model are unable to take into account this effect. The new void closure model Cicaporo is able to predict the effect of initial geometry with excellent accuracy.

A general overestimation of all models was observed, and is mainly explained by the assumptions that are used at the meso-scale to calibrate these models:

- homogeneity of boundary conditions,
- axisymmetry of boundary conditions,
- uniformity of the deformation direction.

The observation of final void shapes in the explicit process simulations indicated that behaviour of voids in the industrial process is rather different from the one observed at the RVE-scale. From the two first assumptions, the available information was insufficient to clearly determine whether it is the homogeneity, or the axisymmetry which leads to the largest discrepancy. The improvement of boundary conditions at the RVE-scale according to both aspects constitutes a perspective to this work.

The third assumption regarding the uniformity of the main deformation direction results from the fact that the current orientation of the void is unknown when using the *mean-field* model. Using the presented approach, the current orientation parameters are obtained between the current deformation direction and the *initial* orientation of the void. In other words, it is assumed that the initial orientation of the void remains constant during deformation, in a first approximation. Predicting the evolution of the void orientation would be thus of great interest to enhance the model.

In fact, the prediction of the full tridimensional evolution of a void (dimensions and orientation) during closure is a very interesting perspective to the present work. The evolution of the six components of the inertia matrix could be predicted, using the same methodology as the one presented in this work using the void volume (scalar variable). Knowing the current orientation and dimensions of a void shows a double interest. First, as pointed out above, the current orientation parameters can be obtained from the actual state of the void, instead of the initial orientation. Second, knowing the actual dimensions of the void may also spare the use of the term which contains the information regarding the change of shape due to deformation. The current geometry would directly be obtained by the prediction itself.

Finally, it was shown that general overestimation that is observed with all models is also significantly due to the assumption made by the use of a *mean-field* model (regarding the fact that the presence of voids has no impact on the global mechanical fields at the macroscopic scale).

General conclusion and perspectives

A new model for void closure was developed in order to get a better prediction of void volume evolution within an industrial context.

The framework was defined according to an extensive study of industrial requirements (materials, processes and void states) and according to existing models from the literature. The latter are generally based on hypotheses that are too restrictive for a sustainable industrial application. Stress triaxiality based (STB) models are classically used in a first approximation using finite element process simulations, such as the one proposed by Lasne [2008]. These models are mainly limited by the fact that they do not take into account the shape change of the void during deformation. The recent Zhang model [Zhang et al., 2009] exhibits more accurate results, but remains limited to the prediction of spherical voids only.

The industrial observation of voids generally exhibits complex morphologies. The effect of initial void morphology on void closure behaviour is significant. In order to consider the quantitative effect of initial void morphology in the model, the use of equivalent ellipsoids was presented. Although the void behaviour is not strictly identical to the one of a real tortuous void, the use of equivalent ellipsoids showed great advantage compared to the use of spheres that is classically made in the literature.

It was chosen to study void closure at the meso-scale in order to define a *mean-field* model for void volume evolution. This approach enables the closure mechanisms to be accurately studied at the micro-scale using *full-field* finite element simulations in a representative volume element. Boundary conditions were applied in order to represent the thermomechanical remote conditions from the macroscopic scale. The use of a *mean-field* model shows great advantage as it does not require additional computation time during the macroscopic simulations of hot forming processes.

The finite element software FORGE [2011] was used to perform the *full-field* simulations. Real void morphologies were obtained using X-ray microtomography examinations using several samples. An experimental validation was carried out by comparing numerical and experimental results for several samples after hot compression tests.

The feasibility of such an experimental validation was demonstrated. It was shown that the quality of the results can be significantly enhanced with a relevant choice of the void-to-sample dimension ratio. This choice may provide a good compromise between the quality of the tridimensional images and the control of experimental conditions.

Very good agreement was obtained between *full-field* simulations and tridimensional examinations.

A sensitivity study was performed using *full-field* simulations at the micro-scale and numerous parameters were studied regarding their influence on void closure:

- The most influent parameters are the cumulated strain, the stress triaxiality ratio and the initial morphology of the void.

- The material parameters m (strain-rate sensitivity coefficient) and n (strain hardening coefficient) exhibit a certain influence on void closure. However, in the range of values for hot metal forming, these parameters have a second order influence.

- The material consistency A, the remote strain-rate $\dot{\bar{\varepsilon}}$, the temperature T and the initial void volume V_0 have no influence on void closure.

The most influent parameters were attentively studied using a wide campaign of *full-field* simulations at the RVE-scale. This numerical campaign was used to build a new *mean-field* model for void closure. A new analytical function for the void volume was defined and calibrated.

The new model was assessed using four ellipsoids (defined from real industrial voids), under five mechanical conditions. Among these twenty cases, the L^2-norm error remained under 5% in eighteen cases, and raised to 17% for one void under low compressive stress states ($T_X \approx 0$).

The *mean-field* model was finally implemented in the finite element software FORGE [2011] as a user subroutine. Two industrial processes were considered: a case of multi-blow open die forging and a case of hot rolling. The predicted volume evolution was assessed by comparison with *full-field* simulations of these processes containing explicit voids placed at various positions. The prediction of the new model was also compared to the STB model and the Zhang model in order to highlight the benefits with respect to the most advanced models from the literature.

It was pointed out that the use of the Zhang model requires the choice of a material parameter that is not strictly defined in the case of materials with strain hardening. The values of the Zhang model that were obtained using the virtual value $m^* = 0.3$ showed good agreement with the new prediction model in the case of spherical voids.

The benefits of the new model Cicaporo were shown using ellipsoidal voids. The predicted values were compared in terms of final void volume for both industrial processes. The effect of initial geometry (relative dimensions and orientation) was predicted with good accuracy, while it cannot be predicted by any of the STB or the Zhang models.

A general overestimation of the prediction was observed with respect to the *full-field* explicit cases. This was explained by the the assumptions that are made using a *mean-field* model and the use of the meso-scale.

The main perspectives to this work are summarized in the following.

- The overestimation of void closure by the *mean-field* models may remain a significant issue from an industrial point of view. It was demonstrated that this overestimation is partially due to the assumption that considers that the presence of voids has no impact on the global behaviour of the workpiece. The mechanical loading paths observed in the *full-field* explicit case were slightly different than the ones in the void-free case (with the *mean-field* models). The level of cumulated equivalent strain was higher in the void-free case, leading to an overestimation of void closure. This effect might be corrected by adding corrective terms, or by modifying the values of the calibration constants in the model.

- Regarding the boundary conditions at the RVE-scale, the assumption of homogeneity of the mechanical fields, as well as the axisymmetry of the stress state were discussed. They could mainly explain the differences of final void shapes that were obtained between the *full-field* explicit process simulation and the *full-field* RVE simulations. Additional boundary conditions might be defined in order to better represent the mechanical state. For example, the stress triaxiality ratio is insufficient to fully describe the tridimensional stress state. The introduction of non-symmetrical stress boundary conditions may be of great interest to observe the effect on void closure. A quantification would be possible using the Lode angle parameter.

- The model was limited by the fact that the main compression direction may vary during real processes, whereas the model was calibrated using uniform compression cases. The uniformity of the main compression direction may become a strong assumptions in some industrial processes. The effect of non-uniformiry was illustrated in Appendix C.

  This limitation to uniform loadings is in fact due to the definition of the *mean-field* model itself. As a scalar variable is computed (the void volume), the current geometry and orientation of the void is unknown during void closure. The effect of shape change is empirically considered by the coefficient C of the new model. Since the model was built using uniform cases, the validity of this empirical dependence is no longer valid using non-uniform cases.

  In order to get rid of this first approximation, a full prediction of the current geometry and orientation of the void would be required. A prediction of the six components of the inertia matrix during void closure might show great interest.

- The material parameters were not addressed in the Cicaporo model, as they exhibited a second order influence in the range of interest. However, their influence was not negligible and considering the influence of material parameters might be a relevant amelioration to the present model. Attention must be paid to the choice of the material law that is considered. In this work, the Hansel-Spittel law was exclusively considered. This law was convenient since the simple power-law expression can be easily obtained by simplifying the Hansel-Spittel law. However, material behaviour of hot metals are also represented using different laws, such as the Norton-Hoff law, the GNHB-type, or using tabulated data.

- The choice of using equivalent ellipsoids instead of real void morphologies was made according to the definition of morphology parameters (aspect ratios and orientation) in the model. However, it was qualitatively shown that the tortuosity may have a significant influence on the closure behaviour, particularly at the final stages of void closure. However, considering tridimensional tortuosity is delicate for two reasons. Firstly, the quantitative parameters to quantify tortuosity are numerous and remain often subjective [Bullitt et al., 2003]. The definition of an *apparent* tortuosity with respect to the observed mechanisms might thus be of interest [Thorat et al., 2009]. Secondly, even with an accurate description of the void tortuosity, its use in a *mean-field* model requires an accurate tridimensional knowledge of the voids morphology. This can be obtained by X-ray microtomography, but this technique is costly and is limited to small samples. A sufficiently accurate and systematic examination of the internal void state is thus impossible at present within the industrial framework.

- Within this work, isolated voids were exclusively considered. This assumption was implicitly made by the determination of RVE dimensions. By defining the RVE dimensions three times larger than the void's dimensions, it can be considered, in a first approximation, that the presence of another void can be neglected if the distance between both voids centers is greater than three times the average size of the voids. Nevertheless, if this distance is shorter, the effect might eventually become significant. This proximity effect was not addressed within this work, but might be a perspective of interest as well.

- Voids generally result from shrinkage during cooling of an ingot, and are thus considered as empty. A potential presence of gas inside the voids is however sometimes mentioned [Keife and Ståhlberg, 1980, Toda et al., 2009]. An industrial unpublished study also revealed a non-negligible quantity of gas inside several voids. However, experimental measurements of the quantity of gas is still relatively complex due to the small volumes of the considered voids.

  Within this work, the presence of an internal pressure was neglected. Indeed, free boundary conditions were used on the internal surfaces of the voids (apart from the self-contact zones).

  Nevertheless, the presence of a quantity of gas might significantly increase the pressure inside a void, as its volume tends to zero. In addition, at the typical temperatures for the considered hot forming processes, gas diffusion might not be neglected. Considering the presence of internal gas could thus be of great interest in getting a more accurate understanding of void closure mechanisms.

- Finally, as pointed out in introduction, the final elimination of voids requires healing of the internal surfaces in contact, involving diffusion mechanisms [Park and Yang, 1996]. The present work was restricted to the mechanical closure phenomena, only. Final healing thus rises as a great perspective as well.

Bibliography

S. Agouti. *Étude de l'origine de défauts détectés dans des pièces en alliage d'aluminium de la série 7XXX destinées à l'industrie aéronautique.* PhD thesis, École nationale supérieure des Mines de Paris, 2012.

Y. Bai and T. Wierzbicki. A new model of metal plasticity and fracture with pressure and lode dependence. *International Journal of Plasticity*, 24(6):1071–1096, 2008.

G. Banaszek and A. Stefanik. Theoretical and laboratory modelling of the closure of metallurgical defects during forming of a forging. *Journal of Materials Processing Technology*, 177(1-3):238–242, 2006.

G. Banaszek, S. Berski, H. Dyja, and A. Kawalek. Theoretical modelling of metallurgical defect closing-up processes during forming a forging. *Journal of Iron and Steel Research, International*, 20(9):111 – 116, 2013.

J. A. P. Barboza. *Traitement de contact entre corps déformables et calcul parallèle pour la simulation 3D du forgeage multicorps.* PhD thesis, École Nationale Supérieure des Mines de Paris, 2004.

P.-O. Bouchard, L. Bourgeon, H. Lachapèle, E. Maire, C. Verdu, R. Forestier, and R. E. Logé. On the influence of particle distribution and reverse loading on damage mechanisms of ductile steels. *Materials Science and Engineering: A*, 496:223–233, 2008.

B. Budiansky, J. W. Hutchinson, and S. Slutsky. *Void growth and collapse in viscous solids*, pages 13–45. Pergamon Press, Oxford, 1982.

J.-Y. Buffière, E. Maire, P. Cloetens, G. Lormand, and R. Fougères. Characterization of internal damage in a {MMCp} using x-ray synchrotron phase contrast microtomography. *Acta Materialia*, 47:1613–1625, 1999.

E. Bullitt, G. Gerig, S. Pizer, W. Lin, and S. Aylward. Measuring tortuosity of the intracerebral vasculature from mra images. *Medical Imaging, IEEE Transactions on*, 22(9): 1163–1171, 2003.

D. C. Chen. Rigid-plastic finite element analysis of plastic deformation of porous metal sheets containing internal void defects. *Journal of Materials Processing Technology*, 180 (1-3):193–200, 2006.

J. Chen, K. Chandrashekhara, C. Mahimkar, S. N. Lekakh, and V. L. Richards. Void closure prediction in cold rolling using finite element analysis and neural network. *Journal of Materials Processing Technology*, 211(2):245–255, 2011.

J. Chen, K. Chandrashekhara, C. Mahimkar, S. N. Lekakh, and V. L. Richards. Study of void closure in hot radial forging process using 3D nonlinear finite element analysis. *The International Journal of Advanced Manufacturing Technology*, 62(9-12):1001–1011, 2012.

K. Chen, Y. Yang, K. Liu, and G. Shao. Simulation of void defect evolvement during the forging of steel ingot. *Advanced Materials Research*, 97-101:3079–3084, 2010.

M.-S. Chen and Y.C. Lin. Numerical simulation and experimental verification of void evolution inside large forgings during hot working. *International Journal of Plasticity*, 49:53 – 70, 2013.

M. S. Chun, C. J. Van Tyne, and Y. H. Moon. FEM analysis of void closure behaviour during open die forging of rectangular billets. *Steel Research International*, 77(2):116–121, 2006.

S. P. Dudra and Y.-T. Im. Analysis of void closure in open-die forging. *International Journal of Machine Tools and Manufacture*, 30(1):65–75, 1990.

J. M. Duva and J. W. Hutchinson. Constitutive potentials for dilutely voided nonlinear materials. *Mechanics of Materials*, 3(1):41–54, 1984.

R. K. Everett, K. E. Simmonds, and A. B. Geltmacher. Spatial distribution of voids in HY-100 steel by X-ray tomography. *Scripta Materialia*, 44:165–169, 2001.

S. Fayolle. *Etude de la modélisation de la pose et de la tenue mécanique des assemblages par déformation plastique.* PhD thesis, Ecole Nationale Supérieure des Mines de Paris, 2009.

FORGE. *2011*®. Transvalor S.A., 694, av. Donat, 06255 Mougins Cedex, France, 2011.

L. Fourment, J. Barboza, and S. Popa. Master/slave algorithm for contact between deformable bodies and axial symmetries - application to 3D metal forging. In K.J. Bathe, editor, *Computational Fluid and Solid Mechanics 2003*, pages 269–272. Elsevier Science Ltd, Oxford, 2003.

A. L. Gurson. Continuum theory of ductile rupture by void nucleation and growth: Part 1 - yield criteria and flow rules for porous ductile media. *Journal of Engineering Materials and Technology, Transactions of the ASME*, 99 Ser H(1):2–15, 1977.

M. Y. He and J. W. Hutchinson. The penny-shaped crack and the plane strain crack in an infinite body of power-law material. *Journal of Applied Mechanics*, 48:830–840, 1981.

M. F. Horstemeyer, K. Gall, K. W. Dolan, A. Waters, J. J. Haskins, D. E. Perkins, A. M. Gokhale, and M. D. Dighe. Numerical, experimental, nondestructive, and image analyses of damage progression in cast {A356} aluminum notch tensile bars. *Theoretical and Applied Fracture Mechanics*, 39:23–45, 2003.

Z. P. Huang and J. Wang. Nonlinear mechanics of solids containing isolated voids. *Applied Mechanics Reviews*, 59(4):210–229, 2006.

Y. M. Hwang and D. C. Chen. Finite element simulations on void closure behaviour inside the sheet during sheet rolling processes. *Proceedings of the Institution of Mechanical Engineers, Part B: Journal of Engineering Manufacture*, 216(9):1227–1237, 2002.

H. Kakimoto, T. Arikawa, Y. Takahashi, T. Tanaka, and Y. Imaida. Development of forging process design to close internal voids. *Journal of Materials Processing Technology*, 210 (3):415–422, 2010.

H. Keife and U. Ståhlberg. Influence of pressure on the closure of voids during plastic deformation. *Journal of Mechanical Working Technology*, 4(2):133–143, 1980.

P. H. Kim, M. S. Chun, J. J. Yi, and Y. H. Moon. Pass schedule algorithms for hot open die forging. *Journal of Materials Processing Technology*, 130-131:516–523, 2002.

P. Lasne. Calculs supplémentaires : Présence de porosité. internal document, unpublished, September 2008.

B. J. Lee and M. E. Mear. Axisymmetric deformation of power-law solids containing a dilute concentration of aligned spheroidal voids. *Journal of the Mechanics and Physics of Solids*, 40(8):1805–1836, 1992.

B. J. Lee and M. E. Mear. Studies of the growth and collapse of voids in viscous solids. *Journal of Engineering Materials and Technology, Transactions of the ASME*, 116(3): 348–358, 1994.

Y. S. Lee, Y. C. Kwon, Y. N. Kwon, J. H. Lee, S. W. Lee, and N. S. Kim. Analysis on void closure behavior during hot open die forging. *Advanced Materials Research*, 24-25: 69–72, 2007.

Y. S. Lee, S. U. Lee, C. J. Van Tyne, B. D. Joo, and Y. H. Moon. Internal void closure during the forging of large cast ingots using a simulation approach. *Journal of Materials Processing Technology*, 211(6):1136–1145, 2011.

J. Lemaitre. *A course on damage mechanics*. Springer-Verlag Berlin, 1992.

Z. Li, C. Wang, and C. Chen. The evolution of voids in the plasticity strain hardening gradient materials. *International Journal of Plasticity*, 19(2):213–234, 2003.

J. M. Llanos, V. Santisteban, J. Demurger, B. Kieber, R. Forrestier, B. Rogberg, L. Ek, M. De Santis, J. Gelli, and H. Lundback. Improvement of central soundness in long products from a through process control of solidification and reheating and rolling parameters. Technical report, European Commission - Research Fund for Coal and Steel, 2008. EUR 23588 EN.

W. E. Lorensen and H. E. Cline. Marching cubes: A high resolution 3d surface construction algorithm. *SIGGRAPH Comput. Graph.*, 21:163–169, 1987.

E. Maire, J. Y. Buffière, L. Salvo, J. J. Blandin, W. Ludwig, and J. M. Létang. On the application of X-ray microtomography in the field of materials science. *Advanced Engineering Materials*, 3:539–546, 2001.

E. Maire, O. Bouaziz, M. Di Michiel, and C. Verdu. Initiation and growth of damage in a dual-phase steel observed by X-ray microtomography. *Acta Materialia*, 56:4954–4964, 2008.

K. Mocellin. *Contribution à la simulation numérique tridimensionnelle du forgeage à chaud: étude du contact et calcul multigrille.* PhD thesis, École Nationale Supérieure des Mines de Paris, 1999.

T. F. Morgeneyer, M. J. Starink, and I. Sinclair. Evolution of voids during ductile crack propagation in an aluminium alloy sheet toughness test studied by synchrotron radiation computed tomography. *Acta Materialia*, 56:1671–1679, 2008.

M. Nakasaki, I. Takasu, and H. Utsunomiya. Application of hydrostatic integration parameter for free-forging and rolling. *Journal of Materials Processing Technology*, 177(1-3): 521–524, 2006.

H. Överstam and M. Jarl. Fem-simulation of drawing out in open die forging. *Steel Research International*, 75(12):812–817, 2004.

C. Y. Park and D. Y. Yang. A study of void crushing in large forgings I: Bonding mechanism and estimation model for bonding efficiency. *Journal of Materials Processing Technology*, 57(1-2):129–140, 1996.

C. Y. Park and D. Y. Yang. A study of void crushing in large forgings II. Estimation of bonding efficiency by finite-element analysis. *Journal of Materials Processing Technology*, 72(1):32–41, 1997a.

C. Y. Park and D. Y. Yang. Modelling of void crushing for large-ingot hot forging. *Journal of Materials Processing Technology*, 67(1-3):195–200, May 1997b.

E. Parra-Denis. *Analyse morphologique 3D de particules de forme complexe : Application aux intermétalliques dans les alliages d'aluminium.* PhD thesis, Université Jean Monnet de Saint-Etienne, 2007.

M. Pietrzyk, R. Kawalla, and H. Pircher. Simulation of the behaviour of voids in steel plates during hot rolling. *Steel Research*, 66(12):526–529, 1995.

P. Ponte Castañeda. The effective mechanical properties of nonlinear isotropic composites. *Journal of the Mechanics and Physics of Solids*, 39(1):45–71, 1991.

A. R. Ragab. Application of an extended void growth model with strain hardening and void shape evolution to ductile fracture under axisymmetric tension. *Engineering Fracture Mechanics*, 71(11):1515–1534, 2004.

D. A. Rajon and W. E. Bolch. Marching cube algorithm: Review and trilinear interpolation adaptation for image-based dosimetric models. *Computerized Medical Imaging and Graphics*, 27(5):411–435, 2003.

W. S. Rasband. Imagej. U. S. National Institutes of Health, Bethesda, Maryland, USA, 1997-2012. http://imagej.nih.gov/ij/.

J. R. Rice and D. M. Tracey. On the ductile enlargement of voids in triaxial stress fields. *Journal of the Mechanics and Physics of Solids*, 17(3):201–217, 1969.

M. Saby, M. Bernacki, P.-O. Bouchard, and E. Roux. Sensitivity study for void closure relative to macroscopic mechanical loadings, using finite element simulations at a mesoscale. In *8th European Solid Mechanics Conference*, 2012a.

M. Saby, M. Bernacki, E. Roux, S. Brzuchacz, and P.-O. Bouchard. Sensitivity study for closure of real void relative to macroscopic mechanical loadings, using finite element simulations at meso-scale. In *European Congress on Computational Methods in Applied Science and Engineering*, 2012b.

M. Saby, E. Roux, M. Bernacki, and P.-O. Bouchard. Multiscale analysis of void closure during hot forming process. In *Proceedings of the 29th Forging Industry Technical Conference*, 2012c.

M. Saby, M. Bernacki, and P.-O. Bouchard. Analyse multi-échelle de la refermeture de porosités, appliquée à la mise en forme des métaux à chaud. In *Actes du 11e Colloque National en Calcul des Structures CSMA*, 2013a.

M. Saby, M. Bernacki, E. Roux, and P.-O. Bouchard. Three-dimensional analysis of real void closure at the meso-scale during hot metal forming processes. *Computational Materials Science*, 77:194–201, 2013b.

L. Salvo, P. Cloetens, E. Maire, S. Zabler, J. Blandin, J. Buffière, W. Ludwig, E. Boller, D. Bellet, and C. Josserond. X-ray micro-tomography an attractive characterisation technique in materials science. *Nuclear Instruments and Methods in Physics Research Section B: Beam Interactions with Materials and Atoms*, 200:273–286, 2003.

F. Scheyvaerts, P.R. Onck, C. Tekoglu, and T. Pardoen. The growth and coalescence of ellipsoidal voids in plane strain under combined shear and tension. *Journal of the Mechanics and Physics of Solids*, 59(2):373–397, 2011.

N. Schlüter, F. Grimpe, W. Bleck, and W. Dahl. Modelling of the damage in ductile steels. *Computational Materials Science*, 7:27–33, 1996.

K. N. Shah, B. V. Kiefer, and J. J. Gavigan. Finite element simulation of internal void closure in open-die press forging. *Advanced manufacturing processes*, 1(3-4):501–516, 1986.

S. Sternberg. Biomedical image processing. *IEEE Computer*, 16(1):22–34, 1983.

U. Ståhlberg. Influence of spread and stress on the closure of a central longitudinal hole in the hot rolling of steel. *Journal of Mechanical Working Technology*, 13(1):65–81, 1986.

U. Ståhlberg and H. Keife. A study of hole closure in hot rolling as influenced by forced cooling. *Journal of Materials Processing Technology*, 30(1):131 – 135, 1992.

U. Ståhlberg, H. Keife, M. Lundberg, and A. Melander. A study of void closure during plastic deformation. *Journal of Mechanical Working Technology*, 4(1):51–63, 1980.

M. Tanaka, S. Ono, and M. Tsuneno. Factors contributing to crushing of voids during forging. *Journal of JSTP*, 27 (306):927–934, 1986. (translated from Japanese).

I. V. Thorat, D. E. Stephenson, N. A. Zacharias, K. Zaghib, J. N. Harb, and D. R. Wheeler. Quantifying tortuosity in porous li-ion battery materials. *Journal of Power Sources*, 188 (2):592 – 600, 2009.

H. Toda, K. Minami, K. Koyama, K. Ichitani, M. Kobayashi, K. Uesugi, and Y. Suzuki. Healing behavior of preexisting hydrogen micropores in aluminum alloys during plastic deformation. *Acta Materialia*, 57(15):4391–4403, 2009.

A. Tomlison, A. Met, and J. Dstringer. La suppression des cavites internes dans les pieces de forge par refoulement. *Journal of the Iron and Steel Institute*, pages 209–218, 1958.

V. Tvergaard. On localization in ductile materials containing spherical voids. *International Journal of Fracture*, 18(4):237–252, 1982.

V. Tvergaard. On the creep constrained diffusive cavitation of grain boundary facets. *Journal of the Mechanics and Physics of Solids*, 32(5):373–393, 1984.

V. Tvergaard and A. Needleman. Analysis of the cup-cone fracture in a round tensile bar. *Acta Metallurgica*, 32(1):157–169, 1984.

A. Wallerö. Closing of a central longitudinal pore in hot rolling. *Journal of Mechanical Working Technology*, 12(2):233–242, 1985.

A. Wang, P. F. Thomson, and P. D. Hodgson. A study of pore closure and welding in hot rolling process. *Journal of Materials Processing Technology*, 60(1-4):95–102, 1996.

J.-F. Zaragoci. *Simulation numérique directe multiphasique de la déformation d'un alliage Al-Cu à l'état pâteux - Comparaison avec des observations par tomographie aux rayons X in situ en temps réel.* PhD thesis, École nationale supérieure des Mines de Paris, 2012. Chap 2.

J.-F. Zaragoci, L. Silva, M. Bellet, and C.-A. Gandin. Numerical tensile test on a mushy zone sample. *IOP Conference Series: Materials Science and Engineering*, 33(1):012054, 2012.

X. Zhang, F. Ma, K. Ma, and X. Li. Multi-scale analysis of void closure for heavy ingot hot forging. *Modern Applied Science*, 6(10):15–25, 2012.

X.-X. Zhang and Z.-S. Cui. Theoretical study of void closure in nonlinear plastic materials. *Applied Mathematics and Mechanics-english Edition*, 30(5):631–642, 2009.

X.-X. Zhang, Z.-S. Cui, W. Chen, and Y. Li. A criterion for void closure in large ingots during hot forging. *Journal of Materials Processing Technology*, 209(4):1950–1959, 2009.

W. Zutang and R. Meng. Researches on the mechanisms of consolidating big steel ingots and optimization of forming procedure of large forgings. In *12th International Forgemasters Meeting Conference*, 1994.

Appendix A

Finite element simulations using the software FORGE

All finite element simulations in this document are performed using the finite element software FORGE [2011]. This software is widely used in the hot metal forming industry, as it is particularly well suited to large deformation and visco-platic materials. A large variety of behaviour laws can be used, such as various power-laws, the Hansel-Spittel law, or GNHB-type laws.

The main features are:

- resolution of tridimensional thermo-mechanical problems;
- velocity-pressure mixed formulation;
- spatial discretization using linear P1+/P1 tetrahedral elements (with a bubble function at the element's center for the velocity field);
- tridimensional automatic remeshing;
- parallel computation;
- multi-body contact and self-contact capabilities using penalization.

The mechanical and thermal resolutions are briefly recalled in the following.

A.1 Mechanical resolution

The mechanical resolution consists in finding the velocity field $\vec{v}$ and the pressure field $\vec{p}$ at the increment t, using two fundamental equations of mechanics, and boundary conditions.

A.1.1 Fundamental principle of dynamics

The fundamental principle of dynamics is expressed as:

$$\mathrm{div}(\boldsymbol{\sigma}) + \rho\left(\vec{f} - \vec{\gamma}\right) = 0, \tag{A.1}$$

where $\boldsymbol{\sigma}$ is the stress tensor, ρ the mass density, $\vec{f}$ represents gravity forces and $\vec{\gamma}$ the acceleration vector. The effects of gravity and of inertia are usually neglected in conventional forming process simulations, such that:

$$\mathrm{div}(\boldsymbol{\sigma}) = 0. \tag{A.2}$$

A.1.2 Mass conservation

The equation of mass conservation is expressed as:

$$\frac{\partial \rho}{\partial t} + \mathrm{div}(\rho \vec{v}) = 0, \tag{A.3}$$

where $\vec{v}$ is the velocity vector. According to the incompressibility condition of the material ρ is constant and the equation of mass conservation is expressed as:

$$\mathrm{div}(\vec{v}) = 0. \tag{A.4}$$

A.1.3 Boundary conditions

At the boundaries of a body, several conditions may be encountered.

Free boundary condition The free boundary condition is applied when the part of a body's surface is stress-free.

$$\boldsymbol{\sigma}.\vec{n} = \vec{0}, \tag{A.5}$$

where $\vec{n}$ is the outward normal.

Prescribed–velocity boundary condition The prescribed–velocity boundary condition is applied when the surface is submitted to a prescribed velocity field $\vec{v_0}$.

$$\vec{v} = \vec{v_0}. \tag{A.6}$$

Prescribed–stress boundary condition The prescribed–stress boundary condition is applied when the surface is submitted to a prescribed stress $\vec{\sigma_0}$.

$$\boldsymbol{\sigma}.\vec{n} = \vec{\sigma_0}. \tag{A.7}$$

Contact condition Contact is defined according to the Signorini's conditions for the non-penetration of two bodies A and B:

$$\begin{cases} \left(\vec{v_A} - \vec{v_B}\right).\vec{n_A} \leq 0 & \text{(non-penetration)} \\ \sigma_n^{AB} \leq 0 & \text{(mechanical contact)} \\ \sigma_n^{AB}\left(\vec{v_A} - \vec{v_B}\right).\vec{n_A} = 0 & \text{(tangent sliding)} \end{cases} \tag{A.8}$$

where $\sigma_n^{AB} = \left(\boldsymbol{\sigma}_A \vec{n_A}\right).\vec{n_A} = \left(\boldsymbol{\sigma}_B \vec{n_B}\right).\vec{n_B}$. The penalty method is used to solve these equations. This method consists in applying a repulsive force to a infinite small authorized penetration between the two bodies A and B. Further details can be found in [Fayolle, 2009].

Three types of contact may be encountered:

- Contact between a deformable body A and a rigid body B, which classically occurs in process simulation, between a deformable workpiece and a rigid tool [Mocellin, 1999].

- Contact between two deformable bodies A and B, which may occur in the case of simulations involving several deformable bodies (joining of several workpieces, or using deformable tools). The condition is handled using a master-slave description of bodies A and B [Mocellin, 1999, Barboza, 2004].

- Self-contact of two subsets of a single body A, which typically occurs for void closure simulations. The condition is handled using a pseudo-symmetrical slave-slave description of the two subsets of the body A [Fourment et al., 2003, Barboza, 2004].

Friction When contact is encountered, friction can also be handled [Mocellin, 1999, Fayolle, 2009]. Several friction laws (e.g. Coulomb, Tresca) can be used in FORGE [2011].

Note that the self-contact is over-constrained and a sticky condition is implicitly considered, as friction cannot be handled in this case [Fourment et al., 2003].

A.2 Thermal resolution

The thermal resolution consists in finding the temperature field T using the heat equation:

$$\rho c \frac{\partial T}{\partial t} = \mathrm{div}(k \Delta T) + \dot{W}, \tag{A.9}$$

where c is the specific heat capacity, k the thermal conductivity, Δ the gradient operator and $\dot{W} = \boldsymbol{\sigma} : \dot{\boldsymbol{\varepsilon}}$ the internal energy dissipation.

Boundary conditions are also handled using:

- radiation (prescribed heat flow);
- conduction and convection with other bodies/environment (prescribed heat flow);
- friction (prescribed temperature).

A.3 Formalisms

The actualized Lagrangian formalism is used.

The geometrical problem is spatially discretized using linear tetrahedral elements P1+/P1 (see Fig. A.1). The pressure field is computed at the four vertices of the tetrahedron. The velocity field is enriched using an additional degree of freedom at the center (called "bubble") of the tetrahedron.

(a) Velocity (P1+ element)

(b) Pressure (P1 element)

Figure A.1: Degrees of freedom for each element.

For more information about the software FORGE [2011], the reader can refer to Fayolle [2009, chap. 3].

Appendix B

Subroutines

B.1 The STB model

The STB model is currently available in FORGE [2011]. The required input parameters are the values of constant closure coefficients K_C, K_T, the initial field of predicted volume V^0. The volume increment ΔV^t is computed at each increment t, for every integration point of the tridimensional mesh of the workpiece, and the new field of predicted volume is obtained using an explicit scheme $V^t = \Delta V^t + V^{t-1}$. The algorithm is given below, and a snapshot of the interface in the the software GLPre is given as well.

```
Initial parameters (user-defined):
$K_C, K_T$ (constant closure coefficients)
$V^0$ (initial void volume field)

At each time increment $t$: begin
    Data: $\Delta t^t$ (increment time step)
    $p^t$ (isostatic pressure)
    $\bar{\sigma}^t$ (von Mises equivalent stress)
    $\dot{\bar{\varepsilon}}^t$ (equivalent strain-rate)
    $V^{t-1}$ (void volume from increment $t-1$)

    For each integration point: begin
        if $\bar{\sigma}^t > 0$ and $\dot{\bar{\varepsilon}}^t > 0$ and $V^{t-1} > 0$ then
            $T_X^t = \frac{-p^t}{\bar{\sigma}^t}$

            if $p^t \geq 0$ then
                $V^t = V^{t-1} + K_C T_X^t \dot{\bar{\varepsilon}}^t \Delta t^t$
            else
                $V^t = V^{t-1} + K_T T_X^t \dot{\bar{\varepsilon}}^t \Delta t^t$
            end
        end
        $V^t = \max(0, V^t)$
    end
end
Result: $V^t$ (void volume at increment $t$)
```

Algorithm 1: Computation of the STB model

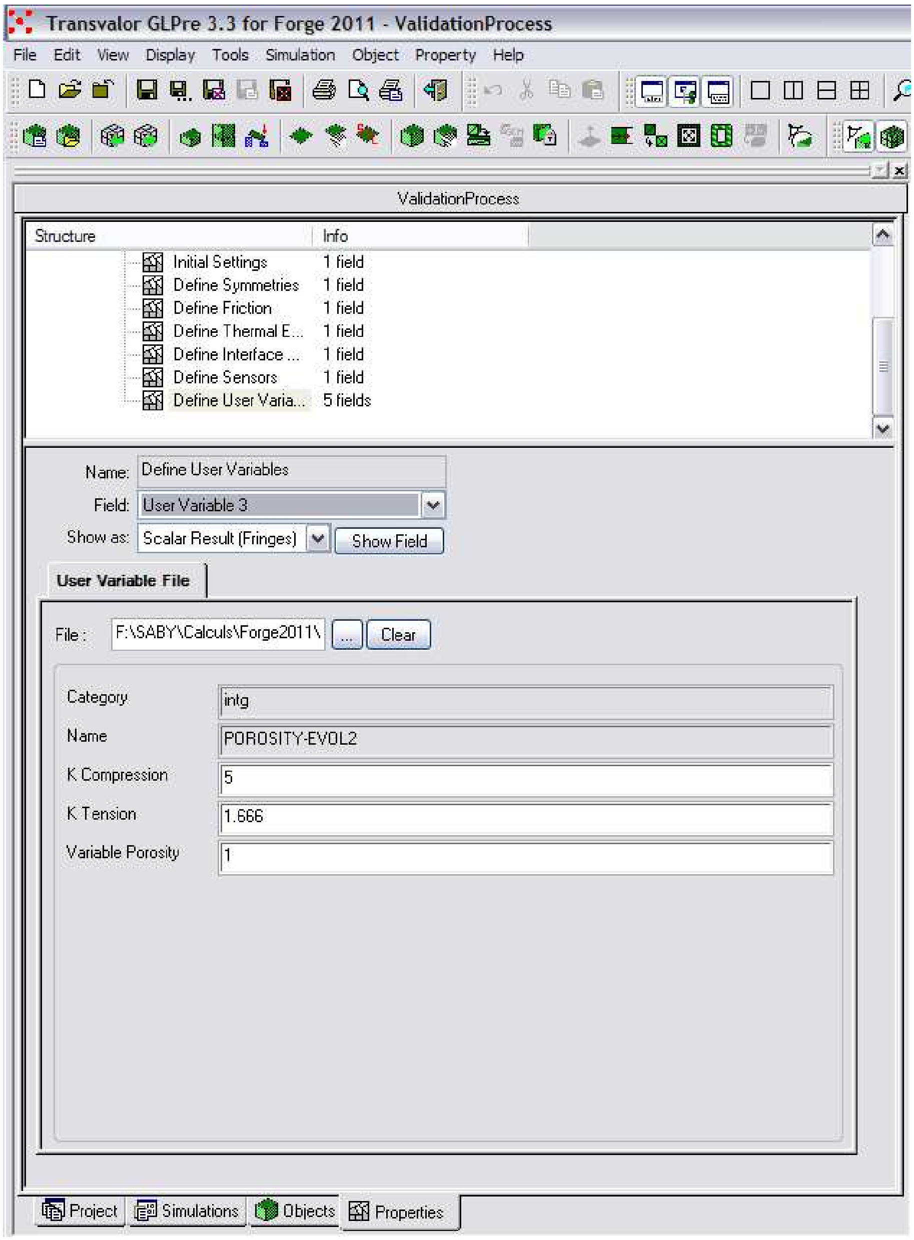

Structure	Info
Initial Settings	1 field
Define Symmetries	1 field
Define Friction	1 field
Define Thermal E...	1 field
Define Interface ...	1 field
Define Sensors	1 field
Define User Varia...	5 fields

Name: Define User Variables
Field: User Variable 3
Show as: Scalar Result (Fringes)

File : F:\SABY\Calculs\Forge2011\

Category	intg
Name	POROSITY-EVOL2
K Compression	5
K Tension	1.666
Variable Porosity	1

Figure B.1: Caption of the subroutine for the STB model in GLpre.

B.2 Implementation of the Zhang model

The implementation of the model is based on the same methodology as for the STB model. The volume increment ΔV^t is computed at each increment t, for every integration point of the tridimensional mesh of the workpiece, and the new field of predicted volume is obtained using an explicit scheme $V^t = \Delta V^t + V^{t-1}$.

The required input parameters are m^* (constant material parameter) and the initial field of predicted volume V^0. The model constants are automatically obtained according to Table B.1 and the value of m^*.

The algorithm is given below, and a snapshot of the interface in the the software GLPre is given as well.

m^*	1.0	0.5	0.2	0.3	0.1	0.01
q_1	0.5048	0.4911	0.6016	1.1481	2.9132	6.5456
q_2	6.4675	0.8002	-0.6981	-4.2026	-11.6464	-15.3775
q_3	14.2610	53.8018	72.6397	108.2114	185.5622	324.4417
q_4	-0.3379	-0.2314	-0.1243	-0.2480	-0.6511	-1.9575

Table B.1: Values of coefficients q_1, q_2, q_3 and q_4 proposed by Zhang et al. [2009]

```
Initial parameters (user-defined):
$m^*$ (constant material parameter)
$V^0$ (initial void volume field)

Initialization:
$q_1, q_2, q_3, q_4$ (obtained from Table B.1 for the adequate value of $m^*$)
$n^* = \frac{1}{m^*}$

At each time increment $t$: begin
    Data: $\Delta t^t$ (increment time step)
    $p^t$ (isostatic pressure)
    $\bar{\sigma}^t$ (von Mises equivalent stress)
    $\dot{\bar{\varepsilon}}^t$ (equivalent strain-rate)
    $V^{t-1}$ (void volume from increment $t-1$)

    For each integration point: begin
        if $\bar{\sigma}^t > 0$ and $\dot{\bar{\varepsilon}}^t > 0$ and $V^{t-1} > 0$ then
            $T_X^t = \frac{-p^t}{\bar{\sigma}^t}$

            $V^t = V^{t-1} +$
            $\left(\left\{\frac{3}{2}\left[\frac{3}{2n^*}|T_X^t| + \frac{(n^*-1)(5n^*+2)}{(n^*)^2}\right]^{n^*} + q_1|T_X^t| + 3q_2(\bar{\varepsilon}^t)^2 + 5q_4(\bar{\varepsilon}^t)^4 + q_4\dot{\bar{\varepsilon}}^t\Delta t^t\right\}\right) V^{t-1}$
        end
        $V^t = \max(0, V^t)$
    end
end
Result: $V^t$ (void volume at increment $t$)
```

Algorithm 2: Computation of the prediction model of Zhang et al. [2009]

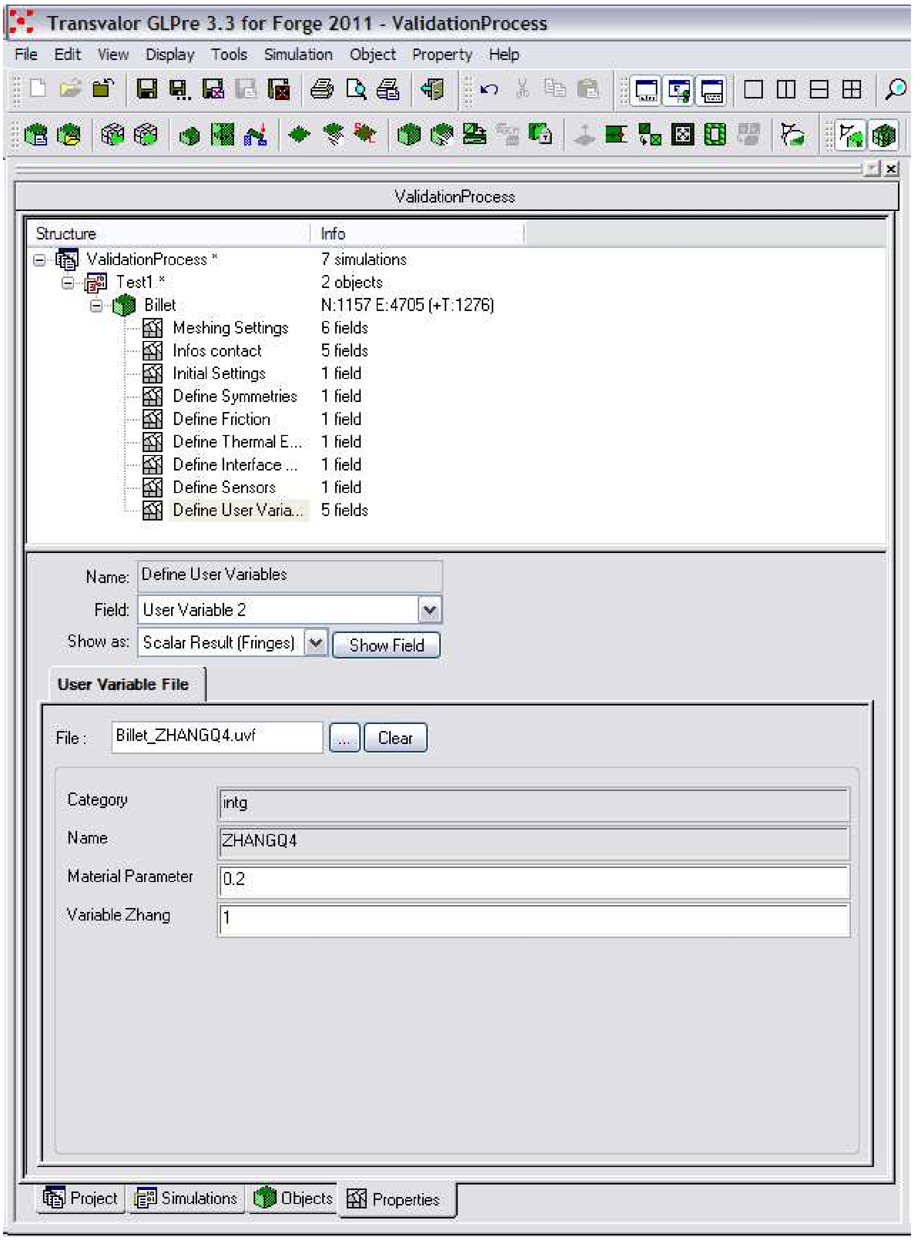

Structure	Info
ValidationProcess *	7 simulations
Test1 *	2 objects
Billet	N:1157 E:4705 (+T:1276)
Meshing Settings	6 fields
Infos contact	5 fields
Initial Settings	1 field
Define Symmetries	1 field
Define Friction	1 field
Define Thermal E...	1 field
Define Interface ...	1 field
Define Sensors	1 field
Define User Varia...	5 fields

Name: Define User Variables
Field: User Variable 2
Show as: Scalar Result (Fringes)

File : Billet_ZHANGQ4.uvf

Category	intg
Name	ZHANGQ4
Material Parameter	0.2
Variable Zhang	1

Figure B.2: Caption of the subroutine Zhang in GLpre.

B.3 Implementation of the new model Cicaporo

A similar methodology was used as for the other models. Here, the required input parameters are the three principal dimensions of the initial void, three rotation angles, and the initial field of predicted volume V^0.

The volume increment ΔV^t is computed at each increment t, for every integration point of the tridimensional mesh of the workpiece, and the new field of predicted volume is obtained using an explicit scheme $V^t = \Delta V^t + V^{t-1}$. The algorithm is given below, and a snapshot of the interface in the the software GLPre is given as well.

Note here the definition of a *modified* value of void volume V_B^0. A new condition is added for the computation of V_B^t, with respect to the one of V^t. When stress triaxiality ratio is positive, the evolution of void volume is ignored. The value thus remains constant $V_B^t = V_B^{t-1}$ at increments for which the stress triaxiality ratio is positive.

Indeed, during a process, positive stress triaxialty values may be encountered, even temporarily. As the model comes out (temporarily) from its validity domain, a value is obtained but its accuracy is not ensured. This comes from the definition of the initial framework, as void opening was not addressed within this work.

- The value of V_B indicates the value of void volume that would be obtained by neglecting void opening.
- The value of V indicates the value of void volume by extrapolating the validity of the model towards positive values.

By comparing the values of V and of V_B, information can be obtained. If both values are different, positive values of stress triaxiality were encountered during the process. The difference between the values gives a first approximation of the void opening that is predicted by extrapolating the model towards positive values.

A dedicated variable for cumulated equivalent strain is also defined in the subroutine. In the model, the value of cumulated equivalent strain is used to compute the change of void shape during computation (with the coefficient C). The cumulated equivalent strain must therefore be reset to zero for each definition of void morphology.

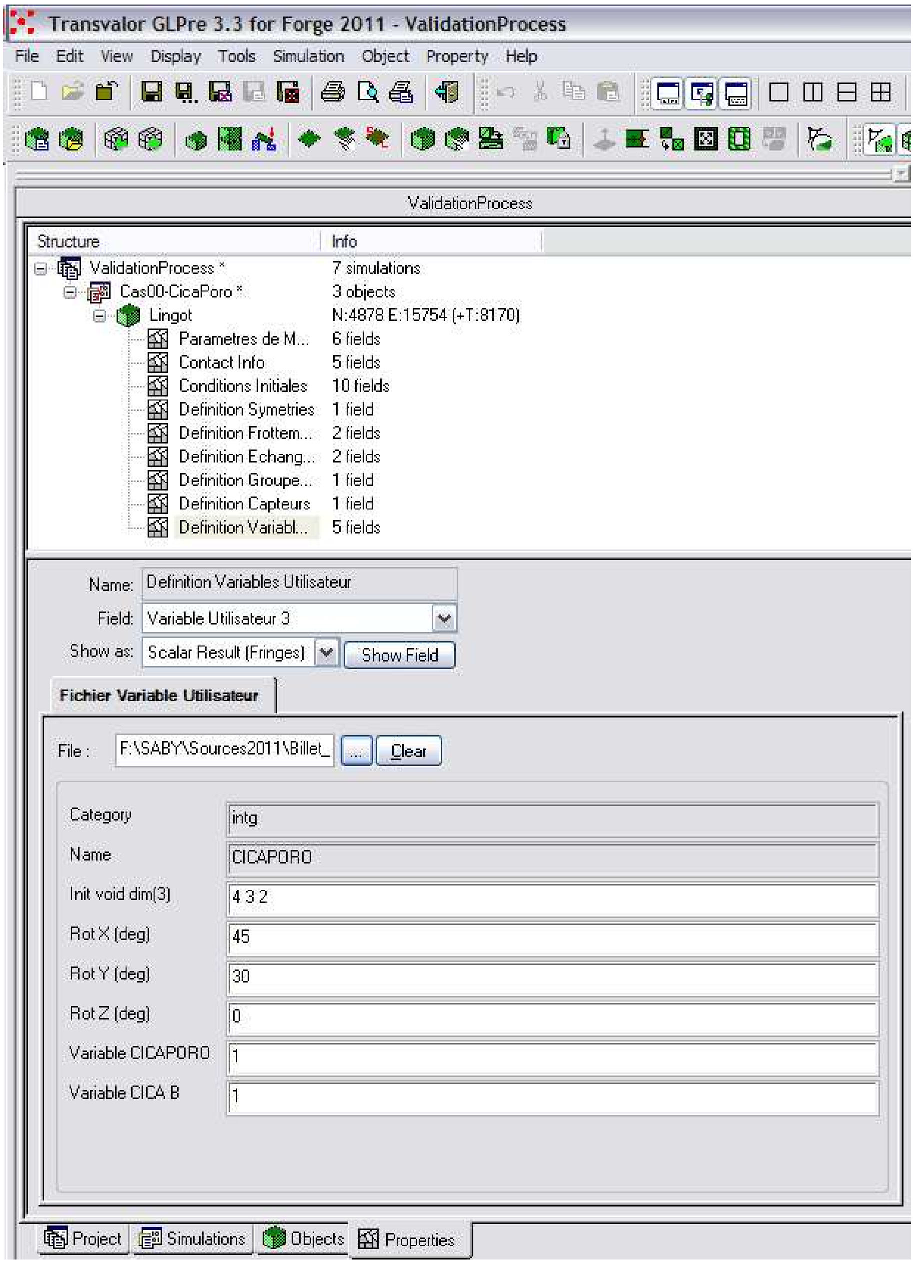

Structure	Info
ValidationProcess *	7 simulations
Cas00-CicaPoro *	3 objects
Lingot	N:4878 E:15754 (+T:8170)
Parametres de M...	6 fields
Contact Info	5 fields
Conditions Initiales	10 fields
Definition Symetries	1 field
Definition Frottem...	2 fields
Definition Echang...	2 fields
Definition Groupe...	1 field
Definition Capteurs	1 field
Definition Variabl...	5 fields

Name: Definition Variables Utilisateur
Field: Variable Utilisateur 3
Show as: Scalar Result (Fringes)

File : F:\SABY\Sources2011\Billet_

Category	intg
Name	CICAPORO
Init void dim(3)	4 3 2
Rot X (deg)	45
Rot Y (deg)	30
Rot Z (deg)	0
Variable CICAPORO	1
Variable CICA B	1

Figure B.3: Caption of the subroutine Cicaporo in GLpre.

```
Initial parameters (user-defined):
$r_1, r_2, r_3$ (initial void dimensions)
$\theta_X, \theta_Y, \theta_Z$ (initial rotation angles around each direction)
$V^0, V_B^0$ (initial void volume field, initial modified void volume field)
$\bar{\varepsilon}^0 = 0$ (initial cumulated equivalent strain is reset to zero)

Initialization: $V_0 = \frac{4}{3}\pi r_1 r_2 r_3$ ; $\gamma_1 = \sqrt[3]{V_0}/r_1$ ; $\gamma_2 = \sqrt[3]{V_0}/r_2$ ; $\gamma_3 = \sqrt[3]{V_0}/r_3$
$R_X = \begin{pmatrix} 1 & 0 & 0 \\ 0 & \cos(\theta_X) & -\sin(\theta_X) \\ 0 & \sin(\theta_X) & \cos(\theta_X) \end{pmatrix}$ ; $R_Y = \begin{pmatrix} \cos(\theta_Y) & 0 & \sin(\theta_Y) \\ 0 & 1 & 0 \\ -\sin(\theta_Y) & 0 & \cos(\theta_Y) \end{pmatrix}$ ;
$R_Z = \begin{pmatrix} \cos(\theta_Z) & -\sin(\theta_Z) & 0 \\ \sin(\theta_Z) & \cos(\theta_Z) & 0 \\ 0 & 0 & 1 \end{pmatrix}$
$\begin{pmatrix} \overrightarrow{u_1} & \overrightarrow{u_2} & \overrightarrow{u_3} \end{pmatrix} = R_Z R_Y R_X$ (void's orthonormal basis)

At each time increment $t$: begin
    Data: $\Delta t^t$ (increment time step)
    $p^t$ (isostatic pressure)
    $\bar{\sigma}^t$ (von Mises equivalent stress)
    $\dot{\bar{\varepsilon}}^t$ (equivalent strain-rate)
    $\bar{\varepsilon}^{t-1}$ (equivalent strain from increment $t-1$)
    $\dot{\boldsymbol{\varepsilon}}^t$ (strain rate tensor)
    $V^{t-1}$ (void volume from increment $t-1$)
    $V_B^{t-1}$ (modified void volume from increment $t-1$)

    For each integration point: begin
        $\bar{\varepsilon}^t = \bar{\varepsilon}^{t-1} + \dot{\bar{\varepsilon}}^t \Delta t^t$ (cumulated equivalent strain)
        $\begin{pmatrix} \overrightarrow{e_1}^t & \overrightarrow{e_2}^t & \overrightarrow{e_3}^t \end{pmatrix}$ by diagonalizing $\dot{\boldsymbol{\varepsilon}}^t$ such that $\dot{\varepsilon}_1 \leq \dot{\varepsilon}_2 \leq \dot{\varepsilon}_3$
        $p_1^t = (\overrightarrow{u_1}.\overrightarrow{e_1}^t)^2$ ; $p_2^t = (\overrightarrow{u_2}.\overrightarrow{e_1}^t)^2$ ; $p_3^t = (\overrightarrow{u_3}.\overrightarrow{e_1}^t)^2$

        if $\bar{\sigma}^t > 0$ and $\dot{\bar{\varepsilon}}^t > 0$ and $V^{t-1} > 0$ then
            $T_X^t = \frac{-p^t}{\bar{\sigma}^t}$
            $B^t = \sum_{i=1}^{3} \sum_{j=0}^{2} \sum_{k=0}^{1} b_{jk} (T_X^t)^k (\gamma_i)^j p_i^t$
            $C^t = \sum_{i=1}^{3} \sum_{j=0}^{2} \sum_{k=0}^{2} c_{jk} (T_X^t)^k (\gamma_i)^j p_i^t$
        end

        $\Delta V^t = (B^t + 2C^t \bar{\varepsilon}^t) \dot{\bar{\varepsilon}}^t \Delta t^t$
        $V^t = V^{t-1} + \Delta V^t$
        $V^t = \max(0, V^t)$

        if $T_X^t > 0$ then
            $\Delta V^t = 0$
        end
        $V_B^t = V_B^{t-1} + \Delta V^t$
        $V_B^t = \max(0, V_B^t)$ (modified volume, ignoring the positive stress triaxiality values)

    end
end
Result: $V^t$, $V_B^t$ (void volume and modified void volume, at increment $t$)
```

Algorithm 3: Computation of the prediction model

Appendix C

Cases of non-uniform loadings

In order to illustrate the effect of non-uniform loadings on void closure, multi-axial compression cases were performed using a spherical void.

On a cubic RVE, the velocity boundary condition was successively imposed along the z- and x-axes, as presented in Tab. C.1. Case A corresponds to a constant compression along z-axis. In the case B, compression along z-axis is interrupted at $\bar{\varepsilon} = 0.1$ and is switched to x-axis. In the case C, compression direction is successively switched from z- to x- and back to z-axis. Cases D, E and F are similar to case B, but switching compression direction later at $\bar{\varepsilon} = 0.2$, $\bar{\varepsilon} = 0.3$ and $\bar{\varepsilon} = 0.5$ respectively. The prescribed stress triaxiality ratio was $T_X = -1/3$.

Interval	$\bar{\varepsilon} = [0 - 0.1]$	$[0.1 - 0.2]$	$[0.2 - 0.3]$	$[0.3 - 0.5]$	$[0.5 - 1.0]$
Case A	Z	Z	Z	Z	Z
Case B	Z	X	X	X	X
Case C	Z	X	Z	Z	Z
Case D	Z	Z	X	X	X
Case E	Z	Z	Z	X	X
Case F	Z	Z	Z	Z	X

Table C.1: Compression axes for all tested cases for non-uniform loadings

Void volume evolutions in Fig. C.1 exhibit significant changes of slope at each switching direction. The z-axis compression deforms the initially spherical shape into an oblate shape, which therefore becomes harder to close in a perpendicular direction (see Fig. C.2). The change of slope is stronger when the switch occurs at larger values of deformation. This effect is illustrated in Figs. C.3, C.4, C.5 and C.6.

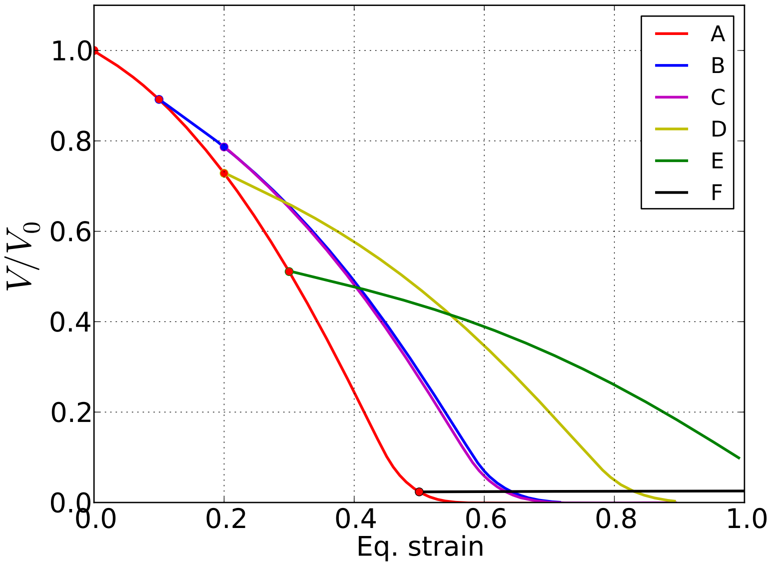

Figure C.1: Non-uniform compression cases on spherical void.

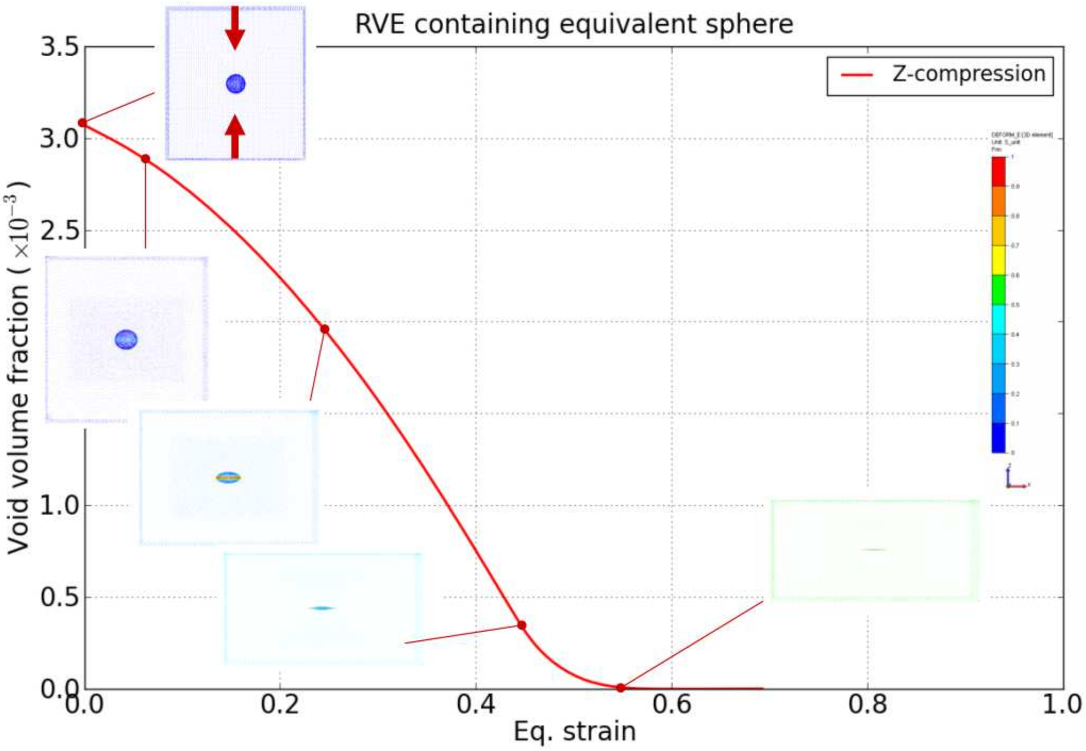

Figure C.2: Detail of void evolution for Case A

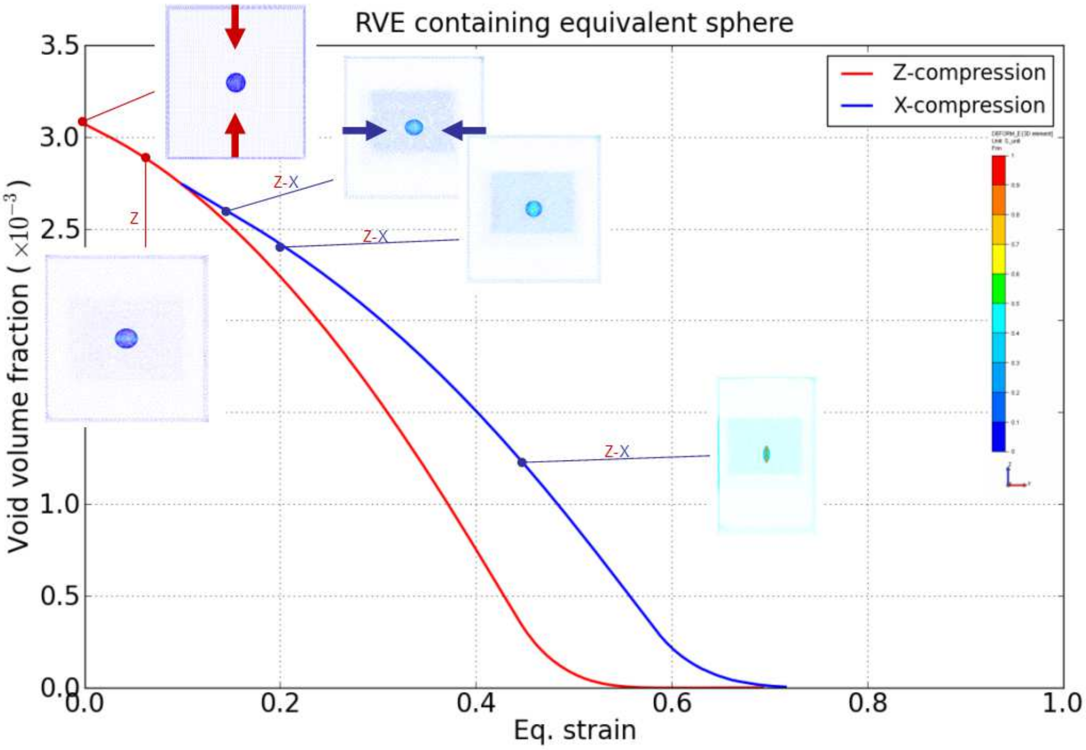

Figure C.3: Detail of void evolution for Case B

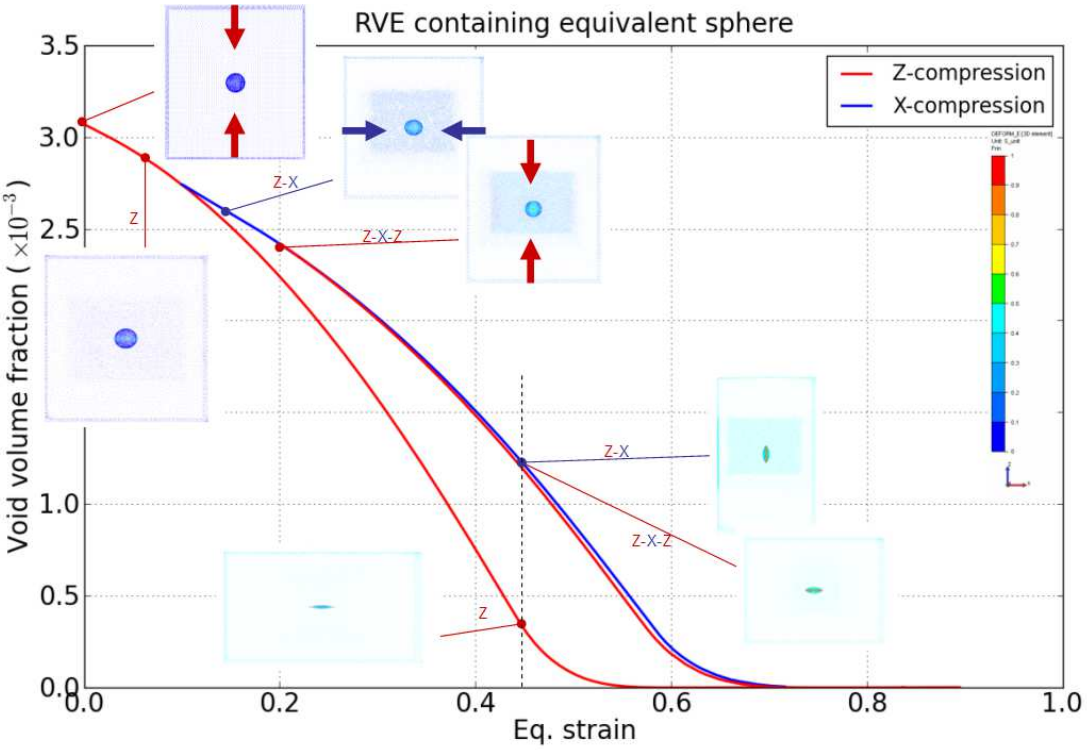

Figure C.4: Detail of void evolution for Case C

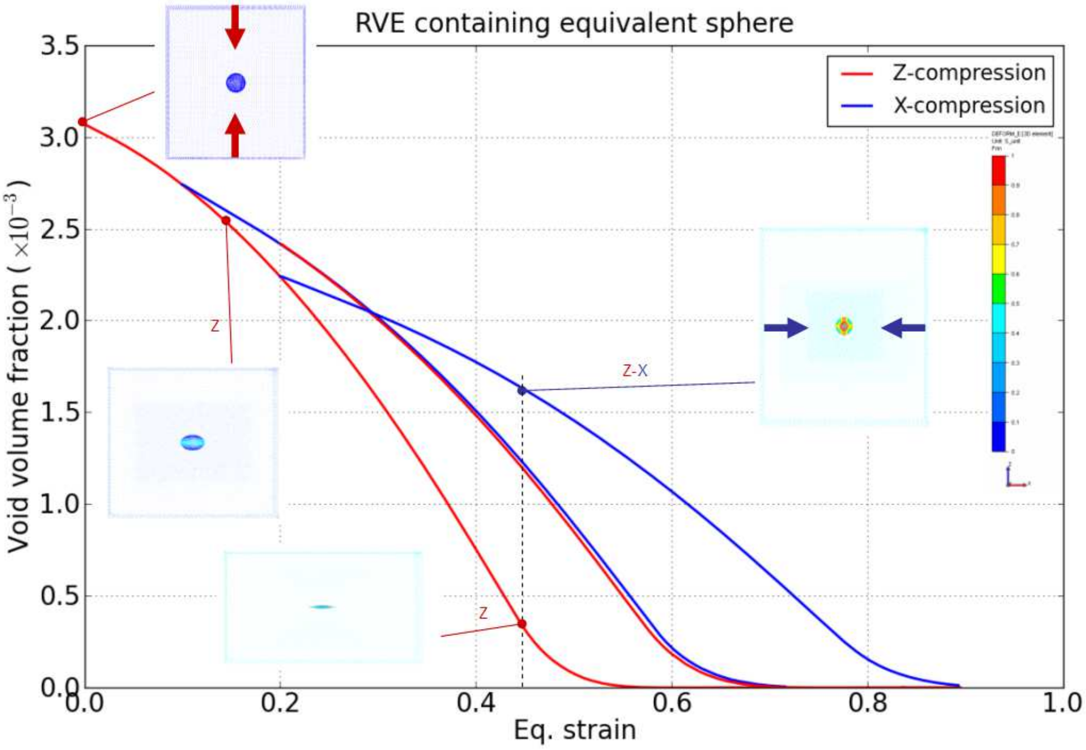

Figure C.5: Detail of void evolution for Case D

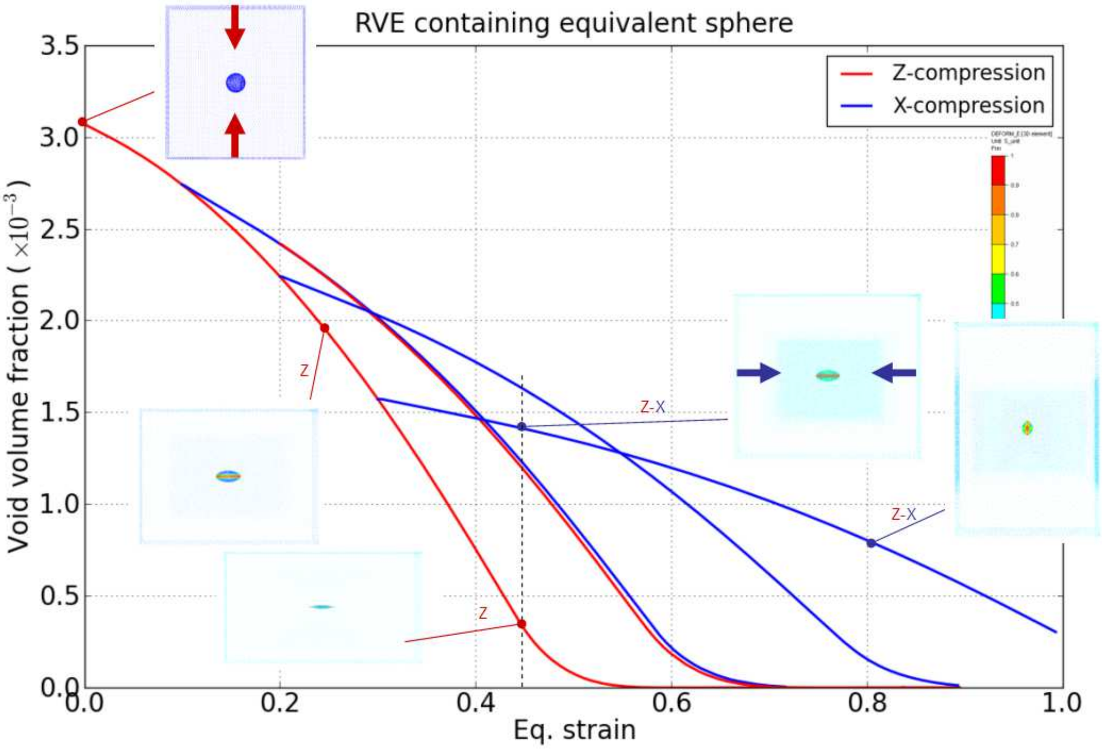

Figure C.6: Detail of void evolution for Case E

Compréhension et modélisation des mécanismes de refermeture de porosité dans les procédés de mise en forme des métaux à chaud

RESUME : Lors de l'élaboration de pièces métalliques de grandes dimensions, la présence interne de pores est habituellement observée. Ces défauts internes sont généralement refermés lors des premières passes de transformation à chaud. Ce travail vise à mieux comprendre les mécanismes de refermeture en identifiant les paramètres procédés, matériaux et morphologiques clés. Les deux approches (explicite en champ complet, et micro-analytique) classiquement utilisées dans littérature sont discutées. Il est montré que ces deux approches ne sont pas suffisantes pour établir un modèle de prédiction dont la précision réponde aux enjeux industriels. Une nouvelle approche est donc proposée dans cette thèse à l'échelle mésoscopique. Les mécanismes de refermeture sont étudiés à l'échelle d'un volume élémentaire représentatif (VER), permettant une description 3D particulièrement précise des mécanismes locaux, tout en appliquant des conditions aux limites représentatives des états mécaniques mis en jeu à l'échelle macroscopique. Les mécanismes locaux ont été étudiés au moyen d'une vaste campagne de simulations éléments-finis 3D à l'échelle d'un VER. Les paramètres étudiés sont : les paramètres matériaux, la morphologie du pore, et le chargement thermomécanique subi durant la déformation. L'étude a montré que la morphologie et l'état de contraintes sont de premier ordre sur le comportement en refermeture. Ces influences ont ensuite été quantifiées afin de proposer un modèle de prédiction de refermeture robuste. Le modèle a finalement été implémenté dans un code éléments finis et une validation sur cas industriels est présentée afin d'évaluer les bénéfices de nouveau modèle. Une validation expérimentale a été menée par des essais d'écrasements d'échantillons poreux dont l'état de porosité a été mesuré par micro-tomographie aux rayons X avant et après les essais.

Mots clés : refermeture de porosité, modèle moyenné, éléments finis, échelle mésoscopique

Understanding and modeling of void closure mechanisms in hot metal forming processes

ABSTRACT: During production of large metal workpieces, an internal presence of voids is usually observed. Such internal defaults are generally closed up during the first passes of hot forming processes. The present work aims to better understand void closure mechanisms with respect to the involved materials, processes and voids' morphological parameters. An extensive study regarding existing models in the literature is first presented. Two main approaches are discussed: the explicit full-field approach and the micro-analytical approach. It is shown that none of both approaches is sufficient to precisely predict void closure according to the industrial issues. A new approach is thus proposed at the mesoscale. Void closure mechanisms are studied using a representative volume element (RVE). Local mechanisms of void closure are studied using a large campaign of 3D finite element simulations at the RVE-scale. The studied parameters are: the materials parameters, the void's morphology and the thermomechanical loading during hot forming processes. Both the void's morphology and the stress state exhibit a first-order influence on void closure. A new reliable prediction model is proposed with respect to these parameters. The void's morphology is quantitatively studied in terms of equivalent dimensions (tridimensional aspect ratios), and orientation (with respect to principal deformation direction). The stress state is expressed using the stress triaxiality ratio. The proposed model was finally implemented in a material forming finite element software. Validation cases are presented using industrial processes in order to highlight the benefits of this new model. An experimental validation was also performed using compression tests of porous samples. The samples were examined using X-ray micro-tomography before and after compression.

Keywords : void closure, mean-field model, finite element, meso-scale

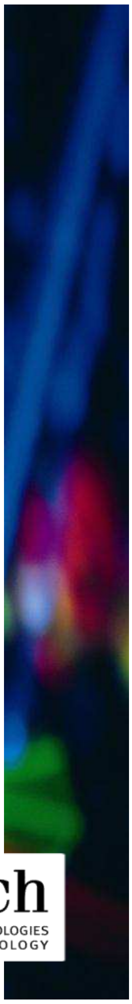

MINES ParisTech

ParisTech
INSTITUT DES SCIENCES ET TECHNOLOGIES
PARIS INSTITUTE OF TECHNOLOGY